International Journal of Industrial Electronics, Control and Optimization © 2021 IECO
Vol.4, No. 1, pp. 1-11, Jan (2021)

Designing an Indirect Adaptive Multiple Controller for LTI Systems with Large Time-Varying and Unknown Delays in Control Input Based on Online Estimation of Delay by Kalman Filtering

Hadi Chahkandi Nejad[1,†], Mohsen Farshad[2], and Ramazan Havangi[3]

[1, 2, 3] Department of Electrical and Computer Engineering, University of Birjand, Birjand, Iran

ABSTRACT

The present study presents an adaptive controller for LTI systems with an unknown and time-variant input time delay with the purpose of tracking. Due to the wide area considered for time delay variations, the structure of the proposed controller is considered to be in the form of Multiple Adaptive Control (MAC). The presented adaptive control system is of indirect type, i.e., at any moment, one band of time delay is first identified using a proposed estimator, and then the main control signal, which is a linear combination of multiple controllers output, is formed with a switching rule in the supervisory subdivision. In fact, each multiple controller in the MAC structure with fit weights participates in forming the main control signal. The multiple controllers used in this study are of PID type. It should be noted that the parameters for the individual multiple controllers, for the system under control, are adjusted offline and proportional to its corresponding time-delay sub-band using a genetic algorithm. Finally, simulation results show the relatively desirable performance of the proposed control system and observer in facing with wide unknown and time-variant delays.

Article Info

Keywords:
Adaptive control, Delay estimator, Input delay, Kalman filtering, LTI Systems, Satellite telecommunications, Time-Variant uncertainty.

Article History:
Received 2020-01-14
Accepted 2020*-08-31

I. INTRODUCTION

The control of delayed systems is among the issues of the day in the world of Control Engineering. The existence of delays in most real and manmade systems has attracted the attention of many researchers to this issue. The importance of this issue arises from the fact that delay in a control loop is accompanied by the system divergence from the desirable performance, and if the necessary preparations are not considered, it may even lead to system instability. Since inherent delays are an inseparable component of a delayed system, considering delays in the controller design process is the only strategy for encountering this issue. Even if an open-loop system could be modeled without any delay, this point should be kept in mind that the closed-loop control process itself, i.e. measurement, decision-making, and reaction of the controller, causes a delay in the plant input; a delay that can also be affected by the varying environment. Time delay systems introduce a class of systems with an infinite dimension, which is related to mechanisms such as dispersion, transmission, traffic, exhaustion, flexibility, inertia, and other factors that are created after time drop-off. From the perspective of time delay certainty and variability, delayed systems are generally categorized into four groups: (1) systems with a certain and time-invariant delay, (2)

[†] **Corresponding Author**: hchahkandin@birjand.ac.ir
Faculty of Electrical and Computer Engineering, University of Birjand, Birjand, Iran

systems with a certain and time-variant delay, (3) systems with an uncertain and time-invariant delay and, (4) systems with an uncertain and time-variant delay.

All these four types may appear in different systems. Concerning the fourth group, it is of great importance to discuss a control algorithm that can fulfill the stability or tracking performance. In general, a delay may exist in a state vector or an input. In this article, time delay means the delay in control input. In most real systems, time delay affects the system performance either inherently or under the impression of environmental conditions. The problems that mainly emerge in a closed-loop control process of delayed systems are caused by the following factors [1]:

1- The effect of disturbances is not felt until a considerable time has elapsed.

2- The effect of the control action takes some time to be felt in the controlled variable.

3- The control action that is applied based on the actual error tries to correct a situation that has originated some time before.

4- Since system equations are nonlinear in relation to time delay parameters, the sensitivity of control characteristics to these parameters is relatively high, so researchers usually look for a robust design given the uncertain nature of time delay.

5- Changes in an open-loop transfer function time delay in closed-loop control systems lead to phase margin change and gain margin indirect change too; this may lead to closed-loop system instability or may decrease relative stability, and hence it may cause transient response characteristics to become undesirable.

Considering that the system behavior is nonlinear to the delay factor, designing techniques for making appropriate control reaction gets more complicated by delay change over time because the designer will also face a time-variant system (certain or uncertain). When a delay is time-varying and unknown, it is often dealt with as a parameter with uncertainty, so the designing robustness against any changes in this parameter should be discussed. Robust control always provides appropriate control strategies for parametric uncertainties [2]-[3], but if these uncertainties change slowly, adaptive control would definitely be a more appropriate option. In particular, the largeness of the variation area for an uncertain parameter always persuades the designer to use a specific area in adaptive control, named Multiple Adaptive Control (MAC). This study assumes that any change in an unknown parameter, i.e., time delay, is in the LTI system, so the MAC structure is used to control this system. In this structure, the wide uncertainty band is partitioned into smaller sub-bands, and for each selected band, a suitable controller is designed. The controller at any moment is selected based on the delay estimation at that very moment. Also, regarding time delay estimation, this paper presents a new method with a rather high accuracy and speed. In the multiple control structure, the supervisory subdivision is responsible for switching between controllers. Switching between the designed controllers, due to its discrete nature, may by itself be a reason for instability. Picking a suitable switching rule decreases the undesired effects of the controller variation in the control loop and the control signal effort. Using combined methods, in which the control signal is a weighted combination of multiple controllers output, is accompanied by the risk of instability because of the increase in control signal gain. Therefore, choosing a suitable switching rule is as important as appropriately designing the controllers of each band. Using modern optimization methods, in addition to providing an appropriate stability margin for switching operation, may provide optimal conditions for controlling a delayed system. In this study, it has been tried to use an optimal approach in the structure of a MAC to reduce the switching effect of controllers and optimally adjust the parameters of the controllers related to each delay band in order to provide a rather desirable performance for systems with wide variable delay. Further, Subsection *A* provides a brief history of what has been done in this regard so far. Subsection *B* focuses on the challenges of the current control methods. Section II introduces the structure of the plant, and then Section III presents the proposed estimator for estimating a time-variant delay. Section IV provides a brief description of the MAC control structure and the proposed controller. Finally, Section V presents the results of the simulations for a sample system and Section VI analyzes the performance of the proposed controller and concludes the paper.

A. Research Literature

The difficulty of time delay identification comes from the fact that the process model is nonlinear in relation to the delay parameter. Based on the literature studied in Ref. [4], the delay identification methods are divided into four groups: (a) time delay approximation methods, (b) time delay explicit parameter methods, (c) area and moment methods, and (d) higher-order statistics (HOS) methods. Several methods of this category have been presented in papers [4]-[11] such that in case of adaptive control and real-time control, methods of groups (a) and (b) are mainly used. Particularly, for time-varying delay estimation in LTI systems, many articles have been published [12]-[19].

Generally, a time delay in open-loop systems is a non-minimum phase factor. It has been proven in many studies that the stability of control loops, in the presence of delay, is too sensitive to time delay parameters, so this has made researchers try hard to present reliable criteria for creating a safe stability margin in the area of designing controllers for such systems [20]-[26].

Also particularly for LTI systems with uncertainty in time delay factor, a lot of efforts have been put on presenting criteria for guaranteeing robust stability [27]-[29].

The importance of controlling systems with a time-varying delay has provoked researchers to design controllers that are acceptably robust and adaptable against variations of the sensitive time delay parameter in order to satisfy the supreme control purposes such as reference input tracking.

Some of these controllers are as follows: robust controllers [30]-[32], fuzzy controllers [33], predictive controllers [34]-[37], sliding mode controllers [38]-[39], and optimal controllers [40]-[42]. In particular, the presented controllers are mostly of adaptive type for LTI systems with an unknown and time-varying delay [43]-[48].

B. Challenges of the Current Control Methods

Pondering upon the works done in the area of controlling systems with a time-varying delay, it seems that they have some problems and challenges. Generally, in all studies on delayed systems, the band of time delay variations and uncertainty are assumed to be rather small. Although robust controllers and sliding mode show rather appropriate response in small uncertainty bands, since the nature of these controllers is unit and constant, the control system response in great perturbations of the nominal model, even with precise modeling of uncertainties, would be of undesired transient characteristics, especially if the variations in time delay parameters is rapid. Particularly, in sliding mode controllers, large and fast time delay variations result in chattering and hence control effort.

Predictive and optimal controllers are often presented for systems in which the time delay is known (constant or time-variant) because if the delay parameter is time-varying and unknown, these controllers perform weakly, since both of these controllers have an optimization operation, and if the delay is time-varying and unknown, the designer should deal with a time-variant and unplanned optimization problem, the solution of which, due to the computational complications, may in turn cause time delay in the control process of real-time mode [49].

Also, intelligent controllers, such as fuzzy and neural ones, partly have lower spreading speed in comparison to real time due to the computational and decision making complications of the network, which, in turn, results in time delays in control loops.

Eventually, the adaptive controllers presented for systems with a time-varying and unknown delay are mainly assumed to have a small band of uncertainty. The reason for this is that the large band of uncertainty causes a decrease in the estimation speed, hence a decrease in the adaptability of the controller and a decrease in the speed of control reactions, which by themselves lead to the emergence of undesired transient mode errors in response to the control system.

II. PROBLEM STATEMENT

The plant in this research is an LTI and a stable system (BIBO Stable). The state-space equations and the Laplace transfer function of the assumed system are as follows:

$$\begin{cases} X(\dot{t}) = A_g X(t) + B_g u_C(t - d(t)) \\ y(t) = C_g X(t) \end{cases} \tag{1}$$

$$P(s,t) = G(s)e^{-d(t)s} \tag{2}$$

in which t is the variable of real-time domain, $X(t) \in R^n$ is the state vector of the system, scalars $u_C(t), y(t)$ are control input and plant output, respectively, and A_g, B_g, C_g are the constant matrices with appropriate dimensions. Also, s is the variable of the Laplace domain and $P(s,t)$ is the system transfer function at the time t, in which $G(s)$ is obtained from Eq. (3).

$$G(s) = C_g(sI - A_g)^{-1}B_g \tag{3}$$

In addition, the $e^{-d(t)s}$ factor is the Laplace transfer function of the time delay. In Eq. (1) and (2), $d(t)$ is the same input time delay of the system, which is assumed to be time-variant and unknown in this study, and it is also assumed that the considered system, except for t from a time delay factor, is a linear and time-invariant system. In general, this study makes the following assumptions for the time delay [50]:

1- $0 \leq d_{min} \leq d(t) \leq d_{max} \leq \infty$
2- $-\infty < d(t)^{\bullet} < 1$

The main purpose of this research is to design a tracking controller in the presence of a time-variant and unknown time delay, in which the band of the time delay uncertainty is rather wide.

III. PROPOSED DELAY ESTIMATOR

In general, an estimator is a dynamical system that estimates one or more unknown parameter(s) of the real system using the real system input and output. Particularly, in this study, one of the important goals is to design an estimator system in that the only unknown and time-variant parameter of the system is identified at an online mode and with an acceptable speed using the input and output of the system with Eq. (2). A simple block diagram of the system and delay estimator is shown in Fig. 1. As can be seen in Fig. 1, the estimator inputs are the same input and output of the real system, and the only output of the estimator is an estimation of the time delay ($\hat{d}(t)$).

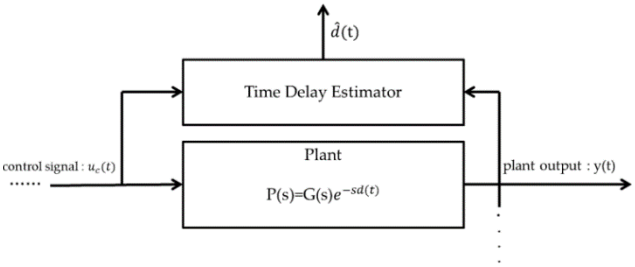

Fig. 1. The general diagram of the time delay estimator.

According to Eq. (2), a delayed system transfer function includes a time delay factor (exponential and non-rational). In this research, to design the proposed estimator, instead of a time delay exponential factor, a pade approximation is first used to rationalize the system transfer function. In this case, the new transfer function, which is an approximation of the main transfer function of the system, will include a time delay parameter (time-variant). After writing a state-space realization from the mentioned transfer function, and by regarding the time delay parameter as an extra state variable parameter, a system with nonlinear state equations will be established. Eventually, using a Kalman filter (linear or extended for linearized or non-linear state equations, respectively), the states of this system, e.g. the system time delay, are predicted.

In this research, to further describe the estimator design in detail, a first-order pade approximation is used as an alternative for the time delay factor. Obviously, higher-order pade approximations can be used to improve the estimation accuracy. Eq. (4) is indicative of a first-order pade approximation for the time delay factor in the Laplace area [1].

$$C'(s) = \frac{1-\frac{\hat{d}}{2}s}{1+\frac{\hat{d}}{2}s} \quad , \quad \hat{d} = \hat{d}(t) \tag{4}$$

Substituting Eq. (4) in Eq. (2), the system transfer function will be as follows:

$$P(s) = G(s)\ \frac{1-\frac{d}{2}s}{1+\frac{d}{2}s} \tag{5}$$

Considering that the $G(s)$ transfer function is of *n*-order, the $P(s)$ transfer function will definitely be of (*n+1*)-order. If the delay is assumed a constant parameter, in general, $A_p\,, B_p\,, C_p$ matrixes, for a realization of $P(s)$ system, will be a function of delay parameter, i.e. d. Therefore, $P(s)$ system state equations could be written as Eq. (6).

$$\begin{cases} \dot{Z(t)} = A_p(d).Z(t) + B_p(d).u(t) \\ y(t) = C_p(d).Z(t) \end{cases} \tag{6}$$

Where $Z(t) \in R^{n+1}$ is the $P(s)$ system state variables vector, and $A_p(d), B_p(d), C_p(d)$ are the matrixes with appropriate dimensions, which are dependent on the time delay parameter. Also, $y(t)$ and $u(t)$ scalars are the input and output of $P(s)$ system, respectively. Given that the parameter d is constant, the equations in Eq. (6) will be relevant to an (*n*+*1*)-order LTI system. Considering that $d(t)$ is, in reality, an unknown and time-variant parameter, it could be regarded as an extra state variable in Eq. (6). In this case, Eq. (6) will turn into a group of nonlinear state-space equations, whose order is changed from (*n+1)* to (*n+2*) due to the addition of a new state variable (time delay). State-space equations for this system will conform to Eq. (7).

$$\begin{cases} \dot{w_1}(t) = \dot{z_1}(t) = f_1\big(w_1(t), w_2(t), \dots, w_{n+1}(t), w_{n+2}(t)\big) + \\ \qquad g_1\big(w_1(t), w_2(t), \dots, w_{n+1}(t), w_{n+2}(t), u(t)\big) + v_1(t) \\ \qquad\qquad . \\ \qquad\qquad . \\ \qquad\qquad . \\ \dot{w}_{n+1}(t) = \dot{z}_{n+1}(t) = f_{n+1}\big(w_1(t), w_2(t), \dots, w_{n+1}(t), w_{n+2}(t)\big) + \\ \qquad g_{n+1}\big(w_1(t), w_2(t), \dots, w_{n+1}(t), w_{n+2}(t), u(t)\big) + v_{n+1}(t) \\ \dot{w}_{n+2}(t) = \dot{d}(t) = f_{n+2}\big(w_1(t), w_2(t), \dots, w_{n+1}(t), w_{n+2}(t)\big) + \\ \qquad g_{n+2}\big(w_1(t), w_2(t), \dots, w_{n+1}(t), w_{n+2}(t), u(t)\big) + v_{n+2}(t) \\ y(t) = h\big(w_1(t), w_2(t), \dots, w_{n+1}(t), w_{n+2}(t)\big) + n(t) \end{cases} \tag{7}$$

$$\begin{cases} \dot{W}_{(t)} = F\big(W_{(t)}\big) + G\left(W_{(t)}, u(t)\right) + V_{(t)} \\ y(t) = h\big(W_{(t)}\big) + n(t) \end{cases} \tag{8}$$

Comparing Eq. (7) and Eq. (8), $G(.)\, and\, F(.)$ matrix functions and also $V_{(t)}$ vector in the above equation are identified. After computing the system state space equations in the structure of Eq. (7), all the system state variables, including the system time delay, should be estimated using a state observer in the next step. At this point, all system states can be estimated with a Kalman filter (linear or extended) [51]. Further details on the design of this estimator are provided in Ref. [18].

IV. PROPOSED CONTROLLER

In general, controlling the system based on the estimated situation is an adaptive control issue, in which the controller parameters are adjusted either directly or indirectly. Experience shows that using adaptive control in cases where the band of uncertainty for one or more parameter(s) is rather large, large transient state errors occur because the convergence speed of controller parameters (direct or indirect adjustment) towards the desired parameters is low. In such cases, an alternative method is to use MACs to control an unknown system; a method that is considered a higher level of adaptive control. The advantages of this control method, as mentioned in the literature, are high speed, ability to control systems with rather wider parametric uncertainties, and smaller control effort (in case of optimal designing for a safe and soft switching) [52]-[55].

In general, a multiple adaptive controller can be used in two structures, direct and indirect. In both control structures, an essential element in the MAC controller is the supervisory and switching section of the controller. Thus, presenting better methods in the switching section to improve stability and transient behavior of the plant has always been among the concerns of researchers while designing these controllers [52].

Fig. 2 presents an indirect multiple adaptive controller (IMAC), in which, an estimation of the plant's unknown parameters is first obtained by an estimator block, and then, considering the band in which the estimated parameters exist, each of the multiple controllers, with specific weights, take part in forming the main control signal [52].

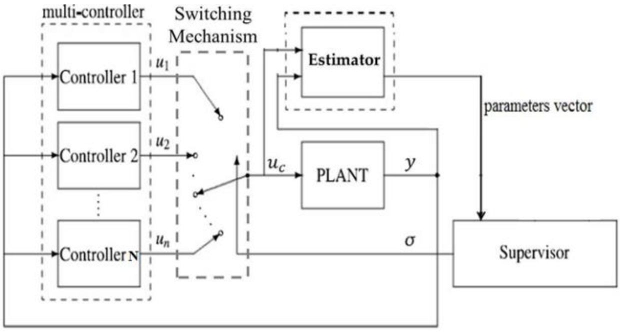

Fig. 2. The proposed structure of the IMAC controller.

Given the challenges and difficulties of control methods for systems with a varying delay, presented in Section I (subsection B), and also taking into account the advantages of multiple adaptive controllers, this study uses an IMAC control structure to control LTI systems with an input time-varying delay. For this purpose, the considered time delay of the plant is an unknown and variable parameter. The control process will be such that first, according to Fig. 3, the area of the time delay variations will be partitioned into smaller sub-bands (N sub-bands). Then, depending on the band in which the system delay has been estimated, in the IMAC structure, multiple controllers with fit weights will enter the control loop. In Fig. 3, M_i shows the center of the i^{th} sub-band.

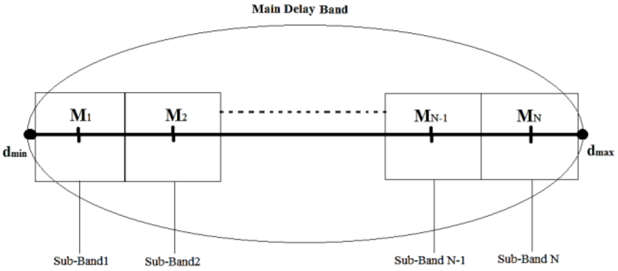

Fig. 3. How to split the main band of the delay into N equal sub-bands.

In this study, assuming that the control structure is the one presented in Fig. 2, a number of PID controllers in the multiple controllers section are used [56]. The parameters of each multiple controller (proportional, integral, and derivative coefficients) are adjusted at offline mode and by solving an optimization problem. The minimization method used in this paper is a genetic algorithm [57]. It should be said that the parameters of each of the multiple controllers are optimized independently for its corresponding delay sub-band .In this regard, the fitness function counted for the optimization problem is considered to be affected by the control signal effort, and the error between plant output and desired output (reference input). Eq. (9) expresses the mentioned fitness function.

$$\int \left(\alpha\left(y(t)-u_R(t)\right)^2+\beta\left(u_c(t+\Delta t)-u_c(t)\right)^2\right)dt \qquad (9)$$

Where α and β are positive and real constants that express the importance of minimization for tracking error and control effort, respectively. These are assumed to be equal in this article. In this study, a suitable method for adjusting controllers weights have been used to avoid the adverse effects of discrete switching of the controllers (hard switching) such that, according to Eq. (10), the main control signal, i.e. $u_c(t)$, is a linear and weighted combination of the output of all multiple controllers.

$$\begin{cases} u_c(t)=A^T\times U(t)=\sum_{i=1}^{N}a_iu_i(t) \\ A=[a_1\ a_2\ \dots\ a_N]^T\ ,\ U(t)=[u_1(t)\ u_2(t)\ \dots\ u_N(t)]^T \end{cases} \qquad (10)$$

Where $u_i(t)$ is the i^{th} controller output at time t, N is the number of multiple controllers, and a_i is the weight of the i^{th} controller, which is obtained from Eq. (11):

$$a_i=\frac{e^{-b_i}}{\sum_{j=1}^{N}e^{-b_j}} \qquad (11)$$

Where b_i, at any moment of time, is obtained from Eq. (12).

$$b_i=\left|K\left(\hat{d}(t)-M_i\right)\right| \qquad (12)$$

Assuming that the main uncertainty band for a time delay is partitioned into N sub-bands, in Eq. (12), M_i will be the center of the i^{th} sub-band. Thus, as seen in the above equations, the weight of the controllers is a function of the absolute value of the error between the average value of delay bands and the value of the estimated delay. It is obvious that, at any moment, the closer the delay estimation is to the average value of the delay in a sub-band, the more weighted the controller corresponding to that band will participate in creating the main control signal, and also at any moment, the sum of the weights of all controllers is equal to one, and this factor always prevents the increase in the open-loop dc gain. Parameter $K\geq 0$ in Eq. (12) is a designing parameter. In this equation, K determines the type of switching such that if $K=0$, switching will be of soft and continuous type (no switching operation), and each controller with a share of $\frac{1}{N}$ will always participate in forming the main control signal, and by an increase in K from zero to infinite, the type of switching tends to be discrete and hard. More details of the design will be presented in Section V for a specific system in a numerical example.

V. SIMULATION RESULTS

In this section, to implement different simulations and assess the proposed estimator and controller, an LTI system with the following open-loop transfer function is selected. It should be noted that the phase margin (PM) for this system is 1.7068 [rad] and the delay margin is 2.6364 [sec]. This transfer function relates to a direct current (DC) servo motor system, which expresses the relationship of the motor output (rotation angle) to its input (electricity current). Since the motor in a telecommunication satellite is responsible for adjusting the orientation of an antenna, there is always a time-varying unknown delay between sending the control signal from the earth station and receiving it in the space station [58].

$$P(s,t)=\frac{3(1+s)}{(1+2s)(1+3s)}e^{s\times d(t)} \tag{13}$$

In which $d=d(t)$ is an unknown and time-variant delay. To design the delay estimator, the band of delay variations should be specified, so it is assumed that $d_{min}=0.65[s] \le d \le d_{max}=4.65[s]$. Given that Eq. (4) is used for time delay factor approximation, $P(s)$ could be rewritten as Eq. (14).

$$P(s,t)=\frac{-0.5s^2+\left(\frac{1}{d}-0.5\right)s+\frac{1}{d}}{s^3+\left(\frac{2}{d}+0.83\right)s^2+\left(\frac{1.66}{d}+0.17\right)s+\frac{0.33}{d}} \tag{14}$$

By writing an observer canonical realization for the above system, the state space equations of this system will be obtained as follows:

$$\begin{cases}\begin{bmatrix} z_1(t)\\ z_2(t)\\ z_3(t)\end{bmatrix}^{\bullet}=\begin{bmatrix} 0 & 0 & \frac{-0.33}{d}\\ 1 & 0 & -(\frac{1.66}{d}+0.17)\\ 0 & 1 & -(\frac{2}{d}+0.83)\end{bmatrix}\begin{bmatrix} z_1(t)\\ z_2(t)\\ z_3(t)\end{bmatrix}+\begin{bmatrix} \frac{1}{d}\\ \frac{1}{d}-0.5\\ -0.5\end{bmatrix}u(t)\\ y(t)=\begin{bmatrix}0 & 0 & 1\end{bmatrix}\begin{bmatrix} z_1(t)\\ z_2(t)\\ z_3(t)\end{bmatrix}\end{cases} \tag{15}$$

Considering d(t) as the fourth state variable ($d=w_4(t)$), and defining $w_1(t)=z_1(t)$, $w_2(t)=z_2(t)$, $w_2(t)=z_2(t)$, nonlinear state space equations for this system are obtained according to Eq. (16):

$$\begin{cases}\dot{w_1}(t)=\frac{-0.33w_3(t)}{w_4(t)}+\frac{u(t)}{w_4(t)}+v_1(t)\\ \dot{w_2}(t)=w_1(t)-\left(\frac{1.66}{w_4(t)}+0.17\right)w_3(t)+\left(\frac{1}{w_4(t)}-0.5\right)u(t)+v_2(t)\\ \dot{w_3}(t)=w_2(t)-\left(\frac{2}{w_4(t)}+0.83\right)w_3(t)-0.5u(t)+v_3(t)\\ \dot{w_4}(t)=v_4(t)\\ y(t)=w_3(t)+n(t)\end{cases} \tag{16}$$

It is obvious that these equations are used to design the extended Kalman filter (EKF); and to implement the delay estimator, based on a linear Kalman filter (LKF), the system with equations presented in Eq. (16) should be linearized around a fixed operating point.

In this research, the results of the simulations will be presented along with two main objectives; the first is to design a time delay estimator for the system with Eq. (13), and the second is to design a tracking adaptive controller for this system. In all simulations, the reference input signal for the system has been considered a periodic pulse wave; a two-level periodic pulse wave with a periodicity of 40 seconds and a pulse width of 20 seconds (levels with the values of 10 and 0, respectively). It should be noted that all measurements are in the presence of noise.

The results of the simulations are presented below to estimate the system delay with Eq. (13). It should be noted that this estimate is in the loop and in the presence of the controller. Fig. 4 shows the performance of the proposed estimators in estimating sinusoidal delay. In this figure, the real delay of the system equals $d(t)=2.65+2\sin(0.025\pi t)$. To accurately compare the performance of these estimators, the mean of squares of estimation error (MSE) for all two estimators have been calculated, which are shown in Table I. According to what is presented in Fig .4 and Table I, it could be said that the accuracy of the second proposed estimator is higher than that of the first proposed estimator.

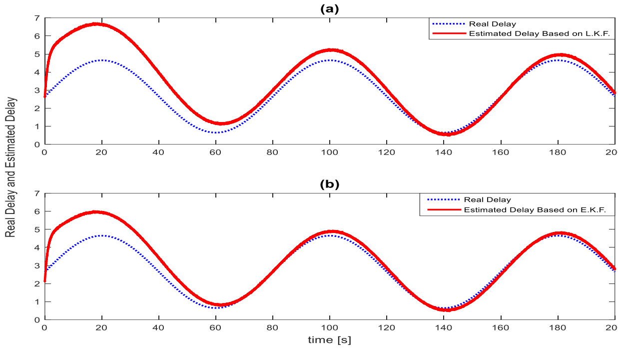

Fig. 4. The comparison of the two proposed estimators in the sinusoidal time delay estimation problem.

(a) Delay estimator based on LKF, (b) Delay estimator based on EKF.

TABLE I

THE COMPARISON OF THE ACCURACY OF THE PROPOSED ESTIMATORS IN SINUSOIDAL TIME DELAY ESTIMATION PROBLEM.

Delay Estimator	Mean of Squares of Estimation Error
Proposed Method 1 (P.M.1)	0.68
Proposed Method 1 (P.M.2)	0.32

Next, the design of a tracker controller in accordance with the proposal in Section IV will be the goal so that the output of the closed-loop system will follow the reference input signal with a minimum error. For this purpose, four PID controllers are considered as multiple controllers ($N=4$); that, in an offline optimization problem, with the cost function according to Eq. (9), the parameters of these controllers have to be calculated. It should be noted that the interval of delay variations should also be divided into the following four sub-intervals:

$$\begin{cases}0.65\le d<1.65 & \rightarrow M_1=1.15\\ 1.65\le d<2.65 & \rightarrow M_2=2.15\\ 2.65\le d<3.65 & \rightarrow M_3=3.15\\ 3.65\le d\le 4.65 & \rightarrow M_4=4.15\end{cases} \tag{17}$$

As was mentioned in Section IV, M_i is the center of the i^{th} sub-frame of delay. It should be noted that each of the multiple controllers corresponds to a sub-band of the time delay. The corresponding transfer functions for multiple controllers are as follows:

$$\begin{cases}PID_1(s)=K_{P1}+K_{I1}\frac{1}{s}+K_{D1}s\\ PID_2(s)=K_{P2}+K_{I2}\frac{1}{s}+K_{D2}s\\ PID_3(s)=K_{P3}+K_{I3}\frac{1}{s}+K_{D3}s\\ PID_4(s)=K_{P4}+K_{I4}\frac{1}{s}+K_{D4}s\end{cases} \tag{18}$$

Where $PID_i(s)$ is the i th controller transfer function $(for\ i = 1, \dots, N = 4)$. In Eq. (18) K_{Pi}, K_{Di} and K_{Pi} are proportional, derivative, and integral coefficients for the i^{th} controller, respectively. Also according to Eq. (10)-(12) in Section IV, the supervisory rule for switching the above controllers will be as displayed in Fig. 5 where it is assumed that $K = 1$ is assumed.

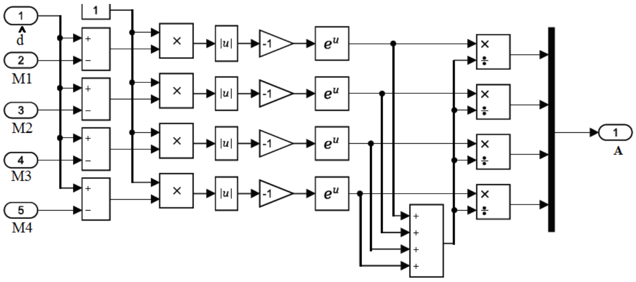

Fig. 5. The block diagram of the switching mechanism of multiple controllers.

After solving four optimization problems in the 3D space by a genetic algorithm, the parameters of the multiple controllers are set as follows:

$$\begin{cases} PID_1: & K_{P1} = 0.74\ , K_{I1} = 0.11\ , K_{D1} = 0.12 \\ PID_2: & K_{P2} = 0.55\ , K_{I2} = 0.08\ , K_{D2} = 0.25 \\ PID_3: & K_{P3} = 0.25\ , K_{I3} = 0.06\ , K_{D3} = 0.11 \\ PID_4: & K_{P4} = 0.17\ , K_{I4} = 0.04\ , K_{D4} = 0.02 \end{cases} \quad (19)$$

By specifying the delay estimator, switching, and multiple controllers mechanisms, simulation results for the proposed controller performance in several scenarios are presented below. To understand the importance of controlling the system specified in Eq. (13), the Nyquist diagram of this system for various time delays (available in the main band of delay variations) is shown in Fig. 6. As can be seen in this figure, the closed-loop system becomes unstable for delays of more than DM=2.6364 seconds because the Nyquist plot for the open-loop system has encircled clockwise the critical point -1. In such a situation, due to the variability of the time delay of the system, by fluctuating the delay signal around its critical value, the closed-loop system experiences various states of stability and instability, making it important to control these types of systems.

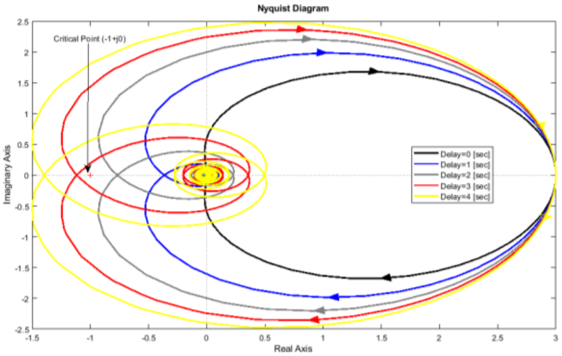

Fig. 6. The Nyquist diagrams of the open-loop system, $d = 0,1,2,3,4$.

Fig. 7 illustrates the closed-loop system response in various conditions. In part (a) of Fig. 7, the closed-loop system response is observed in the presence of a PID controller whose parameters are set for the minimum delay ($d = 0.65$). Also In part (b) of this figure, the closed-loop system response is observed in the presence of a PID controller, but this time the parameters of this controller are set for the maximum delay ($d = 0.65$).

The parameters of these controllers, adjusted for minimum and maximum delay, are given in Eq. (20) and (21), respectively.

$$PID\ for\ d_{min}: \quad K_P = 0.68\ , K_I = 0.20\ , K_D = 0.10 \qquad (20)$$

$$PID\ for\ d_{max}: \quad K_P = 0.19\ , K_I = 0.04\ , K_D = 0.01 \qquad (21)$$

In part (c) of Fig. 7, the closed-loop system response is plotted in the presence of a multiple adaptive controller, which is actually the proposed controller. It should be noted that for this controller, a hard switching for the proposed controller is considered. That is, the constant of switching for the supervisory subsystem is assumed to be $K = 100$. Fig. 8 also shows the control effort signal corresponding to each of the above three control systems.

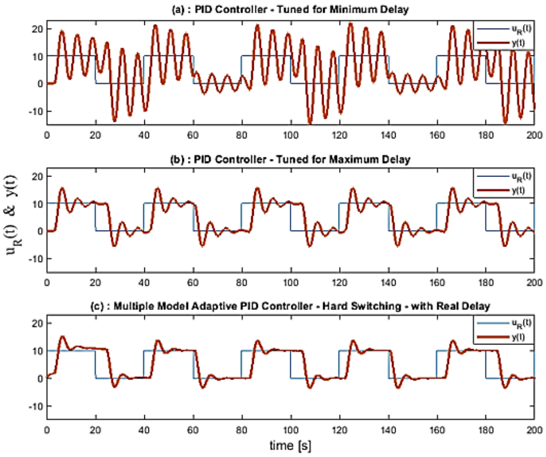

Fig. 7. The closed-loop system response depending on different controllers.

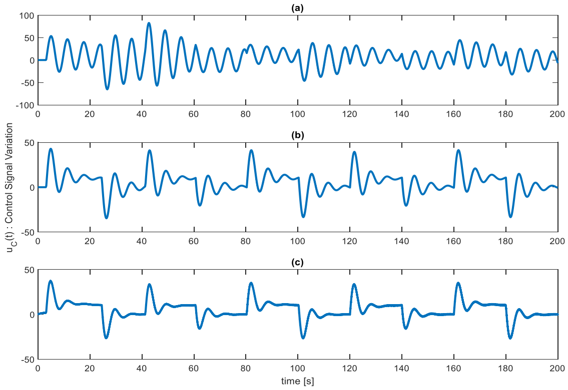

Fig. 8. The variations of the control signal for different control systems.

Fig. 9 shows the closed-loop system response in the presence of the proposed controller. In parts (a) and (b) of this figure, the first and second proposed estimators (based on LKF and EKF) have the task of estimating the delay in the control system, respectively. Fig. 10 also shows the control effort corresponding to each of these two control systems above.

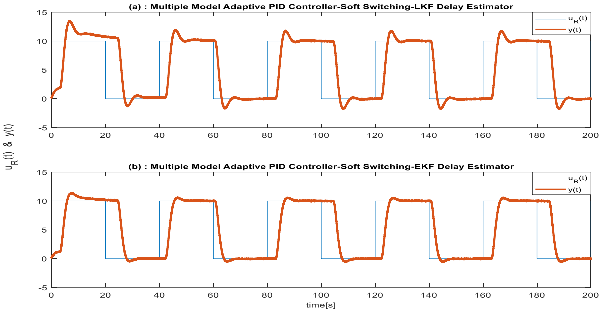

Fig. 9. The closed-loop system response for the proposed controller, with soft switching, in the presence of the two proposed estimators.

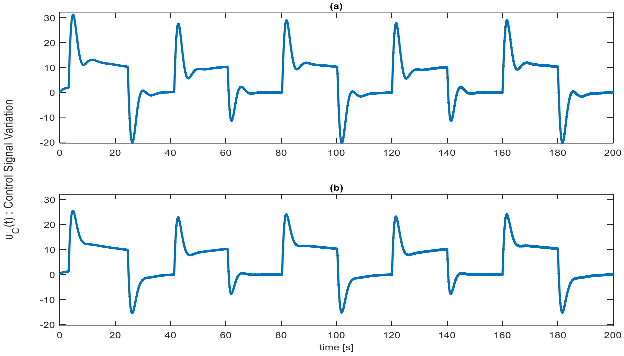

Fig. 10. The variations of the control signal for the proposed controller, with soft switching, in the presence of the two proposed estimators.

To accurately compare the performance of the above controllers, two important control criteria in these systems are evaluated:

1- Mean of squares of tracking error (MSTE): This criterion is used to measure the traceability of a controller and its exact value for a control system is derived from Eq. (22).

$$\mathrm{MSTE} = \frac{1}{n+1}\sum_{k=0}^{n}(y(kT) - u_R(kT))^2 \qquad (22)$$

2- Mean of squares of control signal variations (MSCV): This criterion is to measure the effort of the control signal and its exact value in a control system can be calculated using Eq. (23).

$$\mathrm{MSCV} = \frac{1}{n}\sum_{k=1}^{n}(u_C(kT) - u_C((k-1)T))^2 \qquad (23)$$

In which n is the number of samples recorded for measuring the aforementioned criteria and T is the sampling time for data recording. Tables II and III present MSTE and MSCV for all control systems included in this study, respectively.

TABLE II

THE COMPARISON OF TRACEABILITY

Controller type	$MSTE$
PID controller set for minimum delay time	58.28
PID controller set for maximum delay time	2265
MAC-hard switching- certain equivalent estimated delay	20.02
MAC-soft switching- LKF delay estimator	17.49
MAC-soft switching- EKF delay estimator	15.62

TABLE III

THE COMPARISON OF THE CONTROL SIGNAL EFFORT

Controller type	MSCV
PID controller set for minimum delay time	0.0002
PID controller set for maximum delay time	0.00003
MAC-hard switching- certain equivalent estimated delay	0.02
MAC-soft switching- LKF delay estimator	0.006
MAC-soft switching- EKF delay estimator	0.004

Finally, the input-output stability for the proposed control system should be analyzed in the BIBO sense [56]. Since the delay estimator and the switching mechanism are two essential parts of the control system, the stability of the closed-loop system should be examined in the presence of the proposed switching mechanism with different amounts of delay estimation (in the main band of delay changes). For this purpose, the stability of the proposed control system is examined for different values of $\hat{d}(t)$. Fig. 11 and 12 represent bode and Nyquist diagrams of the open-loop system for the proposed control system, respectively. As can be seen in these figures, the system is BIBO-stable at a relatively safe margin for different estimates of the time delay. It should be noted that these diagrams have been plotted assuming the presence of multiple controllers and a supervisory mechanism in the control loop. It can be seen in Fig. 11 that, for the largest estimated delay, the closed-loop system with a gain margin of 7.44dB and a phase margin of 48.76deg is input-output stable. It is also apparent in Fig. 12 that, for the largest amount of delay, the closed-loop system is stable with a relatively safe margin.

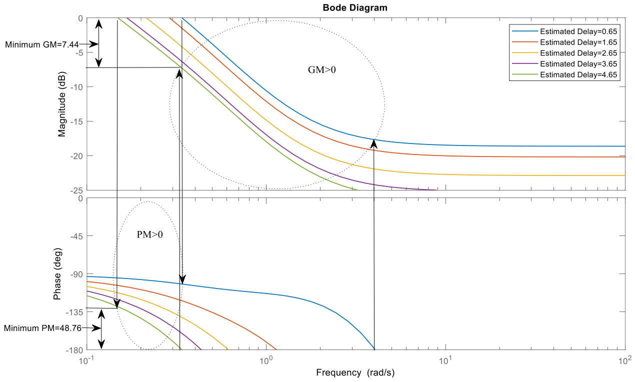

Fig. 11. The Bode diagrams for the open-loop system in the proposed control system for different values of estimated delay.

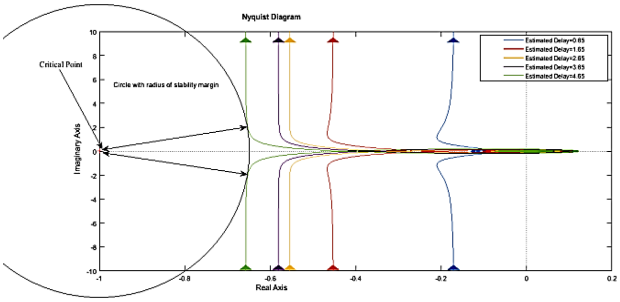

Fig. 12. The Nyquist diagrams for the open-loop system in the proposed control system for different values of estimated delay.

VI. CONCLUSIONS

This study presented a controller in MAC structure for a specific class of LTI systems with an unknown and time-varying delay. The most important reason that encouraged designers into using MAC structure is that the time delay variation band (uncertainty band) was large. In this designing process, the used adaptive controller is of the indirect type. It is obvious that an essential element in this type of controllers is the estimation mechanism of the plant parameters. In this paper, a novel method for designing a fast and accurate estimator was presented. The main idea behind this method is based on the performance of the Kalman filter observer (linear and extended) in estimating the states of linear and nonlinear systems. Particularly, considering the subject mentioned in Section II of this paper, the plant time delay was estimated using the proposed observer at an online mode and with acceptable precision. Multiple controllers used in this study are considered four PIDs corresponding to the four sub-bands of the delay. It should be noted that the parameters for each of the multiple controllers, for the system under control, were calculated offline and proportional to its corresponding time-delay sub-band, from solving several independent optimization problems in a 3D space using a genetic algorithm. Also in this study, a soft and continuous switching mechanism was presented in the adaptive subdivision to reduce the undesired effects of discrete switching in the MAC control structure, especially to reduce control effort. The simulation of different types of reference input signal and time delay signal were made on a sample system. The simulation results presented in Section V are indicative of a rather desired tracking performance for the proposed controller, a decrease in control effort in the proposed control system, a very low estimation error for the proposed estimator, as well as the closed-loop system stability. Two important points that are definitely effective in performance improvement of the proposed controller and estimator are as follows:

1- In designing the estimator, using higher-order pade approximations for the time delay factor will definitely increase estimation precision.

2- In designing the controller, an increase in the number of sub-bands for time delay, and hence an increase in the number of multiple controllers, will definitely decrease tracking error and control effort.

Also, it should be noted that in case of optimal designing, the use of other controllers such as Smith controller and fuzzy PID, as well as using other continuous switching rules such as TSK fuzzy switching, in the proposed control structure may improve the efficiency of the proposed controller.

REFERENCES

[1] J. E. Normey-Rico, E. F. Camacho, *Control of Dead-time Processes*, Springer-Verlag, 1th ed, London, UK, 2007.

[2] Q. C. Zhong, *Robust Control of Time-delay Systems*, Springer-Verlag, 1th ed, London, UK, 2006.

[3] M. Wu, Y. He, J. H. She, *Stability Analysis and Robust Control of Time-Delay Systems*, Science Press Beijing and Springer-Verlag Berlin Heidelberg, 2010.

[4] S. Bjorklund, L. Ljung, "A review of time-delay estimation techniques," *42nd IEEE International Conference on Decision and Control* (IEEE Cat. No.03CH37475), Maui, HI, pp. 2502-2507, Vol.3, 2003.

[5] A. O. Dwyer, R. Gao, “Comparison of two B-polynomial Methods Application to the Identification of Time delayed Processes,” *Proceedings of the Irish Signals and Systems Conference*, NUI Maynooth, Ireland, pp. 105-111, June 2001.

[6] J. Roe, R. Gao, A. Dwyer, “Identification of a Time-delayed Process Model using an Overparameterization Method,” *Proceedings of the China-Ireland International Conference on Information and Communications Technologies (CIICT)*, DCU, August 2007.

[7] K. Taarita, L. Belkoura, M. Ksouri, J.P. Richard , “A Fast Identification Algorithm For Systems With Delayed Inputs,” *International Journal of Systems Science*, Taylor & Francis, Vol. 42, No. 3, pp. 449-456. 2011.

[8] L. Belkoura, J. P. Richard, M. Fliess, “On-line identification of systems with delayed inputs,” *17th Symposium on Mathematical Theory of Networks and Systems (MTNS)*, Kyoto, Japon, July 2006.

[9] A. O'Dwyer, J. V. Ringwood, “Model Parameter And Time Delay Estimation Using Gradient Methods,” *Proceedings of the Irish Colloquium on DSP and Control*, Dublin City University, pp. 211-218, July 1994.

[10] D. Etter and S. Stearns, "Adaptive estimation of time delays in sampled data systems," *IEEE Transactions on Acoustics, Speech, and Signal Processing*, vol. 29, no. 3, pp. 582-587, June 1981.

[11] S. Ahmed, B. Huang, S. L. Shah, “Parameter and delay estimation of continuous-time models using a linear filter,” *Journal of Process Control*, vol. 16, No. 4 pp. 323–331, April 2006.

[12] S.V. Drakunov, W. Perruquetti, J.-P. Richard, L. Belkoura, "Delay identification in time-delay systems using variable structure observers," *Annual Reviews in Control*, Vol. 30, Issue 2, pp. 143-158, 2006.

[13] J. Kozłowski, Z. Kowalczuk. “On-line Parameter and Delay Estimation of Continuous-Time Dynamic Systems,” *International Journal of Applied Mathematics and Computer Science*, vol. 25, Issue 2, pp. 223-232, June 2015.

[14] V. Léchappé, E. Moulay and F. Plestan, "Dynamic observation-prediction for LTI systems with a time-varying delay in the input," *IEEE 55th Conference on Decision and Control (CDC)*, Las Vegas, NV, 2016, pp. 2302-2307.

[15] C. Lai and P. Hsu, "Design the Remote Control System With the Time-Delay Estimator and the Adaptive Smith Predictor," *IEEE Transactions on Industrial Informatics*, vol. 6, no. 1, pp. 73-80, Feb. 2010.

[16] R.M.C.De Keyser, "ADAPTIVE DEAD-TIME ESTIMATION", *2nd IFAC Workshop on Adaptive Systems in Control and Signal Processing*, Lund, Sweden, vol 20, Issue 2, pp. 385-389, July 1986.

[17] J. Tuch, A. Feuer and Z. J. Palmor, "Time delay estimation in continuous linear time-invariant systems," *IEEE Transactions on Automatic Control*, vol. 39, no. 4, pp. 823-827, April 1994.

[18] H. C. Nejad, M. Farshad, Havangi, "Presentation of a New Online Method, for Time Variant and Unknown Input Time Delay Estimation, in Continuous SISO-LTI Systems", *International Journal of Sensors, Wireless Communications and Control* (2020) 10: 1. https://doi.org/10.2174/2210327910666191216155745

[19] X. Hong, Q. Zhu, "An on-line algorithm of uncertain time delay estimation in a continuous system," *International Conference on Networking, Sensing and Control*, Okayama, pp. 498-501, 2009.

[20] M. Krstic, "Lyapunov Stability of Linear Predictor Feedback for Time-Varying Input Delay," *IEEE Transactions on Automatic Control*, vol. 55, no. 2, pp. 554-559, Feb. 2010.

[21] N. Nguyen, E. Summers, "On Time Delay Margin Estimation for Adaptive Control and Robust Modification Adaptive Laws," *AIAA Guidance, Navigation, and Control Conference*, Guidance, Navigation, and Control and Co-located Conferences, Portland, Oregon, 2011.

[22] Y. Liu, L. –S. Hu, P. Shi, "A novel approach on stabilization for linear systems with time-varying input delay", *Applied Mathematics and Computation*, Vol. 218, No. 10, pp. 5937-5947, 2012.

[23] F. Cacace, F. Conte, A. Germani, "State Feedback Stabilization of Linear Systems with Unknown Input Time Delay," *IFAC-PapersOnLine*, Vol. 50, Issue 1, PP. 1245-1250, 2017.

[24] Y. Wei, Z. Lin, "A delay-independent output feedback for linear systems with time-varying input delay", *International Journal of Robust and Nonlinear Control*, PP. 1-11, 2018.

[25] D. Yue, Q. L. Han, "Delayed feedback control of uncertain systems with time-varying input delay," *Automatica*, Vol. 41, Issue . 2, PP. 233-240, 2005.

[26] C. Y. Kao, B. Lincoln, "Simple Stability Criteria For Systems With time-Varying Delays," *Automatica*, vol. 40, No. 8, pp. 1429–1434, August 2004.

[27] [27] W. -A. Zhang, L. Yu, "A robust control approach to stabilization of networked control systems with time-varying delays," *Automatica*, Vol. 45, No. 10, pp. 2440-2445, October 2009.

[28] A. Polyakov, A. Poznyak, J. Richard, "Robust output stabilization of time-varying input delay systems using attractive ellipsoid method," *52nd IEEE Conference on Decision and Control*, Florence, pp. 934-939, 2013.

[29] C. Yuan and F. Wu, "$\mathcal{H}\infty$ state-feedback control of linear systems with time-varying input delays," *IEEE 55th Conference on Decision and Control (CDC)*, Las Vegas, NV, pp. 586-591, 2016.

[30] D. B. Pietri, F. Mazenc, N. Petit, "Robust compensation of a chattering time-varying input delay with jumps," *Automatica*, Vol. 92, PP. 225-234, 2018.

[31] S. Roy, I. N. Kar, "Robust Control of Uncertain Euler-Lagrange Systems with Time-Varying Input Delay," *Proceedings of the Advances in Robotics (AIR '17)*, ACM, New York, NY, USA, Article 16, 6 pages, 2017.

[32] R. Matusu,, R. Prokop, "Control of systems with time-varying delay: A comparison study," *12th WSEAS International Conference on Automatic Control*, Modelling and Simulation, ACMOS '10, pp. 125-130, 2010.

[33] J. G. Dawson, "Fuzzy logic control of linear systems with variable time delay," *Proceedings of 9th IEEE International Symposium on Intelligent Control*, Columbus, OH, USA, pp. 5-10, 1994.

[34] D. Srinivasagupta, H. Schättler, B. Joseph, "Time-stamped model predictive control: an algorithm for control of processes with random delays," *Computers and Chemical Engineering*, Vol. 28, No. 8, July, pp. 1337–1346, 2004.

[35] S. Y. Yoon, Z. Lin, "Truncated predictor feedback control for exponentially unstable linear systems with time-varying input delay," *Systems & Control Letters*, Vol. 62, Issue. 10,PP. 837-844, 2013.

[36] F. Cacace , A. Germani , C. Manes, "Predictor-based control of linear systems with large and variable measurement delays," *International Journal of Control*, Taylor & Francis, Vol. 87, No. 4, PP. 704-714, 2014.

[37] V. Léchappé and E. Moulay and F. Plestan "Prediction-based control for LTI systems with uncertain time-varying delays and partial state knowledge," *International Journal of Control*, Taylor & Francis, vol. 91, No. 6, pp. 1403-1414, 2018.

[38] X. Han, E. Fridman, S.K. Spurgeon, "Sliding mode control in the presence of input delay: A singular perturbation approach," *Automatica*, Vol. 48, Issue. 8, pp. 1904-1912, 2012.

[39] Y. Farid, N. Bigdeli, "Robust adaptive intelligent sliding model control for a class of uncertain chaotic systems with unknown time-delay," *Nonlinear Dynamics*, Vol. 67, NO. 3, pp. 2225–2240, February 2012.

[40] F. Carravetta, P. Palumbo and P. Pepe, "Quadratic Optimal control of linear systems with time-varying input delay," *49th IEEE Conference on Decision and Control (CDC)*, Atlanta, GA, pp. 4996-5000, 2010.

[41] F. Cacace, F. Conte and A. Germani, "Memoryless Approach to the LQ and LQG Problems With Variable Input Delay,"*IEEE Transactions on Automatic Control*, vol. 61, no. 1, pp. 216-221, 2016.

[42] F. Cacace, F. Conte, A. Germani, G. Palombo, "Optimal control of linear systems with large and variable input delays," *Systems & Control Letters*, Vol. 89, pp. 1-7, 2016.

[43] J. K. Pieper, B. W. Surgenor, J. Z. Liu, "On Self-Tuning Control of Processes with Time Varying Dead Time" , *American Control Conference* , Boston, MA, USA, PP. 2166-2171, 26-28 June. 1991.

[44] H. kurzt , W. goedecke, "Digital Parameter-Adaptive Control of Processes with Unknown Dead Time," *Automatica*, Vol. 17, No. I, pp. 245-252, January 1981.

[45] G. A. Dumont, A. Elnaggar, A. Elshafelt, “Adaptive Predictive Control Of Systems With Time-Varying Time Delay,” *International Journal Of Adaptive Control And Signal Processing*, Vol. 7,No. 2, pp. 91-101, March 1993.

[46] C. Chandra Prasad, V. Hahn, H. Unbehauen, U. Keuchel, “Adaptive Control of a Variable Dead Time Process with an Integrator,” *IFAC Proceedings Volumes*, Vol. 18, Issue. 15, PP. 71-75, 1985.

[47] J. P. Nelson, M. J. Balas, "Direct model reference adaptive control of linear systems with input/output delays,” *Numerical Algebra, Control & Optimization*, Vol. 3,NO. 3, PP. 445-462, 2013

[48] M. T. Nihtilä, “Adaptive control of a continuous-time system with time-varying input delay,” *Systems & Control Letters*, Vol. 12, Issue 4, PP. 357-364, 1989.

[49] P. S. Agachi, Z. K..Nagy, M. V. Cristea, A. L. Imre-Lucaci, “*Model Based Control*,” WILEY-VCH Verlag GmbH & Co. KGaA, Weinheim, 2006.

[50] N. B. Liberis, M. KrsticJ, “Nonlinear Control Under Nonconstant Delays,” *Advances in Design and Control*, Society for Industrial and Applied Mathematics, 2013.

[51] C. K. Chui, G. Chen, *Kalman Filtering with Real-Time Applications*, Springer-Verlag, 5th ed, Berlin Heidelberg, Germany, 2009.

[52] J. D. Landau , R. Lozano , M. M’Saad , A. Karimi, *Adaptive Control Algorithms, Analysis and Applications*, Springer, 2th ed, London, UK, 2011.

[53] B. D. O. Anderson, T. S. Brinsmead, F. De Bruyne, J. Hespanha, D. Liberzon, A. S. Morse, “Multiple Model Adaptive Control, Part 1: Finite Controller Coverings,” *International Journal of Robust and Nonlinear Control*, Vol. 10, No. 11-12, pp. 909–929, September - October 2000.

[54] J. O. Hespanha, D. Liberzon, A. S. Morse, B. D. O. Anderson, T. S. Brinsmead, F. De Bruyne, “Multiple model adaptive control. Part 2: switching,” *International Journal of Robust And Nonlinear Control*, Vol. 11, No. 5, pp. 479–496, 30 April 2001.

[55] B. D. O. Anderson, T. Brinsmead, D. Liberzon, A. S. Morse, “Multiple model adaptive control with safe switching,” *International Journal Of Adaptive Control And Signal Processing*, Vol. 15, No. 1, pp. 445-470, 2001.

[56] K. Ogata, *Modern Control Engineering*, Prentice-Hall Instrumentation and Controls Series, Englewood Cliffs, New Jersey: Prentice-Hall, 1970.

[57] D.E. Goldberg, *Genetic Algorithms in Search, Optimization, and Machine Learning*, Addison-Wesley, Reading, MA, 1989.

[58] P.D. Cha, J.J. Rosenberg, C.L. Dym, *Fundamentals of Modeling and Analyzing Engineering Systems*, Cambridge University Press, 2000.

Hadi Chahkandi Nejad was born in Birjand, Iran, in 1985. He received the B.Sc. and M.Sc. degrees in Control Engineering from I.A.U., Iran and he received his Ph.D. degree in Control Engineering from Birjand University, Iran. He was employed in I.A.U. University, Birjand Branch, Iran, as a Faculty member in the department of computer and Electrical engineering, since 2009 and he is head of electrical engineering department now. His research interests are in Fuzzy Control, Adaptive Control, System Identification, Artificial Neural Networks, Optimization, biomedical signal processing and Biological system modelling & control.

Mohsen Farshad was born in Birjand, Iran, in 1967. He received the B.S. degree in electrical engineering from Sharif University of Technology, Tehran, Iran, in 1990 and the M.S. degree in electrical engineering from the University of Tehran, Tehran, Iran, in 1994. He received the Ph.D. degree from the Department of Electrical and Computer Engineering, University of Tehran in 2006. Now, he is an associate professor at Department of power Engineering, computer and electrical engineering faculty, university of birjand, Birjand, South Khorasan, Iran. His teaching and research interests are soft computing (including intelligent optimization algorithms, neural networks and fuzzy logic), modeling and control of electric drives (particularly Switched Reluctance machine), systems identification and control, modelling and control of vehicular traffic.

Ramazan Havangi was born in Birjand, Iran. He received the M.Sc. and Ph.D. degrees in control engineering from the K. N. Toosi University of Technology, Tehran, Iran, Now, he is an Assistant Professor at Department of power Engineering, computer and electrical engineering faculty, university of birjand, Birjand, South Khorasan, Iran.. His current research interests include inertial navigation, integrated navigation, estimation and filtering, evolutionary filtering, simultaneous localization and mapping, fuzzy, neural network, and soft computing.

IECO

This page intentionally left blank.

International Journal of Industrial Electronics, Control and Optimization © 2021 IECO
Vol. 4, No. 1, pp. 13-22, Jan (2021)

Adaptive Robust Tracking Control Based on Backstepping Method for Uncertain Robotic Manipulators Including Motor Dynamics

Javad Keighobadi[1†], Mohammad Mehdi Fateh[2]

[1,2] Department of Electrical and Robotic Engineering, Shahrood University of Technology, Shahrood, Iran

ABSTRACT

Recent research on the backstepping control of robotic systems has motivated us to design a robust backstepping voltage-based controller with computational simplicity and ease of implementation. In this paper, an adaptive robust tracking controller based on backstepping method (ARTB) is presented for uncertain electrically-driven robotic manipulators in the framework of voltage control strategy. It is intended to convert robot control problem to motor control problem. In the design procedure, the manipulator dynamics are incorporated into a lumped uncertainty, such that the proposed adaptation law promptly compensates for it. Hence, high tracking accuracy, robust behavior and less complexity are the prominent features of the proposed control system in the presence of external disturbances, parametric uncertainties and un-modeled dynamics. The stability of the closed-loop system is guaranteed based on the Lyapunov theory and the tracking error converges to zero asymptotically. As a case study, the proposed ARTB is simulated on a two-link robot manipulator driven by permanent magnet DC motors. Numerical simulations are included to show the superiority of the proposed controller to a state augmented adaptive backstepping method, a sliding backstepping controller and an adaptive backstepping sliding mode control in tracking the desired trajectory.

Article Info

Keywords:
Adaptation Mechanism, Backstepping Method,
Electrically-driven Robotic Manipulators, Robust Tracking Control,
Voltage-based Control

Article History:
Received 2019-09-29
Accepted 2020-04-28

I. INTRODUCTION

Robotic manipulators play an important role in many applications; hence, tracking purpose is a significant and challenging issue in robotics. As a result, numerous control techniques have been reported in the literature to achieve proper tracking of robotic systems in the presence of uncertainties [1]–[4]. In [5], a neuro fuzzy sliding mode control was proposed for a two-link robot manipulator, in which the parameters of sliding surface were optimized using PSO algorithm. Yin et al. [6] developed an adaptive robust tracking controller for an industrial robot such that the parametric estimation errors were compensated for through the projection-type adaptation mechanism. Yovchev et al. [7] suggested an iterative learning method to control the motion of the robot arm in a constrained state space in the presence of uncertainties. In [8], velocity and disturbance observers were designed to construct a tracking controller for uncertain robot manipulators.

Among the control approaches, the backstepping method is a powerful systematic Lyapunov-based control scheme which solves the regulation and tracking control problems of nonlinear strict-feedback systems [9]–[12]. To achieve high-accuracy tracking and extend the applicability of the backstepping method for robotic systems, it has been combined with other techniques as clearly reported in the literature. In [13], an adaptive backstepping control based on state augmentation was designed for a robotic manipulator. Nikdel et al. [14] proposed a fractional-order adaptive backstepping control for robotic systems in the presence of uncertainties. A fuzzy backstepping approach was proposed for robot manipulators using the funnel control technique [15].

[†] **Corresponding Author**: javad_keighobadi@yahoo.com
Department of Electrical and Robotic Engineering, Shahrood University of Technology, Shahrood, Iran

In [16], a PID fuzzy backstepping algorithm was presented to control the flexible-joint robot manipulator. Vijay et al. [17] suggested an observer-based backstepping terminal sliding mode control for robot manipulator, so that a neural network system was employed to approximate the unknown terms. In [18], an adaptive fuzzy backstepping control was reported for flexible-joint robotic manipulators with full state constraints. Likewise, a time-varying output constrained control was addressed for robotic manipulator on the basis of adaptive neural backstepping method [19]. Furthermore, an adaptive backstepping fixed-time control was constructed for MIMO systems, with a focus on the robotic manipulator subject to the output constraints [20]. Similarly, an adaptive finite-time control based on the backstepping method was proposed for robotic manipulators with funnel boundary [21]. Although [18]-[21] can be considered as the recent backstepping-based studies on the robotic manipulators, the design structures were based on the torque control strategy (TCS), the same as other studies reported in [1]- [17]. In other words, the actuator dynamics were ignored in the control designs. As a result, there would seem to be some problems (such as sensing limits and long process time) with the practical implementation of the TCS [22]. Moreover, the TCS-based control suffers from computational burden since the highly coupled nonlinear model of robot manipulators is directly involved in the construction of the control signal. Another drawback of the aforesaid studies [18]-[21] is that it may be difficult to be implemented on a real industrial robot in practice due to the complexity of the adaptation mechanism.

To overcome the drawbacks caused by TCS, voltage control strategy (VCS) was introduced by Fateh [22] to control electrically-driven robotic manipulators; in this case, the robot control problem was converted into the motor control problem with the aid of current feedback. The control law based on VCS is a model-free approach that also can be used in the high-speed tracking purposes for robotic manipulators. Several VCS-based control methods have been applied to robotic systems [23]-[26]. However, design of robust backstepping-based control using VCS is still an open issue for the robotic system. It is worth noting that even though some studies on the robotic manipulator have considered the motor dynamics in the modeling of the system, they have not followed the VCS since the manipulator dynamics were also involved in the control input, which made it more complex [27]-[30].

Inspired by the above discussions, this paper attempts to investigate the problem of adaptive voltage-based backstepping tracking control for uncertain robotic manipulators including actuator dynamics. First, a strict-feedback form of the integrated robotic system is proposed in the presence of external disturbances, un-modeled dynamics and parametric uncertainties. Then, two simple adaptation laws are obtained to compensate for lumped uncertainties in the framework of VCS. As a result, the proposed Lyapunov-based method has a robust behavior and the complexity of the control signal is reduced accordingly. Briefly, the contributions of the paper can be summarized as follows:

- Under external disturbances, un-modeled dynamics and parametric uncertainties, the model of robotic manipulator including actuator dynamics is presented in the form of an uncertain strict-feedback system.
- An adaptive robust voltage-based backstepping tracking controller is developed for electrically-driven robotic manipulators. To this end, two simple adaptive laws are obtained to compensate for the lumped uncertainties in the framework of VCS.
- With the aid of VCS, the practical restrictions of TCS are eliminated for the robotic system. Accordingly, the complexity of the control signal is reduced.
- Robust behavior, guaranteed stability and acceptable tracking error are the features of the proposed control law.

The rest of this paper is organized as follows: Section 2 presents the strict-feedback form of the electrically-driven robot manipulator. Section 3 introduces the proposed ARTB and the stability analysis is described in Section 4. Results and discussions are expressed in Section 5 in two subsections: first, the simulation results of ARTB are illustrated; then, three different backstepping-based controllers are simulated for comparison and the results are depicted. Finally, Section 6 concludes the paper.

II. MODELING

Deriving the strict feedback form of the robotic system is necessary for designing a suitable backstepping controller. All the equations are presented for a general n-DOF robot manipulator and a two-link manipulator including actuators is regarded as a case study. The manipulator dynamics is described [31] as

$$D(q)\ddot{q} + C(q.\dot{q})\dot{q} + G(q) = \tau \tag{1}$$

where $q, \dot{q} \in R^n$ and $\ddot{q} \in R^n$ are the joint positions, the vector of joint velocity and acceleration, respectively. $D(q) \in R^{n\times n}$ represents the inertia matrix, $C(q.\dot{q}) \epsilon R^{n\times n}$ is the Coriolis and Centrifugal torques, $G(q) \in R^n$ is the vector of gravitational torques and $\tau \in R^n$ represents the vector of the joint torque provided by electrical motors as follow

$$J_m\ddot{\theta}_m + B_m\dot{\theta}_m + r\tau = \tau_m \tag{2}$$

where J_m and B_m are the inertia and damping diagonal matrices for the motors. The motor torque (τ_m) is produced by the motor current (I_a) regarding the following equation as

$$\tau_m = K_m I_a \tag{3}$$

in which K_m is a diagonal constant matrix. The proportion of motor position vector (θ_m) to the joint position vector is introduced as

$$q = r\theta_m \;\rightarrow\; \theta_m = r^{-1}q \tag{4}$$

where $r \in R^{n*n}$ is the gear coefficient matrix. Substituting Equ. (3) and the derivatives of Equ. (4) up to the second order into Equ. (2) results in

$$\begin{aligned} &J_m r^{-1}\ddot{q} + B_m r^{-1}\dot{q} + r\tau = K_m I_a \;\rightarrow \\ &\quad \ddot{q} = -J_m^{-1}B_m\dot{q} + rJ_m^{-1}K_m I_a - r^2 J_m^{-1}\tau \end{aligned} \tag{5}$$

The voltage of motors is considered as the control inputs. The electrical dynamic of motors is represented as

$$V = RI_a + L\dot{I}_a + k_b\dot{\theta}_m + \phi(t) + F(\dot{q}) \tag{6}$$

where k_b, R and L are $n \times n$ diagonal matrices for the back-emf constant, the resistance and inductance of motors, respectively. Moreover, $\phi(t)$ stands for external disturbances while the un-modeled dynamics are represented by $F(\dot{q})$. Equ. (6) can be written as

$$\begin{aligned} \dot{I}_a = L^{-1}V - L^{-1}RI_a - L^{-1}k_b r^{-1}\dot{q} - L^{-1}(\phi(t) \\ + F(\dot{q})) \end{aligned} \tag{7}$$

By defining the state vector as $X = (q, \dot{q}, I_a)^T$ and using Equs. (1), (5) and (7), the state-space model of the integrated robotic system is introduced as

$$\begin{aligned} &\dot{x}_1 = x_2 \\ &\dot{x}_2 = -J_m^{-1}B_m x_2 + rJ_m^{-1}K_m x_3 - r^2 J_m^{-1}(D(q)\ddot{q} \\ &\qquad\qquad + C(q.\dot{q})\dot{q} + G(q)) \\ &\dot{x}_3 = -L^{-1}K_b r^{-1}x_2 - L^{-1}Rx_3 + L^{-1}V - L^{-1}(\phi(t) \\ &\qquad\qquad + F(\dot{q})) \end{aligned} \tag{8}$$

For the sake of simplicity, Equ. (8) is formed as

$$\begin{aligned} &\dot{x}_1 = x_2 \\ &\dot{x}_2 = -a_1x_2 + a_2x_3 - r^2J_m^{-1}(D(q)\ddot{q} + C(q.\dot{q})\dot{q} \\ &\qquad\qquad + G(q)) \\ &\dot{x}_3 = -a_3x_2 - a_4x_3 + a_5u - a_5(\phi(t) + F(\dot{q})) \end{aligned} \tag{9}$$

where

$$\begin{aligned} &a_1 = J_m^{-1}B_m \;,\; a_2 = rJ_m^{-1}K_m \;, a_3 = L^{-1}K_b r^{-1}, \\ &a_4 = L^{-1}R \;,\; a_5 = L^{-1} \end{aligned} \tag{10}$$

With respect to the nominal values of the weighted functions $(a_1, \dots, a_5)$, Equ. (9) can be expressed as

$$\begin{aligned} &\dot{x}_1 = x_2 \\ &\dot{x}_2 = -\hat{a}_1x_2 + \hat{a}_2x_3 + d_1 \\ &\dot{x}_3 = -\hat{a}_3x_2 - \hat{a}_4x_3 + \hat{a}_5u + d_2 \end{aligned} \tag{11}$$

where $\hat{a}_1, \dots, \hat{a}_5$ are the nominal values and d_1 and d_2 are represented as

$$\begin{aligned} &d_1 = -r^2J_m^{-1}(D(q)\ddot{q} + C(q.\dot{q})\dot{q} + G(q)) \\ &\qquad\qquad + (\hat{a}_1 - a_1)x_2 - (\hat{a}_2 - a_2)x_3 \\ &d_2 = -a_5\big(\phi(t) + F(\dot{q})\big) + (\hat{a}_3 - a_3)x_2 \\ &\qquad\qquad + (\hat{a}_4 - a_4)x_3 - (\hat{a}_5 - a_5)u \end{aligned} \tag{12}$$

The terms $D(q), G(q), C(q,\dot{q}), F(\dot{q}), \phi(t)$ and the differences between the real values and the nominal values of the weighted functions are included in the lumped uncertainties d_1 and d_2 as described by Equ. (12) and considered in the state space model Equ. (11). Note that $\hat{a}_i\,, i = 1, \dots, 5$ are known constant matrices, however $d_j\,, j = 1,2$ are unknown terms which are estimated via adaptation laws in the next section. Backstepping control is developed for Equ. (11) since it can be written in the form of strict feedback as follows:

$$\begin{aligned} &\dot{\eta} = f(\eta) + g(\eta)\zeta + d_1 \\ &\dot{\zeta} = f_a(\eta,\zeta) + g_a(\eta,\zeta)u + d_2 \end{aligned} \tag{13}$$

where

$$\begin{aligned} &\eta = \begin{pmatrix} x_1 \\ x_2 \end{pmatrix}, \zeta = x_3\,, \\ &f(\eta) = \begin{pmatrix} x_2 \\ -\hat{a}_1x_2 \end{pmatrix} \;,\quad g(\eta) = \begin{pmatrix} 0 \\ \hat{a}_2 \end{pmatrix}, \\ &f_a(\eta,\zeta) = -\hat{a}_3x_2 - \hat{a}_4x_3\,, \\ &g_a(\eta,\zeta) = \hat{a}_5 \end{aligned} \tag{14}$$

III. CONTROL DESIGN

In this section, a robust voltage controller based on backstepping method is designed for robot manipulator. The voltage-based controller obviates the complexity explosion of control effort and make the design too simple since the lumped uncertainties are compensated by two simple adaptation laws. More details and stability proof are given in what follows.

Step1) The position error is defined as

$$e_1 = x_1 - x_{1d} \tag{15}$$

where x_{1d} is the desired angle and e_1 represents the tracking error. The derivative of e_1 is defined as

$$\dot{e}_1 = \dot{x}_1 - \dot{x}_{1d} = x_2 - \dot{x}_{1d} = e_2 \tag{16}$$

For the first subsystem, the Lyapunov function is suggested as

$$V_1 = \frac{1}{2}e_1^Te_1 \tag{17}$$

Taking the derivative of V_1 results in

$$\dot{V}_1 = e_1^T\dot{e}_1 = e_1^Te_2 \tag{18}$$

while the virtual control signal is chosen as $e_2 = -\lambda_1e_1$, the first subsystem become stable ($\dot{V}_1 = -e_1^T\lambda_1e_1 \le 0$).

Step2) We define z for the second subsystem as

$$z = e_2 + \lambda_1e_1 \tag{19}$$

where λ_1 is a positive diagonal matrix. Using the second subsystem of Equ. (11), the derivative of Equ. (19) can be written as

$$\dot{z} = \dot{e}_2 + \lambda_1 \dot{e}_1 = (-\hat{a}_1 x_2 + \hat{a}_2 x_3 + d_1 - \ddot{x}_{1d}) + \lambda_1 z - \lambda_1^2 e_1 \quad (20)$$

The Lyapunov function is defined as

$$V_2 = V_1 + \frac{1}{2} z^T z + \frac{1}{2} \tilde{d}_1^T \gamma^{-1} \tilde{d}_1 \quad (21)$$

where $\tilde{d}_1 = d_1 - \hat{d}_1$. Thus, the derivative of V_2 is calculated as

$$\dot{V}_2 = \dot{V}_1 + z^T \dot{z} - \tilde{d}_1^T \gamma_1^{-1} \dot{\hat{d}}_1 \quad (22)$$

Substituting Equs. (18), (19) and (20) into Equ. (22) is written as

$$\dot{V}_2 = e_1^T (z - \lambda_1 e_1) + z^T (-\hat{a}_1 x_2 + \hat{a}_2 x_3 + d_1 - \ddot{x}_{1d} + \lambda_1 z - \lambda_1^2 e_1) - \tilde{d}_1^T \gamma_1^{-1} \dot{\hat{d}}_1 \quad (23)$$

Now by defining the $e_3 = x_3 - x_{3d}$, $\dot{V}_2$ is rewritten as

$$\begin{aligned} \dot{V}_2 &= -e_1^T \lambda e_1 + e_1^T z - \tilde{d}_1^T \gamma_1^{-1} \dot{\hat{d}}_1 \\ &+ z^T (-\hat{a}_1 x_2 + \hat{a}_2 e_3 + \hat{a}_2 x_{3d} + d_1 - \ddot{x}_{1d} + \lambda_1 z - \lambda_1^2 e_1) \end{aligned} \quad (24)$$

x_{3d} is regarded as the virtual control input which can be chosen as

$$x_{3d} = (\hat{a}_2)^{-1} (\hat{a}_1 x_2 + \ddot{x}_{1d} - \lambda_1 z + \lambda_1^2 e_1 - e_1 - \lambda_2 z - \hat{d}_1) \quad (25)$$

where λ_2 is a positive gain matrix. Substituting Equ. (25) into Equ. (24), the derivative of V_2 is simplified as

$$\dot{V}_2 = -e_1^T \lambda_1 e_1 - z^T \lambda_2 z + z^T \hat{a}_2 e_3 - \tilde{d}_1^T \left(z - \gamma_1^{-1} \dot{\hat{d}}_1\right) \quad (26)$$

Thus, if the first adaptation law is chosen as $\dot{\hat{d}}_1 = \gamma_1 z$, ($\gamma_1$is a positive constant matrix) then $\dot{V}_2$ is obtained as

$$\dot{V}_2 = -e_1^T \lambda_1 e_1 - z^T \lambda_2 z + z^T \hat{a}_2 e_3 \quad (27)$$

Step3) Taking the derivative of e_3 and replacing the third subsystem of Equ. (11) yields

$$\dot{e}_3 = \dot{x}_3 - \dot{x}_{3d} = -\hat{a}_3 x_2 - \hat{a}_4 x_3 + \hat{a}_5 u + d_2 - \dot{x}_{3d} \quad (28)$$

The final positive definite Lyapunov function is introduced as

$$V_3 = V_2 + \frac{1}{2} e_3^T e_3 + \frac{1}{2} \tilde{d}_2^T \gamma_2^{-1} \tilde{d}_2 \quad (29)$$

Then, substituting Equ. (28) into the derivative of Equ. (29) results in

$$\dot{V}_3 = -e_1^T \lambda_1 e_1 - z^T \lambda_2 z + z^T \hat{a}_2 e_3 - \tilde{d}_2^T \gamma_2^{-1} \dot{\hat{d}}_2 + e_3^T (-\hat{a}_3 x_2 - \hat{a}_4 x_3 + \hat{a}_5 u + d_2 - \dot{x}_{3d}) \quad (30)$$

We choose the control input u in the following form

$$u = (\hat{a}_5)^{-1} \left[\hat{a}_4 x_3 + \hat{a}_3 x_2 - \hat{d}_2 + \dot{x}_{3d} - \lambda_3 e_3 - \hat{a}_2^T z\right] \quad (31)$$

where λ_3 is a positive gain and the second adaptation law is chosen as

$$\dot{\hat{d}}_2 = \gamma_2 e_3 \quad (32)$$

Finally, substituting Equ. (31) and Equ. (32) into Equ. (30) results in

$$\dot{V}_3 = -e_1^T \lambda_1 e_1 - z^T \lambda_2 z - e_3^T \lambda_3 e_3 \leq 0 \quad (33)$$

Therefore, the voltage control law Equ. (31) guarantees the stability of the closed-loop system. The Block diagram of the proposed controller is shown in Fig.1.

IV. STABILITY ANALYSIS

Some assumptions are considered to verify the stability and well tracking of the proposed ARTB in the presence of uncertainties. It is worth noting that the assumptions are very common for nonlinear systems as clearly found in the literature.

Assumption 1: The desired trajectory q_d is required to be continuous and smooth such that its derivatives up to a necessary order are available and all uniformly bounded [23].

Assumption 2: The external disturbance $\phi(t)$ is bounded as $|\phi(t)| \leq \phi_{max}$ where ϕ_{max} is a positive constant [23].

Assumption 3: In general, the adaptation loop is processed with infinite operating frequency. Since the sampling interval is short enough as compared with the variation of d_1 and d_2, the lumped uncertainty terms are also assumed to be constant during estimation. As a result, the variations of the lumped uncertainties are considered to be zero in the adaptation process [32], [33].

Assumption 4: In order to protect the electrical motor against over voltage, we assume that the motor voltage is bounded as $|u(t)| \leq u_{max}$ [23], [25].

According to the previous section, the Lyapunov function is presented as

$$V_f = \frac{1}{2} e_1^T e_1 + \frac{1}{2} z^T z + \frac{1}{2} e_3^T e_3 + \frac{1}{2} \tilde{d}_2^T \gamma_2^{-1} \tilde{d}_2 + \frac{1}{2} \tilde{d}_2^T \gamma_2^{-1} \tilde{d}_2 \quad (34)$$

and the derivative of Equ. (34) results in

$$\dot{V}_f = -e_1^T \lambda_1 e_1 - z^T \lambda_2 z - e_3^T \lambda_3 e_3 \leq 0 \quad (35)$$

From Equ. (34) and Equ. (35), the boundedness of $e_1, z, e_3, \tilde{d}_1$ and $\tilde{d}_2$ are verified [34]. Based on the Assumption 1, q_d and $\dot{q}_d$ are bounded; hence boundedness of e_1 and z follows the boundedness of q and $\dot{q}$, respectively. The boundedness of I_a is depended on the boundedness of x_{3d} due to $I_a = x_3 = e_3 + x_{3d}$; From Equ. (25), x_{3d} is the virtual input composed of $\ddot{x}_{1d}, e_1, z$ and $\hat{d}_1$. According to the Assumption 3, d_1 is bounded. hence $\hat{d}_1$ is bounded with respect to the definition $\hat{d}_1 = d_1 - \tilde{d}_1$. Therefore, x_{3d} is bounded so the boundedness of I_a is confirmed. Moreover, the boundedness of $\hat{d}_2$ is proven similar to the boundedness of $\hat{d}_1$. Assumption 4 implies that the motor voltage is bounded, thus the proposed control signal Equ. (31) is valid. So the guaranteed stability of the proposed ARTB is concluded.

V. RESULTS AND DISCUSSIONS

Two subsections are considered to show the feasibility and effectiveness of the proposed controller. First, the proposed ARTB is applied to the uncertain electrically-driven robotic system and the results are presented; then, the second subsection is devoted to the comparison scenarios. The case study is a two-link robot manipulator driven by permanent magnet DC motors. The actuator specifications are presented in Table. 1 [35]. The desired trajectory for each joint is shown in Fig.2 since it is a smooth and differentiable path. As shown in Fig.3, the rectangular wave is an example of the external disturbance, similar to the one used in [25]. The ability of the proposed controller can be evaluated when facing the jumps in the external disturbance. In addition, $F(\dot{q})$ in (12) is also regarded as $0.1\dot{q}$ for the simulation. To consider the parametric uncertainties for the weighted functions, $\hat{a}_i$ is assumed to be 90% of the real value a_i.

A. *Tracking Performance of the Proposed Controller*

The proposed ARTB given by Equ. (31) is simulated with the following parameters:

$$\begin{gathered}\lambda_1 = \lambda_2 = \lambda_3 = 100 \times I_{2\times 2},\\ \gamma_1 = [100\;0; 0\;500], \gamma_2 = 50 \times I_{2\times 2}\end{gathered} \tag{36}$$

The satisfactory tracking performance of the proposed ARTB under the uncertainties is shown in Fig. 4. The four impulses in the zoomed mode of tracking performances are due to the four jumps in the profile of the external disturbance. It is shown that the jump times in Fig. 3 match the impulse times in Fig. 4(c) and (d). In addition, the impulses in the tracking performances are about 10^{-5} rad which are ignorable. As shown in Fig. 5, the behavior of the control inputs is smooth without the chattering problem. At first, the tracking error is high, so the controller injects high voltage into the system. Thus, the saturation is utilized to limit the voltage in the acceptable range. However, the input saturation influences for a short period in the control system. Afterwards, the range of voltages is permitted considering the type of motors. Hence, the effect of input saturation can be neglected after passing the transient state. Fig. 6 depicts the responses of d_1 and its estimation $\hat{d}_1$. It is demonstrated that the difference is ignorable. Likewise, d_2 and its estimation are given in Fig. 7, where $\hat{d}_2$ tracks d_2 as well. Therefore, the behavior of estimations is acceptable.

From this part of this study, it is concluded that the proposed control law succeeds in tracking the desired trajectory against uncertainties. In other words, the ARTB design is simple as well as more efficient since the complexity of control signal is eliminated by the voltage control strategy.

B. *Comparison Scenarios*

1) *Example 1: State augmented adaptive backstepping control (SAAB)*

First, it is worth noting that recent relevant papers on robotic systems have been developed based on the TCS, while the VCS has been rarely addressed in the literature, as clearly mentioned in this research. To this reason, the VCS is employed in this study. However, our control design is compared with three relevant papers applied to the robotic manipulators. The first scheme considered for the comparison is a state augmented adaptive backstepping (SAAB) control, adopted from [13]. To have a fair comparison, the model of robotic system is rewritten considering the motor dynamics. To this end, the final control law is obtained as

$$u = \phi\hat{\theta} + M\begin{pmatrix} k_p x_3 + k_i x_2 + n x_2 \\ +k_d\left(x_3 + k_p x_2 + \frac{k_i}{n}x_1\right)\end{pmatrix} \tag{37}$$

where k_p, k_i, k_d are positive constants. Variables x_1, x_2 and x_3 are also defined as $n\int_0^t e dt, e$ and $\dot{e}$. The adaptation law is suggested as

$$\dot{\hat{\theta}} = \gamma\phi^T M^{-1}\left(x_3 + k_p x_2 + \frac{k_i}{n}x_1\right) \tag{38}$$

Vector ϕ is the regressor of the system derived from $M(q)\ddot{q}_d + H(q,\dot{q}) = \phi\theta$, where

$$\begin{gathered}M(q) = RK_m^{-1}J_m r^{-1} + RK_m^{-1} r D(q)\\ H(q,\dot{q}) = \begin{pmatrix} RK_m^{-1}B_m r^{-1} + K_b r^{-1} \\ +RK_m^{-1} r C(q,\dot{q})\end{pmatrix}\dot{q} + RK_m^{-1} r G(q)\end{gathered} \tag{39}$$

The mathematical proof is omitted for brevity. More details of the design procedure can be found in [13]. The tuning parameters are chosen as $n = 5, k_p = 10, k_d = 5$ and $k_i = 0.1$. The tracking responses as well as tracking errors are shown in Fig. 8. The voltage of motors is depicted in Fig. 9. According to Figs. 8-9, the SAAB controller behaves well in tracking the desired trajectory with ignorable errors. However, the manipulator dynamics is involved in the control signal and adaptive law, which increases the complexity of design. In addition, the amplitude of the voltages is larger than our proposed method, in which some limitations may exist in practice with regard to the type of motors.

2) *Example 2: Sliding mode-based adaptive backstepping design (SMAB)*

To evaluate the strength of our proposed voltage-based controller, the control technique reported in [36] is also considered for the comparison. The actuator dynamics were included in the design procedure as addressed in the mentioned paper. The control input is provided as

$$u = RI_a + k_b\dot{q} + LH^{-1}f_2 - \rho z_2 \tag{40}$$

where the sliding surface s is defined as $\dot{q} - \dot{q}_d + K(q - q_d)$ and also z_2 and f_2 can be obtained through the backstepping method in the following form:

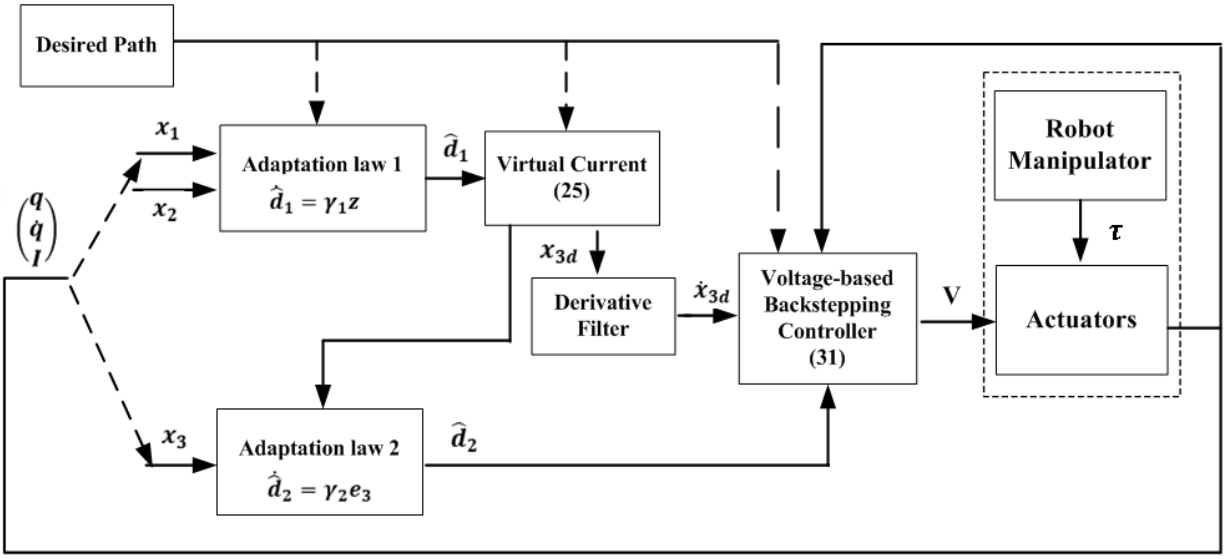

Fig. 1. The Block diagram of the proposed voltage-based backstepping control law (31)

TABLE I

SPECIFICATIONS OF DC MOTORS

$Motors$	u_{max} (v)	R (Ω)	J_m $(\frac{Nm.s^2}{rad})$	B_m $(\frac{Nm.s}{rad})$	L (H)	K_b $(\frac{V.s}{rad})$	r
1,2	50	1.6	0.0002	0.001	0.001	0.26	0.01

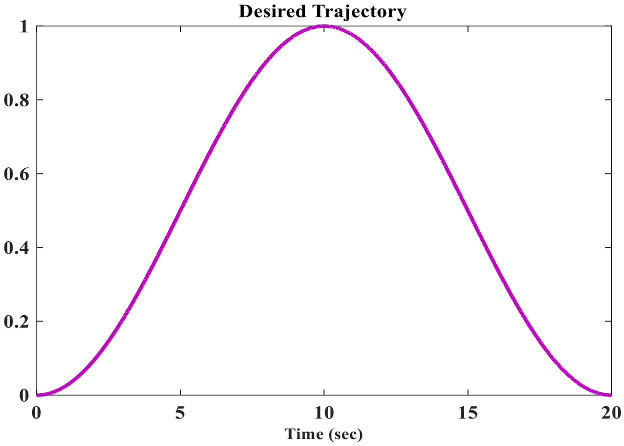

Fig. 2. The desired trajectory

$$z_2 = I_a - H^{-1}(Y\hat{\theta} - D(q)sat(\frac{S}{\epsilon})) \tag{41}$$

$$f_2 = \dot{Y}\hat{\theta} + Y\dot{\hat{\theta}} - \dot{D}(q)sat\left(\frac{S}{\epsilon}\right) - D(q)s\dot{a}t\left(\frac{S}{\epsilon}\right) - HI_a + Y\hat{\theta} \tag{42}$$

in which the adaptive law is expressed as

$$\dot{\hat{\theta}} = -\Gamma(D^{-1}(q)s + H^{-1}z_2)Y \tag{43}$$

The tuning parameters are set to $K = 25 \times I_{2\times2}$, $\Gamma = 48 \times I_{2\times2}$ and $\rho = 100 \times I_{2\times2}$. More details were given in [36]. The initial conditions, the trajectory and the external disturbances are the same as the one used in our proposed method. As shown in Fig. 10, the tracking performance of SMAB is acceptable in the presence of uncertainties. The control inputs are located under the valid limited value as depicted in Fig. 11. However, the SMAB suffers from computational burden with respect to Equs. (40)-(43). In other words, the control effort has become more complex and difficult to be implemented on the industrial robotic manipulators.

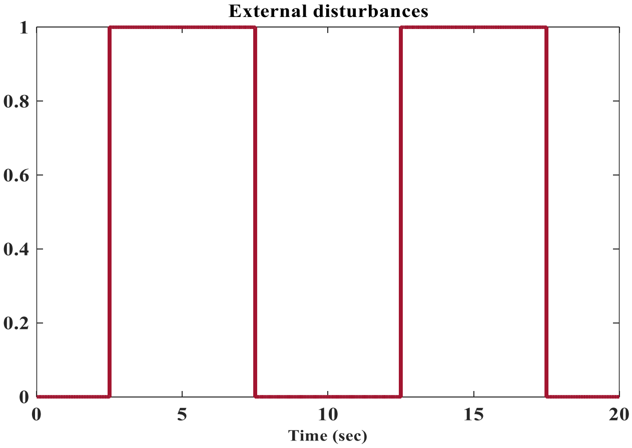

Fig. 3. The shape of external disturbance

3) Example 3: Adaptive backstepping sliding mode control (ABSM)

For comparison, an adaptive backstepping sliding mode control approach is also adopted from [37] and redesigned for the model of integrated robotic system. Similar to the previous subsections, all the simulation configuration (initial

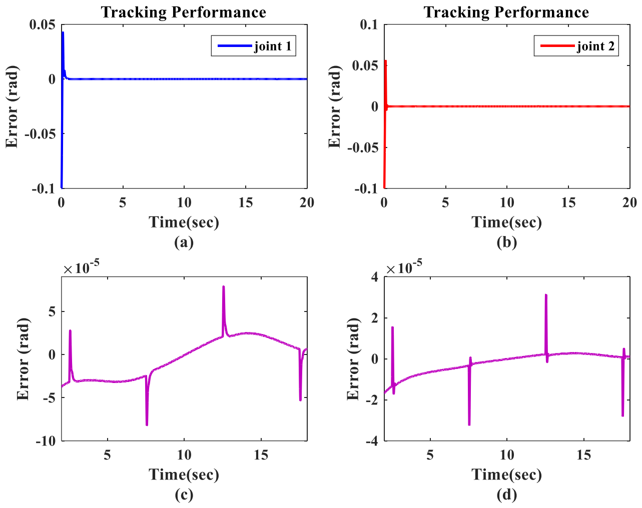

Fig. 4. (ARTB): (a) Tracking performance of first joint **(b)** Tracking performance of second joint **(c)** Zooming of (a) **(d)** Zooming of (b)

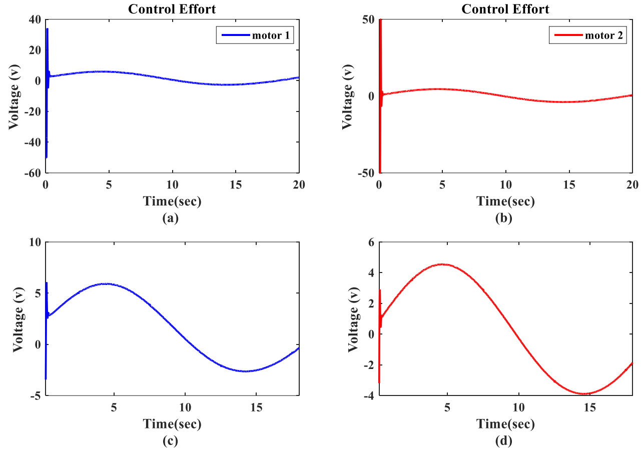

Fig. 5. (ARTB): (a) The control input of first joint **(b)** The control input of second joint **(c)** Zooming of (a) **(d)** Zooming of (b)

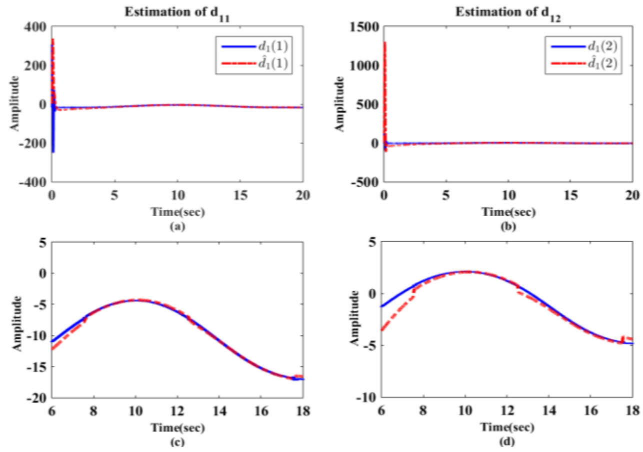

Fig. 6. Lumped Uncertainty Estimation 1: **(a)** d_{11} and $\hat{d}_{11}$ **(b)** d_{12} and $\hat{d}_{12}$ **(c)** Zooming of (a) **(d)** Zooming of (b)

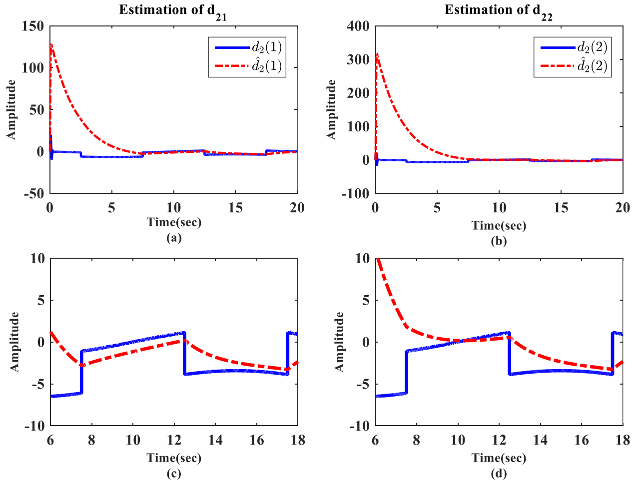

Fig. 7. Lumped Uncertainty Estimation 2: **(a)** d_{21} and $\hat{d}_{21}$**(b)** d_{22} and $\hat{d}_{22}$ **(c)** Zooming of (a) **(d)** Zooming of (b)

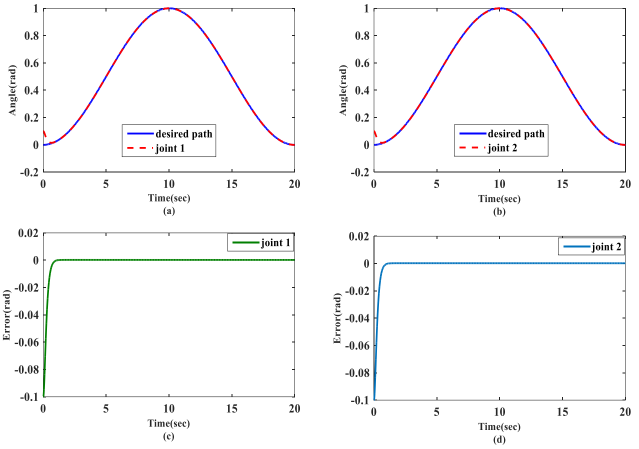

Fig. 8. Comparison 1: (SAAB) (a) Tracking response-first joint **(b)** Tracking response-second joint **(c)** Tracking error-first joint **(d)** Tracking error- second joint

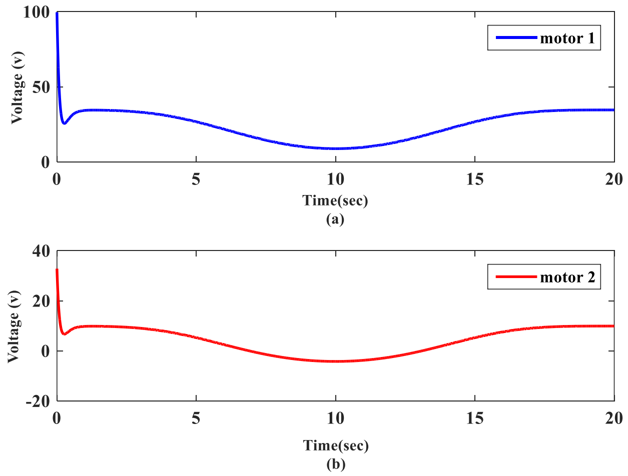

Fig. 9. Comparison 1: (SAAB) (a) Control input 1 **(b)** Control input 2

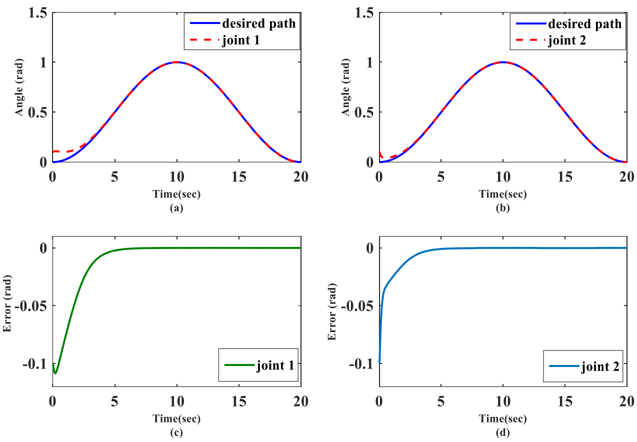

Fig. 10. Comparison 2: (SMAB) (a) Tracking response of first joint **(b)** Tracking response of second joint **(c)** Tracking error of first joint **(d)** Tracking error of second joint

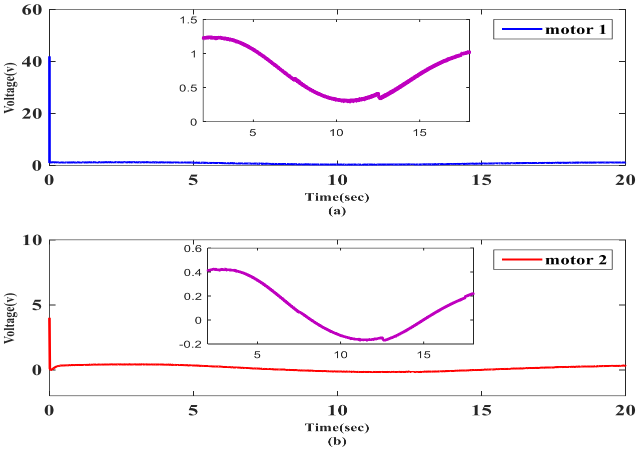

Fig. 11. Comparison 2: (SMAB) (a) Control effort of first joint **(b)** Control effort of second joint

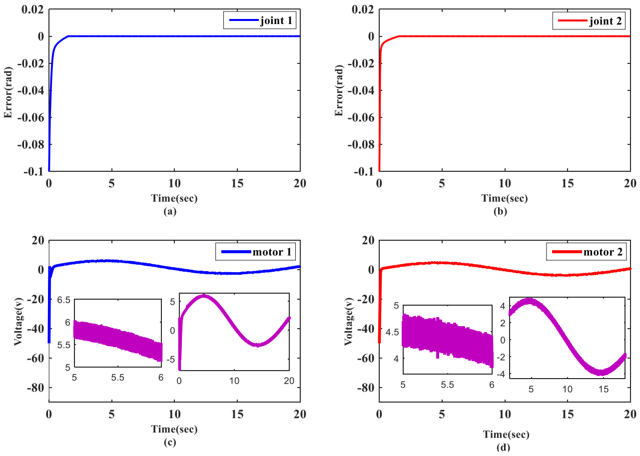

Fig. 12. Comparison 3: (ABSM) (a) Tracking error of first joint **(b)** Tracking error of second joint **(c)** Voltage of motor 1 **(d)** Voltage of motor 2

conditions, desired trajectory, external disturbance) are the same as one employed in the proposed ARTB controller. Therefore, the virtual input and the control input were derived as

$$x_{3d} = \hat{a}_2^{-1}\left(\hat{a}_1\dot{q} + \ddot{q}_d - k_1(\dot{q} - \dot{q}_d) - \lambda_1 s_1 - \gamma_1 sgn(s_1)\right) \quad (44)$$

$$u = \hat{a}_5^{-1}\left(\hat{a}_3\dot{q} + \hat{a}_4 I - \lambda_2 s_2 + \dot{I}_d - \hat{a}_2 s_1 - \gamma_2 sgn(s_2)\right) \quad (45)$$

in which $s_1 = (\dot{q} - \dot{q}_d) + k_1(q - q_d)$ and $s_2 = I_a - x_{3d}$. Furthermore, the upper bound of uncertainties can be obtained as

$$\dot{\gamma}_1 = \alpha_1\|s_1\|, \quad \dot{\gamma}_2 = \alpha_2\|s_2\| \quad (46)$$

The tuning parameters are chosen as $k_1 = 150 \times I_{2\times2}, \lambda_1 = 20 \times I_{2\times2}, \lambda_2 = 10 \times I_{2\times2}, \alpha_1 = diag(10{,}50)$ and $\alpha_2 = 2 \times I_{2\times2}$. Fig. 12(a)-(b) shows the tracking responses of ABSM controller. The voltage of motors is also exhibited in Fig. 12(c)-(d). Due to the existence of sign function in Equ. (44) and Equ. (45), the chattering phenomenon is appeared in the control inputs, which may damage to the actuators. To reduce the mentioned drawback, the saturation function can be used instead of sign function. However, it may lead to increase the tracking errors. Thus, a trade-off needs to considered between the stability and performance. It should be mentioned that our proposed method (ARTB) is relaxed from the aforesaid drawback.

To make a better comparison between the results of the control methods, we employ the performance criterion IAE (integral of absolute value of error), such that the superiority of the proposed ARTB to SAAB [13], SMAB [36] and ABSM [37] is shown in Table 2.

As a result, the main differences of the proposed controller ARTB with other methods can be listed as follows:

1) According to the IAE criterion, ARTB plays better performance in comparison with other methods.

2) ARTB is free from the manipulator dynamics while it is involved in SAAB and SMAB. Besides, our proposed adaptation mechanism is simpler than the laws described by (38) and (43).

3) ARTB is relaxed from the chattering phenomenon while ABSM suffers from it.

TABLE II

THE PERFORMANCE INDEX (IAE)

Control approach	*Joint 1*	*Joint 2*
The proposed ARTB	0.0082	0.0065
SAAB	0.0312	0.0102
SMAB	0.1988	0.0782
ABSM	0.0183	0.0094

VI. CONCLUSIONS

In this paper, an adaptive robust backstepping control law was proposed for the robot manipulator driven by electrical motors. First, a strict feedback form of the integrated robotic system was presented and, then, the robust voltage-based controller was developed through the backstepping steps to facilitate the backstepping tracking problem for robotic systems. From the control point of view, the proposed method was effective since the heavily coupled nonlinear model of manipulator did not directly influence the design procedure and the suitable estimation of the manipulator dynamics was only utilized in the control scheme. Moreover, the performance of the proposed technique was satisfactory in terms of reducing the complexity of the control signal under uncertainties. Stability analysis guaranteed the boundedness of the closed-loop system using the Lyapunov function and acceptable tracking errors were satisfied by the simulation results. Finally, the comparison between the tracking performance of the ARTB and three recent relevant studies demonstrated the superiority of the proposed control technique.

REFERENCES

[1] M. Van, H.-J. Kang, and Y.-S. Suh, "Second Order Sliding Mode-Based Output Feedback Tracking Control for Uncertain Robot Manipulators," *Int. J. Adv. Robot. Syst.*, vol. 10, no. 1, pp. 1–9, 2013.

[2] Z. Zhang, L. Zheng, J. Yu, Y. Li, and Z. Yu, "Three Recurrent Neural Networks and Three Numerical Methods for Solving a Repetitive Motion Planning Scheme of Redundant Robot Manipulators," *IEEE/ASME Trans. Mechatronics*, vol. 22, no. 3, pp. 1423–1434, 2017.

[3] S. S. Saab and P. Ghanem, "A Multivariable Stochastic Tracking Controller for Robot Manipulators without Joint Velocities," *IEEE Trans. Automat. Contr.*, no. c, pp. 1–16, 2017.

[4] F. Sabahi, "Robot Action Space of Tractable Subsumption Architecture," *Int. J. Ind. Electron. Control Optim.*, vol. 2, no. 4, pp. 297–304, 2019.

[5] M. Vijay and D. Jena, "PSO based neuro fuzzy sliding mode control for a robot manipulator," *J. Electr. Syst. Inf. Technol.*, pp. 1–14, 2016.

[6] X. Yin and L. Pan, "Direct adaptive robust tracking control for 6 DOF industrial robot with enhanced accuracy," *ISA Trans.*, vol. 72, pp. 178–184, 2018.

[7] K. Yovchev, K. Delchev, and E. Krastev, "State Space Constrained Iterative Learning Control for Robotic Manipulators," *Asian J. Control*, vol. 20, no. 1, pp. 1–6, 2018.

[8] F. Bouakrif, "Trajectory tracking control using velocity observer and disturbances observer for uncertain robot manipulators without tachometers," *Meccanica*, vol. 52, no. 4–5, pp. 861–875, 2017.

[9] T. K. Roy, M. A. Mahmud, W. Shen, A. M. T. Oo, and M. E. Haque, "Robust nonlinear adaptive backstepping excitation controller design for rejecting external disturbances in multimachine power systems," *Int. J. Electr. Power Energy Syst.*, vol. 84, pp. 76–86, 2017.

[10] B. Xu, "Disturbance Observer-Based Dynamic Surface Control of Transport Aircraft With Continuous Heavy Cargo Airdrop," *IEEE Trans. Syst. Man Cybern. Syst.*, vol. 47, no. 1, pp. 161–170, 2017.

[11] W. Lv, F. Wang, and Y. Li, "Finite-time adaptive fuzzy output-feedback control of MIMO nonlinear systems with hysteresis," *Neurocomputing*, vol. 296, pp. 74–81, 2018.

[12] N. T. Binh, N. A. Tung, D. P. Nam, and N. H. Quang, "An Adaptive Backstepping Trajectory Tracking Control of a Tractor Trailer Wheeled Mobile Robot," *Int. J. Control. Autom. Syst.*, vol. 17, no. X, pp. 1–9, 2019.

[13] N. Nikdel, M. A. Badamchizadeh, V. Azimirad, and M. A. Nazari, "Adaptive backstepping control for an n-degree of freedom robotic manipulator based on combined state augmentation," *Robot. Comput. Integr. Manuf. Elsevier*, vol. 44, pp. 129–143, 2017.

[14] N. Nikdel, M. Badamchizadeh, V. Azimirad, and M. A. Nazari, "Fractional-Order Adaptive Backstepping Control of Robotic Manipulators in the Presence of Model Uncertainties and External Disturbances," *IEEE Trans. Ind. Electron.*, vol. 63, no. 10, pp. 6249–6256, 2016.

[15] S. I. Han and J. M. Lee, "Prescribed performance fuzzy backstepping control for nonlinear large-scale systems," *Int. J. Control. Autom. Syst.*, vol. 13, no. 6, pp. 1508–1520, 2015.

[16] A. Khajeh, F. Piltan, M. R. Rashidian, and A. Salehi, "Design New Intelligent PID like Fuzzy Backstepping Controller," *I.J Mod. Educ. Comput. Sci.*, vol. 2, no. February, pp. 15–26, 2014.

[17] M. Vijay and D. Jena, "Backstepping terminal sliding mode control of robot manipulator using radial basis functional neural networks," *Comput. Electr. Eng.*, pp. 1–18, 2017.

[18] W. Sun, S. F. Su, J. Xia, and V. T. Nguyen, "Adaptive Fuzzy Tracking Control of Flexible-Joint Robots With Full-State Constraints," *IEEE Trans. Syst. Man, Cybern. Syst.*, vol. PP, no. 99, pp. 1–9, 2018.

[19] Y. Wu, R. Huang, X. Li, and S. Liu, "Adaptive neural network control of uncertain robotic manipulators with external disturbance and time-varying output constraints," *Neurocomputing*, vol. 323, pp. 108–116, 2019.

[20] X. Jin, "Adaptive Fixed-Time Control for MIMO Nonlinear Systems with Asymmetric Output Constraints Using Universal Barrier Functions," *IEEE Trans. Automat. Contr.*, vol. 64, no. 7, pp. 3046–3053, 2019.

[21] J. Bao, H. Wang, and X. P. Liu, "Adaptive finite-time tracking control for robotic manipulators with funnel boundary," *Adapt. Control Signal Process.*, pp. 1–15, 2020.

[22] M. M. Fateh, "On the Voltage-based Control of Robot Manipulators," *Int. J. Control. Autom. Syst.*, vol. 6, no. 5, pp. 702–712, 2008.

[23] M. Souzanchi-K, A. Arab, M. R. T. Akbarzadeh, and M. M. Fateh, "Robust Impedance Control of Uncertain Mobile Manipulators Using Time-Delay Compensation," *IEEE Trans. Control Syst. Technol.*, vol. 26, no. 6, pp. 1943–1953, 2018.

[24] J. Keighobadi, M. M. Fateh, and H. Chenarani, "Adaptive fuzzy passivation control based on Backstepping Method for Electrically Driven Robotic Manipulators," *2018 6th RSI Int. Conf. Robot. Mechatronics*, no. IcRoM, pp. 292–297, 2018.

[25] M. M. Fateh and S. Fateh, "Decentralized direct adaptive fuzzy control of robots using voltage control strategy," *Nonlinear Dyn.*, vol. 70, no. 3, pp. 1919–1930,

2012.

[26] R. Gholipour and M. M. Fateh, “Adaptive task-space control of robot manipulators using the Fourier series expansion without task-space velocity measurements,” *Meas. J. Int. Meas. Confed.*, vol. 123, no. April, pp. 285–292, 2018.

[27] N. Nasiri, H. Sadjadian, and A. M. Shahri, “Voltage-based control of a flexible-joint electrically driven robot using backstepping approach,” *4th Annu. Int. Power Electron. Drive Syst. Technol. Conf.*, pp. 541–546, 2013.

[28] J. B. Mbede and J. J. B. Mvogo Ahanda, “Exponential Tracking Control Using Backstepping Approach for Voltage-Based Control of a Flexible Joint Electrically Driven Robot,” *J. Robot.*, pp. 1–11, 2014.

[29] C. Kwan and F. L. Lewis, “Robust backstepping control of nonlinear systems using neural networks,” *Syst. Man Cybern. Part A Syst. Humans, IEEE Trans.*, vol. 30, no. 6, pp. 753–766, 2000.

[30] S. E. Shafiei and M. R. Soltanpour, “Robust neural network control of electrically driven robot manipulator using backstepping approach,” *Int. J. Adv. Robot. Syst.*, vol. 6, no. 4, pp. 285–292, 2009.

[31] M. W. Spong, S. Hutchinson, and M. Vidyasagar, *Robot modeling and control*. New York, 2006.

[32] F.-J. Lin, S.-G. Chen, and I.-F. Sun, “Intelligent Sliding-Mode Position Control Using Recurrent Wavelet Fuzzy Neural Network for Electrical Power Steering System,” *Int. J. Fuzzy Syst.*, vol. 19, no. 5, pp. 1344–1361, 2017.

[33] F. J. Lin, C. K. Chang, and P. K. Huang, “FPGA-based adaptive backstepping sliding-mode control for linear induction motor drive,” *IEEE Trans. Power Electron.*, vol. 22, no. 4, pp. 1222–1231, 2007.

[34] J. E. Slotine and W. Li, *Applied Nonlinear Control*. Prentice-Hall, 1991.

[35] M. M. Zirkohi, M. M. Fateh, and M. A. Shoorehdeli, “Type-2 fuzzy control for a flexible-joint robot using voltage control strategy,” *Int. J. Autom. Comput.*, vol. 10, no. 3, pp. 242–255, 2013.

[36] Y. Hsiao, P. Tu, and J. Lin, “Sliding Backstepping Control Design for Robotic Manipulator Systems with Motor Dynamics,” *IEEE Int. Conf. Control Autom.*, pp. 667–672, 2014.

[37] M. A. M. Basri, “Design and application of an adaptive backstepping sliding mode controller for a six-DOF quadrotor aerial robot,” *Robotica*, vol. 36, no. 11, pp.1680-1700, 2018.

Javad Keighobadi was born in Sabzevar, Iran. He received the B.Sc. and M.Sc. degrees in Control engineering from Shahrood university of Technology, Iran in 2012 and 2014, respectively. He is currently working toward the Ph.D. degree at the Department of Electrical and Robotic Engineering, Shahrood University of Technology, Iran. His research interests include advanced nonlinear control, fuzzy learning control, robotics, and adaptive control.

Mohammad Mehdi Fateh received the B. Sc. degree from Isfahan University of Technology, Iran in 1988, the M. Sc. degree in electrical engineering from Tarbiat Modares University, Iran in 1991, and the Ph.D. degree from Southampton University, UK in 2001. He is a full professor at Department of Electrical and Robotic Engineering, Shahrood University of Technology, Iran. His research interests include nonlinear control, fuzzy control, robotics, intelligent systems, mechatronics and automation.

International Journal of Industrial Electronics, Control and Optimization © 2021 IECO
Vol. 4, No. 1, pp. 23-31, Jan (2021)

Analyzing the Advantage of Combination of Density Forecasts in Tehran Stock Exchange

S.Raheleh Shahrokhi[1], Hamid Khaloozadeh[2], and HamidReza Momeni[3,†]

[1,3] Department of Electrical and Computer Engineering, Tarbiat Modares University, Tehran, Iran.
[2] Department of Electrical Engineering, K.N. Toosi University of Technology, Tehran, Iran.

ABSTRACT

Today, stock market plays a key role in the economy of any country and is considered as one of the growth indicators of any economy. Gaining the skills of gathering and analyzing data simultaneously, as well as using this knowledge in economic investigations, make time and precision factors to be the drawcard of any investor in competition with others. Therefore, having a predictive approach with the lowest degree of error will lead to smarter management of resources. Due to the complex and stochastic nature of the stock market, conventional forecasting approaches in this field have usually faced serious challenges, most notably losing the robustness when the data type changed over time. Moreover, by focusing on point forecasting, some useful statistical information about the objective random variable has been ignored inadvertently, undermining the prediction efficiency. The focus of this study is on density forecasting models which, unlike point forecasting, contain a description of uncertainty. Also, to take advantage of the diversity and robustness features of the combination, instead of an individual prediction, a combination of the density forecasting given by different structures of ARMA, ANN, and RBF models is presented. In order to analyze the capabilities of these approaches in Tehran Stock Exchange (TSE), two basic methods of this category have been used to predict the price of MAPNA stock -one of the fifty active companies in this market- in the period 2012 to 2019.

Article Info

Keywords:
Density Forecasting, Forecast Combination, Neural Networks, Simple Average, Stock Market

Article History:
Received 2019-12-31
Accepted 2020-04-26

I. INTRODUCTION

Basically, all managers need efficient predictions for the appropriate management of their resources. Therefore, forecasting plays a key role in their precise decision making. However, in practice, predictions are not usually accurate, so one of the most important objectives of the management systems is to decrease forecasting errors as much as possible.

On the other hand, it is clear that, nowadays, stock market investment is a significant part of every country's economy. Therefore, the national economic indicators are heavily influenced by stock market performance [1]. The multiplicity of effective factors on stock market and the existence of many other unknown factors cause uncertainty in the field of financial time series forecasting; and consequently, it has inappropriate impacts on the investments which are based on these forecasts. Thus, it is necessary to use such appropriate scientific methods in order to make applicable and reliable predictions. In this particular application, due to the nature of prediction, the occurrence of an error in different forecasting models is unavoidable. So, naturally, a model with a lower prediction error rate is preferred over others. Hence, the necessity of a relevant forecasting model that maximizes the efficiency of investment via optimizing resource allocation is extremely sensible.

The prediction of stock return and price is possible by discovering behavioral patterns of the stock price generating process. The ability to detect such behavioral patterns determines the efficiency of the prediction method. This process may be a linear, nonlinear, or stochastic model [2]. The stock market forecasting methods can be classified into three general categories: traditional or classic methods, modern

---

[†] **Corresponding Author**: momeni_h@modares.ac.ir
Tel: +98-21-82883375, Fax: +98-21-8006544
Department of Systems and Control, Faculty of Electrical and Computer Engineering, Tarbiat Modares University, Tehran, Iran.

methods, and combined methods.

In different forecasting fields, several approaches with various success degrees have been applied; however, it should be noted that each of these approaches has such disadvantages as the inability to model nonlinear relationships, getting stuck in local optimums, over-fitting, and the difficulty of choosing numerous regulation parameters, each directly affecting prediction accuracy. In addition, sometimes the prediction accuracy of these approaches is different for data with various behaviors. In other words, in case of using a particular approach, the robustness is likely to be lost while the data type changes. Therefore, determining which one is the best choice for any given situation is not straightforward and depends on many factors. Indeed, when only one particular approach is used to solve a problem, other structures of this method and even other methods, each with its own advantages and disadvantages, are ignored and actually removed from the solution set.

To solve this problem and, simply put, to take advantage of the different approaches simultaneously, combination mechanisms are proposed, in which a combination of the solution of different approaches for a specific problem is considered. Using these methods will lead to many achievements, such as reducing the uncertainty in parameter setting, decreasing the randomness of the training process, and so on. Therefore, a suitable combination mechanism to achieve the stated goals would be very useful.

One approach to improve the structure of forecast combination mechanisms is to change components that are combined together in order to make the final prediction. In this regard, by substituting the point forecasting models instead of the density forecasting models, in addition to predicting price as the only advantage of the point forecasting, further useful information can be achieved, too.

The focus of this study is on two basic forecast combination method, namely Simple Average (SA) and Bates & Granger (B&G). Although these methods were proposed a long time ago, they are still being widely used. In particular, it may be interesting to know that some researchers are still attempting to improve their forecast combination methods such that the robustness of their mechanisms can be comparable with SA. According to the key role of risk management in investment, helping investors to minimize the risk of their investments is one of this study's goals. So, by using those forecast combination methods and then applying them to combine some density forecast models, the advantages of using these approaches in Tehran Stock Exchange (TSE) will be investigated, in this study.

The remainder of this paper is outlined as follows. In section II, an overview of related work is provided. The structure of the desired combination system is described in section III. Also, two famous linear combination methods are explained in this section. Then, the method of producing the system inputs is presented. Simulation results are provided in the next section and finally the paper is concluded in section V.

II. LITERATURE REVIEW

Since financial time series is dynamic, nonlinear, complex, nonparametric and disordered in nature, it is a generally challenging task to predict the stock market [3]. Many people have made the prediction with different approaches. Before the advent of computers and their being used for forecasting in the financial domain, classic methods, such as technical and fundamental analysis, had been employed to solve these problems. Since the mid-1970s, great efforts have been made to investigate the predictability of stock prices using new mathematical methods based on time series and more advanced tools [4]- [6]. Among the classic methods that have been widely used to predict the stock market, one can refer to Autoregressive (AR), Autoregressive Moving Average (ARMA) and Autoregressive Integrated Moving Average (ARIMA) models [7]. Also, a number of these methods that are the practical approach for time series prediction have been introduced in [8] by Boxes and Jenkins. These models and, in particular, the ARIMA model are widely used in many different fields, but they can only perform linear prediction in time series. This feature makes such models inappropriate for predicting time series with nonlinear components [9].

Through the efforts of mathematical and dynamic systems scientists to address the deficiencies of linear models, new methods, called modern methods, have been proposed to predict prices in the stock market [10]. They are able to be applied in various sciences, especially economics. Therefore, nonlinear system practitioners have tried to explain stock price behavior and predict it through advanced nonlinear methods in financial markets, too. Due to the uncertainty of stock market and based on the articles reviewed in the survey article [11], soft computing techniques, belonging to the modern methods, are suitable for considering nonlinear relationships in the stock and, in most cases, outperform classic methods as they have better results for financial systems and have higher prediction accuracy without prior knowledge about the statistical distribution of input data. Machine learning’s popularity is still increasing in financial forecasting. The ability of data mining and the flexibility of these algorithms have made them a very proper option for working on complex financial data [12]. There are different machine learning algorithms, each with respect to its own strengths, designed to solve a specific problem. Some of them work like the decision tree, where the user can fully understand the steps of the machine inference, and some act like neural networks similar to a black box. Artificial Neural Network (ANN) is one of the computational tools that is known as the most practical and widely used method for modeling large and complex problems [3], [13]. After an initial study of White in [14], the artificial neural network was first applied in the financial field and was subsequently considered as a suitable model for predicting the stock market. A review of the application of ANN in stock market forecasting is presented in [11], [15]. The results of the studies show that ANN is robust in model specification compared to parametric models, and, for this reason, it has been used frequently to predict stock prices and other financial derivatives [16]. The long history of using ANN in the financial field has led to more advanced versions of it, like the Radial Basis Function (RBF) network, being released in order to improve its performance. Reference [17] is one of the first articles that uses Support Vector Machines (SVMs) for financial forecasting. Then, the performance of SVMs is compared with the performance of other algorithms, such as backpropagation and RBF. Support Vector Regression (SVR) is another nonlinear forecasting algorithm used to predict financial time series. The efficiency of SVR as a predictive method is shown in [18]- [20]. Artificial neural networks and their variants have been widely used in the literature, but with the appearance of kernel-based methods such as SVR and considering their advantages, they fell out of fashion over time. Then, in 2006, Hinton et al. rekindled interest in neural networks by demonstrating an excellent performance of deep neural networks in [21]. Since then, researchers have conducted numbers of studies on using deep learning for financial time series.

With numerous choices in forecasting tools, to address the shortcomings of various approaches, perhaps one obvious way is to combine two or more models and present one prediction. In this way, the strengths of a method can be used to overcome the weaknesses of the others. In this regard, the combination of linear and nonlinear models has been suggested by several studies [22]- [24]. McDonald et al. in [9] showed that among several combined models, the combination of ARIMA models and Self-Organizing Fuzzy Neural Networks (SOFNN) performs better than others. Raoofi et al. in [25] compared several combined methods for forecasting Tehran Stock Exchange Index based on ARIMA, Fuzzy ARIMA (FARIMA), ANN and Adaptive Neuro-Fuzzy Inference System (ANFIS) models. By using some forecast accuracy measures such as Root Mean Square Error (RMSE) and Mean Absolute Error (MAE), they concluded that the combined models of ANFIS and FARIMA have outperformed other models. Also, Fallahpour et al. in [26] showed that the prediction of the combined SVM model based on Genetic Algorithm (GA) for stock price movement trend is far better and more accurate than simple SVM. The application of different types of neural network and their combined models for the financial forecasting is one of the areas of interest to researchers. [27]-[29] can be mentioned as proper examples.

Some researchers believe that it is better to forecast the time series with high uncertainty, like financial market time series, by using forecast combination methods instead of using only one forecast model. Timmermann made a thorough review of the forecast combination mechanisms in [30]. He expressed the reasons for using forecast combination methods in order to produce better forecast and also discussed the conditions under which these mechanisms are admissible and useful. Due to the key role of forecast combination in different fields of forecasting, particularly in financial market and economic, after Timmermann's paper in 2006, many researchers are keeping their study on it till now. Most of these literatures ([31]- [36]) are about the structures of the combination and the weight assignment mechanisms. The large number of researcher concord on this point that even the simplest structure of the forecast combination can be helpful when necessary conditions are available. According to [37], [38], even if a simple forecast combination method does not be able to improve the forecast accuracy, it can decrease model selection risk. more recently, Atiya in [39] provides a brief analysis of the reasons for the success of forecast combination. Ultimately, reviewing the literature shows that the forecast combinations generally perform well [40].

As mentioned in economic forecasting and some other similar fields, the inability of point forecasting to describe the uncertainty of the variables leads to the use of density forecasting which has been used recently in forecasting the variables with high degree of uncertainty, like financial forecasting, [41]- [43]. That is, in order to forecast variables with a high degree of uncertainty, a density forecast is a comprehensive form of the point forecast. So, one idea is to use the density forecast combination to take advantage of both combination and density forecast abilities that is addressed in this paper.

According to all superiority of forecast combination and also density forecast combination in forecasting field, it will be very helpful to investigate the advantages of their application in Tehran Stock Exchange, which unfortunately is not done so far. Therefore, more researches still need to be done in this field for helping investors to have accurate decision making in this market.

III. METHODOLOGY

To take advantage of several available prediction models, one can derive the results of each model and combined them by the appropriate approach to achieve a single prediction, rather than using them to present an improved hybrid model. Actually, faced with various forecasts of the same variable, an issue that immediately arises is whether one should identify the best prediction or combine the underlying forecasts. Different conditions must be considered to answer this question, but in general and from a theoretical point of view, if a specific prediction model can be found having smaller prediction error than its competitors, then it justifies relying on a single prediction; otherwise, diversification gains of combination makes this approach more attractive than choosing the best model. Even if the best model can be recognized at any moment, the combination may still be an absorbing diversification strategy, though its success will depend on the structure of the combination and method of determining its weights. In fact, the diversification of a simple portfolio was the initial idea and the reason for using the forecast combinations [44].

Also, if each predictor model has useful and effective input variables, using all of which leads to a comprehensive model, the comprehensive model must be used in order to improve the outcome. Yet, when these variables are not available, the only option is the combination.

The next reason for using forecast combinations that have been mentioned by many researchers, including Stock and Watson in [45], [46], is that individual forecasting models may be subject to misspecification bias of unknown form. It is clear that even the best model at the specific time may not be preferred over other models at all times. Also, the best model may be time-variant, so it can be hard to track based on past forecasting performance. Forecast combinations can be viewed as a way to making the forecast more robust against such misspecification biases and measurement errors in the data sets underlying the individual forecasts [47].

Another argument for combining predictions is that basic prediction models may be based on different loss functions. Given the structure of the desired loss functions, forecast combinations can be helpful in improving the outcome, in these conditions, too.

Therefore, to benefit from the capabilities of combining forecasts, this approach can be applied to the stock market domain or any other domain with a similar data structure. If a combination mechanism, as shown in Fig.1, is considered as a system, the individual forecasts and the final predictions for the desired variable are input and output of this system, respectively. It combines predictions in such a way that, in the worst case, the use of combination theory is justified. In order to improve the performance of each system, one can change various parts of the system such as input, output and main structure of the system.

Fig. 1. Forecast Combination System.

Due to the important role of the combination in the field of prediction and the achievements of its application, several good review articles such as [30], [48], [49] have been published so far, but among them, Timmerman's survey article in 2005 [30] is the most recent and also the most comprehensive, according to numerous subsequent articles, including [50]. After developing the initial idea of the combination, different researchers have worked on its weights with various approaches to improving this idea; in this article, however, the combination is done by two primary and, of course, basic methods.

A. *Simple Average*

For the reasons stated, the researchers decided to use a combination of several predictions instead of the results of a single prediction model, in which the new problem was how to combine these results, appropriately. In this regard, SA based on Equal Weights (EW) is considered as the simplest and most primitive way that comes to mind. It is defined as:

$$f_{t+h|t}^{EW} = \frac{1}{m}\sum_{i=1}^{m} f_{i,t+h|t} \qquad (1)$$

where

h	forecast horizon;
y_{t+h}	target variable of forecast;
$f_{i,t+h\|t}$	output of i-th forecast model;
m	number of forecast models;
$f_{t+h\|t}^{EW}$	output of SA forecast combination method.

This simple method of combination, as people in different fields asserted, has been able to improve the prediction results [30] and even performs better than other approaches presented later.

B. *Linear Combination with Optimal Weights*

After developing the SA method, in order to improve its results, the researchers decided to obtain the optimal value of the combination weights to minimize the prediction error instead of the equal weights. This idea was first proposed in 1969 by Bates and Granger in [44] as Optimal Weights (OW). The weights are determined by the Least Square (LS) estimation method using previous prediction error data. They call the weights optimal so that the variance of the in-sample error is minimized. The result of their work is:

$$f_{t+h|t}^{BG} = \widehat{W}_{OLS}' F_{t+h|t} = \left(\left(\iota' \hat{\Sigma}_e^{-1} \iota\right)^{-1} \hat{\Sigma}_e^{-1} \iota\right)' F_{t+h|t} \,,$$

$$\hat{\Sigma}_e = (t-h)^{-1} \sum_{\tau=1}^{t-h} \boldsymbol{e}_{\tau+h|\tau} \boldsymbol{e}_{\tau+h|\tau}' \qquad (2)$$

where

ι	column vector of ones;
$\boldsymbol{e}_{\tau+h\|\tau}$	prediction error vector;
$\hat{\Sigma}_e$	estimation of covariance matrix;
$\widehat{W}_{OLS}$	weight vector;
$f_{t+h\|t}^{BG}$	output of B&G forecast combination method.

It should be noted that in the optimization process, the weights are considered to be positive and the sum of them equal to one. In this study, this method is known as B&G.

It is notable that if all the predictions in the combination have the same error variance and the correlation between them is equal, the optimal weights will have the same value, too. In other words, under these conditions, the optimal weights are EW [30].

In this combination approach, the role of estimation error in the efficiency of the method is very prominent, so researchers have made many efforts to reduce this error and its consequences.

C. Density Forecast Combinations

So far, the focus was on the combination of point forecasts, which is influenced by the fact that a large proportion of academic studies are focused on these types of forecasts. Nevertheless, the tendency of researchers to study density forecasts is also growing, and published articles in the field of economics employ combination methods for these categories of forecasts. In addition, similar approaches have also been used for forecasting in other fields, such as meteorology.

One reason for the tendency of researchers to density forecasts is that a density forecast is an estimate of the probability distribution of the probable values of a random variable at some future time. Therefore, in contrast to a point forecast, which by itself has no description of the prediction uncertainty, a density forecast provides a full description of the associated uncertainty.

Today in many contexts of finance and economics, it is helpful and even in some cases necessary to provide density forecasts and evaluate them. Therefore, the next cause of people's shift from point forecasting to density forecasting is its valuable application in important financial fields, such as risk management. Many peoples have investigated density forecasts and their applications in macroeconomics and finance. Among them [43], [51]– [53] can be noted. Besides, [54] has addressed how to evaluate density forecasts. In this article, the combination of density forecasts is computed as follow:

$$p(y_{t+h}|D) = \sum_{i=1}^{m} w_i p(y_{t+h}|M_i,D) \qquad (3)$$

where

D	data and observations;
M_i	i-th forecast model;
w_i	i-th weight determined by density forecast combination methods.

D. Input Generation Process

As mentioned above, inputs of the system shown in Fig. 1, have been generated using the predictions of several models. What the forecast models are and how they are selected can be a separate research topic, but this article focuses on a number of points for these choices. For example, both linear and nonlinear methods exist in the models and, from each category, select methods that are widely used for forecasting in the financial field. Therefore, in the first step, different structures of selected models including ARMA, ANN and RBF are used to predict the target random variable.

In the density forecasting literature, the density function is often assumed to be a normal or Gaussian distribution, whereas in practice, many financial time series exhibit asymmetric features or patterns [43]. In this study, the density forecasts are estimated by a non-parametric method, named kernel smoothing algorithm. As a result, no specific distribution is considered for densities.

IV. RESULTS AND DISCUSSION

To demonstrate the advantages of density forecasting methods and their combinations in Tehran Stock Exchange, they are used to forecast the price of MAPNA company as one of the 50 active companies in this market. Then, daily price of this stock, from 1 January 2012 to 31 August 2019 (1447 data), is considered. Fig.2 shows the real values of MAPNA stock price over this period. For each type of prediction models, they are first trained with specific n-observation (75% of total data) input-output patterns. Then, the models are employed to forecast the remaining observations (25% of total data) and the performances are evaluated in terms of Mean Squared Error (MSE). All data are normalized by Min_Max method as follows:

$$D_{Normal} = \frac{D_{Real} - min(D_{Real})}{max(D_{Real}) - min(D_{Real})} \qquad (4)$$

where

D_{Real}	real value of data;
D_{Normal}	normalized data.

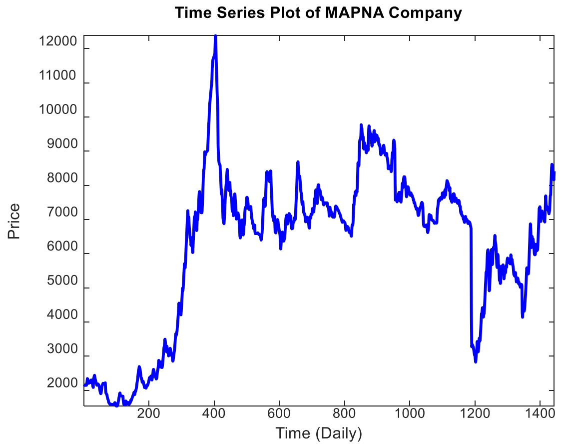

Fig. 2. Real Values of MAPNA Stock Price from Jan. 2012 to Aug. 2019.

Due to the structures, considered for ARMA, ANN, and RBF models, finally 8 prediction models have been used and their characteristics are presented in Table I. The parameter settings and the model structure selections are done such that both high-performance and low-performance models are included in the combination. Given these assumptions, the key role of combination in decreasing the sensitivity of model selection becomes evident, that is one of the purposes of this study. In this regard, no attempt was made to provide the best structures of the prediction models.

Normalized data are given to all forecast models as input, and each of them predicts a value of price for h-day ahead (where 'h' is the prediction horizon and it is considered 3 in this study, arbitrarily).

TABLE I
STRUCTURE OF PREDICTION MODELS

Model	Structure				
ARMA	**Model Order**		**Estimation Method**		
	$AR = 2, MA = 0$		RLS		
	$AR = 2, MA = 1$		ELS		
ANN	**Learning Method**	**No. of Hidden Layers**	**No. of Neurons**	**Epochs**	**Learning Parameters**
	Gradient Descent	$l_h = 1$	$n_h = 3$	500	$\eta = 0.001$
	Gradient Descent	$l_h = 1$	$n_h = 5$	500	$\eta = 0.001$
	Levenberg Marquardt	$l_h = 1$	$n_h = 3$	60	$\alpha = 5$
	Levenberg Marquardt	$l_h = 1$	$n_h = 5$	60	$\alpha = 5$
RBF	**Learning Method**	**Radial Function**	**No. of Neurons**	**Epochs**	**Learning Parameters**
	Levenberg Marquardt	$l_h = 1$	$n_h = 30$	100	$\alpha = 1$
	Levenberg Marquardt	$l_h = 1$	$n_h = 50$	100	$\alpha = 1$

To performance comparison, MSE values of all models have been computed. For brevity, Table II shows this value for only three selected models.

TABLE II
PERFORMANCE COMPARISON OF SELECTED PREDICTION MODELS

Forecast Model	MSE	
	In-Sample	Out-of-Sample
ARMA	58663	202246
ANN_LM_3	101784	209364
RBF_LM_50	567971	381534

For more clarity of figures and to make them understandable, Figs. 3 and 4 show the true and forecasted value of MAPNA stock price, obtained by only selected models for part of in-sample (from sample 800 to 1000) and out-of-sample (from sample 100 to 290) data, respectively. It has been attempted to select a range of samples in which high volatility of price has occurred to illustrate the difference between the performance of selected methods in the face of this event. According to these diagrams, it is obvious that different models, selected to be in the combination system, have various performance and accuracy over time. But it should be noted that, as it can be seen by the comparison of the efficiency of the RBF_LM_50 model for in-sample and its performance for out-of-sample data, the performance of these forecast models may be changed in any other period or for any other data.

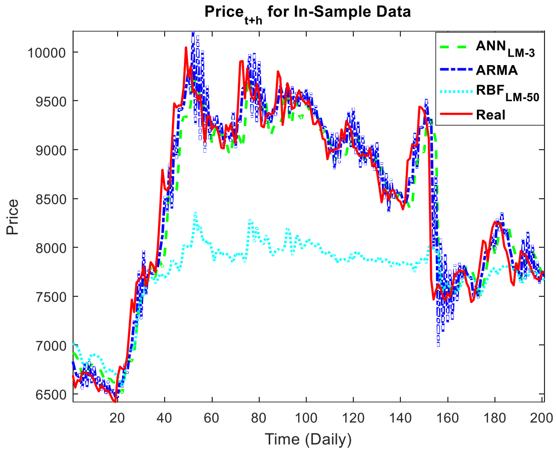

Fig. 3. Real vs. Predicted Values of MAPNA Stock Price for the Part of In-Sample Data (Related to Three Selected Forecast Models).

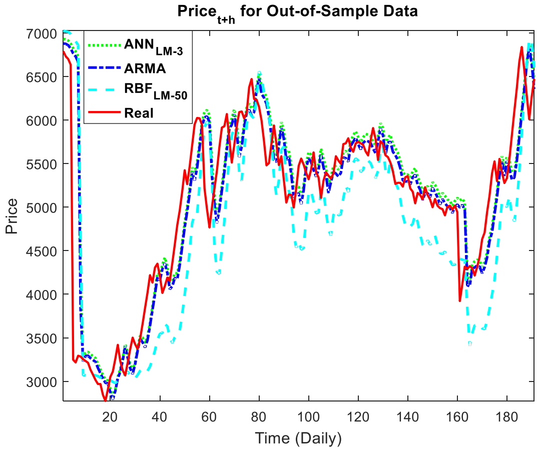

Fig. 4. Real vs. Predicted Values of MAPNA Stock Price for the Part of Out-of-Sample Data (Related to Three Selected Forecast Models).

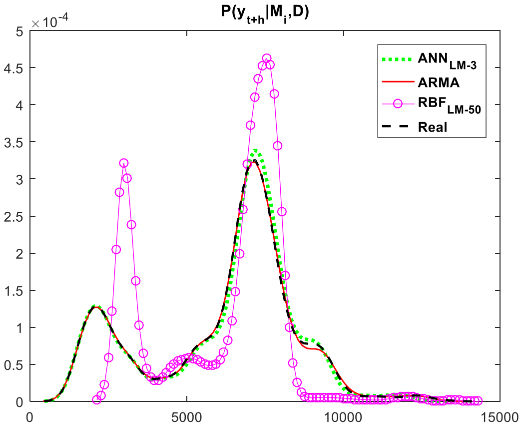

Fig. 5. Real vs. Predicted Density of MAPNA Stock Price (Related to Three Selected Forecast Models).

So far, all models are used to generate some point forecasts while the inputs of the combination system must be in the form of density forecasts. Then in the next step, the probability density of each prediction model output is computed by using a kernel smoothing algorithm. The comparison between Figs. 4 and 5 shows that if one model has a good or poor relative performance in point forecasting, it has a similar performance in density forecasting, too; however, the density forecasting has additional useful information that makes it more valuable. For instance, in contrast to the point forecasts, the density prediction has a description of the stock price uncertainty. In addition, based on the information included in probability density, an investor can be able to have better risk management.

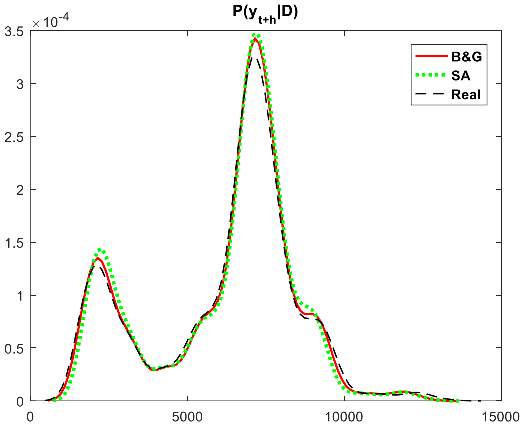

Fig. 6. Density Forecast Combinations for MAPNA Stock Price Using SA and B&G methods.

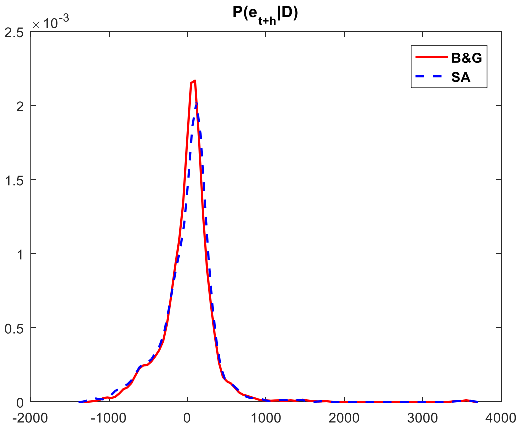

Fig. 7. Probability Density of Error for Two Forecast Combination Mechanisms.

Finally, for two different combination methods, SA and B&G, forecast combination system output is shown in Fig. 6. It demonstrates that both of them have been able to cover the poor performance of some models by relying on the results of the superior models and, ultimately, they have predicted the probability density of the MAPNA stock price with reasonable accuracy.

For a better illustration of the accuracy of density forecasts, probability densities of their errors are shown in Fig. 7. The similarity of these error densities to white noise and this fact that they are relatively symmetric around zero shows that these methods have been able to use the effective information, approximately.

As mentioned above, the efficiency of the same model may be changed for different data or in various periods. Now, assume that the RBF_LM_50 model was an efficient prediction model to forecast the MAPNA stock price in all the times before the period considered in this study. Consequently, according to the good past performance of the RBF_LM_50 model, it is selected as the best model to forecast this specific data. However, according to Fig. 3 can be found that, if so the investor will suffer heavy losses. But his losses were decreased seriously if he considered the RBF_LM_50 model as one of the selected models in forecast combination (see Fig. 6).

Besides the mentioned advantage, the investor can estimate Value at Risk (VaR) and Conditional VaR (CVaR) values of this stock by using density forecast combination. In other words, by using the density forecast, the investor can forecast the risk value of MAPNA or any other stock. Fig. 5 shows that if the investor has only the density forecast obtained by the RBF_LM_50 model, he cannot estimate the CVaR value of MAPNA stock with a reasonable error; and hereby the important advantage of using the density forecast combination is determined. It should be noted that one of the reasons for selecting MAPNA, among the 50 active companies in Tehran Stock Exchange, is that the density of this stock price is such that the selected methods can forecast it with significantly different performances. This property, in particular at the left tail of the probability density is very useful to demonstrate the advantage of density forecast combinations in computing VaR and CVaR.

V. CONCLUSIONS

This study was undertaken to investigate the advantages of using a density forecast combination vs. individual point forecast in Tehran Stock Exchange. The simulation results show that the sensitivity of forecast model selection is decreased by applying combination mechanisms such that, although some individual models have poor efficiency, the precision of forecast combination models are adequate. In addition, because of its diversity property of these mechanisms, the robustness of these prediction methods against the model misspecification biases of the individual forecasts increases. On the other hand, the simulation results confirm that density forecasting implicitly includes point forecasting and also provides more helpful information. For example, investors can apply this probability density function (PDF) to recognize maximum and minimum of any stock price in a specific period of time (from past to future), which helps them to make appropriate decisions. Moreover, they can use these densities to compute risk based on some risk assessments, like VaR and

CVaR. These findings could be exploited in any situation where the prediction of time series with structures similar to stock price is needed. Future work will involve the application of these densities to improve portfolio management in order to have maximum return and minimum risk. Another one will be proposing a proper nonlinear combination mechanism that is able to upgrade the result subject to the nature of these density functions.

REFERENCES

[1] A. Azar, and S. Karimi, "Stock return prediction using accounting ratio with the neural network approach," Financial Research Journal, Vol. 11, No. 28, pp. 3-20, 2009.

[2] H. Khaloozadeh, and A. Khaki Sedigh, "Stock Price Modeling and Forecasting Using Stochastic Differential Equations," Journal of Economic Research, No. 69, pp. 1-6, 2005.

[3] S. A. Ghoreishi, and H. Khaloozadeh, "Application of Covariance Matrix Adaptation-Evolution Strategy to Optimal Portfolio," International Journal of Industrial Electronics, Control and Optimization, Vol. 2, No. 2, pp. 81-90, 2019.

[4] H. Abrishami, M. Mehrara, M. Ahrari, and S. Mirghasemi, "Forecasting The GDP in Iran Based on GMDH Neural Network," Journal of Economic Research, No. 88, pp. 1-24, 2009.

[5] H. Abrishami, A. Moeini, M. Mehrara, M. Ahrari, and F. Soleymanikia, "Forecasting Gasoline Price Using GMDH Neural Network Based on GA," Iranian Journal of Economic Research, No. 36, pp. 37-58, 2008.

[6] S. Soni, "Applications of ANNs in Stock Market Prediction: A Survey," International Journal of Computer Science & Engineering Technology, Vol. 2, pp. 71-83, 2011.

[7] G. S. Atsalakis, K. P. Valavanis, "Surveying Stock Market Forecasting Techniques-Part I: Conventional Methods," Journal of Computation Optimization in Economics and Finance Research Compendium, pp. 49-104, 2010.

[8] G. E. Box, G. M. Jenkins, and G. C. Reinsel, "Time Series Analysis: Forecasting and Control," Wiley, New York, 2013.

[9] S. McDonald, S. Coleman, T. M. McGinnity, Y. Li, and A. Belatreche, "A Comparison of Forecasting Approaches for Capital Markets," Computational Intelligence for Financial Engineering & Economics (CIFEr) IEEE Conference, pp. 32-39, 2014.

[10] H. A. Sinai, S. Mortazavi, and Y. Teimoori asl, "Tehran Exchange Price Index Forecasting by Artificial Neural Networks," Accounting and auditing Review, Vol. 2, No. 3, pp. 59-83, 2005.

[11] G. S. Atsalakis, K. P. Valavanis, “Surveying Stock Market Forecasting Techniques–Part II: Soft Computing Methods,” Expert Systems with Applications, Vol. 36, No. 3, pp. 5932–5941, 2009.

[12] S. McDonald, S. Coleman, T. M. McGinnity, Y. Li, and A. Belatreche, "A Comparison of Forecasting Approaches for Capital Markets," Computational Intelligence for Financial Engineering & Economics (CIFEr) IEEE Conference, pp. 32-39, 2014.

[13] D. Gholamiangonabadi, S. D. Mohseni Taheri, A. Mohammadi, and M. B. Menhaj, "Investigating the Performance of Technical Indicators in Electrical Industry in Tehran's Stock Exchange Using Hybrid Methods of SRA, PCA and Neural Networks," 5th IEEE Conference on Thermal Power Plants (CTPP), pp. 75-82. 2014.

[14] H. White, "Economic Prediction Using Neural Networks: The Case of IBM Daily Stock Returns," IEEE International Conference, pp. 451–458, 1988.

[15] Y. Li, W. Ma, "Applications of Artificial Neural Networks in Financial Economics: A Survey, "International Symposium on Computational Intelligence and Design, IEEE Computer Society, Vol. 01, pp. 211–214, 2010.

[16] Y. Wang, I. Ch. Choi, "Market Index and Stock Price Direction Prediction Using Machine Learning Techniques: An Empirical Study on the KOSPI and HIS," ScienceDirect, pp. 1–13, 2013.

[17] T. B. Trafalis, H. Ince, "Support Vector Machine for Regression and Applications to Financial Forecasting," Proceedings of the IEEE-INNS-ENNS International Joint Conference on Neural Networks (IJCNN), Vol. 6, 2000.

[18] F. E. Tay, L. Cao, “Application of Support Vector Machines in Financial Time Series Forecasting,” Omega, Vol. 29, No. 4, pp. 309– 317, 2001.

[19] L. J. Cao, F. E. H. Tay, “Support Vector Machine with Adaptive Parameters in Financial Time Series Forecasting,” IEEE Transactions on Neural Networks, Vol. 14, No. 6, pp. 1506–1518, 2003.

[20] R. Khemchandani, S. Chandra, and others, “Regularized Least Squares Fuzzy Support Vector Regression for Financial Time Series Forecasting,” Expert Systems with Applications, Vol. 36, No. 1, pp. 132–138, 2009.

[21] G. Hinton, S. Osindero, and Y. W. Teh, “A Fast Learning Algorithm for Deep Belief Nets,” Neural Computation, Vol. 18, No. 7, pp. 1527–1554, 2006.

[22] L. Wang, H. Zou, J. Su, L. Li, and S. Chaudhry, “An ARIMA-ANN Hybrid Model for Time Series Forecasting,” Systems Research and Behavioral Science, 2013.

[23] Z. Hua and B. Zhang, “A Hybrid Support Vector Machines and Logistic Regression Approach for Forecasting Intermittent Demand of Spare Parts,” Applied Mathematics and Computation, Vol. 181, No. 2, pp. 1035–1048, 2006.

[24] G. P. Zhang, “Time Series Forecasting Using a Hybrid ARIMA and Neural Network Model,” Neuro-computing, Vol. 50, pp. 159–175, 2003.

[25] A. Raoofi, A. H. Montazer-Hojjat, and P. Kiani, “Comparison of Several Combined Methods for Forecasting Tehran Stock Exchange Index,” International Journal of Business Forecasting and Marketing Intelligence, Vol. 2, No. 4, pp. 315-333, 2016.

[26] S. Fallahpour, Gh. Golarzi, and N. Fatourechian. "Predicting Stock Price Movement Using Support Vector Machine Based on Genetic Algorithm in Tehran Stock Exchange Market," Financial Research Journal, Vol. 15, No. 2, pp. 269-288, 2013.

[27] A. M. Rather, A. Agarwal, V. N. Sastry, "Recurrent Neural Network and a Hybrid Model for Prediction of Stock Returns," Expert Systems with Applications, Vol. 42, No. 6, pp. 3234-3241, 2015.

[28] R. Bisoi, P. K. Dash, "A Hybrid Evolutionary Dynamic Neural Network for Stock Market Trend Analysis and Prediction Using Unscented Kalman Filter," Applied Soft Computing, Vol. 19, pp. 41-56, 2014.

[29] J. Patel, S. Shah, P. Thakkar, K. Kotecha, "Predicting Stock and Stock Price Index Movement Using Trend Deterministic Data Preparation and Machine Learning Techniques," Expert Systems with Applications, Vol. 42,

No. 4, pp. 259-268, 2015.
[30] A. Timmermann, “Forecast Combinations,” CEPR Discussion Paper, No. 5361, 2005.
[31] I. Sánchez, "Adaptive Combination of Forecasts with Application to Wind Energy," International Journal of Forecasting, Vol.24, No. 4, pp. 679-693, 2008.
[32] G. Claeskens, J. R. Magnus, A. L. Vasnev, and W. Wang, "The Forecast Combination Puzzle: A Simple Theoretical Explanation," International Journal of Forecasting, Vol. 32, No. 3, pp. 754-762, 2016.
[33] S. M. Blanc, and T. Setzer, "When to Choose the Simple Average in Forecast Combination," Journal of Business Research, Vol. 69, No. 10, pp. 3951-3962, 2016.
[34] S Ch. G. Gibbs, and A. L. Vasnev, "Conditionally Optimal Weights and Forward-Looking Approaches to Combining Forecasts," UNSW Business School Research Paper, 2017.
[35] J. D. Samuels, and R. M. Sekkel, "Model Confidence Sets and Forecast Combination," International Journal of Forecasting, Vol. 33, No. 1, pp. 48-60, 2017.
[36] F. X. Diebold, and M. Shin, "Machine Learning for Regularized Survey Forecast Combination: Partially-Egalitarian LASSO and Its Derivatives," International Journal of Forecasting, Vol.35, No. 4, pp. 1679-1691, 2019.
[37] D. Shaub, "Fast and Accurate Yearly Time Series Forecasting with Forecast Combinations," International Journal of Forecasting, Vol. 36, No. 1, pp. 116-120, 2020.
[38] Y. Wang, N. Zhang, Y. Tan, T. Hong, D. S. Kirschen, and C. Kang, "Combining Probabilistic Load Forecasts," IEEE Transactions on Smart Grid, Vol. 10, No. 4, pp. 3664-3674, 2018.
[39] A. F. Atiya, "Why Does Forecast Combination Work So Well? ," International Journal of Forecasting, Vol. 36, No. 1, pp. 197-200. 2020.
[40] K. C. Lichtendahl Jr, and R. L. Winkler, "Why Do Some Combinations Perform Better than Others? ," International Journal of Forecasting, Vol. 36, No. 1, pp. 142-149, 2020.
[41] M. P. Clements, and D. I. Harvey, "Combining Probability Forecasts," International Journal of Forecasting, Vol. 27, No. 2, pp. 208-223, 2011.
[42] J. Nowotarski, and R. Weron, "Recent Advances in Electricity Price Forecasting: A Review of Probabilistic Forecasting," Renewable and Sustainable Energy Reviews, Vol. 81, pp. 1548-1568, 2018.
[43] G. Kapetanios, J. Mitchell, S. Price, and N. Fawcett, "Generalised Density Forecast Combinations," Journal of Econometrics, Vol. 188, pp. 150–165, 2015.
[44] J. M. Bates, and C. W. Granger, "The Combination of Forecasts," Journal of the Operational Research Society, Vol. 20, No. 4, pp. 451-468, 1969.
[45] J. H. Stock, M. W. Watson, “A Comparison of Linear and Nonlinear Univariate Models for Forecasting Macroeconomic Time Series,” National Bureau of Economic Research, 1998.
[46] J. H. Stock, M. W. Watson, "Combination Forecasts of Output Growth in a Seven ‐ Country Data Set," Journal of Forecasting, Vol. 23, No. 6, pp. 405-430, 2004.
[47] A. Timmermann, “Forecast combinations,” Handbook of economic forecasting, Vol. 1, pp. 135-196, 2006.
[48] R. T. Clemen, "Combining Forecasts: A Review and Annotated Bibliography," International Journal of Forecasting, Vol. 5, No. 4, pp. 559-583, 1989.
[49] F. X. Diebold, J. A. Lopez, "Forecast Evaluation and Combination," Handbook of Statistics, Vol. 14, pp. 241-268, 1996.
[50] S. M. Blanc, and T. Setzer, "When to Choose the Simple Average in Forecast Combination," Journal of Business Research, Vol. 69, No. 10, pp. 3951-3962, 2016.
[51] A. S. Tay, and K. F. Wallis, "Density Forecasting: A Survey," Journal of forecasting, Vol. 19, No. 4, pp. 235-254, 2000.
[52] K. F. Wallis, "Combining Density and Interval Forecasts: A Modest Proposal," Oxford Bulletin of Economics and Statistics, Vol. 67, pp. 983-994, 2005.
[53] Z. Hua, and B. Zhang, "Improving Density Forecast by Modeling Asymmetric Features: An Application to S&P500 Returns," European Journal of Operational Research, Vol. 185, No. 2, pp. 716-725, 2008.
[54] J. Mitchell, and K. F. Wallis, "Evaluating Density Forecasts: Forecast Combinations, Model Mixtures, Calibration and Sharpness," Journal of Applied Econometrics, Vol. 26, No. 6, pp. 1023-1040, 2011.

S. Raheleh Shahrokhi received the B.Sc. degree in Computer Engineering from Iran University of Science & Technology, Tehran, Iran, in 2009, and the M.Sc. degree in Control Engineering from K. N. Toosi University of Technology, Tehran, Iran, in 2013. Since 2014, she has been working toward Ph.D. degree in Control Engineering at Tarbiat Modares University, Tehran, Iran. Her current research interests are Adaptive Control, Robust Control, Evolutionary Algorithms, System Identification, and Time Series Analysis.

Hamid Khaloozadeh received the B.Sc. degree in control engineering from Sharif University of Technology, Tehran, Iran, in 1990, the M.Sc. degree in control engineering from K. N. Toosi University of Technology, Tehran, Iran, in 1993, and the Ph.D. degree from Tarbiat Modares University, Tehran, Iran, in 1998.

He is currently a Professor with the Department of Systems and Control, Faculty of Electrical Engineering at K. N. Toosi University of Technology. His interest area is Stochastic Estimation and Control, System Identification, Optimal Control, Adaptive Control, and Time Series Analysis.

HamidReza Momeni received his B.Sc., M.Sc., and Ph.D. degrees in Electrical Engineering from Sharif University of Technology, Tehran, Iran, in 1977, University of Wisconsin, Madison, U.S.A, in 1979, and Imperial College, London, England, in 1987, respectively. He is currently a Professor with the Department of Systems and Control, Faculty of Electrical and Computer Engineering at Tarbiat Modares University. His research interests included Adaptive Control, Robust Control, Industrial Control, System Identification, and Time Series Analysis.

IECO

This page intentionally left blank.

International Journal of Industrial Electronics, Control and Optimization © 2021 IECO
Vol. 4, No. 1, pp. 33-45, Jan (2021)

Multi-Objective Optimization and Online Control of Switched Reluctance Generator for Wind Power Application

Hojjat Hajiabadi[1], Mohsen Farshad[2,†], and Mohammad Ali Shamsinejad[3]

[1,2,3] Department of Electrical and Computer Engineering, University of Birjand, Birjand, Iran.

ABSTRACT

Fossil fuel combustion in power plants is the world's most significant threat to people's health and the environment. Recently, wind power, as a clean, sustainable and renewable source of energy, has attracted many researchers. The present paper studies how to maximize the extraction of wind power and the efficiency of a switched reluctance generator (SRG) by firing angles control. The proposed scenario comprises the optimization of turn-on and turn-off angles in the offline mode using a particle swarm optimization algorithm to control the system in the online mode with linear interpolation. The present approach simultaneously investigates the firing angles; also, it has simple structure, low execution time, and efficient convergence rate that are independent of machine characteristics (regardless of high nonlinearity of SRG). Furthermore, copper losses, as well as switching and conduction losses of semiconductors, were considered in simulations to achieve a more realistic outcome. Ultimately, the simulation results of a typical three-phase 6/4 generator using Matlab confirmed the validity of the presented control strategy that can easily find applications in the future.

Article Info

Keywords:
Control of firing angles, Maximum efficiency, Particle swarm optimization, Renewable energy, Sustainable energy, Switched reluctance generator, Wind turbine

Article History:
Received 2019-12-20
Accepted 2020-04-29

I. INTRODUCTION

Depletion of fossil fuels, current fuel economy, and environmental issues have made researchers search for clean sources of energy. Wind power is an important source of renewable energy that is capable of application in various regions, so it has appealed to scientists in recent years. Numerous pieces of wind power generation equipment have been designed and operated worldwide and their different aspects have been investigated so far.

In recent years, switched reluctance generators (SRG) have been introduced as new equipment for wind power generation. Its simple structure, low cost and maintenance, robustness, high efficiency, and wide range of velocity encourage researchers to contribute to SRG development [1]. Interestingly, considering a broad spectrum of SRG performance, it is possible to directly connect wind turbines to generators and eliminate the gearboxes. Simple structure and low cost make SRG not only to be economically feasible but also financially competitive with other machines available in the market. After three decades of progress, it is commercially applied in vacuum cleaners, washing machines [2], water pumps, automatic doors, hybrid electric vehicle [3], [4], automotive application [5], electrified powertrain [6], starter-generator [7], turbocharger application [8], gas turbine [9], textile machines, and many others [10], [11]. Linear switched reluctance motors (SRM) are also employed in the food industry, machine tools, and medical equipment [12]. They can also be utilized in sea wave electricity generation. Moreover, there are some fields, including aerospace or automobile industries, that can exploit the generator operation of linear SRM. Furthermore, as its application in low-speed ranges is currently under investigation, its commercial use in the wind

---

[†] **Corresponding Author**: mfarshad@birjand.ac.ir
Tel: +98-5632202008, Fax: +98-5632202163
Faculty of Electrical and Computer Engineering, University of Birjand, Birjand, Iran

industry seems to be in initial steps [13].

SRG application in wind generation has previously been addressed with the trial and error procedure to find optimum control parameters in most studies. Chang and Liaw [14] introduced a control strategy to fix a desirable DC-link voltage with optimum performance, high efficiency, minimum DC-link voltage ripples, and low acoustic noise. Sozer and Torrey [15] presented an approach for determining firing angles in order to achieve maximum efficiency in the single pulse mode through considering the turn-on and turn-off angles as control parameters. They found that the optimal efficiency and output power could be described as a function of the turn-off and turn-on angle, respectively. Optimization of excitation angles through minimizing root-mean-square (RMS) value of the phase current or through maximizing the average ratio of the output power per input power is focused on in [16]. In order to find the excitation angles based on the desirable DC-link current with a minimum current ripple, an online algorithm is suggested in [17]. The turn-on and conduction angles are determined under various speeds via finite element method in [18]. As the results are sensitive to the variations in system parameters as well as operating conditions, Wang and Chang [19] apply fuzzy control to determine firing angles that can reduce the effect of parameter changes. At higher speeds and single pulse mode, the turn-off angle is optimized using the fitted curve, which is a function of power and speed, followed by the determination of the turn-on angle to adjust the produced power [20].

In [21], controlling the optimal turn-on and turn-off angles for maximum output power is studied and the relation between exciting current and conducting time is investigated. Ziapour et al. [22] described the commutation angles and the output power relevance following with controlling output voltage at high speeds via choosing optimum commutation angles. A 12/8 three-phase switched reluctance generator and a digital controller are established for wind power generation in [23] in which switching signals are generated by a controller based on the rotor position, the phase current, and the DC-link voltage. In [24], optimal firing angles are determined for torque ripple reduction and acoustic noise minimization. In [25], a dsPIC30F microcontroller is utilized to investigate different strategies to control angles positions and current chopping for a three-phase 12/8 switched reluctance generator. The power generation procedure in the generator is studied as well. The performance of a single-phase 12/12 SRG with U-cores is analyzed in [26] by two methods: single pulse control method (SPCM) and SPCM adopting the freewheeling technique. The output power, efficiency, torque ripple, and DC current ripple of SRG are compared in these two control modes. Ivanov and Kalanchin [27] study the maximum power point tracking (MPPT) through the hill climb search (HCS) method by controlling the turn-on and turn-off angles of SRG while the rotational speed of the rotor and the current value is used as the controller inputs. In [28], the output performance of a generator is evaluated by dynamic simulation where finite-element is used to analyze the magnetic field. A 1.5 kW three-phase 12/8 SRG is then designed for low speed micro-wind turbine optimally. SRG voltage control and voltage stabilization methods are discussed and compared in [29]. Considering core saturation, magnetic and windings losses, the mathematical model is improved and the adequacy of the model is established.

A passivity-based control of SRG for small-size wind energy systems is proposed in [30]. The main goals are maximum power point tracking and controlling the output voltage. An adaption scheme is included in the proposed adaptive controller to deal with the back-emf of SRG and time-varying inductance. The closed-loop stability is guaranteed by Lyapunov theorem. In [31], the DC voltage control of a stand-alone SRG is addressed using a robust controller based on discrete-time sliding mode control. A disturbance estimator is used to achieve robustness. The proposed controller is compared to a PI controller. The control of SRG based on firing angles and reference current is investigated by Sh. Jagwani et al. [32]. A single-phase grid-interactive inverter is utilized operating in both current control and voltage control modes. Robust power flow control for various case studies is also presented. In [33], a hierarchical Markov model is presented to evaluate the reliability of a double-sided linear switched reluctance generator. The equilibrium point of reliability evaluation accuracy and model complexity can be found using this model. Zhang et al. [34] report the design and optimization of an SR machine in terms of mathematical modeling of electromagnetic and thermal fields, efficiency, torque ripple, acoustic noise, and the application of SRM in wind generators. In [35], a direct instantaneous torque controller is utilized for SRG at low speeds in which the turn-on and turn-off angles are fixed in the negative slope of the inductance profile. A Cuk converter is applied to control the generated voltage. In [36], a fly-wheeling pulse train (FW-PT) control approach is suggested to decreasing voltage ripple besides achieving faster response as well as better dynamic behavior. Further techniques are also compared to the FW-PT approach. In order to reduce steady-state error and increase the generated power of asymmetric bilateral linear SRG, a dual-loop compensation voltage control scenario is proposed in [37].

Chen et al. [38] present a set of control strategies for small-scale wind power SRG connected to energy storage system in an off-grid mode. A step control scheme, merging MPPT with power balance control, is suggested to improve the SRG efficiency. In order to generate AC output, a two-stage inverter is established using a boost circuit in the front stage following with a PI controller in the second stage. A simple current-rise model is proposed to guesstimate the steady state peak-current in an SRG for the diversity of conditions. The turn-off current level and turn-off position are used to estimate the current rise in a given generation interval. For better accuracy, the interval is subdivided into multiple sections to a certain extent. As the number of sections is increased, the accuracy of the proposed model is improved except near to unaligned position [39]. In order to control the SRG power, a proportional plus resonant (P+RES) controller is presented [40]. The proposed scheme consents to control the power delivered to DC link using turn-off angle. Additionally, the controller provides power ripple reduction in comparison with the PI controller. Moreover, the proposed control methodology is implemented on a digital signal processor (TMS320F2835).

Direct search algorithms have been vastly used in scientific and industrial optimizations that can be simply coded [41]. Such methods like downhill simplex [42] or Hooke and Jeeves approach [43] appear to be suitable when the cost function is nonlinear, non-differentiable, and non-smooth. Population-based methods including the controlled random search algorithm [44], the genetic algorithm (GA) [45], and also the evolutionary algorithms [46], [47] are some other methodologies to tackle multimodal problems. These techniques outperform the gradient-based algorithms due to their capability in searching for an optimum point of multimodal functions as well as efficient performance in non-continuous feasible regions. In an attempt to attain an optimum firing angles range to control the maximum torque in various circumstances through GA, Fisch et al. [48] select the turn-on angles according to the optimization of generator efficiency. Moreover, in [49] the fuzzy logic is applied to control the DC-link voltage. The conduction angle is calculated based on the error signal of the output voltage via a fuzzy controller, and the turn-off angle is then computed from the linear relationship of velocity. The optimum design of a 1 kW SRG is addressed for wind applications using GA [50]. This optimization approach uses the design variables based on the main model and exploits LHS[1] for variable sampling. In [51], the optimization of a linear switched reluctance generator is explored based on energy efficiency. A genetic algorithm is used as the optimization method while the generator's magnetic field proceeded by the finite element method. In [52], two of the most important problems in wind conversion systems are addressed. A new MPPT scheme to improve the HCS technique as well as the modified torque ripple minimization method for a four-phase 8/6 SRG based on the artificial neural network is proposed. An experimental methodology is presented to control the SRG voltage using a fuzzy logic system [53]. The turn-on angle is fixed while the turn-off angle is varied. The suggested method is executed using a high processing capacity DSP/FPGA.

To avoid complex analytical calculations of cost functions, numerical optimizations provide an efficient route to find optimum local points. Accordingly, in the present work, a particle swarm optimization (PSO) algorithm is employed due to the extreme nonlinearity of the generator, the prevention of the nonlinear analytical equations, simplicity, and the lower execution time of the simulation. The main advantages of this technique include well-organized memory usage, cooperation and information sharing between particles, high conversion speed, and simple establishment and execution. In contrast to the aforementioned works, simultaneous investigations of firing angles are presented in this paper. It should be noted that some of the similar works have investigated the effect of both firing angles separately. For instance, the first objective function is optimized using one firing angle, and the other objective function is then optimized using another one. However, each angle affects both objective functions. Therefore, it is more efficient to investigate them simultaneously. In this regard, a 60 kW three-phase 6/4 SRG was considered that supplied local load by an inverter in an off-grid mode, which was poorly addressed. Moreover, the excess generated power was stored in a battery bank. In order to eliminate the harmonics, the inverter was equipped with an LC filter. Contrary to the related works, where a linear model of SRG is used, this paper applies an actual nonlinear model of real SRG considering the effect of losses in simulations to approach reality. This model is based on the magnetization curves of an actual SRG where the saturation effect is included. On the other hand, an online control scheme is finally presented in this study whereas all the similar works have proposed offline methods. In this approach, the best offline obtained control variables are collected in a lookup table. Then, using this table, the online controller employs linear interpolation to achieve the maximum power generation. All parts of the system and their relations are presented in detail in Fig. 1.

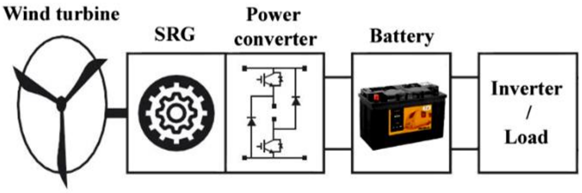

Fig. 1. The relationship between different parts of the system.

Section II focuses on a wind turbine, mathematical relations, and control strategies. The remaining of the paper is organized as follows. Section III describes the SRG structure, principles of its performance, nonlinear model, and power losses in this machine. Section IV explains the proposed methodology. Simulation results are shown in Section V. Finally, Section VI concludes the paper.

---

[1] Latin hypercube sampling (LHS)

II. WIND TURBINE

Wind turbines convert the kinetic energy of wind to electrical power. The maximum power generation depends on not only mechanical constrains but also wind speed [54]. The capacity of a turbine for power generation is often presented by companies as a curve in which power is plotted versus wind speed, called an ideal power curve [1]. An example of such curves is shown in Fig. 2.

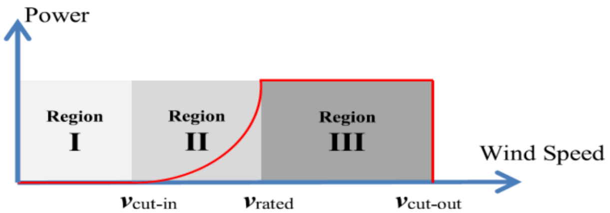

Fig. 2. The power curve of a variable-speed wind turbine [55].

Mechanical power generation (P_{areo}) follows a nonlinear relationship with air density, wind speed, and power coefficient (C_p) as:

$$P_{aero}=\frac{1}{2}.\rho.\pi.R^2.v^3.C_p \qquad (1)$$

where R is the radius of the area covered by the blades, v is the wind speed and ρ is the air density. The power coefficient obeys a non-linear function of the blade pitch angle (β) and the tip speed ratio (λ), which is the ratio between the tip speed of the blades and the wind speed [56]. It can be formulated as:

$$C_p \propto (\lambda,\beta) \quad , \quad \lambda=\frac{\omega_t R}{v} \qquad (2)$$

where ω_t is the rotational speed of the turbine axis. This coefficient is an especial factor for each turbine and plays an important role in control purposes. It also gives information upon the aerodynamic efficiency of the turbine [57].

$$C_p(\lambda,\beta)=c_1.(\frac{c_2}{\lambda_i}-c_3.\beta-c_4).e^{\frac{-c_5}{\lambda_i}}+c_6.\lambda \qquad (3)$$

The coefficients c_1 to c_6 are: $c_1 = 0.5176$, $c_2 = 116$, $c_3 = 0.4$, $c_4 = 5$, $c_5= 21$, $c_6 = 0.0068$, and:

$$\frac{1}{\lambda_i}=\frac{1}{\lambda+0.08\cdot\beta}-\frac{0.035}{\beta^3+1} \qquad (4)$$

The variation of C_p with β and λ is illustrated in Fig. 3.

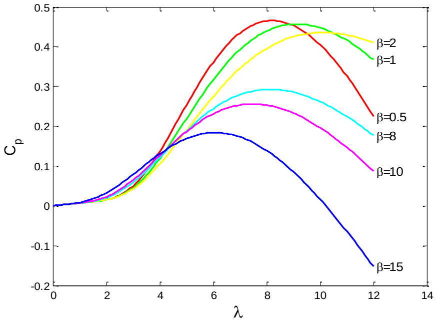

Fig. 3. Power coefficient of a variable speed wind turbine.

As can be seen in Fig. 2, the wind turbine power curve is divided into three regions. The first one is associated with the time when wind speed is less than a cut-in speed and the turbine is in standby mode. The generated power of the turbine in this region can often be ignored in comparison with its dissipations. Hence, there is not any power exchange and the turbine fails to operate. In the second region, wind speed falls between cut-in and rated speed and the main goal is to obtain the highest power via an MPPT algorithm. According to Equ. (1), C_p needs to be maximized to attain MPPT in various wind speeds which is possible if β is set to be minimized, as evident in Fig. 3. Therefore, $\beta=0$, and C_p shrinks to a function of λ, which is a function of the rotor speed. The received wind power would then be regulated by varying the rotor speed. Fig. 4 shows the turbine power versus the rotation speed of its axis in a range of wind speed. The maximum power can be obtained by the turbine speed of 1 pu and the wind speed of 14 m/s [13], [58]. At other wind speeds, the optimum rotation speed of the turbine axis that can be attained from the turbine power curve must be less than the nominal speed to generate the maximum wind power.

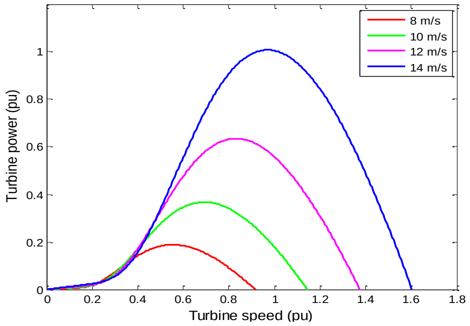

Fig. 4. Power curve of a variable-speed wind turbine.

The third region covers wind speeds of higher than the rated speed. Due to electrical constraints, to diminish mechanical stresses and also to avoid turbine damages in this region, the output power ought to be constant in the rated value. Accordingly, one can keep the power constant at the rated value by increasing the blade pitch angle that decreases the power coefficient. Actually, the turbine must be tuned to lose some of the wind energy. Hence, the control objective involves adjusting the rotor speed in nominal value and fixing the power in nominal value by controlling the blade pitch angle [55], [59]. This paper investigates the SRG performance in the second region.

III. SWITCHED RELUCTANCE GENERATOR

Switched reluctance generators (SRG), which have attracted the interests of researchers in recent years, are synchronous generators with a salient pole in rotor and stator and can be excited by stator like an induced machine. SRG benefits from its solid structure, simple performance, low cost, high assurance capability, and wide speed range (which is capable of eliminating the gearbox at low speed). Showing efficient performance in a broad spectrum of speed, SRG seems to be competitive with an induced machine regarding the required investment. Moreover, its converter is less expensive and enjoys more reliability and efficiency in terms of torque response, torque per unit volume, and torque per unit weight [10].

A. Switched Reluctance Generator Structure

Rotor and stator pole of SRG are made of solid steel plates. The machine coils wound around the stator poles and there is no magnetic material embedded in the machine structure. The rotor also lacks any magnetic material, coil, and brush and consequently it is called a cold rotor [60].

Considering the number of poles in rotor and stator, different machine arrangements emerge such as three-phase 6/4 or 12/8 and four-phase 8/6 or 16/12 in which the right and left numbers show the rotor poles and the stator poles, respectively. Examples of four-phase 8/6 and three-phase 12/8 are represented in Fig. 5 [61].

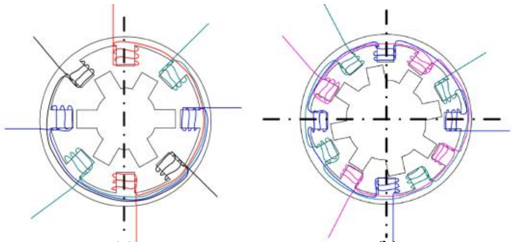

(a) (b)

Fig. 5. Switched reluctance generator structure (a) four-phase 8/6, (b) three-phase 12/8 [61].

B. Principles of SRG Performance

In order to explain the SRG performance, it is vital to elucidate how a phase inductance changes. In a situation where the stator pole and the rotor pole are aligned, the air gap turns out to be minimum and the magnetic reluctance will then be minimum, resulting in the maximum inductance. Conversely, when the poles are non-aligned, the air gap and the magnetic reluctance will be maximum while the inductance drops to its minimum level. Clearly, the more the rotor pole approaches the stator pole, the more the inductance will be and vice versa. The inductance profile variations versus rotor position for one phase are illustrated in Fig. 6.

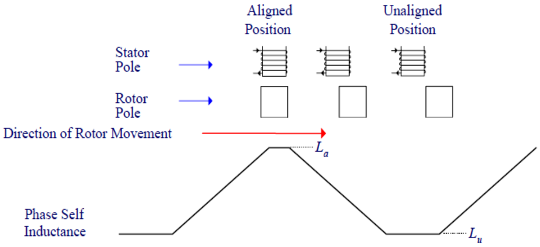

Fig. 6. Inductance variations versus rotor position [62].

The SR motor performance matches its generator performance in some aspects; however, they vary in some other aspects. As shown in Fig. 7, in the motor performance, phase excitation occurs in the positive slope of the inductance profile whereas in the generator mode, it takes place in the negative slope of the inductance profile. In an SR motor, with phase excitation, the rotor tends to position in a way that minimum magnetic resistance happens [62], [63].

In the generator operation mode, the rotor is rotated by a prime mover and the phase excites in the negative slope of the inductance profile. At this stage, the energy is supplied to the phase winding by a converter from a DC source, and the current of this winding gradually starts to increase (due to high inductance) and the energy is saved in the magnetic field. The opposing torque in the prime mover increases the saved energy.

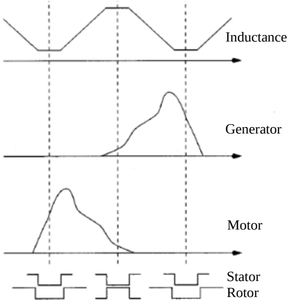

Fig. 7. Phase excitation period in motor and generator operation modes [64].

After reaching the turn-off angle in the negative slope of the inductance profile, the electromotive force (EMF) reverses and the phase current increases with a decrease in the inductance. At the end of the production period (reaching the minimum inductance), the saved energy in the field is transferred to the DC source or the load through a converter [65]. The phase excitation procedure of the generator is depicted in Fig. 8. At high speeds, due to shortness of the rotor position period (sum of excitation and production cycle when the rotor pole is moving away from the stator pole), the flux and current may fail to sufficiently grow. After terminating the excitation period, not only is there no production, but the received energy from the machine is also less than the delivered energy due to dissipation as shown in Fig. 8(b). In order to avoid such situations at high speeds, the phase is often excited sooner (in the positive inductance profile) to ensure sufficient current generation in the short period of the rotor position, considering the time constant of the system, as shown in Fig. 8(a) [64], [65].

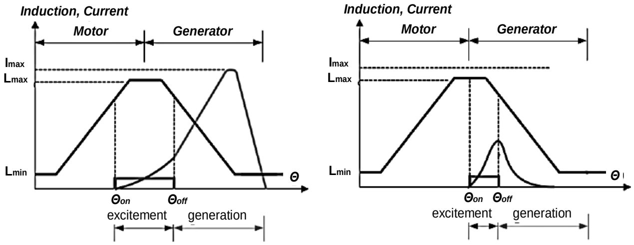

(a) (b)

Fig. 8. The phase excitation procedure of the generator with (a) production (b) no production [65].

The SRG generated power is of DC type and an inverter is needed for AC load. Schematic of the asymmetric half bridge converter (AHBC) circuit and excitation/production mode are represented in Figs. 9 and 10, respectively. The AHBC appears to be of the most commonly used converter applied to operate SRG. As shown in Fig. 10, each phase of the converter consists of two IGBTs and two diodes. As the DC-link voltage has to be remained constant with low ripple, the filter capacitor must be large enough.

The phase inductance in an SRG is shown with L_a, L_b, L_c and the coil resistance for each phase is represented with r. As observed in Fig. 9, two transistors in each phase turn on and off simultaneously. Moreover, in each moment only one phase is on and according to Fig. 10(a) only one phase is connected to the DC source and the coil of that special phase is excited.

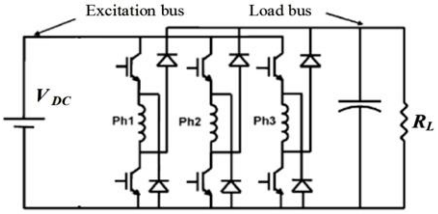

Fig. 9. The schematic of an asymmetric half bridge converter circuit [22].

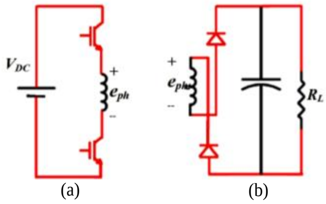

Fig. 10. The converter circuit in (a) excitation mode and (b) generation mode [22].

Equs. (5)-(8) show the relationship of the corresponding phase dynamics.

$$V_{DC} = e_{ph} + r \cdot i_{ph} \tag{5}$$

where e_{ph} and i_{ph} are the voltage and current of the corresponding phase, respectively.

$$e_{ph} = -N_{ph} \frac{d\varphi_{ph}}{dt} \tag{6}$$

where φ_{ph} is the phase flux and N_{ph} is the number of phase windings. Since $\varphi_{ph} = L_{ph} \, . \, i_{ph}$ then:

$$e_{ph} = -N_{ph} \frac{d\left(L_{ph} \cdot i_{ph}\right)}{dt} = -N_{ph} \cdot \left(L_{ph} \frac{di_{ph}}{dt} + i_{ph} \frac{dL_{ph}}{d\theta} \cdot \omega \right) \tag{7}$$

Substituting (7) in (5), we have:

$$V_{DC} = -N_{ph} \cdot i_{ph} \frac{dL_{ph}}{d\theta} \cdot \omega \; - N_{ph} \cdot L_{ph} \frac{di_{ph}}{dt} + r \cdot i_{ph} \tag{8}$$

where $d\theta/dt=\omega$ is the angular velocity of the rotor. Equ. (5) explains the main relationship for the voltage of an excited generator phase and the first term from the right-hand side of Equ. (8) is called the back EMF which is proportional to the generated electrical power. The equivalent circuit of a generator phase is depicted in Fig. 10(b) while its switches are off. In this situation, the phase inductance current gradually reaches zero and the load resistance is provided via diodes. Equs. (9)-(11) show the relationship of the SRG phase dynamics concerning Fig. 10(b) [66].

$$e_{ph} = r \cdot i_{ph} + R_L \cdot i_{ph} \tag{9}$$

Substituting e_{ph} from Equ. (6), it can be rewritten as:

$$N_{ph} \frac{d\varphi_{ph}}{dt} = r \cdot i_{ph} + R_L \cdot i_{ph} \tag{10}$$

and substituting φ_{ph} from Equ. (7) in Equ. (10):

$$N_{ph} \cdot i_{ph} \frac{dL_{ph}}{d\theta} \cdot \omega + N_{ph} \cdot L_{ph} \frac{di_{ph}}{dt} = r \cdot i_{ph} + R_L \cdot i_{ph} \tag{11}$$

C. Nonlinear Model of Torque and Flux Production

Unsaturated (linear) switched reluctance machines suffer from an insufficient energy conversion ratio and their drive characteristics are not fully exploited. But, real switched reluctance machines are nonlinear with satisfactory efficiency. Understanding electromagnetic energy conversion needs a nonlinear analysis in which the saturation effect is included. One of those analyses is based on magnetization curves in which induced flux is considered proportional to the current in specific rotor positions. The magnetization curves of a 6/4 SR machine are shown in Fig. 11. The relationship of flux, inductance, and current can be expressed via Equ. (12) where λ, L, i, and θ denote linkage flux, phase inductance, phase current, and rotor position, respectively. Therefore, machine behavior can be expressed using linkage flux [67].

$$\lambda(i,\theta) = L(i,\theta) \cdot i \tag{12}$$

The torque characteristic curves of a 6/4 SR machine calculated from the magnetization curves are also depicted in Fig. 12.

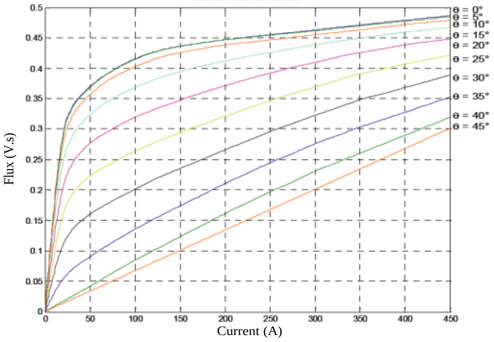

Fig. 11. The 6/4 SRG magnetization curves [68].

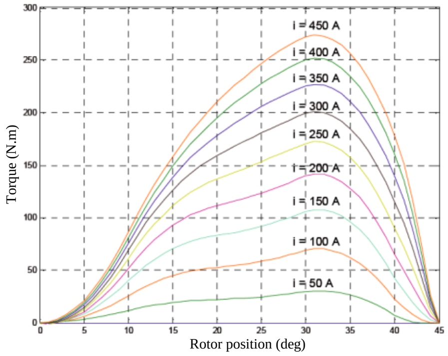

Fig. 12. The 6/4 SRG torque characteristic curves [68].

The SRG generated power is hardly introduced by an analytical relation due to its switching and nonlinear behavior of produced current [69]. Regardless of losses, the average output power of an SRG can be represented as follows, using some simplifications [62]:

$$P_{out}=\frac{N_s N_r V_{DC}^2}{\omega}\left(\int_{\theta_{on}}^{\theta_{off}}\frac{(\theta-\theta_{on})d\theta}{L(\theta)}-\int_{\theta_{off}}^{\theta_e}\frac{(\theta_{off}-\theta_{on}-\theta)d\theta}{L(\theta)}\right) \tag{13}$$

where N_r and N_s are the number of rotor and stator poles, respectively, and θ_e stands for the extinction angle that represents the position where the current falls to zero after θ_{off} and it equals to:

$$\theta_e = 2\theta_{off} - \theta_{on} \tag{14}$$

Ignoring the saturation of SRG, the instantaneous electromagnetic torque per phase is defined as:

$$T(i,\theta)=\frac{1}{2}i^2\frac{dL}{d\theta} \tag{15}$$

Torque ripple damages the generator and shortens its life. It can be expressed as:

$$T_{ripple}=\frac{T_{\max}-T_{\min}}{T_{ave}} \tag{16}$$

where T_{max} and T_{min} are the instantaneous maximum and minimum value of torque, respectively, and T_{ave} is the average torque. The level of torque ripple suppression can be achieved via torque smoothness factor defined as:

$$T_{SF}=\frac{1}{T_{ripple}} \tag{17}$$

The battery is charged via SRG DC link current. Since excessive current ripple decreases the battery life, it necessarily must be reduced. Accordingly, the current smoothness factor is defined as:

$$I_{SF}=\frac{I_{ave}}{I_{\max}-I_{\min}} \tag{18}$$

where I_{max}, I_{min} and I_{ave} are the maximum instantaneous DC link current, the minimum instantaneous DC link current, and the average DC link current, respectively. The efficiency of SRG is given by:

$$\eta=\frac{P_{out}}{P_{in}}\times 100 \tag{19}$$

where P_{out} is the generated electrical power and P_{in} is the mechanical input power provided by the wind turbine [62], [69].

D. Power Losses in SRG

The SRG efficiency is diminished because of losses, which are categorized into machine and power converter losses. Machine losses are divided into copper and iron losses, depending on the RMS stator current and the peak of the magnetic flux, respectively. Given the fact that all phases carry identical current, the average copper losses can be easily expressed as:

$$P_{Cu}=nrI_{rms}^2 \tag{20}$$

where n and I_{rms} are the number of phases and RMS value of phase current, respectively. The iron loss is approximately formulated based on Steinmetz equation as follows:

$$P_{Fe}=c_h f B^{a+bB}+c_e\left(\frac{dB}{dt}\right)^2 \tag{21}$$

where f is the stroke frequency, c_h and c_e are the hysteresis and eddy-current loss coefficients, respectively, a and b are the coefficients that could be extracted from the loss curves, and B is the flux density.

Power converter losses are mostly composed of switching loss and conduction loss. The switching loss, which is affected by switching frequency, is usually higher than the conduction loss. The control strategy and the number of machine phases play an important role in determining switching frequency [2]. Modeling of switching loss based on the lookup table is of the most efficient routes describing the turn-on and turn-off energy losses as a function of device parameters such as voltage and current among others. The power of switching loss can consequently be estimated via multiplying the energy loss by the switching frequency [70]. The conduction losses of a power converter are calculated as follows:

$$P_{con}=\frac{2}{T}\left[\int_0^T v_{ce}\,i_c\,dt+\int_0^T v_D\,i_D\,dt\right] \tag{22}$$

where v_{ce} shows the collector-emitter voltage of the transistors, v_d represents the forward voltage of the diodes, i_c and i_D are the transistor and diode currents respectively [71].

IV. METHODOLOGY

The present paper introduces a robust strategy in which the firing angles of a SRG are controlled to maximize the efficiency as well as the wind power generation. In this approach, the controller of the converter circuit is initially trained via the particle swarm optimization algorithm in the offline mode and it is then applied for maximum power generation in the online mode using the obtained results and linear interpolation. The first step includes the PSO algorithm with accelerated coefficient to search the optimum control variable (firing angles). Unlike most previous studies in which the effect of only one of those angles has been considered, the simultaneous exploration for optimum firing angles is represented. Moreover, the turn-on and turn-off angles are examined simultaneously and the SRG performance is assessed based on the evaluation parameters. The flowchart of the PSO algorithm and the block diagram of the SRG control are shown in Figs. 13 and 14, respectively.

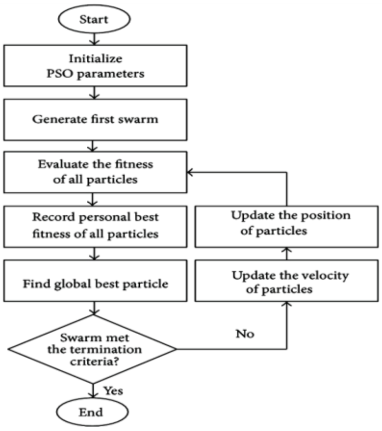

Fig. 13. The particle swarm optimization algorithm [72].

As shown in Fig. 14, to reach a desirable current level, the current error signal is passed through a hysteresis regulator located in the controller.

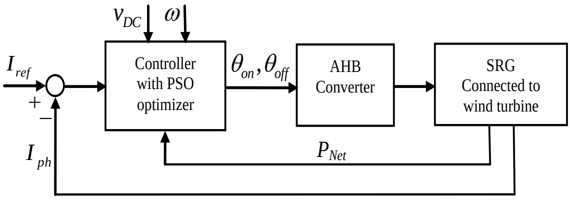

Fig. 14. The block diagram of an SRG control.

The presented strategy mainly aims to maximize power generation from wind, maximize generator efficiency, and minimize current ripple and torque ripple. Simultaneous speed and voltage feedbacks are used to generate maximum power. Accordingly, the generator is posed to a special voltage source and constant speed –via a wind turbine with extremely high inertia– and the firing angles (or the particles) that are generated accidentally under special constraints are transferred to the simulation part. For each couple of the turn-on and turn-off angles, the evaluation parameters including net output power (the difference between the power of load and the excitation power), the RMS current of each phase, torque ripple, and DC link current ripple are measured, and the best control variables (particles) of each group and the best general control variables (best particle) of the whole complex are selected. Having estimated the new variables (new position of the particles), the PSO algorithm transfers them to the simulation section and this procedure continues until the algorithm terminates. The objective function (*F*) for the optimization problem is considered:

$$\begin{aligned} &Max.\ F(\theta_{on},\theta_{off}) = \omega_1 \frac{P_{Net}}{P_{\max}} + \omega_2 \frac{I_{rms\ \min}}{I_{rms}} + \omega_3 \frac{T_{SF}}{T_{SF\max}} + \omega_4 \frac{I_{SF}}{I_{SF\max}} \\ &subject\ to: \quad \theta_{on} \in [75,110] \\ &\qquad\qquad\qquad \theta_{off} \in [95,135] \\ &\qquad\qquad\qquad \theta_{on} < \theta_{off} \end{aligned} \tag{23}$$

where P_{net}=P_{load}-$P_{excitation}$, P_{load} is the power of load, $P_{excitation}$ is the power of excitation source, and ω_1, ω_2, ω_3, and ω_4 are weight coefficients considered to efficiently raise the importance of each term, which are selected as to be 0.5, 0.3, 0.1, and 0.1, respectively. The parameters of the PSO algorithm are the number of particles, the maximum number of iterations, and the inertia that are set to 20, 20 and 0.6, respectively. The best control variables obtained at the end of the first step are collected in a lookup table for each speed and nominal voltage. Then, using this table, the online controller employs linear interpolation to generate maximum power and efficiency for the variable-speed wind turbine.

V. SIMULATION RESULTS AND DISCUSSION

This paper proposes an efficient approach to generating maximum wind power as well as the maximum efficiency of SRG. Simulation in MATLAB is presented in this section to assess the validity of the present methodology. The simulation has performed on a three-phase 6/4 generator with realistic conditions based on the information given in Table I.

TABLE I
THREE-PHASE 6/4 SR GENERATOR PARAMETERS [67]

Parameter	Value
Nominal power	60 kW
Nominal speed	5500 rpm
Max. coil current	450 A
Reference current	200 A
Stator coil resistance	0.05 Ω
Coefficient of inertia	0.05 kg.m^2
Coefficient of friction	0.02 N.m.s

The simulation and optimization procedure for the SRG control system is schematically illustrated in Fig. 15. It is composed of two parts: a Stateflow control chart and an SRG simulator.

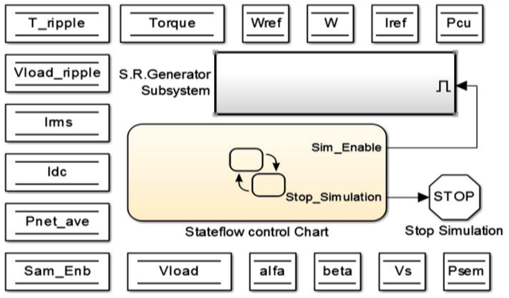

Fig. 15. The simulation of the system in MATLAB.

In the SRG simulator subsystem, the generator model is simulated according to the fundamental mathematical relations of an actual generator and also magnetic flux curves and torque. According to Fig. 16, the output of the generator is connected to a battery and a local load through a D/A inverter and a filter.

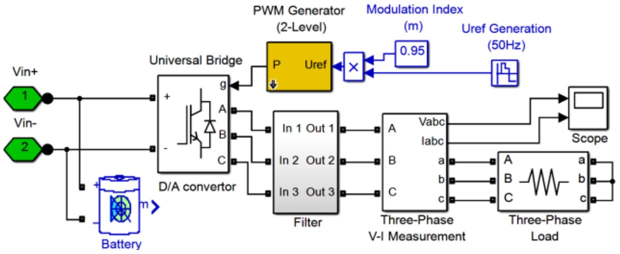

Fig. 16. The simulation of a battery and the load connected to the generator output in MATLAB.

Before controlling the generator, the effect of firing angles, as factors underpinning the output power, was investigated. Therefore, the generator model was executed for all of the possible arrangements of firing angles when the speed was 5000 rpm, the excitation voltage was 240 V, and the current was 200 A. The results are depicted in Fig. 17. As is evident, there is a pair of firing angles at which the corresponding generator power maximizes.

Prior to executing the SRG subsystem, the firing angles were randomly generated in Stateflow subject to system constraints, in the control chart subsystem. Meanwhile, the evaluation parameters were fed back to the Stateflow. The optimum particle was then selected based on the objective function defined in Equ. (23). After assessing the results, considering the parameters (particles) and also the coefficient of inertia, new firing angles (new position of particles) were selected and transferred to the SRG subsystem again for evaluation. This procedure continued until the end of the PSO algorithm and the methodology was extended such that the run time decreased in accordance with the rotor speed increase.

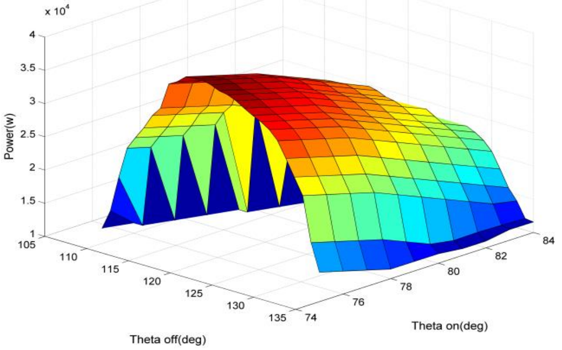

Fig. 17. The generator power versus the firing angles.

Consequently, the firing angles controller was initially learned in the offline mode. The optimum control variables for each speed and nominal voltage were then stored in a lookup table located in the controller part of the converter to be used to obtain the maximum power in the online mode. The offline calculation results of the proposed methodology for a voltage of 240 V and various speeds are summarized in Table II.

TABLE II

THE OFFLINE CALCULATION RESULTS OF THE METHODOLOGY

ω (rpm)	θ_{on} (deg)	θ_{off} (deg)
1000	87.4	107.2
2000	85.8	115.4
3000	83.2	125.8
4000	80.2	126.9
5000	77.9	122.5
5500	74.98	115

The convergence curves of the optimum firing angles, as well as the generator net power for several executions of the PSO algorithm in the offline mode, are illustrated in Figs. 18 and 19 where voltage and speed were 240 V and 5500 rpm, respectively. As can be seen, the minimum and maximum growth rates of the algorithm are 5 and 28 percent, respectively.

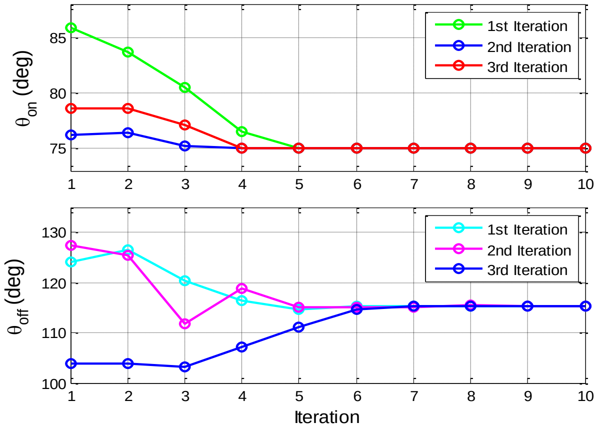

Fig. 18. The convergence curve of the proposed method for the SRG firing angles in the offline mode.

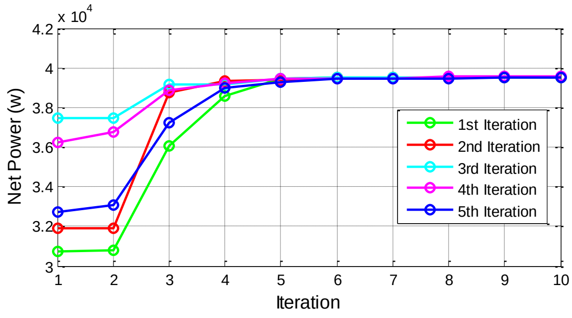

Fig. 19. The convergence curve of the proposed method for the generator net power.

The net power of the generator, as well as the efficiency for an exciting voltage of 240 V and various speeds, are obtained and presented in Table III.

TABLE III

THE GENERATOR NET POWER AND EFFICIENCY

ω (rpm)	Net power (kW)	Efficiency (%)
1000	1.5	21.5
2000	14.9	50.6
3000	21	68
4000	29.8	73.5
5000	32.9	82.4
5500	39.75	84.2

The average copper losses and power converter losses are calculated according to Table IV.

TABLE IV

THE AVERAGE COPPER LOSSES AND POWER CONVERTER LOSSES OF THE GENERATOR

ω (rpm)	P_{cu} (kW)	$P_{converter}$ (kW)
1000	0.54	0.16
2000	1.12	0.26
3000	2.05	0.47
4000	2.78	0.52
5000	3.23	0.69
5500	3.93	0.72

To reveal the productivity of the proposed methodology, the generator efficiency results of the PSO technique are compared to GA, as shown in Fig. 20. The initial population is set to be the same for both methods, and the results are plotted for 100 iterations. Consequently, the PSO enjoys a better convergence rate and better outcomes than the GA.

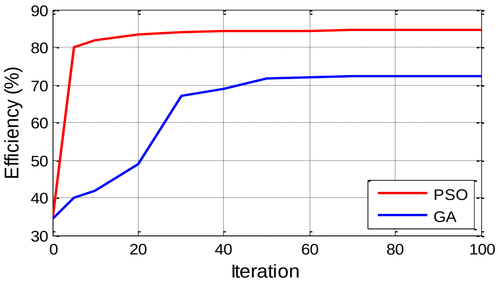

Fig. 20. The convergence curves of the proposed method vs the GA for the SRG efficiency.

In order to assess the proposed methodology, a hypothetical worst case of wind profile like Fig. 21 with a variable speed was applied to a turbine while the performance of the system was investigated in a rough situation. It is obvious that if the controller overcomes these instant changes, it will definitely show a good response to actual wind profiles.

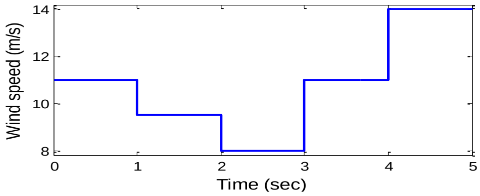

Fig. 21. A hypothetical variable-speed wind profile.

Since the nominal wind speed is 14 m/s, the turbine performance falls in the second region. Therefore, the maximum turbine power occurs in the nominal wind speed and the pitch angle of zero.

To achieve MPPT, the reference value of the rotor speed is selected equivalent to its optimum value based on the turbine power curve (Fig. 4) and instantaneous wind speed. Fig. 22 shows the optimum rotor speed (reference value) and also its actual speed after applying the methodology.

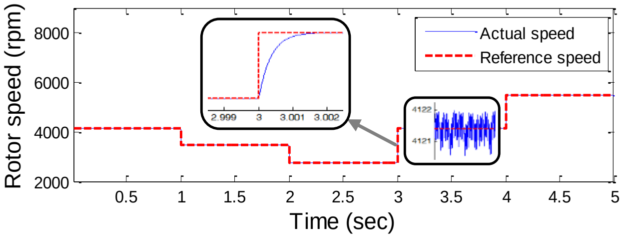

Fig. 22. The rotor speed corresponding to the wind profile.

Obviously, the presented approach efficiently pursues the optimum speed and the actual speed approximates to its reference value. Variations in the firing angles leading to the maximum power and the generator efficiency are illustrated in Figs. 23 and 24, corresponding to the wind profile and the rotor speed.

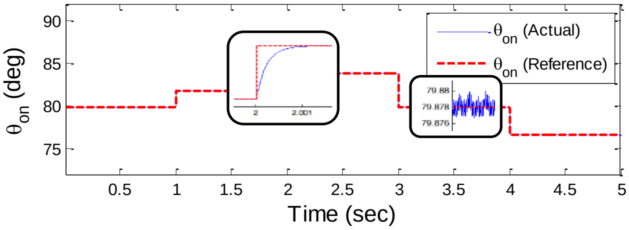

Fig. 23. The turn-on angle control corresponding to the rotor speed.

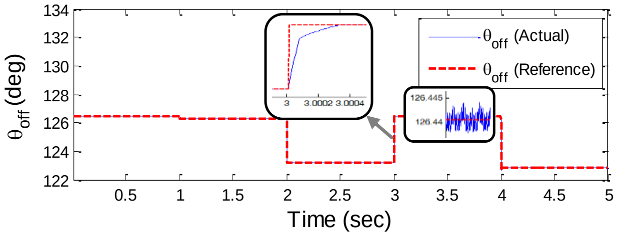

Fig. 24. The turn-off angle control corresponding to the rotor speed.

As observed, both firing angles were simultaneously varying with the changes in wind speed that accurately follow the reference firing angles in the offline mode (Table II). Since the first column of Table II fails to cover the entire range of generator axis speeds, linear interpolation is used if necessary. As evident in Fig. 22, for a rotor speed of 4121.5 rpm, the turn-on and turn-off angles were interpolated as 79.878 and 126.44, respectively, which are consistent with the simulation results in Figs. 23 and 24.

Fig. 25 shows inductance, phase current, linkage flux, and generator torque in optimum firing angles. The voltage and current of the three-phase load are also depicted in Fig. 26.

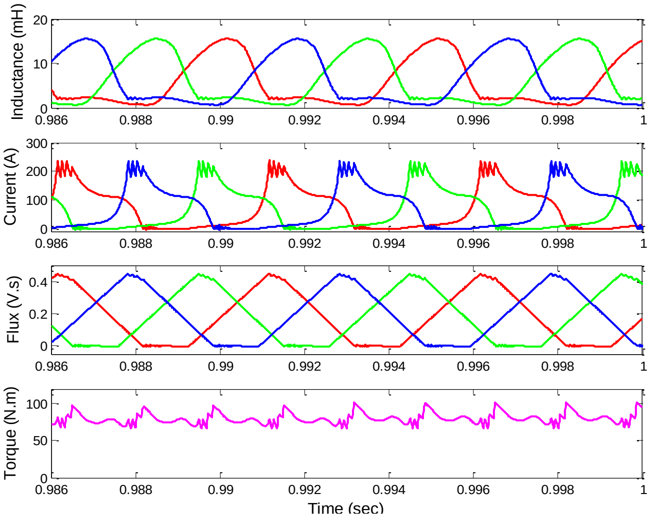

Fig. 25. The inductances, phases currents, linkage fluxes, and generator torque in optimum firing angles.

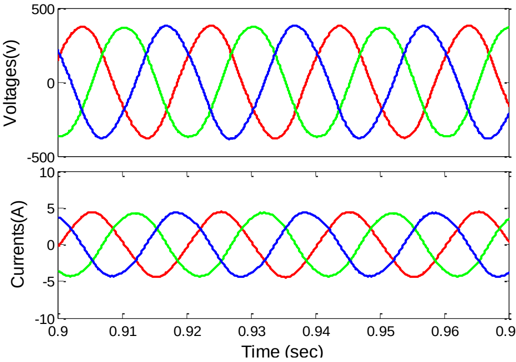

Fig. 26. The voltage and current of 3-phase local load.

VI. CONCLUSION

The present paper used a switched reluctance generator to generate maximum electrical power from wind to supply the local load demand, followed by a battery bank to store the excess generated power. As the firing angles appeared to be of importance in generator control, they were firstly optimized via a PSO algorithm in the offline mode according to the maximum wind power generation, maximum generator efficiency, and minimum ripple of torque and current. The optimum firing angles were stored in a lookup table for some speeds and nominal voltage to be employed for various speeds and voltages in the online mode. The PSO algorithm was launched in the Stateflow toolbox. Accordingly, the methodology was developed such that the execution time decreased as the rotor speed increased. Consequently, the execution time was different for various speeds. Moreover, the required signals were sampled precisely. In contrast to the previous works in which the effect of each firing angle was studied separately, our contribution scrutinizes the simultaneous optimization of both firing angles resulting in a substantial reduction in computation and simulation time as well. Consequently, the algorithm provided a precise outcome. Some other major features of the present work include simple structure, reasonable convergence rate that is independent of machine characteristics, and utilizable methodology for any other SRG machine. Additionally, an actual nonlinear model of SRG considering copper losses, switching and conduction losses of semiconductors were included in the simulations to approach real conditions, which has poorly been addressed before. Ultimately, unlike similar works that have considered the offline mode, this study presented an online control scheme. Matlab was used to apply the proposed method to a typical 60 kW three-phase 6/4 generator and the results confirmed the validation of the proposed method.

REFERENCES

[1] P. Carlin, A. Laxson, and E. Muljadi, “The History and State of the Art of Variable-Speed Wind Turbine Technology,” *Wind Energy*, vol. 6, pp. 129–159, Apr. 2003.

[2] M. Farshad, “Modeling and Intelligent Control of Switched Reluctance Motor in Washing Machine,” Ph.D. Dissertation, University of Tehran, Iran, 2006.

[3] M. Takeno, A. Chiba, N. Hoshi, S. Ogasawara, M. Takemoto, and M. A. Rahman, “Test Results and Torque Improvement of the 50-kW Switched Reluctance Motor Designed for Hybrid Electric Vehicles,” *IEEE Trans. Ind. Appl.*, vol. 48, no. 4, pp. 1327–1334, 2012.

[4] F. L. M. dos Santos, J. Anthonis, F. Naclerio, J. J. C. Gyselinck, H. Van der Auweraer, and L. C. S. Góes, “Multiphysics NVH Modeling: Simulation of a Switched Reluctance Motor for an Electric Vehicle,” *IEEE Trans. Ind. Electron.*, vol. 61, no. 1, pp. 469–476, 2014.

[5] D.-M. Nguyen, I. Bahri, G. Krebs, E. Berthelot, and C. Marchand, “Vibration study of the intermittent control for a switched reluctance machine,” *Math. Comput. Simul.*, vol. 158, pp. 308–325, 2019.

[6] H. Cheng, L. Wang, G. Han, and H. Chen, “The Design and Control of an Electrified Powertrain with Switched Reluctance Machines for Series Hybrid Electric Vehicle,” in *2019 IEEE Vehicle Power and Propulsion Conference (VPPC)*, 2019, pp. 1–5.

[7] J. A. Domínguez-Navarro, J. S. Artal-Sevil, H. A. Pascual, and J. L. Bernal-Agustín, “Fuzzy-logic strategy control for switched reluctance machine,” in *2018 Thirteenth International Conference on Ecological Vehicles and Renewable Energies (EVER)*, 2018, pp. 1–5.

[8] A. El-Shahat, A. Hunter, M. Rahman, and Y. Wu, “Ultra-High Speed Switched Reluctance Motor-Generator for Turbocharger Applications,” *Energy Procedia*, vol. 162, pp. 359–368, 2019.

[9] D. Pham, A. Klein-Hessling, and R. W. De Doncker, “Control of a DC-DC Converter as an Active Filter in Combination with Switched Reluctance Generators for Gas Turbine Applications,” in *2019 AIAA/IEEE Electric Aircraft Technologies Symposium (EATS)*, 2019, pp. 1–17.

[10] A. M. S. Arifin, “Switched reluctance generator drive in the low and medium speed operation : modelling and analysis,” Ph.D. Dissertation, Massey University, New Zealand, 2013.

[11] T. J. E. Miller, *Electronic Control of Switched Reluctance Machines*, Jan. 2001.

[12] J. Llibre, N. Martinez, P. Leprince, and B. Nogarede, “Analysis and Modeling of Linear-Switched Reluctance for Medical Application,” *Actuators*, vol. 2, pp. 27–44, Jun. 2013.

[13] O. Anaya-Lara, N. Jenkins, J. Ekanayake, P. Cartwright, and M. Hughes, “Wind Energy Generation: Modelling and Control,” in *John Wiley & Sons*, 2009.

[14] Y. Chang and C. Liaw, “On the Design of Power Circuit and Control Scheme for Switched Reluctance Generator,” *IEEE Trans. Power Electron.*, vol. 23, no. 1, pp. 445–454, 2008.

[15] Y. Sozer and D. A. Torrey, “Closed loop control of excitation parameters for high speed switched-reluctance generators,” *IEEE Trans. Power Electron.*, vol. 19, no. 2, pp. 355–362, 2004.

[16] H. Chen, “Implementation of a Three-Phase Switched Reluctance Generator System for Wind Power Applications,” in *2008 14th Symposium on Electromagnetic Launch Technology*, 2008, pp. 1–6.

[17] K. Ogawa, N. Yamamura, and M. Ishda, “Study for Small Size Wind Power Generating System Using Switched Reluctance Generator,” in *2006 IEEE International Conference on Industrial Technology*, 2006, pp. 1510–1515.

[18] R. Cardenas, R. Pena, M. Perez, J. Clare, G. Asher, and P. Wheeler, “Control of a switched reluctance generator for variable-speed wind energy applications,” *IEEE Trans. Energy Convers.*, vol. 20, no. 4, pp. 781–791, 2005.

[19] Q. Wang and L. Chang, “An intelligent maximum power extraction algorithm for inverter-based variable speed wind turbine systems,” *IEEE Trans. Power Electron.*, vol. 19, no. 5, pp. 1242–1249, 2004.

[20] A. Fleury, D. A. de Andrade, F. d. S. e Silva, and J. L. Domingos, “Switched Reluctance Generator for complementary Wind Power Generation in Grid Connection,” in *2007 IEEE International Electric Machines & Drives Conference*, 2007, vol. 1, pp. 465–470.

[21] N. Sun, D. Choi, J. Li, and Y. Cho, “The Angle Control of Switched Reluctance Generator for Maximum Output Power,” in *2012 Sixth Int. Conf. on Electromagnetic Field Problems and Applications*, 2012, pp. 1–4.

[22] M. Ziapour, E. Afjei, and M. Yousefi, “Optimum commutation angles for voltage regulation of a high speed switched reluctance generator,” in *4th Annual International Power Electronics, Drive Systems and Technologies Conference*, 2013, pp. 271–276.

[23] X. Deng *et al.*, “Design of switched reluctance generator system for wind power maximization,” in *2015 IEEE NW Russia Young Researchers in Electrical and Electronic Engineering Conference*, 2015, pp. 306–310.

[24] M. V Zaharia, A. A. Laczko, A. A. Pop, M. M. Radulescu, and F. Gillon, “Optimal commutation angles of a switched reluctance motor/generator,” in *2015 Tenth International Conference on Ecological Vehicles and Renewable Energies (EVER)*, 2015, pp. 1–8.

[25] W. Wang *et al.*, "Control system of switched reluctance generator," in *2017 IEEE Conference of Russian Young Researchers in Electrical and Electronic Engineering (EIConRus)*, 2017, pp. 1064–1069.

[26] L. Ling, L. Dong, and X. Liao, "Comparison of two control methods of switched reluctance generator," *2017 12th IEEE Conf. Ind. Electron. Appl.*, pp. 792–796, 2017.

[27] A. Ivanov and I. Kalanchin, "Application of maximum power point tracker method in wind energy conversion system based on the switched reluctance generator," in *2017 International Multi-Conference on Engineering, Computer and Information Sciences (SIBIRCON)*, 2017, pp. 472–476.

[28] M. A. Dranca and M. M. Radulescu, "Comparative Design Analysis of Three-Phase Switched Reluctance Generators for Micro-Wind Power Applications," in *2018 XIII International Conference on Electrical Machines (ICEM)*, 2018, pp. 597–601.

[29] M. O. Shykhnenko, L. I. Mazurenko, O. V Dzhura, and O. A. Bilyk, "Mathematical Model, Research and Improvement of the Switched Reluctance Generator Voltage Stabilization Methods," in *2018 IEEE 3rd International Conference on Intelligent Energy and Power Systems (IEPS)*, 2018, pp. 338–342.

[30] M. M. Namazi, S. M. S. Nejad, A. Tabesh, A. Rashidi, and M. Liserre, "Passivity-Based Control of Switched Reluctance-Based Wind System Supplying Constant Power Load," *IEEE Trans. Ind. Electron.*, vol. 65, no. 12, pp. 9550–9560, 2018.

[31] H. Ačkar, S. Huseinbegović, Š. Mašić, S. Smaka, and A. Tahirbegović, "Voltage Control of a Switched Reluctance Generator Using Discrete Sliding Mode Technique," in *2018 XIII International Conference on Electrical Machines (ICEM)*, 2018, pp. 1731–1737.

[32] S. Jagwani, G. K. Sah, and L. Venkatesha, "MPPT Based Switched Reluctance Generator Control for a Grid Interactive Wind Energy System," in *2018 7th International Conference on Renewable Energy Research and Applications (ICRERA)*, 2018, pp. 998–1003.

[33] H. Chen, S. Xu, W. Wei, J. Yang, and R. Nie, "Reliability Assessment of Double-Sided Linear Switched Reluctance Generator System Based on Hierarchical Markov Model," *IEEE Trans. Ind. Electron.*, vol. 66, no. 6, pp. 4901–4911, 2019.

[34] S. Li, S. Zhang, T. G. Habetler, and R. G. Harley, "Modeling, Design Optimization, and Applications of Switched Reluctance Machines—A Review," *IEEE Trans. Ind. Appl.*, vol. 55, no. 3, pp. 2660–2681, 2019.

[35] E. H. Catata, D. B. Luque, J. L. Azcue-Puma, and E. R. Filho, "Direct Instantaneous Torque Control of Three Phase 6/4 Switched Reluctance Generator Operating at Low Speeds," in *2019 IEEE XXVI International Conference on Electronics, Electrical Engineering and Computing (INTERCON)*, 2019, pp. 1–4.

[36] X. Zan *et al.*, "A New Control Strategy for SR Generation System Based on Modified PT Control," *IEEE Access*, vol. 7, pp. 179720–179733, 2019.

[37] P. Xiao, J. Pan, C. Wang, R. Huang, and P. Fu, "Dual-Loop Compensation Voltage Control for Linear Switched Reluctance Generators," in *2019 22nd International Conference on Electrical Machines and Systems (ICEMS)*, 2019, pp. 1–5.

[38] H. Chen, D. Xu, and X. Deng, "Control for Power Converter of Small-scale Switched Reluctance Wind Power Generator," *IEEE Trans. Ind. Electron.*, p. 1, 2020.

[39] A. Kushwaha and R. Kanagaraj, "Peak-current estimation using simplified current-rise model of switched reluctance generator operating in single-pulse mode," *Int. J. Electr. Power Energy Syst.*, vol. 120, p. 105971, 2020.

[40] K. Chirapo, A. Oliveira, A. Sguarezi, A. Pelizari, S. Di Santo, and E. Costa, "P+RES Controller Applied to the Direct Power Control of Switched Reluctance Generator," *J. Control. Autom. Electr. Syst.*, vol. 31, Jan. 2020.

[41] M. M. Ali, C. Storey, and A. Törn, "Application of Stochastic Global Optimization Algorithms to Practical Problems," *J. Optim. Theory Appl.*, vol. 95, no. 3, pp. 545–563, 1997.

[42] J. A. Nelder and R. Mead, "A Simplex Method for Function Minimization," *Comput. J.*, vol. 7, no. 4, pp. 308–313, Jan. 1965.

[43] B. S. A. Gottfried and J. A. Weisman, *Introduction to Optimization Theory*. Prentice-Hall, 1973.

[44] W. L. Price, "Global optimization by controlled random search," *J. Optim. Theory Appl.*, vol. 40, no. 3, pp. 333–348, 1983.

[45] D. E. Goldberg, *Genetic Algorithms in Search, Optimization and Machine Learning*, 1st ed. Boston, MA, USA: Addison-Wesley Longman Publishing Co., Inc., 1989.

[46] R. Yang and I. Douglas, "Simple Genetic Algorithm with Local Tuning: Efficient Global Optimizing Technique," *J. Optim. Theory Appl.*, vol. 98, no. 2, pp. 449–465, 1998.

[47] J. Ronkkonen, S. Kukkonen, and K. V Price, "Real-parameter optimization with differential evolution," in *2005 IEEE Congress on Evolutionary Computation*, 2005, vol. 1, p. 506–513 Vol.1.

[48] J. H. Fisch, Y. Li, P. C. Kjaer, J. J. Gribble, and T. J. E. Miller, "Pareto-optimal firing angles for switched reluctance motor control," in *Second International Conference On Genetic Algorithms In Engineering Systems: Innovations And Applications*, 1997, pp. 90–96.

[49] K. Liu and M. Stiebler, "Voltage Control Of A Switched Reluctance Generator By Means Of Fuzzy Logic Approach," in *Proceedings of the 6th International Conference on Optimization of Electrical and Electronic Equipments*, 1998, vol. 2, pp. 443–446.

[50] H. Shin and K. Lee, "Optimal design of a switched reluctance generator for small wind power system using a genetic algorithm," in *2015 9th International Conference on Power Electronics and ECCE Asia (ICPE-ECCE Asia)*, 2015, pp. 2209–2214.

[51] M. Tchavychalov and V. A. Detistov, "Optimum Design of Linear Switched Reluctance Generator," in *2018 X International Conference on Electrical Power Drive Systems (ICEPDS)*, 2018, pp. 1–4.

[52] N. H. Saad, A. A. El-Sattar, and M. E. Metally, "Artificial neural controller for torque ripple control and maximum power extraction for wind system driven by switched reluctance generator," *Ain Shams Eng. J.*, vol. 9, no. 4, pp. 2255–2264, Dec. 2018.

[53] G. P. Viajante, E. N. Chaves, L. C. Miranda, M. A. A. freitas, C. A. Queiroz, and J. A. Santos, "Design and Implementation of a Fuzzy Control System Applied to a 6x4 SRG," in *2019 IEEE International Conference on Environment and Electrical Engineering and 2019 IEEE Industrial and Commercial Power Systems Europe (EEEIC / I&CPS Europe)*, 2019, pp. 1–6.

[54] H. E. M. Lopez, "Maximum power tracking control scheme

for wind generator systems," M.S. Thesis, Texas A&M University, 2007.

[55] H. Moodi and D. Bustan, "Wind turbine control using T-S systems with nonlinear consequent parts," *Energy*, vol. 172, pp. 922–931, Apr. 2019.

[56] M. Heidari, "Maximum Wind Energy Extraction by Using Neural Network Estimation and Predictive Control of Boost Converter," *Int. J. Ind. Electron. Control Optim.*, vol. 1, no. 2, pp. 115–120, 2018.

[57] A. Pintea, D. Popescu, and P. Borne, "Robust control for wind power systems," in *18th Mediterranean Conference on Control and Automation, MED'10*, 2010, pp. 1085–1091.

[58] E. Rahmanian, H. Akbari, and H. Sheisi, "Maximum Power Point Tracking in Grid Connected Wind Plant by Using Intelligent Controller and Switched Reluctance Generator," *IEEE Trans. Sustain. Energy*, vol. 8, p. 1, Jul. 2017.

[59] L. Y. Pao and K. E. Johnson, "A tutorial on the dynamics and control of wind turbines and wind farms," in *2009 American Control Conference*, 2009, pp. 2076–2089.

[60] Ji.-W. Ahn, "Switched Reluctance Motor," in *Torque Control*, Rijeka: IntechOpen, 2011, p. Ch. 8.

[61] A. Arifin and I. Al-Bahadly, "Switched Reluctance Generator for Variable Speed Wind Energy Applications," *Smart Grid Renew. Energy*, vol. 2, pp. 27–36, Jan. 2011.

[62] P. Asadi, "Development and application of an advanced switched reluctance generator drive," Ph.D. Dissertation, Texas A&M University, 2006.

[63] Y. Gao, "Speed control of switched reluctance motors," Hong Kong University of Science and Technology, 2000.

[64] D. A. Torrey, "Switched reluctance generators and their control," *IEEE Trans. Ind. Electron.*, vol. 49, no. 1, pp. 3–14, 2002.

[65] T. Sawata, P. C. Kjaer, C. Cossar, and T. J. E. Miller, "A control strategy for the switched reluctance generator," in *international conference on Electrical Machines*, 1998, pp. 2131–2136.

[66] N. Faridnia, "Voltage Control of a 12/8 Pole Switched Reluctance Generator Using Fuzzy Logic," *Int. J. Mod. Nonlinear Theory Appl.*, vol. 1, pp. 107–112, Jan. 2012.

[67] D. A. Torrey, X. Niu, and E. J. Unkauf, "Analytical modelling of variable-reluctance machine magnetisation characteristics," *IEE Proc. - Electr. Power Appl.*, vol. 142, no. 1, pp. 14–22, 1995.

[68] H. Le-Huy and P. Brunelle, "A versatile nonlinear switched reluctance motor model in Simulink using realistic and analytical magnetization characteristics," in *31st Annual Conference of IEEE Industrial Electronics Society, 2005. IECON 2005.*, 2005, p. 6 pp.-pp.

[69] P. J. d. S. Neto, T. A. d. S. Barros, M. V. de Paula, R. R. de Souza, and E. R. Filho, "Design of Computational Experiment for Performance Optimization of a Switched Reluctance Generator in Wind Systems," *IEEE Trans. Energy Convers.*, vol. 33, no. 1, pp. 406–419, 2018.

[70] A. Bryant *et al.*, "A Fast Loss and Temperature Simulation Method for Power Converters, Part I: Electrothermal Modeling and Validation," *IEEE Trans. Power Electron.*, vol. 27, no. 1, pp. 248–257, 2012.

[71] J. Faiz and R. Fazai, "Optimal Excitation Angles of a High Speed Switched Reluctance Generator by Efficiency Maximization," in *2006 12th International Power Electronics and Motion Control Conference*, 2006, pp. 287–291.

[72] K. Lee, *Modern Heuristic Optimization Techniques : Theory and Applications to Power Systems*. 2008.

Hojjat Hajiabadi was born in Birjand, Iran, on March 23, 1983. He attended both the middle school and the high school run by National Organization for Developing Exceptional Talents (NODET) and received his B.Sc. and M.Sc. degrees in Electrical Engineering from Ferdowsi University of Mashhad, Iran, in 2006, and 2012, respectively. Currently, he is a Ph.D. candidate at the University of Birjand in the field of Electrical Engineering. His research interests include renewable and sustainable energies, switched reluctance generators, optimization and control of power systems, and networked control systems.

Mohsen Farshad was born in Birjand, Iran, in 1967. He received the B.S. degree in Electrical Engineering from Sharif University of Technology, Tehran, Iran, in 1990 and the M.S. and the Ph.D. degrees in Electrical Engineering from University of Tehran, Tehran, Iran, in 1994 and 2006, respectively. Now, he is an associate professor at the department of Power Engineering, Computer and Electrical Engineering faculty, university of Birjand, Birjand, Iran. His teaching and research interests are soft computing (including intelligent optimization algorithms, neural networks and fuzzy logic), modeling and control of electric drives (particularly Switched Reluctance Machine), systems identification and control, modeling and control of vehicular traffic.

Mohammad Ali Shamsinejad received the B.Sc. and M.Sc. degrees in Electrical Engineering from Sharif University of Technology, Tehran, Iran, in 1990 and 1996, respectively, and the Ph.D. degree from the "Institut National Polytechnique de Lorraine", Nancy, France, in 2007. He is an Associate Professor at the department of Power Engineering, Computer and Electrical Engineering faculty, university of Birjand, Birjand, South Khorasan, Iran.

IECO

This page intentionally left blank.

International Journal of Industrial Electronics, Control and Optimization © 2021 IECO
Vol. 4, No. 1, pp. 47-57, Jan (2021)

A New Method for Detection and Classification of Power Quality Events Using Discrete Wavelet Transform and Correlation Coefficients

Navid Ghaffarzadeh[1,†]

[1]Department of Electrical Engineering, Faculty of Technical and Engineering, Imam Khomeini International University, Qazvin, Iran.

ABSTRACT

This paper presents a novel and simple approach to detecting and classifying a wide range of power quality (PQ) events based on the discrete wavelet transform (DWT) and correlation coefficient. For this purpose, two new indices are proposed and the type of PQ event is detected by comparing the values of the correlation coefficient between the value of these indices for the pre-stored PQ events and for a recorded indistinct signal. This algorithm enjoys the advantages of DWT and correlation coefficient and it does not suffer the disadvantages of neural networks or neural network-fuzzy based algorithms such as training and high dimension input matrices or the disadvantages of Fourier transform-based approaches such as unsuitability for non-stationary signals as it does not track signal dynamics properly due to the limitation of fixed window width. The effectiveness of the method tested by numerous PQ disturbance and simulation results confirms the competency and the ability of the proposed method in detection and automatic diagnosis of PQ disturbances. Compared with the other methods, the simulation under different noise conditions verifies the effectiveness of the noise immunity and the relatively better accuracy of the proposed method.

Article Info

Keywords:
Classification, Correlation Coefficient, Discrete Wavelet Transform, Power Quality.

Article History:
Received 2020-03-16
Accepted 2020-07-25

I. INTRODUCTION

Power quality (PQ) has become an important topic of research in recent years. PQ is a quality of service issue for customers and electric power service providers, and it covers a variety of transient electromagnetic phenomena in electric power distribution systems [1]. Today, the proliferation of power electronic devices and nonlinear loads in electric power networks has triggered a growing concern for power quality issues from both utilities and power users. A power quality problem usually involves a variation in the electric service voltage or current, e.g. sag, swell, DC offset, flicker, interrupt, notching, harmonic, and transient. These disturbances can downgrade service quality and also cause different problems. Also, the recognition of the PQ event waveform is often bothersome because it includes a wide range of event categories or classes from dc offsets with low frequency to transients with high frequency.

Currently, some powerful tools are available to monitor and classify electrical PQ disturbances. Based on these tools, several methods have been suggested for PQ disturbance detection and classification in the last few years. A brief review of these methods is as follows.

So far, various methods have been proposed based on discrete wavelet packet and discrete wavelet transform for power quality disturbance identification [2-8].

Fuzzy logic has been used for PQ disturbance detection in several methods. In [9], both the Fourier transform and fuzzy approaches are suggested for PQ disturbance classification. Other fuzzy logic and discrete wavelet transform-based

---

[†]**Corresponding Author**: ghaffarzadeh@eng.ikiu.ac.ir
Tel: +98-2833901294, Fax: +98- 2833780073, Imam Khomeini International University
Faculty of Technical and Engineering, Imam Khomeini International University, Qazvin, Iran.

methods have also been presented [10,11]. Another methodology [12] uses a wavelet packet-based hidden Markov model for the detection and classification of PQ disturbances. It is noteworthy that this method employs the hidden Markov model to determine the existence of disturbance.

The neural network detection approach has been introduced in some methods [13-15]. In [13], the authors describe how a neural network, trained to recognize patterns of transmission line faults, has been incorporated in a PC-based system that analyzes data files from substation digital fault recorders. In [14], a real-time power quality monitoring scheme was implemented using an artificial neural network and Labview. In this method, the artificial neural network was used to detect and classify the voltage sag and swell in real time.

Hybrid schemes using an artificial neural network and DWT were presented in [16-23]. At first, the discrete wavelet transform provides the features of the events, and then, the artificial neural network classifies them. In [16], the features extracted from wavelet transform coefficients are inputted into a radial basis function (RBF) network for power quality disturbance pattern classification. Applications of the wavelet transform, fuzzy logic, expert systems, neural networks, and genetic algorithms in power quality detection and classification, in particular, are reviewed in [17]. The PQ event detection scheme in [19] was carried out in the wavelet domain using a set of multiple neural networks. With the configuration used in this reference, the classifier is capable of providing a degree of belief for the identified PQ disturbance waveform. In the method presented by Kanirajan et al., the features extracted by the wavelet are trained by an RBF neural network for the classification of PQ events [21]. Sridhar et al. presented a method for PQ disturbance classification. The PQ disturbances are first identified using discrete wavelet transform and they are, then, classified using ANN [22]. The overall performance evaluation of the method is more than 97%. In [23], DWT with a multi-resolution analysis was used for the feature extraction of the PQ events. The probabilistic neural network classifier was used as an effective classifier for the detection and classification of PQ disturbances.

Moreover, in [24-28], combined neuro-fuzzy methodologies were utilized to identify and classify PQ disturbances. In these approaches, the discrete wavelet transform decomposition was used to form feature vectors.

In [24], the input PQ waveforms were preprocessed by the wavelet transform for feature extraction, and the neural network outputs were not taken as the final classification but were used to activate the fuzzy-associative-memory recalling for identifying the most possible type that the input waveform may belong to. A two-stage PQ violation classification approach that uses the potentials of the wavelet transform and the adaptive neuro-fuzzy networks was presented in [25].

In [26], the selected features were extracted from amplitude, phase, and frequency and were instantly used as input to an adaptive neuro-fuzzy system for PQ disturbance classification. To extract PQ disturbance features, the energy distribution of the wavelet part at each decomposition level was introduced by Zhu et al. [27]. Based on these features (as an input), a neuro-fuzzy algorithm was used for the classification of PQ disturbances. Reaz et al. [28] employed a different type of univariate randomly optimized neural network combined with discrete wavelet transform and fuzzy logic in their method to have a better power quality disturbance classification accuracy.

Also, an approach based on a combination of genetic algorithm (GA) and artificial neural network was presented in [29]. A wavelet network-based PQ disturbance detection and classification method was introduced in [30]. The support vector machine (SVM) has also been applied for the detection of PQ events [31-32]. An approach presented in [31] used the histogram of oriented gradients for PQ event detection and SVM for PQ disturbance classification. Thirumala et al. presented a PQ disturbance detection method based on wavelet transform and dual multiclass support vector machines [32]. Ucar et al. proposed a PQ event detection and classification method using the DWT-based extreme machine learning (ELM) technique [33]. Fuzzy systems oriented by the particle swarm optimization algorithm are used for PQ event detection [34]. Recently, a novel detection and classification method for PQ using the least mean square (LMS) and neural network was proposed [35]. In [36], a PQ event detection algorithm using a balanced neural tree is introduced. In this method, the Hilbert-Huang transform is utilized to study non-stationary PQ disturbances. Generally, this technique is an amalgamation of two techniques including empirical mode decomposition and Hilbert transform. Biswal et al. proposed a PQ event detection method using hyperbolic S-transform for feature extraction and genetic algorithm-based fuzzy C-means for automatic recognition of PQ events [37]. Ray et al. presented a PQ disturbance classification technique using a combination of S-transform and SVM for PQ disturbance detection [38]. A fuzzy product aggregation reasoning rule classifier was adopted for the classification of PQ events in [39] in which the DWT technique was used as the feature extraction technique. The S-transform was combined with an extreme machine learning technique for automatic nonstationary power quality disturbance recognition in [40]. In [41], an approach was proposed for optimal placement of PQ meters in a power system on a seeker optimization algorithm.

The performance of a PQ event detection approach generally depends on the accuracy of the signal processing techniques.

Several signal processing approaches have been used for PQ events detection, such as discrete Fourier transform, fast Fourier transform, short-time Fourier transform, discrete wavelet transform, and Gabor-Wigner transform.

Discrete Fourier transform is mostly suitable for stationary PQ events. Since PQ events are generally nonstationary-type signals, it is unsuitable to sense the immediate variations in PQ disturbances, for example, their initial and finale points by using the discrete Fourier transform. The signal information, such as amplitude frequencies and phases, cannot be acquired correctly by using the fast Fourier transform because of the leakage, aliasing effects, and picket fence formed by fast Fourier transform. It is hard to analyze nonstationary signals by short-time Fourier transform. The main drawback of this signal processing technique is the limited time-frequency resolution. Moreover, it cannot give the exact time and frequency info simultaneously to categorize the power quality events as stated by the IEEE-1159 standard. In the Gabor-Wigner transform, the computational burden directly depends on the sampling frequency. Moreover, the Wigner distribution will cause critical cross-interference, which promotes incorrect frequency components.

In contrast to Fourier and Gabor-Wigner transform, the wavelet transform can offer time and frequency information of a signal simultaneously. In other words, wavelet transform provides local representation in both time and frequency. Therefore, it is suitable where good time-frequency resolution is required.

The neural network-based PQ detection method has such disadvantages as its convergence speed, and the accuracy of the method depends on the network architecture as well as noise in the signal. Poor classification accuracy when training samples are minimum is the disadvantage of the support vector machine-based PQ detection method. In the fuzzy logic technique, the training set for every case is fixed, so it is not suitable for new disturbances.

This paper introduces a new algorithm based on the discrete wavelet transform and correlation coefficient for the PQ disturbance waveform recognition and classification. This algorithm has the advantages of DWT and correlation coefficient, while it does not have the disadvantage of neural network or neural network-fuzzy-based algorithms such as training and high dimension input matrices.

In the algorithm, the DWT is first used in an offline operation to de-noise and decompose the known power quality events signal, and for each event (8 types), the ratio of the sum of the absolute value of the detail coefficients of distorted the signal S(t) at decomposition levels 1 to 13 to the sum of the absolute value of detail coefficients of the pure sinusoid signal at the same decomposition levels is calculated and stored in the vector (totally 8 vectors are obtained for 8 events). Similarly, for the second index, the difference between the standard deviation obtained from the detail coefficients of the distorted signal S(t) at decomposition levels 1 to 13 and the standard deviation obtained from the detail coefficients of the pure sinusoid signal at the same decomposition levels is computed and stored in the vector. In the proposed algorithm (online operation), the unknown PQ voltage signal containing noise is first sampled by a 20-kHz sampling rate. Then, the signal is denoised by sym4 to get a higher SNR signal. Next, using sym4, the signal is decomposed into 13 decomposition levels and the proposed criterion is computed. Assuming that the condition is true, the proposed indices will be obtained. Then, the correlation coefficient between the first computed vector of pre-stored PQ violations and a recorded unknown signal will be calculated. So, eight numbers are achieved and the maximum number is considered. The indistinct PQ event belongs to this group. If the number of maximum digits is two or more, the second index will be considered. This means that the correlation coefficient between the second computed vector of pre-stored PQ events and a recorded unknown PQ signal will be calculated. The maximum number will specify the PQ class. The results demonstrate that the proposed approach has excellent efficiency.

The rest of the paper is organized as follows. Section II introduces the proposed algorithm and shows how the two indices can be calculated by using DWT. In Section III, simulation results are demonstrated, and the concluding points are presented in Section IV.

II. PROPOSED METHOD

The paper presents a new method for the detection and classification of PQ disturbances based on DWT and correlation coefficient.

The correlation between two variables X and Y is defined as [42]:

$$Corr(X,Y)=\frac{Cov(X,Y)}{\sqrt{Var(X)Var(Y)}} \tag{1}$$

The strength of the dependence between the two variables increases as the correlation moves further away from 0 to 1 or -1 [42].

The different steps of the proposed method are described below:

A. De-noising

In practice, signals sampled by measuring devices have noise. The presence of noise reduces the identification capability of the DWT-based PQ disturbance monitoring system. A DWT-based de-noising approach is used in the proposed algorithm to prevent the detrimental impact of noise and to improve the efficiency of discrete wavelet transform-based monitoring systems. The reconstructed signal is noise-free and has the same energy content.

The general de-noising procedure involves three steps as follows [43].

1. Decomposing
2. Threshold selecting
3. Reconstructing

The performance of a discrete wavelet-based denoising technique depends on two points: how to choose the appropriate threshold value (γ) and how to perform the thresholding.

There are two kinds of thresholding rules: hard thresholding and soft thresholding. Hard thresholding can be described as the usual process of setting the elements whose absolute values are lower than the threshold to zero. Soft thresholding is an extension of hard thresholding in which the elements whose absolute values are lower than the threshold value are first set to zero, and then the nonzero coefficients are shrieked towards zero [43]. We use soft thresholding in the paper.

But the main problem in statistical discrete wavelet denoising is how to choose a proper threshold value (γ). Selecting a threshold with very large value will shrink almost all coefficients at higher frequency bands to zero, possibly resulting in a pure power quality waveform even in the presence of a disturbance. Conversely, choosing a threshold with a very small value would result in inefficient denoising. So, the selection of a proper threshold value (γ) is the key to the success of the denoising technique. We use a mixture of Stein's unbiased risk estimate (SURE) approach and universal fixed thresholding method for the selection of a proper threshold value. As a result, if the signal-to-noise ratio is very small, the SURE estimate will be very noisy. So, in case this situation is identified, the fixed form threshold is utilized as follows:

$$\gamma = \left(\frac{\sum_{i=1}^{N_{d_j}} \left| d_j(i) \right|}{0.6745 \cdot 2^j \cdot N_{d_j}} \right) \cdot \sqrt{2 \log N_{d_j}} \qquad (2)$$

where N_{d_j} is the number of detailed coefficients at the desire resolution level j.

After denoising, the reconstructed signal is noise-free and has the same energy content.

B. *Proper Mother Wavelet selecting*

The proper mother wavelet selection has an important role in identifying and localizing different kinds of signal disturbances. Selecting the mother wavelet also depends on the essence and type of the application. For the detection of a low domain, short duration, rapid decaying, and oscillating type of signals, the most popular wavelets are Daubechies and Symlets family (Db2, Db3, ... and Sym2, Sym3,....). But, the Symlets were proposed by Ingrid Daubechies as modifications to the db family [44]. Furthermore, when the scale is increased, the accuracy of the event time localization will be decreased. Also, the width and smoothness of the mother wavelet depend on its number. So, we should be cautious to select the appropriate discrete wavelet family and its number. In this paper, after many examinations, the sym4 mother wavelet was selected.

Each PQ event is related to one or more discrete wavelet transform coefficients. For example, Figures 1-5 show voltage sag, swell, transient (capacitor bank switching) event, notching, flicker, and their detail coefficients at resolution levels 1, 2, and 3 using sym4, respectively.

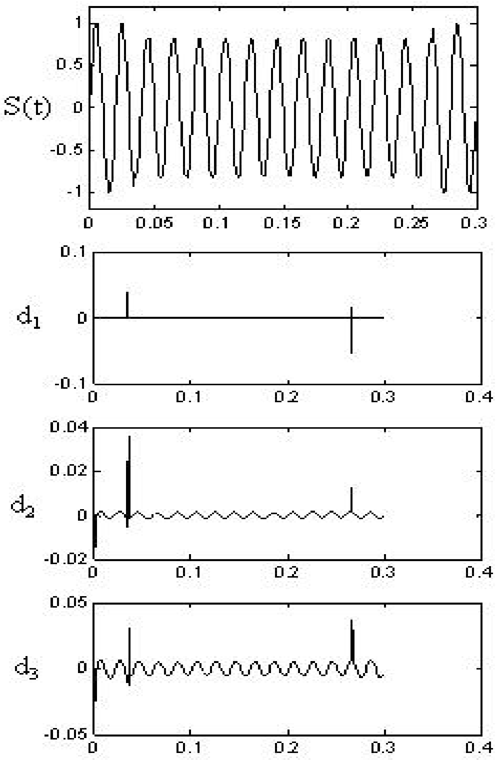

Fig. 1. Voltage sag signal with its detail coefficients (d1, d2, d3).

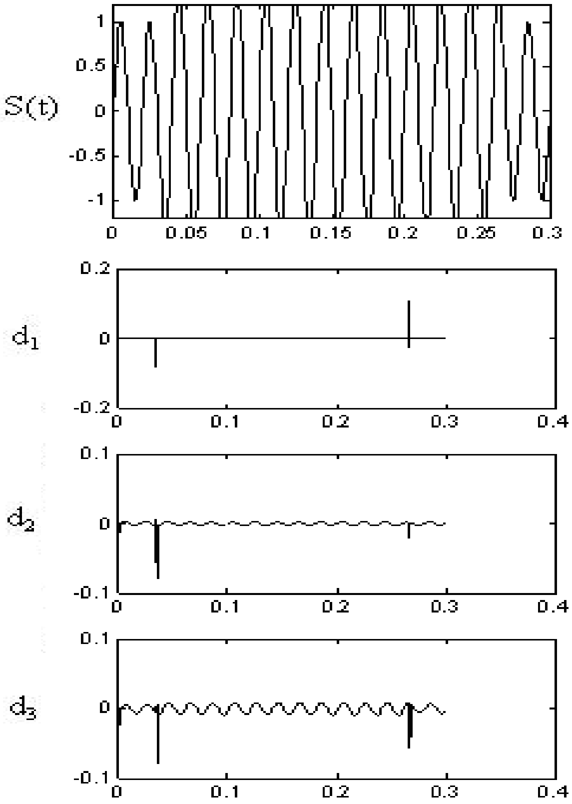

Fig. 2. Voltage swell signal with its detail coefficients (d1, d2, d3).

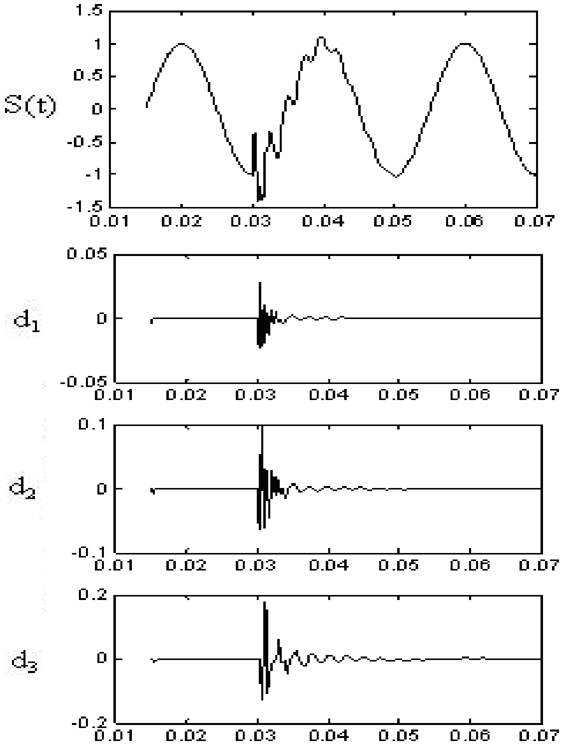

Fig. 3. Capacitor bank switching signal with its detail coefficients (d1, d2, d3).

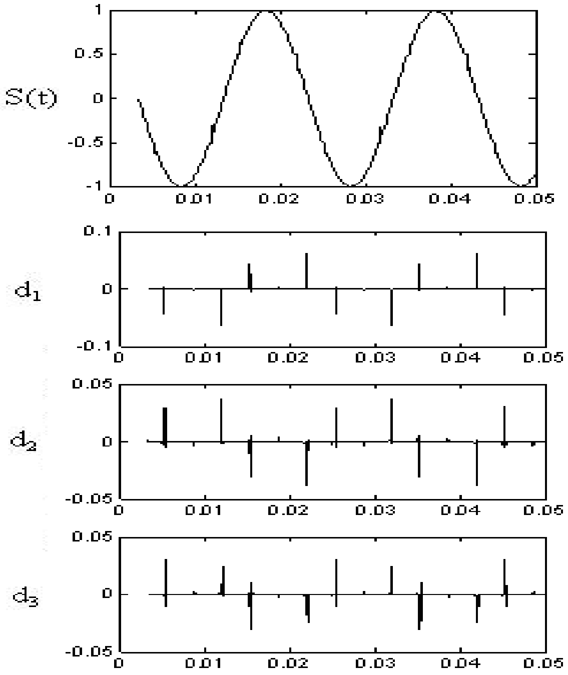

Fig. 4. Notching signal with its detail coefficients (d1, d2, d3).

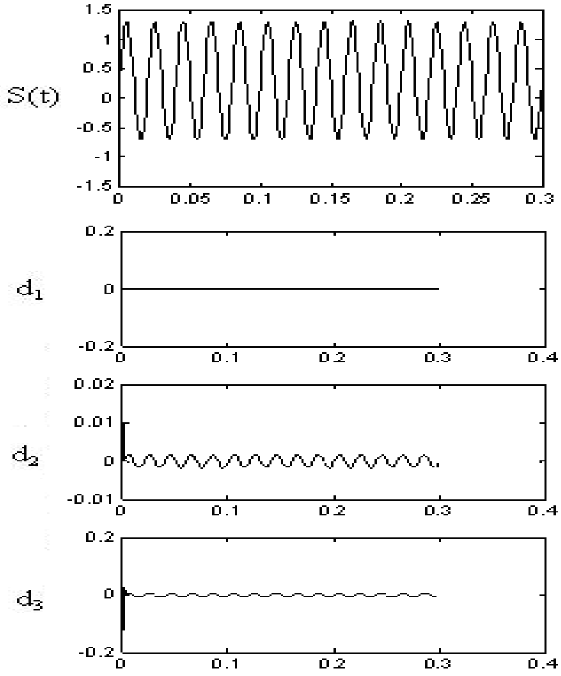

Fig. 5. DC offset signal with its detail coefficients (d1, d2, d3).

C. Proposed Algorithm Methodology

The paper presents a novel method for the detection and classification of PQ disturbances based on DWT and correlation coefficient.

For this purpose, DWT is first utilized in an offline operation to decompose the known power quality events signal. It is noteworthy that eight types of PQ disturbances (sag, swell, DC offset, flicker, interrupt, notching, harmonic, transient) are considered in the proposed method. Then, for each event (8 types), the ratio of the sum of the absolute value of detail coefficients of distorted signal S(t) at decomposition levels from 1 to 13, ($Sum\_absS_{d_j}^{Dist}(t) \quad j=1,2,...,13$) to sum of the absolute value of detail coefficients of the pure sinusoid signal at the same decomposition levels ($Sum\_absS_{d_j}^{Sin}(t) \quad j=1,2,...,13$) was calculated and stored in a vector (totally 8 vectors were obtained for 8 events). Similarly, for the second index, the difference between the standard deviation obtained from the detail coefficients of the distorted signal S(t) at decomposition levels 1 to 13 ($Std\_absS_{d_j}^{Dist}(t) \quad j=1,2,...,13$) and the standard deviation obtained from the detail coefficients of the pure sinusoid signal at the same decomposition levels was computed ($Std\_absS_{d_j}^{Sin}(t) \quad j=1,2,...,13$) and stored in the vector (In this case, 8 vectors were computed for eight PQ disturbances).

After proposing the vectors of the appropriate indices, we show how these proposed indices can be obtained.

Let's assume that signal S(t) was decomposed into N levels by discrete wavelet transform as follows:

$$S(t)=S_{c1}(t)+S_{d1}(t)+S_{d2}(t)+S_{d3}(t)+....+S_{dN}(t) \qquad (3)$$

$$S(t)=\sum_{i} c_0(i)\phi(t-i)+\sum_{i}\sum_{j=1}^{N} d_j(i)2^{\frac{j}{2}}\psi\left(2^{j}t-i\right) \qquad (4)$$

Also, we know that in a multi-resolution analysis, a set of involute subspaces Vj and Wj are denoted as:

$$V_N \supset V_{N-1} \supset V_{N-2} \supset ... \supset V_j \supset ... \supset V_2 \supset V_1 \qquad (5)$$

$$V_{j+1} = V_j \oplus W_j \qquad (6)$$

$$V_j \cap W_j = \{0\} \qquad (7)$$

where $\oplus$ defines a summation of two subspaces.

Therefore, an input signal S(t) can be decomposed into their subset signals Sc1(t) and Sdj(t) in accordance with the subsets V1 and Wj, respectively as follows [45]

$$S_{c1}(t)=\sum_{i} c_1(i)\phi(t-i) \qquad (8)$$

$$S_{dj}(t)=\sum_{i} d_j(i)2^{\frac{j}{2}}\psi\left(2^{i}t-i\right) \qquad (9)$$

where $\phi,\psi \in R.$

So, the sum of the absolute value of the detail coefficients of distorted signal S(t) at decomposition level j ($Sum\_absS_{d_j}^{Dist}(t)$) is obtained as follows:

$$Sum\_absS_{d_j}^{Dist}(t)=\sum_{i=1}^{N_{d_j}}\left|d_j(i)\right| \qquad (10)$$

where

j = the level of decomposition

dj = the detailed coefficients at level j

N_{d_j} = the number of detailed coefficients at level j

$Sum\_absS_{d_j}^{Dist}(t)$ = the sum of the absolute value of detail coefficients of distorted signal S(t) at resolution level j

Accordingly, the abovementioned first index (the ratio between the sum of the absolute value calculated from detail coefficients of the PQ disturbances and pure sin) is defined as:

$$Index1=\frac{Sum\_absS_{d_j}^{Dist}(t)}{Sum\_absS_{d_j}^{Sin}(t)} \quad j=1,2,...13 \qquad (11)$$

The first index for some PQ events is shown in Figures 6-9.

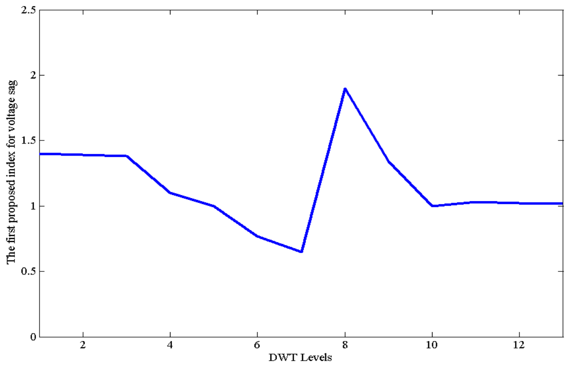

Fig. 6. The first proposed index for the voltage sag signal

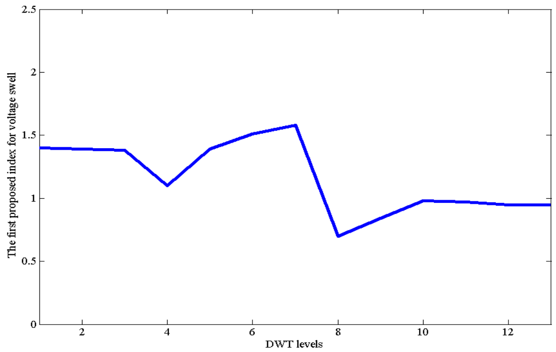

Fig. 7. The first proposed index for the voltage swell signal

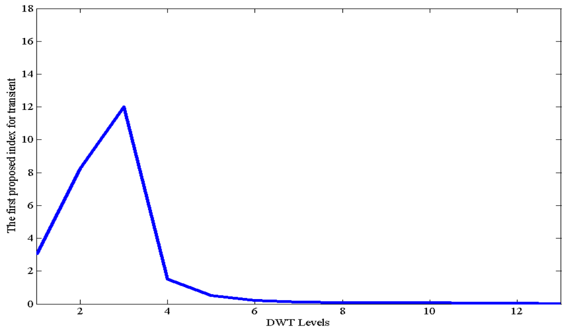

Fig. 8. The first proposed index for transient

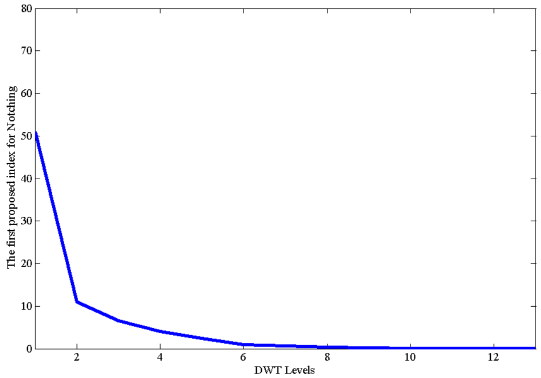

Fig. 9. The first proposed index for notching

The standard deviation of the absolute values of the detailed coefficients at decomposition level j ($Std\_absS_{d_j}(t)$) is:

$$Std\_absS_{d_j}^{Dist}(t)=\sqrt{\frac{1}{2^j N_{d_j}}\sum_i\left(\left|d_j(i)\right|-Mean\_absS_{d_j}(t)\right)^2} \qquad (12)$$

Accordingly, the abovementioned second index (the difference between the standard deviation obtained from the detail coefficients of the distorted PQ voltage signal and the pure sinusoidal) can be shown as follows:

$$Index2=Std\_absS_{d_j}^{Dist}(t)-Std\_absS_{d_j}^{Sin}(t) \quad j=1,2,\dots 13 \qquad (13)$$

The second index for some PQ events is shown in Figures 10-13.

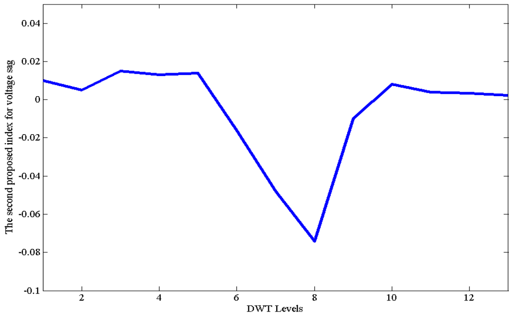

Fig. 10. The second proposed index for the voltage sag

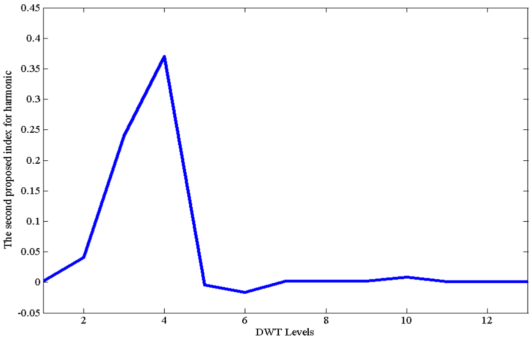

Fig. 11. The second proposed index for harmonic

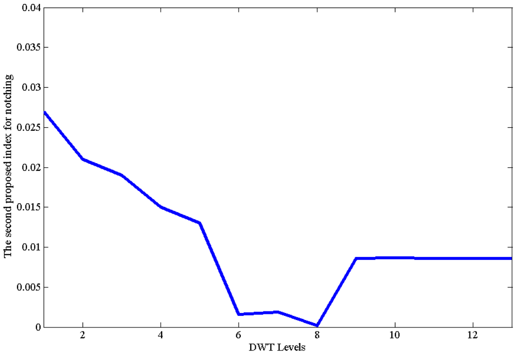

Fig. 12. The second proposed index for the notching

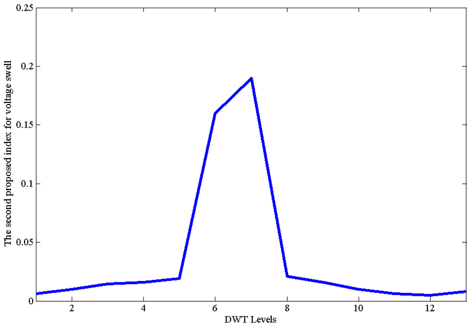

Fig. 13. The second proposed index for the voltage swell

The online operation of the proposed detection method is defined below:

First, an unknown PQ voltage signal having noise is sampled at a 20-kHz sampling rate. Then, the signal is denoised by sym4 wavelet to get a signal with a higher signal-to-noise ratio. Next, using sym4 wavelet, the signal is decomposed into 13 levels and the following criterion is computed:

$$Cr=\sqrt{\frac{\sum_{j=1}^{N}2^j\sum_{i=1}^{N_{d_j}}d_j^2(i)}{2^N\sum_{i=1}^{N_{d_N}}a_N^2(i)}} \qquad (14)$$

Eq. (14) is the THD generalization in wavelet domains. In Eq. (14), *N* is the highest decomposition level (*N* is equal 12 in the algorithm), N_{d_j} is the number of detailed coefficients at level j, and *aN* is the approximated coefficients at level N.

It should be noted that only if Cr is greater than 1%, the proposed indices will be calculated by using Eq. (10)-(13). Otherwise (i.e. Cr < 1%), the procedure will not start. In other words, Cr indicates whether the captured signal is the disturbance or not.

Supposing that the condition (14) is correct, the proposed indices will be obtained. Then, by using the proposed algorithm, the kind of captured signal will be detected. The algorithm is as follows:

The correlation coefficient between the first computed vector of a pre-stored PQ event and a recorded indistinct signal will be computed from Eq. (1). So, eight numbers are achieved and the maximum number is considered. The unknown PQ event belongs to this group. If the number of maximum digits is two or more, the second index will be considered. This means that the correlation coefficient between the second computed vector of a pre-stored PQ event and a recorded unknown PQ signal will be calculated and the maximum coefficient will be computed. The unknown PQ event belongs to this group. The second index will increase the reliability of the proposed PQ detection algorithm.

Fig. 14 demonstrates a simplified flowchart of the proposed PQ detection and classification algorithm.

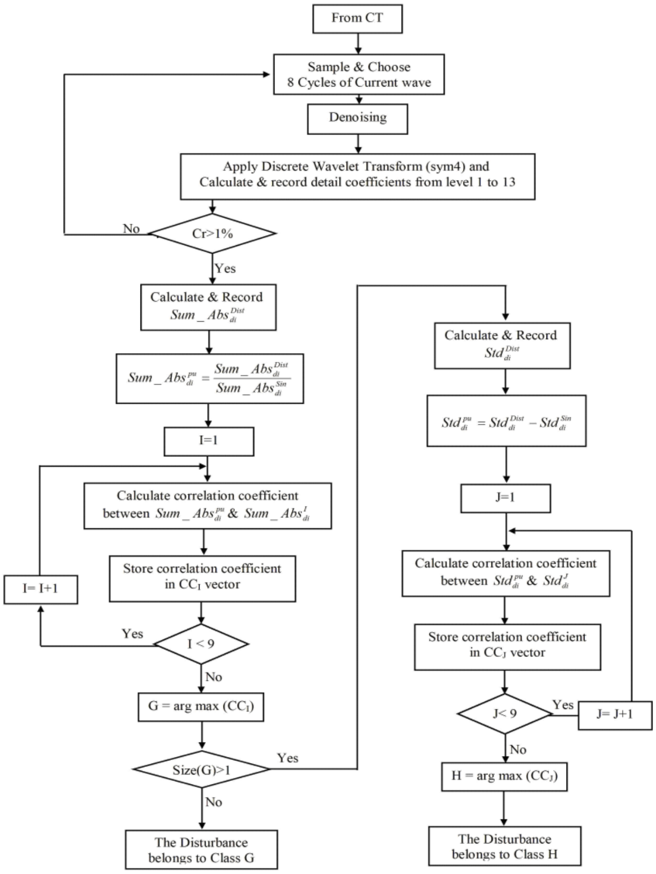

Fig. 14. The flowchart of the proposed algorithm

III. RESULTS

This section presents the simulation results of applying the correlation coefficient for recognizing and classifying PQ event types. The proposed algorithm was run in the MATLAB software. The signal randomly sampled out of 60 signals of each disturbance type is used to test the method accuracy. The combined discrete wavelet transform and correlation coefficient can detect and classify all 8 types for PQ disturbances as shown in Table I.

TABLE I
CORRELATION COEFFICIENTS VALUES FOR THE PROPOSED METHOD

Type of PQ disturbances	Representative vectors							
	DC offset	Flicker	Interrupt	Sag	Swell	Notching	Harmonic	Transient
DC offset	0.93	0.72	-0.42	-0.35	0.26	0.21	0.34	0.12
Flicker	0.67	0.96	-0.64	-0.79	0.81	-0.17	0.31	-0.27
Interrupt	-0.39	-0.69	0.95	0.77	-0.63	0.14	0.17	0.11
Sag	-0.43	-0.81	0.83	0.97	-0.74	0.27	-0.16	0.23
Swell	0.32	0.81	-0.79	-0.71	0.96	-0.32	0.12	-0.26
Notching	0.21	-0.14	0.19	0.25	-0.29	0.93	0.11	0.33
Harmonic	0.34	0.37	0.20	-0.13	0.09	0.07	0.89	0.43
Transient	0.08	-0.21	0.13	0.18	-0.16	0.29	0.38	0.98

TABLE II
CORRELATION COEFFICIENTS FOR THE PROPOSED METHOD WITH SNR=35DB

Type of PQ disturbances	Representative vectors							
	DC offset	Flicker	Interrupt	Sag	Swell	Notching	Harmonic	Transient
DC offset	0.91	0.73	-0.47	-0.39	0.27	0.24	0.31	0.19
Flicker	0.62	0.94	-0.62	-0.82	0.84	-0.23	0.39	-0.24
Interrupt	-0.39	-0.69	0.91	0.79	-0.60	0.17	0.21	0.14
Sag	-0.45	-0.85	0.83	0.93	-0.75	0.29	-0.19	0.27
Swell	0.34	0.82	-0.77	-0.73	0.92	-0.35	0.15	-0.28
Notching	0.28	-0.17	0.23	0.27	-0.31	0.88	0.14	0.34
Harmonic	0.30	0.41	0.25	-0.18	0.13	0.11	0.84	0.47
Transient	0.12	-0.26	0.17	0.22	-0.12	0.35	0.41	0.96

As can be seen in the test results, the proposed method can identify and classify the PQ disturbances correctly.

In order to demonstrate the robustness of the proposed method, the wavelet network was tested with different SNRs. The results with SNR=35 db are shown in Table II.

The percentage of classification accuracy (CA) of the proposed method are presented in Table III where the CA is defined as

$$\text{Classification accuracy (\%)} = \text{CA} = \frac{N_{correctly\ classified\ events}}{N_{total\ number\ of\ disturbances}} \quad (15)$$

Table III
Classification accuracy rate of the proposed algorithm

	PQ events	$N_{\text{disturbances}}$	$N_{\text{correctly identified}}$	CA (%)
1	DC offset	60	60	100%
2	Flicker	60	59	96.67%
3	Interrupt	60	59	98.33%
4	Sag	60	59	98.33%
5	Swell	60	59	98.33%
6	Notching	60	58	96.67%
7	Harmonic	60	60	100%
8	Transient	60	59	96.67%
9	Total	480	473	98.54%

Table IV shows the impact of SNR on the performance of the proposed algorithm and demonstrates the robustness of the approach with different levels of signal-to-noise ratios. This is due to the proper selection of the de-noising method (using the

SURE method and Eq. 2). Therefore, the results indicate that satisfactory performance is achieved under different disturbances and noise backgrounds.

Table IV.
The robustness of the proposed algorithm with different SNRs

SNR (db)	CA (%)
35db	98.33
30db	98.12
20db	97.91
10db	97.50

The proposed method is compared with existing PQ disturbance detection techniques published in recent years. The results are shown in Table V where the PQ disturbance techniques are compared using several criteria, such as the type of data used (synthetic or real world), the number of PQ disturbance types studied, and performance in terms of accuracy (both noiseless and noisy environment). Unfortunately, some literature has not provided the information needed to extract all the criteria.

The proposed algorithm has higher accuracy than all other methods except for ref. [33], [39], and [40]. However, the proposed algorithm is robust for different signal-to-noise ratios and capable to classify more PQ disturbance types. The utilization of a new de-noising approach (using the SURE method and Eq. 2) and an identification criterion (Eq. 14) to detect non-disturbance events to accelerate the solution procedure and prevent extra calculations is another advantage of the proposed method.

Table V.
The comparison of the proposed algorithm performance with other methods

Reference	Year	CA (Without noise)	CA (With noise 30db)	Number of disturbance types	Data
33	2018	100	-	6	Synthetic
34	2010	98.5	-	8	Synthetic
35	2018	96.71	-	7	Synthetic
36	2014	97.9	-	8	Synthetic
37	2009	95.75	-	7	Synthetic
38	2012	97.33	-	8	Synthetic
39	2010	98.75	90.61	8	Synthetic
40	2014	99.5	-	5	Synthetic and real time
Proposed method		98.54	98.12	8	Synthetic

IV. CONCLUSION

A new method for PQ disturbance recognition and classification is introduced in the paper. The proposed algorithm is based on the discrete wavelet transform and correlation coefficient.

This algorithm has advantages of discrete wavelet transform and correlation coefficient, but it does not have the disadvantages of artificial neural networks or neuro-fuzzy-based algorithms such as training and high dimension input matrices. It is not suffering from the disadvantages of Fourier transform-based approaches such as unsuitability for non-stationary signals as it does not track signal dynamics properly due to the limitation of fixed window width either. The existence of the criterion (Eq. 14) is another advantage of the method. This criterion prevents extra calculations, whenever the captured signal is not PQ disturbance. The proposed algorithm compared with the other methods has relatively higher accuracy and capability to classify more PQ disturbance types. The use of a new de-noising approach (the SURE method and Eq. 2) is another advantage of the proposed method. The simulation results at different noise conditions verify the effectiveness of the noise immunity of the proposed method.

V. REFERENCES

[1] J. Arrillaga, M. H. J. Bollen, and N. R.Watson, “Power quality following deregulation,” Proc. IEEE, vol. 88, no. 2, pp. 246–261, Feb. 2000.

[2] M. Karimi, H. Mokhtari, and M. R. Iravani, “Wavelet based on-line disturbance detection for power quality applications,” IEEE Trans. PowerDelivery, vol. 15, pp. 1212–1220, Oct. 2000.

[3] S. Santoso, W. M. Grady, E. J. Powers, J. Lamoree, and S. C. Bhatt, “Characterization of distribution power quality events with Fourier and wavelet transforms,” IEEE Trans. Power Delivery, vol. 15, pp. 247– 254,Jan. 2000.

[4] W. Tong, X. Song, J. Lin, Z. Zhao “Detection and Classification of Power Quality Disturbances Based on Wavelet Packet Decomposition and Support Vector Machines,” ISCP 2006 proceedings, 2006.

[5] P. K. Ra, G. Karmakar, F. Y. S. Eddy, A. Krishnan, H. B. Gooi, “Dual Tree Complex Wavelet Transform based Detection of Power Quality Disturbances,” 2018 IEEE Innovative Smart Grid Technologies-Asia (ISGT Asia), Singapore, pp. 1177-1182, 2018.

[6] Mohammad Barghi Latran, Ahmet Teke, “A novel wavelet transform based voltage sag/swell detection algorithm,” International Journal of Electrical Power & Energy Systems, Vol. 71, pp. 131-139, October 2015.

[7] Adaptive threshold based on wavelet transform applied to the segmentation of single and combined power quality disturbances, Applied Soft Computing, Vol. 38, pp. 967-977, January 2016.

[8] F. R. Zaro and M. A. Abido, "Real-Time Detection and Classification for Voltage Events Based on Wavelet Transform," 2019 IEEE Jordan International Joint Conference on Electrical Engineering and Information Technology (JEEIT), Jordan, pp. 872-877, 2019.

[9] P. K. Dash, S. Mishra, M. M. A. Salama, and A. C. Liew, “Classification of power system disturbance using a fuzzy expert system and a Fourier linear combiner,” IEEE

Transaction on Power Delivery, vol. 15, pp. 472–477, Apr 2000.

[10] T. X. Zhu, S. K. Tso, K. L. Lo "Wavelet-Based Fuzzy Reasoning Approach to Power-Quality Disturbance Recognition," IEEE Transactions on Power Delivery, vol. 19, no. 4, October 2004.

[11] G. S. Hu, J. Xie, F. F. Zhu "Classification Of Power Quality Disturbances Using Wavelet And Fuzzy Support Vector Machines," IEEE Proceedings of the Fourth International Conference on Machine Learning and Cybernetics, Guangzhou, PP. 3981-3984, 18-21 August 2005.

[12] J. Chung, E. J. Powers, W. M. Grady, and S. C. Bhatt, "Power disturbance classifier using a rule-based method and wavelet packet-based hidden Markov model," IEEE Transactions on Power Delivery, vol. 17, pp.233–241, Jan. 2002.

[13] M. Kezunovic and I. Rikalo, "Detect and classify faults using neural nets," IEEE Comput. Appl. Power, vol. 9, no. 4, pp. 42–47, Oct. 1996.

[14] C. B. Khadse, M. A. Chaudhari, V. B. Borghate, "Conjugate gradient back-propagation based artificial neural network for real time power quality assessment," International Journal of Electrical Power & Energy Systems, Vol. 82, pp. 197-206, November 2016.

[15] M. Yilmaz, E. Kayabasi, M. Akbaba, "Determination of the effects of operating conditions on the output power of the inverter and the power quality using an artificial neural network," Engineering Science and Technology, an International Journal, Vol. 22, Issue 4, pp. 1068-1076, August 2019.

[16] L. Hua, W. Yuguo, Z. Wei "Power Quality Disturbances Detection and Classification Using Complex Wavelet Transformation and Artificial Neural Network," IEEE Proceedings of the 26th Chinese Control Conference, Zhangjiajie, Hunan, China, pp. 208-212, July 2007.

[17] R. W. A. Ibrahim, M. Morcos, "Artificial Intelligence and Advanced Mathematical Tools for Power Quality Applications: A Survey," IEEE Trans. Power Delivery, vol. 17, pp. 738–743, Apr. 2002.

[18] S. Santoso, E. J. Powers and W. M. Grady, "Power quality disturbance identification using wavelet transforms and artificial neural networks," in Proc. IEEE Int. Conf. Harmonics and Quality of Power, Las Vegas, NV, pp. 615–618, Oct. 16–18, 1996.

[19] S. Santoso, E. J. Powers, W. M. Grady, A. C. Parsons, "Power Quality Disturbance Waveform Recognition Using Wavelet-Based Neural Classifier- Part1: Theoretical Foundation," IEEE Transaction on Power Delivery, vol. 15, no. 1, pp. 222-228, 2000.

[20] S. Santoso, E. J. Powers, W. M. Grady, A. C. Parsons, "Power Quality Disturbance Waveform Recognition Using Wavelet-Based Neural Classifier- Part2: Application," IEEE Transaction on Power Delivery, vol. 15, no. 1, pp. 229-235, 2000.

[21] P. Kanirajan, V.Suresh Kumar, "Power quality disturbance detection and classification using wavelet and RBFNN," Applied Soft Computing, Vol. 35, pp. 470-481, October 2015.

[22] S. Sridhar, K. U. Rao and S. Jade, "Detection and classification of PQ disturbances in the supply to induction motor using wavelet transform and feedforward neural network," 2015 IEEE International Conference on Electrical, Computer and Communication Technologies (ICECCT), Coimbatore, pp. 1-5, 2015.

[23] S. Khokhar,A.A.M. Zin, A. P. Memon, A. S. Mokhtar, "A new optimal feature selection algorithm for classification of power quality disturbances using discrete wavelet transform and probabilistic neural network," Measurement, Vol. 95, pp. 246-259, January 2017.

[24] J. Huang, M. Negnevitsky, and D. T. Nguyen, "A neural-fuzzy classifier for recognition of power quality disturbances," IEEE Transactions on Power Delivery, vol. 17, pp. 609–616, Apr. 2002.

[25] A. Elmitwally, S. Farghal, M. Kandil, S. Abdelkar, M. Elketab, "Proposed Wavelet Neurofuzzy Combined System for Power Quality Violations Detection and Diagnosis," IEE proc. Transm. Distrib., vol. 148, no. 1, pp. 15-20, 2001.

[26] B. Kiruthiga, R. Narmatha Banu, D. Devaraj, Detection and classification of power quality disturbances or events by adaptive NFS classifier, Soft Computing, volume 24, pp.10351–10362, 2020.

[27] T. X. Zhu,S. K. Tso and K. L. Lo "wavelet-based fuzzy reasoning approach to power-quality disturbance recognition," IEEE Transactions on Power Delivery, vol. 19, no. 4, pp. 1928-1935, October 2004.

[28] M. B. I. Reaz, F. Choong, M. S. Sulaiman, F. M.Yasin and M. Kamada, "Expert System for Power Quality Disturbance Classifier," IEEE Transactions on power delivery, vol. 22, no. 3, pp. 1979-1988, July 2007.

[29] O. Sen, S. Zhengxiang, W. Jianhua, C. Degui, "Application of LVQ neural networks combined with genetic algorithm in power quality signals classification," Power System Technology, vol. 1, pp. 491-495, 13-17 Oct. 2002.

[30] M.A.S. Masoum, S. Jamali, N. Ghaffarzadeh, "Detection and classification of power quality disturbances using discrete wavelet transform and wavelet networks," Vol. 4, Issue 4, pp. 193 – 205, July 2010.

[31] R. Kapoor, R. Gupta, L.H. Son, S. Jha, R. Kumar, Detection of power quality event using histogram of oriented gradients and support vector machine, Measurement, Vol. 120, pp. 52-75, May 2018.

[32] K. Thirumala, M. S. Prasad, T. Jain and A. C. Umarikar, "Tunable-Q Wavelet Transform and Dual Multiclass SVM for Online Automatic Detection of Power Quality Disturbances," IEEE Transactions on Smart Grid, vol. 9, no. 4, pp. 3018-3028, July 2018.

[33] Ucar F, Alcin OF, Dandil B, Ata F. "Power quality event detection using a fast extreme learning machine," Energies, vol. 11, no. 1 pp.145, 2018.

[34] Hooshmand R, Enshaee A. "Detection and classification of single and combined power quality disturbances using fuzzy systems oriented by particle swarm optimization algorithm". Electric Power System Research, vol. 80, no. 12, pp. 1552-1561, 2010.

[35] Muthusamy TA, Ramanathan N. "An expert system based on least mean square and neural network for classification of power system disturbances," International Journal on Future Revolution in Computer Science & Communication Engineering, vol.1, pp.308-313, 2018.

[36] Biswal B, Biswal M, Mishra S, Jalaja R. "Automatic classification of power quality events using balanced neural tree," IEEE Transactions on Industrial Electronics, vol. 61, no. 1, pp.521-530, 2014.

[37] Biswal B, Dash PK, Panigrahi BK. "Non-stationary power signal processing for pattern recognition using

HS-transform," Applied Soft Computing, vol. 9, no. 1, pp.107-117, 2009.

[38] Ray PK, Mohanty SR, Kishor N, Catalão JP. "Optimal feature and decision tree-based classification of power quality disturbances in distributed generation systems," IEEE Transactions on Sustainable Energy, vol. 5, no. 1, pp.200-208, 2014.

[39] Meher SK, Pradhan AK. "Fuzzy classifiers for power quality events analysis," Electric Power Systems Research, vol. 80, no.1, pp.71-76, 2010.

[40] Babu PR, Dash PK, Swain SK, Sivanagaraju S. "A new fast discrete S-transform and decision tree for the classification and monitoring of power quality disturbance waveforms," International Transactions on Electrical Energy Systems, vol. 24, no. 9, pp.1279-1300, 2014.

[41] Sheibani M, Ketabi A, Nosratabadi M. "Optimal power quality meters placement with consideration of single line and meter loss contingencies," International Journal of Industrial Electronics, Control and Optimization, vol. 1, no. 2, pp. 81-89, September 2018.

[42] A. J. Hayter, Probability and Statistics, 2nd edition, CA, Wadsworth Group, 2002, p. 137.

[43] D.L. Donoho, "De-noising by soft-thresholding," IEEE, Trans. on Inf. Theory, vol. 41, no. 3, pp. 613-627, 1995.

[44] M. Misiti, Y. Misiti, G. Oppenheim, J. M. Poggi, "Wavelet Toolbox 4 for User's Guide," Copyright 1997–2007 By The Mathworks, Inc.

[45] C. S. Burrus, R. A. Gopinath, and H. Guo, Introduction to Wavelets and Wavelet Transform: A Primer. Englewood Cliffs, NJ: Prentice-Hall, 1998.

Navid Ghaffarzadeh is an associate professor in the Department of Electrical Engineering at Imam Khomeini International University, Qazvin, Iran. His main areas of research interest are smart grid, intelligent systems and optimization applications in power systems, power system protection, renewable energy, and power quality. He has over 100 technical publications and has written seven university books on power systems.

IECO

This page intentionally left blank.

International Journal of Industrial Electronics, Control and Optimization © 2021 IECO
Vol. 4, No. 1, pp. 59-65, Jan (2021)

RF Power Harvester Using a Broadband Monopole Antenna and a Quad-Band Rectifier

Nasim Mirzababaee[1], Fatemeh Geran[2†], and Shahram Mohanna[3]

[1] Faculty of Engineering Science and Research Branch, Islamic Azad University, Tehran, Iran.
[2] Faculty of Electrical Engineering, Shahid Rajaee Teacher Training University, Tehran, Iran.
[3] Department of Electrical and Computer Engineering, University of Sistan and Baluchestan, Zahedan, Iran

ABSTRACT

An RF energy harvester (rectenna) consists of a broadband monopole antenna and a quad-band rectifying circuit is designed to harvest EM wave energy in the frequency range of 1.412 GHz to 8.56 GHz, which covers GSM-1800, LTE-band, WiMax, Wi-Fi, and WLAN. The initial component of the rectenna is an antenna that includes a semi-circular radiating patch with 8 circular stubs and a semicircle ground plane. The simulation results show the antenna has −10 dB impedance bandwidth at 7.148 GHz (from 1.412 GHz to 8.56 GHz). The second part of the rectenna is a rectifier circuit with a quad-band matching network for RF to DC conversion. The rectifier benefits from a two-stage Dickson rectifier using Schottky diodes. The RF-DC conversion efficiency and output DC voltage are simulated, and the maximum output voltage of the rectifier is 7.2 V with the optimum load resistance of $R = 12\ k\Omega$ *and the peak conversion efficiency is 65.3%, when the input power of the rectifier is set -4 dBm at 1.71 GHz.*

Article Info

Keywords:
Broadband antenna, Quad-band Matching network, RF Energy Harvesting, Rectenna.

Article History:
Received 2020-06-05
Accepted 2020-08-20

I. INTRODUCTION

The technology of power transmission and energy harvesting from radio frequency electromagnetic waves, to supply power to wireless electronic devices, is of interest [1-2]. This kind of energy sources can be employed to power wireless sensors and networks [3-4]. Fig. 1 shows the components of an RF energy harvesting system (Rectenna) including the receiving antenna, matching network, RF to DC rectifier circuits, and a load [5].

The antenna can operate in one or more frequency bands with linear or circular polarization. The task of the antenna is to harvest the electromagnetic wave energy available in the environment. In the next step, the harvested wave is rectified. The matching network is a resonant circuit operating at the frequency band, and its purpose is to maximize the transmission power between the antenna and the RF to DC converter. The RF to DC converter comprises at least one rectifier circuit to transform the RF power to DC power. The output voltage of this circuit can be stored in a battery or used directly to power a load. The RF conversion efficiency of the receiver depends on the accuracy of the impedance matching between the antenna and the transducer and the power efficiency of the transducer. Also, the antenna bandwidth plays an important role on the efficiency of the system to harvest environmental RF energy.

[†] **Corresponding Author**: f.geran@sru.ac.ir
Tel: +98-2122970025,Fax: +98-2297006, University of Shahid Rajaee Teacher Training
Faculty of Electrical Engineering, Shahid Rajaee Teacher Training University

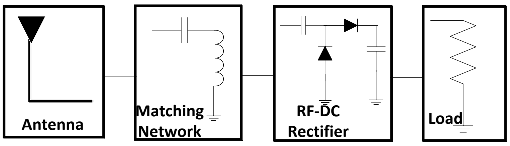

Fig 1. The block diagram of an energy harvesting system

In recent years, various broadband Rectenna (antenna integrated with rectifier circuit) have been introduced for the RF energy harvesting applications. Several broadband antennas are presented in [6-15], and different rectifiers are presented in [6-21]. In [6], the simulated impedance bandwidth of the antenna is 4.39 GHz (0.81 GHz-5.2 GHz). In [7], the impedance bandwidth of the antenna is 1.2 GHz (2.1 GHz-3.2 GHz), and in [10], the impedance bandwidth is 0.7 GHz (from 2 GHz to 2.7 GHz). Besides, several single band rectifiers [16], dual-band rectifiers [17,18], and multiband rectifiers [19-21] have been proposed employing different technologies. The advantages of the broadband antenna are more energy harvesting power than a single band [22], dual-band [23], or triple-band antennas [24] as well as energy harvesting from several bands.

This paper describes a new RF energy harvester (Rectenna) consists of a broadband monopole antenna and a quad-band rectifying circuit. The following sections describe the system. Part II describes the configuration and simulation results of the broadband antenna. Part III interprets the design and simulation results of the rectifier circuit and the matching network. Conclusions are presented in part IV.

II. BROADBAND ANTENNA STRUCTURE

The planar antenna is implemented on RT/duroid 5880 substrate with a thickness of 1.57 mm, having a dielectric constant of 2.2 and a loss tangent of 0.0009. It is designed employing HFSS software. The dimension of the dielectric substrate is 43×44 mm2. The main radiating part of the antenna is a semicircle patch. So this structure can be considered as a circular patch, and its dimensions can be calculated using the formulations given in [25].

The antenna design process is shown in Fig. 2. The initial structure consists of a semicircular patch on the substrate with a 50 Ω feed line and a rectangular ground plate with dimensions 14×44 mm^2 at the bottom of the substrate. In the first structure, the simulation result (Fig. 3) shows that the impedance bandwidth of the antenna is 4.6 GHz (from 1.4 GHz to 6 GHz). In the second structure, by loading the radiating patch with 8 circular stubs with radius $R_C = 2\,mm$, the impedance bandwidth of the antenna is increased to 6.988 GHz (from 1.412 GHz to 8.4 GHz) (Fig. 3). The circular stubs produce inductive reactance and remove the capacitive reactance in the radiating patch, which in turn creates the wideband characteristic.

As shown in Fig. 2, for Structure 3, the ground plane is amended to a semicircle to produce a better matching as well as multiple resonating bands. Hence, the current which flows in the semicircular ground plane, has a longer path in comparison with current in a rectangular ground plane, resulting more resonating bands with improving return loss. As a result, the bandwidth of the antenna increased to 7.148 GHz (from 1.412 GHz to 8.56 GHz). Fig. 3 compares the reflection coefficients for the structures described in Fig. 2. Fig. 4 illustrates the smith chart with and without the 8 circular stubs. It is clear that by adding more stubs, the inductive property of the antenna can be increased.

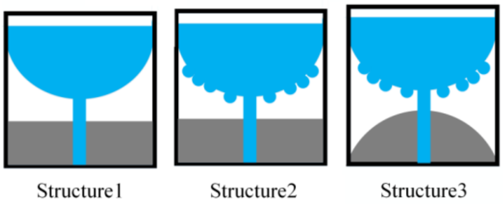

Fig 2. The shape of the antenna at different stages of design process

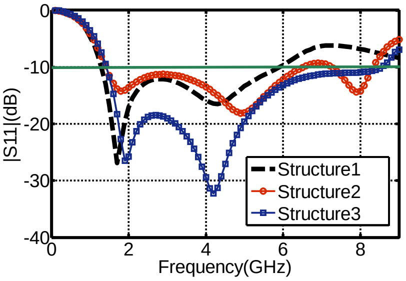

Fig 3. Influence of the rectangular ground, circular stubs, and semicircle ground on the reflection coefficient of the antenna.

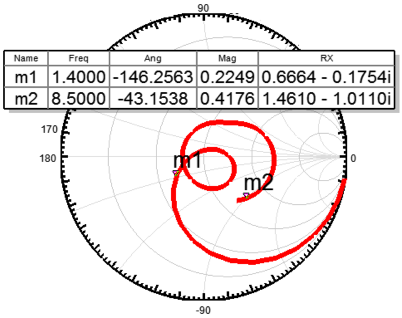

Name	Freq	Ang	Mag	RX
m1	1.4000	-146.2563	0.2249	0.6664 - 0.1754i
m2	8.5000	-43.1538	0.4176	1.4610 - 1.0110i

(a)

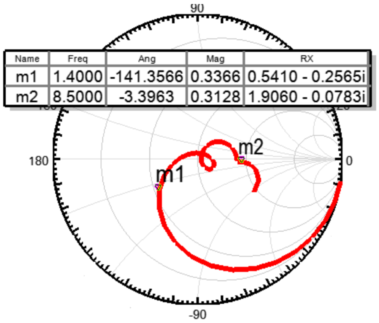

Name	Freq	Ang	Mag	RX
m1	1.4000	-141.3566	0.3366	0.5410 - 0.2565i
m2	8.5000	-3.3963	0.3128	1.9060 - 0.0783i

(b)

Fig 4. Smith chart (a) before adding subs (b) after adding stubs

Fig. 5 and Fig. 6 indicate the surface current distribution of the antenna on the rectangular ground plane and the semicircular ground plane at 1.9 GHz and 4.2 GHz, respectively. It can be observed that the intensity of the current flow in the semicircular ground is much higher than the rectangular ground at the desired frequency. Also, the dimension of the current path is indicated by the black arrows. This verifies that the length of the current path in a semicircular ground is much greater than a rectangular ground at selected frequencies. Therefore, this causes the new antenna to generate multiple resonance in different bands, which gives much higher bandwidth.

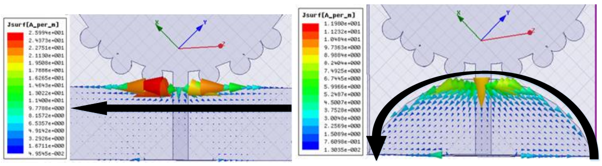

(a) (b)

Fig 5. Surface current distribution at 1.9 GHz, (a) on a rectangular ground plate (b) on a semicircular ground plane

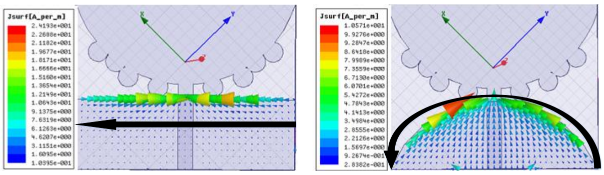

(a) (b)

Fig 6. Surface current distribution at 4.2 GHz, (a) on a rectangular ground plate (b) on a semicircular ground plane

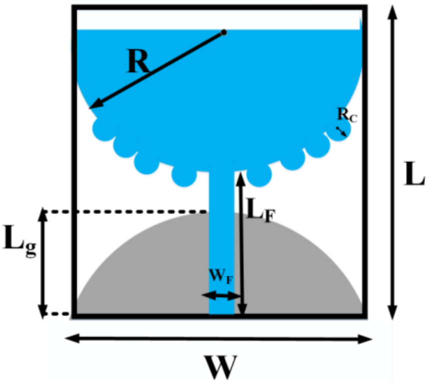

Fig 7. Configuration of the proposed antenna. Physical size of the antenna is equal to:

$L = 43 \quad mm,\ W = 44 \quad mm,\ R = 22 \quad mm,\ W_F = 3 \quad mm,$

$L_F = 18 \quad mm, \quad R_C = 2 \quad mm\ ,\ L_g = 15 \quad mm\ .$

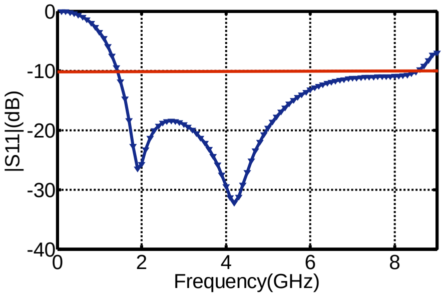

Fig 8. The simulated reflection coefficient ($|S_{11}|$) of the suggested antenna

Considering the effect of the ground plane and circular stubs of the behavior of the patch antenna, the final design of the antenna for the power harvesting system has been proposed. Fig. 7 demonstrates the finalized structure of the monopole antenna indicating the optimized values of the parameters and patch sizes. The simulated reflection coefficient ($|S_{11}|$) of the antenna is demonstrated in Fig. 8, signifying the antenna has −10 dB impedance bandwidth of 7.148 GHz (From 1.412 GHz to 8.56 GHz).

Fig. 9 illustrates the simulated far-field radiation patterns in the x–z plane and y-z plane at frequencies of 1.8, 2.1, 2.4, 3.6, and 5.8 GHz, respectively. The radiation pattern of the proposed antenna is Omni-directional in both the vertical and the azimuthal planes. Thus, this achieved characteristic makes the new antenna suitable for RF energy harvesting applications.

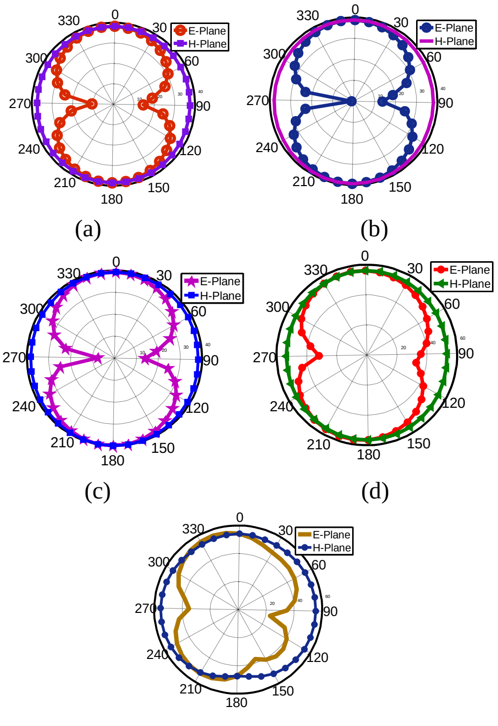

(a) (b) (c) (d) (e)

Fig. 9. Simulated radiation pattern of the proposed antenna for *x-z* plane and x-y plane at (a) 1.8, (b) 2.1, (c) 2.4 (d) 3.6 and (e) 5.8 GHz.

III. MULTI-BAND RECTIFIER STRUCTURE

The design and simulation of a quad-band rectifier are performed on an RT/duroid 5880 substrate with a thickness of 1.57 mm, a dielectric constant of 2.2, and a loss tangent of 0.0009. The design of the rectifier circuits is demonstrated in Fig. 10 and is performed by the Advanced Design System (ADS) software.

The RF signal is rectified by a two-stage Dickson rectifier using the SMS7630 Schottky diode [21]. This type of diode is chosen for the rectifier due to its low biasing voltage requirement for a weak input signal (forward bias voltage: 60–120 mV @ 0.1 mA). To simulate SMS-7630 diode, the SPICE model parameters are utilized from [26]. A resonant impedance matching network at four frequencies is designed to match the antenna and rectifier circuit and thus achieve the maximum output power. The matching network is described in Fig. 10, which include several inductive-capacitive resonator circuit. The proposed quad-band circuit is designed at frequencies 1.71, 2.4, 3.6, and 6.1 GHz. The resonant frequency of the proposed circuit is ω_r. The physical length (l) of the short-circuited stubs is calculated from the following formulas [21]:

$$\omega_r = \frac{1}{\sqrt{LC}} \tag{1}$$

$$\frac{\omega_r L}{2} = Z_0 \tan(\frac{\beta l}{2}) \tag{2}$$

In equation (1), the series capacitance and inductance are denoted by L and C. In equation (2), βl expresses the electrical length of the short-circuited stub and Z_0 represents the characteristic impedance of the transmission line (TL). The calculated sizes of TL components of the circuit are indicated in Fig. 10.

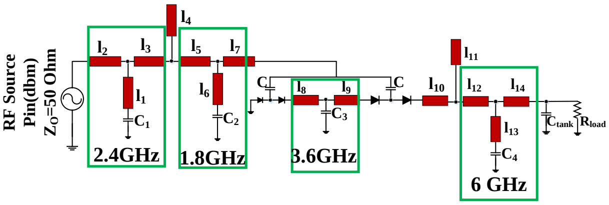

Fig 10. Configuration of the proposed quad-band rectifier with a matching network. Physical size of the antenna is equal to: $l_1 = 14.3$ mm, $l_2 = 3$ mm, $l_3 = 2.8$ mm, $l_4 = 19.8$ mm, $l_5 = 0.66$ mm, $l_6 = 23$ mm, $l_7 = 14.3$ mm $l_8 = 13.5$ mm, $l_9 = 13.5$ mm, $l_{10} = 5.8$ mm, $l_{11} = 10$ mm, $l_{12} = 5.8$ mm, $l_{13} = 4.25$ mm, $l_{14} = 1.3$ mm, W for all transmission lines is 2.24 mm.

The rectifier was simulated by the Large Signal S-Parameter (LSSP) simulator of ADS software. The simulated reflection coefficient versus frequency of the quad-band rectifier at the input power of 0 dBm is plotted in Fig. 11. The circuit resonates at frequencies of 1.71 GHz, 2.43 GHz, 3.68 GHz, and 6.1 GHz. To achieve the output DC voltage and RF-DC conversion efficiency diagrams in terms of various input power levels (from -30 dBm to +30 dBm), the rectifier is simulated using the Harmonic Balance (HB) simulator in ADS, which indicates that, the output voltage is obtained at the optimum load resistance of 12 kΩ.

Equation (3) is used to compute the RF-DC conversion efficiency [12]. As specified in equation (3), P_{input} is the incident RF power while P_0 is the output DC power. The output DC voltage and load resistance are denoted by $V_0(DC)$ and R_{Load}, respectively.

$$Efficiency\ (\%) = \frac{P_o(DC)}{P_{input}} \times 100 = \frac{V_O{}^2(DC)}{R_{Load}} \times \frac{1}{P_{input}} \times 100 \tag{3}$$

Load resistance is one of the most important parameters that play an essential role in calculating conversion efficiency. Fig. 12 describes RF-to-DC efficiency versus input power from -30 dBm to 30 dBm for various load resistors. The efficiency has been maximized at $R_L = 12\ k\Omega$. So, in the rectifier simulation, the optimum value of the resistor is set as $12\ k\Omega$. With increasing the input power from -30 dBm to 30 dBm, the conversion efficiency first increases and then decreases. Also, with the change of the load resistance in the range of input power from -15 dBm to 15 dBm, the RF to DC efficiency is more than 30%.

Fig. 13 describes RF to DC efficiency versus input power for various frequencies with the DC load $R_L = 12\ k\Omega$, representing that, the RF to DC conversion efficiency is 45% (at 1.71 GHz), 20%, (at 2.43 GHz), 4% (at 3.68 GHz), and 4% (at 6.1 GHz) at an input power of −10 dBm. The maximum value of conversion efficiency for the input power of -4 dBm at 1.71 GHz is 65.3%.

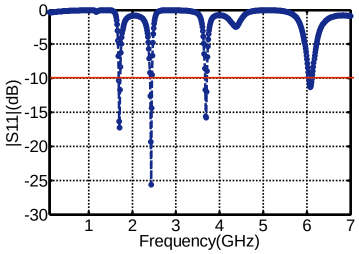

Fig 11. Simulated $|S_{11}|$ of the quad-band rectifier at $P_{in} = 0\ dBm$

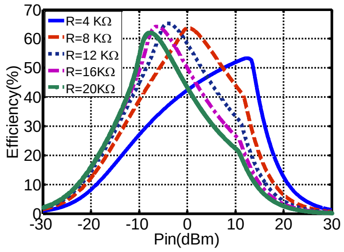

Fig 12. Simulated RF-to-DC conversion efficiency of the suggested rectifier versus input power with various resistive loads.

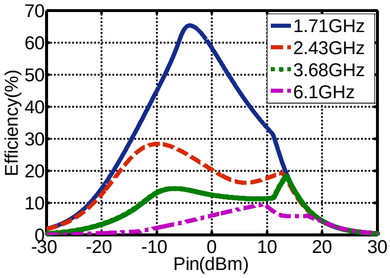

Fig 13. Simulated RF-to-DC conversion efficiency of the proposed rectifier versus input power at four frequencies with $R_L = 12 K\Omega$.

Fig. 14 (a) and (b) show the output DC voltage and the output power versus the input power for various frequencies, respectively. It is found that the maximum output voltage is equal to 7.2 V in $P_{in} = 11\ dBm$ and $R_L = 12\ k\Omega$. Also, it is observed that the maximum output power is corresponded to 4.38 mW in $R_L = 12\ k\Omega$.

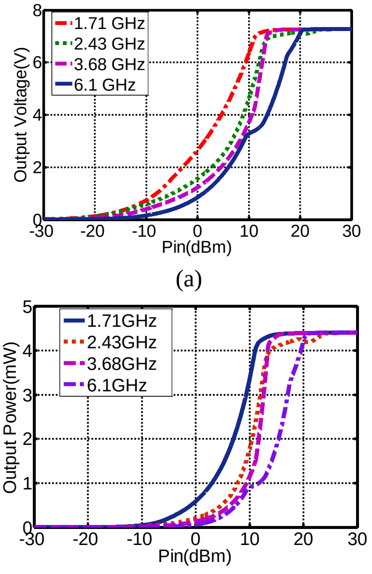

(a)

(b)

Fig 14. (a) Simulated output voltage versus input power of the rectifier (b) Simulated output power versus input power at four frequencies with the DC load $R_L = 12\ k\Omega$.

Table 1 compares the performance of the new multiband rectifier with the parameters indicated in the published papers reporting similar projects. For a fair comparison, the simulation results of this design has been compared with the simulation results reported in the referenced papers. As indicated, the maximum RF-DC efficiency of the new rectifier happens at input powers less than 0 dBm (−4 dBm), which is lower than the factor in other related designs. Moreover, the efficiency of the new rectifier at $P_{in} = -10\ dBm$ is much higher than the reported designs.

TABLE I

PERFORMANCE COMPARISON OF THE SUGGESTED MULTI-BAND RECTIFIER AND OTHER REPORTED RECTIFIERS

Ref.	**Frequency (GHz)**	**Maximum Efficiency (%)** **(Simulation results)**	P_{in} **for Max. Efficiency (dBm)** **(Simulation results)**	**Efficiency (%) at** $P_{in} = -10\ dBm$ **(Simulation results)**
[15]	1.8/2.45	70/58	10/9	30/13
[20]	0.95/1.835/2.45/ 2.62	45/30/44/25	10/10/10/1 0	26/19/14/12
[21]	1.3/1.7 2.4/3.6	40/41/26/ 15	7/4/13/7.5	17/15/2.5/3.5
[24]	0.9/1.8/2.4	9.032/30.5/8.7	20/18/22	0.2/3/0.1
This work	**1.71/2.4/3.6/6.1**	**65.3/21/13/10**	**-4/11/15/10**	**45/20/4/4**

IV. CONCLUSIONS

A rectenna having a new monopole antenna with improved bandwidth is designed and simulated. The system is equipped with a multi-band rectifier circuit to be used as an RF energy harvester. Firstly, a broadband monopole antenna with a semicircle ground plane is designed. The simulations verify that the proposed antenna has the highest bandwidth compared to the reported broadband antennas. Subsequently, a quad-band rectifier circuit has been designed using a two-stage Dickson rectifier and resonant matching network to transform the received AC signal from the antenna to a DC voltage required for powering wireless devices. The simulated results indicate that the rectenna has an RF to DC conversion efficiency of 65.3% for -4 dBm input power and a maximum DC output voltage of 7.2 V at 1.71 GHz with $R_L = 12\ k\Omega$ and $P_{in} = 11\ dBm$.

REFERENCES

[1] R. J. Vullers, R. Van Schaijk, H. J. Visser, J. Penders, and C. Van Hoof, “Energy harvesting for autonomous wireless sensor networks”, *IEEE Solid-State Circuits Magazine*, vol. 2, no. 2, pp. 29-38, 2010

[2] C. R. Valenta and G. D. Durgin, “Harvesting wireless power: Survey of energy-harvester conversion efficiency in far-field, wireless power transfer systems”, *IEEE Microwave Magazine*, vol. 15, no. 4, pp. 108-120, 2014.

[3] C. Fu, O. Elmazria, F. Sarry, T. Mahalingam, S. S. Yang, and K. Lee, “Development of wireless, battery free gyroscope based on one-port SAW delay line and double resonant antenna”, *Sensors and Actuators A: Physical*, vol. 220, pp. 270-280, 2014.

[4] E. O. Torres and G. A. Rincón-Mora, “Electrostatic energy-harvesting and battery-charging CMOS system prototype”, *IEEE Transactions on Circuits and Systems I: Regular Papers*, vol. 56, no. 9, pp. 1938-1948, 2008..

[5] Q. Awais, Y. Jin, H. T. Chattha, M. Jamil, H. Qiang, and B.

A. Khawaja, “A compact rectenna system with high conversion efficiency for wireless energy harvesting”, *IEEE Access*, vol. 6, pp. 35857-35866, 2018.

[6] S. Agrawal, M. S. Parihar, and P. Kondekar, “Broadband rectenna for radio frequency energy harvesting application”, *IETE Journal of Research*, vol. 64, no. 3, pp. 347-353, 2018.

[7] Y. Shi, Y. Fan, Y. Li, L. Yang, and M. Wang, “An efficient broadband slotted rectenna for wireless power transfer at LTE band”, *IEEE Transactions on Antennas and Propagation*, vol. 67, no. 2, pp. 814-822, 2018.

[8] O. M. Dardeer, H. A. Elsadek, and E. A. Abdallah, “Compact broadband Rectenna for harvesting RF energy in WLAN and WiMAX applications”, in *2019 International Conference on Innovative Trends in Computer Engineering (ITCE)*, 2019, pp. 292-296: IEEE.

[9] A. Collado and A. Georgiadis, “Conformal hybrid solar and electromagnetic (EM) energy harvesting rectenna”, *IEEE Transactions on Circuits and Systems I: Regular Papers*, vol. 60, no. 8, pp. 2225-2234, 2013.

[10] M.-J. Nie, X.-X. Yang, G.-N. Tan, and B. Han, “A compact 2.45-GHz broadband rectenna using grounded coplanar waveguide”, *IEEE antennas and wireless propagation letters*, vol. 14, pp. 986-989, 2015.

[11] Y. Shi, J. Jing, Y. Fan, L. Yang, Y. Li, and M. Wang, “A novel compact broadband rectenna for ambient RF energy harvesting”, *AEU-International Journal of Electronics and Communications*, vol. 95, pp. 264-270, 2018.

[12] C. Song, Y. Huang, J. Zhou, J. Zhang, S. Yuan, and P. Carter, “A high-efficiency broadband rectenna for ambient wireless energy harvesting”, *IEEE Transactions on Antennas and Propagation*, vol. 63, no. 8, pp. 3486-3495, 2015.

[13] M. M. Mansour and H. Kanaya, “Compact and broadband RF rectifier with 1.5 octave bandwidth based on a simple pair of L-section matching network”, *IEEE Microwave and Wireless Components Letters*, vol. 28, no. 4, pp. 335-337, 2018.

[14] H. S. Park and S. K. Hong, “Broadband RF-to-DC rectifier with uncomplicated matching network”, *IEEE Microwave and Wireless Components Letters*, 2019.

[15] H. Ozdemir and T. Nesimoglu, “Microwave energy harvesting by using a broadband fractal antenna and a dual-band rectifier”, in *2018 18th Mediterranean Microwave Symposium (MMS)*, pp. 279-282: IEEE.

[16] H. Sun, Y.-x. Guo, M. He, and Z. Zhong, “Design of a high-efficiency 2.45-GHz rectenna for low-input-power energy harvesting”, *IEEE Antennas and Wireless Propagation Letters*, vol. 11, pp. 929-932, 2012.

[17] L. Shen and X. Yang, “A novel rectifier circuit operating at dual-frequencies of 1.8 GHz and 2.4 GHz”, in 2013 *IEEE MTT-S International Microwave Workshop Series on RF and Wireless Technologies for Biomedical and Healthcare Applications (IMWS-BIO)*, 2013, pp. 1-3: IEEE.

[18] D.-K. Ho, I. Kharrat, V.-D. Ngo, T.-P. Vuong, Q.-C. Nguyen, and M.-T. Le, “Dual-band rectenna for ambient RF energy harvesting at GSM 900 MHz and 1800 MHz”, in *Sustainable Energy Technologies (ICSET), 2016 IEEE International Conference on*, 2016, pp. 306-310: IEEE.

[19] L. M. Borges *et al.*, “Design and evaluation of multi-band RF energy harvesting circuits and antennas for WSNs”, in *Telecommunications (ICT), 2014 21st International Conference on*, 2014, pp. 308-312: IEEE.

[20] T. Skaik, “A Quad-band rectifier design with improved matching bandwidth for RF energy harvesting applications”, in *Promising Electronic Technologies (ICPET), 2017 International Conference on*, 2017, pp. 82-86: IEEE.

[21] C.-Y. Hsu, S.-C. Lin, and Z.-M. Tsai, “Quad-band rectifier using resonant matching networks for enhanced harvesting capability”, *IEEE Microwave and Wireless Components Letters*, vol. 27, no. 7, pp. 669-671, 2017.

[22] A. M. Jie, M. F. Karim, L. Bin, F. Chin, and M. Ong, “A proximity-coupled circularly polarized slotted-circular patch antenna for RF energy harvesting applications”, in *Region 10 Conference (TENCON), 2016 IEEE*, 2016, pp. 2027-2030: IEEE.

[23] M. Aboualalaa, A. B. Abdel-Rahman, A. Allam, H. Elsadek, and R. K. Pokharel, “Design of a dual-band microstrip antenna with enhanced gain for energy harvesting applications”, *IEEE Antennas and Wireless Propagation Letters*, vol. 16, pp. 1622-1626, 2017.

[24] S. Datta, K. Kar, M. Pal, and R. Ghatak, “Fractal shaped antenna based tri-band energy harvester”, *Advanced Electromagnetics*, vol. 6, no. 4, pp. 22-26, 2017.

[25] C. A. Balanis, *Antenna Theory: Analysis and Design*, John wiley & sons, 2016.

[26] Skyworks, Datasheet, Surface Mount Mixer and Detector Schottky Diodes.

Nasim. Mirzababaee was born in Tehran, Iran in 1985. She received her B.Sc. degree in Electrical Engineering (Telecommunication) from Sajad University, Mashhad, Iran in 2006. She received her M.Sc. and Ph.D. degree in Electrical Engineering (Telecommunication) at Islamic Azad University, Science and Research Branch, Tehran, Iran in 2011 and 2020, respectively. Her research interests include Microstrip antenna, Microwave passive and active circuits.

Fatemeh Geran was born in Ghaemshar, Iran in 1977. She received her BSc degree in Electrical Engineering (Telecommunication) from Tehran University, Tehran, Iran in 1999. Also, she received her MSc and PhD degrees in Electrical Engineering (Telecommunication) from Tarbiat Modares University, Tehran, Iran, in 2003 and 2009, respectively. She is currently as an assistant professor in Faculty of Electrical Engineering at Shahid Rajaee Teacher Training University, Tehran, Iran. Her research interest fields are antenna, RF subsystems in microwave and mm-wave Bands and RF energy harvesting.

Shahram Mohanna received his PhD degree in Electronics Engineering from the University of Manchester in July 2006. Currently he works as associate professor at the Faculty of Electrical and Computer Engineering at the University of Sistan and Baluchestan. During 2012 to 2016, He worked at the University of Nottingham Malaysia (UNM) as Associate Professor. Shahram have awarded a postgraduate degree and has been recognized as “Fellow of the Higher Education Academy, UK (FHEA)” in 2005. It is 18 years now that Dr Mohanna have been working as an academic and researcher in several international universities including some Russel group universities dedicated his career for Engineering Educations with considerable undergraduate and postgraduate teaching experience in several subjects including fields and waves, electromagnetic propagation and antennas, electronic circuits, impedance and electromagnetic tomography, applied mathematics, image processing, signal and system, wireless sensors as well as high frequency electronics, at UG, PG and PhD Levels. Additionally, he supervised various BEng, MSc and PhD projects and dissertations. Having sensible administrative and research experience, Dr Mohanna can be recognized as multidisciplinary researcher, skilful in electromagnetic field waves and antennas and related physics and mathematics, Tomographic Imaging, ultrasonic, instrumentations and wireless sensors along with contributing to the discipline by delivering 18 articles in international conferences and publishing 26 papers in Indexed Journals.

IECO

This page intentionally left blank.

International Journal of Industrial Electronics, Control and Optimization © 2021 IECO
Vol. 4, No. 1, pp. 67-76, Jan (2021)

Dynamic Improvement of DC Microgrids with CPLs Using Virtual Inertia Concept

Mehran Jami[1, †], Qobad Shafiee[2], and Hassan Bevrani[3]

[1,2,3] Smart/Micro Grids Research Center, University of Kurdistan, Sanandaj, Iran

ABSTRACT

In this paper, a virtual inertia control strategy based on linear feedback is presented that improves dynamic behavior of islanded dc microgrids interfaced with constant power loads (CPLs). In order to solve the stability challenges caused by low inertia and CPLs, the proposed control scheme is composed of a virtual capacitor and a virtual conductance. It is implemented in the inner loop control, i.e. current loop control to be fast enough emulating inertia and damping concept. In addition, the droop characteristic is modeled by using the virtual resistance which adjusts the steady-state response of the system. In this study a multi-level structure is considered, which comprises the source level, interface converter level, and common load level. In addition, an accurate small-signal model is used to investigate the stability of dc MG interlaced with CPLs, and then, an acceptable range of inertia response parameters is determined by using the root locus analysis. Performance of the proposed control structure is demonstrated through numerical simulations.

Article Info

Keywords:

Constant power load, Dc microgrid, Dynamic response, Virtual capacitance, Virtual inertia.

Article History:

Received 2020-02-26
Accepted 2020-05-27

I. INTRODUCTION

Recently dc microgrids (MGs) have attracted more attention because of the increasing use of dc energy sources, energy storages, and loads in power systems. In these systems, challenges like reactive power flow, synchronization and power quality problems-which are challenge for ac systems, do not exist [1]. Fig. 1 shows a typical dc MG. Due to the probable and random nature of wind and solar resources, the bigger and more power imbalance is happened between the generation and consumption. This is a clear reason for reduction of MGs inertia in the presence of distributed generation sources [2]. Furthermore, if these resources are definite and constant, due to the lack of rotating energy and connection of these resources through the power electronic interface to the power system, the system inertia is reduced, which causes an increase in voltage fluctuations from the nominal value and decreases the security of the MGs. Obviously, the high amount of inertia increases the kinetic energy of the grid. This feature reduces the voltage fluctuations and increases the capability of the grid to compensate the energy imbalance that happened due to probable occurrences or load changes [3].

Several solutions are presented to increase the system inertia with high penetration of renewable energy in ac MGs [4]-[8]. Some of the control strategies are designed in such a way that power electronic converter emulates the synchronous machines behavior. The great advantage of power electronic converters is that the desired output power is generated by using proper control mechanism. These methods are based on simple derivative-proportional droop control rules [5]-[6] or more sophisticated control schemes which are called virtual synchronous generators (VSG) [7]-[9]. In VSGs, by using power electronic converter, fast-response energy storage and the special control mechanism, inertia for RESs is created. This strategy is also known as virtual inertia (VI). In some studies, VI is used to operate a grid connected inverter as a VSG [10], [11]. Droop control is well- known method to solve the low inertia issue by limiting the frequency and voltage changes within the permitted range. By comparison between

---

[†] **Corresponding Author**: m.jami@eng.uok.ac.ir
Tel: +98-9363949565, University of Kurdistan.
Department of Electrical and Computer Engineering, University of Kurdistan, Sanandaj, Iran

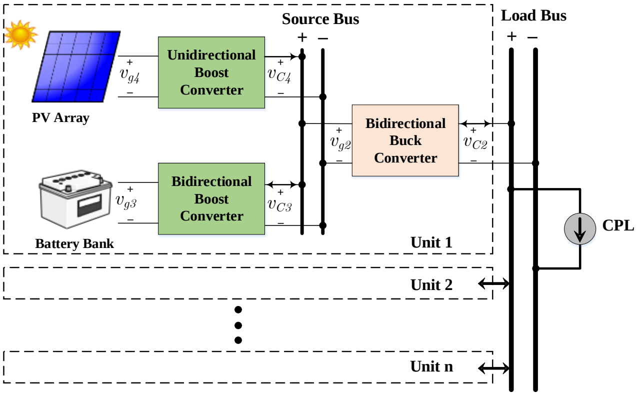

Fig. 1. Structure of a typical dc MG with CPL.

conventional droop control and VSG control, a generalized droop control is presented in [12]. In [13] and [14], a modified droop control method using fuzzy logic is designed based on the inertia injection, which injects adaptive virtual inertia instead of modeling the constant inertia. By selecting appropriate values of inertia and damping, proper performance of a VSG is guaranteed. In [15], a robust control method is used for fine-tuning the virtual parameters.

At present, researches on the VI control in dc MGs are hardly reported. The concept of VI control strategy is derived from the concept of VSG to regulate the dc bus voltage in a dc MG [16], [17]. In [16], a VI control strategy analogized with VSG is proposed to increase the inertia of the dc MG. However, integral feedback that used in this method not provides fast inertia in the first moment after disturbances. Furthermore, for droop-controlled converters in dc grids, the compromise between primary voltage regulation and damping coefficient needs to be considered. Increasing the inertia of photovoltaic (PV) systems through inertia emulation in autonomous MGs is presented in [18] and [19]. In these studies, for increasing inertia in a dc MG, VI control is generally employed in grid connected ac–dc type converters. In [20], adaptive VI control is proposed for the photovoltaic (PV) connected converter to eliminate the need of high-power storage for inertia emulation in a dc MG. However, utility of this method is limited by the availability of PV power and virtual damping coefficient has not been considered in the controller design procedure. In [21], the concept of a virtual dc machine is used to imitate the inertia specification of a dc machine in dc MGs through the control of the bidirectional dc–dc converters. The above mentioned VI control strategies, however, are inefficient in the presence of constant power loads (CPLs).

The research of CPLs in dc systems is essential to marine systems, automotive and aircraft applications [22]. From the source bus point of view, when a power electronic converter tightly regulates its output voltage with resistance load, it behaves like a CPL. The CPL has a positive instantaneous impedance but a negative incremental impedance. Hence, once the source bus voltage increases, the input current decreases and vice versa. This decreases the system's damping and makes the system more prone to oscillation [23]. Many solutions have been introduced for dc-dc power converters interfaced with CPL. One of the basic methods to overcome the CPL problem is by passive damping filters e.g., adding damping resistors in parallel or series with the inductor or capacitor of the filter [24]. Although this solution is simple and effective, it is costly and limited by physical constraints [22]. Another simpler and more effective way to tackle the CPL problem is using active damping. An active damping technique is implemented by control loops while emulating the passive elements. Due to the negative-impedance characteristics of CPLs and the nonlinearity of converters, nonlinear control strategies have been used to stabilize system, for instance, robust control [25], input-output linearization techniques [26], nonlinear control based on back stepping and nonlinear disturbance observer techniques [27]. Comparing with linear control methods, nonlinear ones are limited in practice because of a high requirement for the hardware configuration, more complication and extra cost [28]. In [29], the concept of smart resistor is proposed to dynamically stabilize CPLs at the point of load, wherein the equivalent load impedance can be made resistive instantaneously with energy storage units and high-bandwidth power converters. However, it is usually also not justifiable to install costly power conditioning modules only for stabilization purposes because they reduce the economic prospects and reliability of the whole system. In [30], a virtual resistance is created in series with the output of the converter. However, it leads to a significant drop in the output voltage at heavy loads resulting in poor voltage regulation. To overcome this drawback, the authors in [31] propose a virtual parallel resistive-inductive branch at the output of the source side converters feeding the CPLs. For improving the stability of the dc microgrid system, a virtual negative inductor [32] and virtual impedance [33] are constructed on the output of source-side converter. However, these methods suffer from some disadvantages:1) these methods only focus on solving the stability and voltage regulation problems while they are ineffective in improving the inertia response, and 2) when step changes or random fluctuations occur from the intermittent power resources and load power, low frequency oscillation appears, which results in lower dc voltage quality.

In this paper, the emulation of inertia and damping using derivative and proportional terms is proposed for islanded dc MGs with CPLs. This emulation is implemented in the inner current control loop. The fast and slow dynamics of the system have various effect on the voltage profile. The fast dynamics are directly related to the internal control loop i.e., voltage and current controllers. The slower transient dynamics are established by the virtual impedance control, droop mechanism and interactions between them. Therefore, by adding proportional and derivative signals of dc bus voltage to current controller with a particular mechanism, the rate of

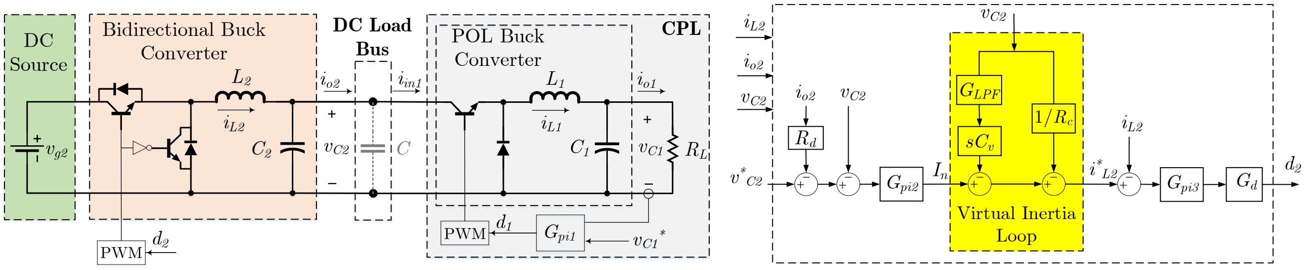

(a) (b)

Fig. 2. Simplified structure of a typical dc MG with CPL: (a) detailed power conversion circuit, (b) proposed control diagram for a bidirectional buck converter.

injection inertia to the system will be increased. The salient features of this paper are as follows:

- The proposed virtual control strategy is based on a linear feedback. It uses measurement of the output voltage and current in source-side converter in order to guarantee the stable operation and to enhance the damping of dc MGs with CPLs. Opposed to the existing virtual-impedance-based stabilizations in [31], [32] and [33], which are focused only on the stability improvement, the proposed controller improves dynamic response with decreasing rate of change of voltage (RoCoV).
- The proposed derivative term in the inner control loop decreases rate of change of dc bus voltage by using virtual capacitance that emulates inertia concept. Comparing with the existing virtual inertia control in [16] and [17], which implements in droop control loop, the proposed virtual inertia provides faster inertia response to decrease the RoCoV in the first moment after disturbances due to the derivative feedback is implemented in inner current loop.
- The proposed proportional term in the inner current control increases damping of dc bus voltage by using virtual conductance that emulates damping coefficient concept. Opposed to the existing virtual damping coefficient in [16] and [17], which increases the negative impact on voltage regulation performance, the proposed proportional term in the virtual inertia loop does not affect the steady state voltage.
- The small-signal stability analysis is used to study the system behavior under small distortion or load deviation at the presence of the proposed control loop. The proposed method is evaluated using the eigenvalue analysis and time-domain simulations.

The rest of this paper is divided into five sections. In Section II, the proposed control strategy is introduced based on the virtual inertia concept for the dc MGs. Section III presents a multistage structure of dc MGs with CPLs and describes an accurate small-signal model of dc MGs. The stability analysis of the system and parameters range selection in the presence of the proposed controller are described in the Section IV. Simulation studies are presented in Section V. Finally, some conclusions are given in final section.

II. PROPOSED VIRTUAL INERTIA CONTROL FOR DC MGS

In traditional power grids, the inertia indicates the ability of the system to prevent high frequency changes through injecting kinetic energy of rotating part in the occurrence of a fault. In this condition, the control system of synchronous generator (SG) will have enough time to compensate the active power. In SGs, the swing equation is a relationship that correlates input mechanical power, output electrical power, and the frequency. The imbalance equation, and the kinetic energy stored in the two poles of SG is given as [16]:

$$P_{set} - P_o - D_p\left(\omega - \omega_n\right) = J\omega\frac{d\omega}{dt} \tag{1}$$

where P_{set}, P_o, D_p, ω, ω_n and J are the reference active power, the output electrical power, the damping coefficient, the angular frequency, the nominal angular frequency, and the amount of inertia, respectively. When J and D_p increase (decrease), the rate of change of frequency (RoCoF) and frequency deviation are decreased (increased), respectively. In MGs, however, the damping coefficient, D_p, is a small value while the total inertia, J, changes mainly depending on the number of distributed generations (DGs) in the system [2]. For dc MGs, the amount of inertia is in fact the ability of the system to prevent high variation of the dc bus voltage due to turbulences. In order to study the virtual inertia concept, a simplified dc MG is shown in Fig. 2(a). By imitating relation (1), the balance current equation in the node connected to the dc load bus capacitor shown in Fig. 2(a) is obtained as follows:

$$i_{o2} - i_{in1} = C\frac{dv_{C2}}{dt} \tag{2}$$

where i_{o2}, i_{in1}, v_{C2}, and C are the injected current into the dc load bus from the source-side converter, the load current, the dc load bus voltage, and the dc load bus capacitor, respectively. Comparing (1) with (2) one can write that the dc link capacitor in a dc MG shows similar behavior as inertia in ac systems. When turbulence occurs in the load current, the dc link capacitor with rapid active power injection prevents the big changes in the dc link voltage. Thus, to increase the inertia in dc MGs, size of the dc link capacitor has to be increased. Accordingly, instead of increasing capacity of the dc link capacitor physically, its size can be increased virtually using a virtual capacitor created by a control loop.

Assume that the variables in (2) are written as the sum of steady-state variables and their small perturbations the corresponding small-signal equation can be expressed as follows

$$\Delta i_{o2} - \Delta i_{in1} = C\frac{d\Delta v_{C2}}{dt} \tag{3}$$

In such a case, the amount of injected current can be obtained as

$$\Delta i_{o2}^{*} = -\left(C_v \frac{d\Delta v_{C2}}{dt} + \frac{1}{R_c}\Delta v_{C2}\right) \tag{4}$$

$$i_{o2}^{*} - I_{o2} = -C_v \frac{d\Delta v_{C2}}{dt} - \frac{1}{R_c}\Delta v_{C2} \tag{5}$$

where i^{*}_{o2}, I_{o2}, C_v and $1/R_c$ are the output current reference, the nominal output current, the virtual capacitor and the virtual-conductance analogous to the damping factor D_p of SGs, respectively. The negative sign in (4) shows negative feedback. By substituting (4) into (3), we obtain

$$-\Delta i_{in1} = (C + C_v)\frac{d\Delta v_{C2}}{dt} + \left(\frac{1}{R_c}\right)\Delta v_{C2} \tag{6}$$

According to (6), increasing the virtual inertia and the virtual damping factor will result in decreasing the rate of change of voltage (RoCoV) and dc voltage deviation.

General scheme of the proposed virtual inertia loop is illustrated in Fig. 2(b), where it is implemented in the primary control level providing reference for the inner current loop. The inner control loop mechanism applied to the system consists of two modules: voltage controller and current controller with their designed set points. The droop control is widely used to reach proper load power sharing in dc MGs. The voltage and current controllers employ conventional proportional-integral controllers due to zero steady state error and easy adjustment. However, the pure differentiator of the virtual capacitance in the proposed method may bring undesired high frequency noises to the system. For avoiding this issue, a first-order low-pass filter (LPF) is constructed in series with the virtual capacitance feedback. Meanwhile, the PWM delay is expressed as a first-order transfer function that depends on the sampling time. The proposed control approach can easily be implemented to all types of dc-dc converters. Here, without loss of generality, a multi-level structure of dc MGs interfaced with bidirectional buck converter is utilized.

III. SMALL-SIGNAL MODELING OF DC MGS WITH CPLS

A. *Structure of dc MGs*

A typical structure of a dc MG is shown in Fig. 1 [23], [27], [33]. In this structure, two types of energy sources i.e., PV and battery are considered. The dc MG shown in Fig. 1 has a three-level configuration. In the first level, namely the source stage, in order to absorb the maximum available power, the interfacing converter is employed for PV. Meanwhile, the interfaced converter for battery is used to generate constant output voltage. The second level is consist of interfacing bidirectional converter which establishes the local output bus. Finally, the third level is a common load bus. CPLs are connected to the common load bus in this stage. Different voltage levels can be used in dc MGs [33]. The PV with rated output voltage of 55 V and battery with rated output voltage of 48 V are selected in the first stage, and the output voltage, i.e., the source bus voltage is fixed at 200 V. In the meantime, the output voltage of the second stage is selected as 100 V.

Due to the nominal voltage of each bus, different types of interface converters are selected. For PVs in the first stage, unidirectional boost converter is used as the interface. For battery in the first stage, bidirectional boost converter is selected to achieve both of the charging and discharging operations. For the interfacing converter in the second stage, bidirectional buck converter is selected. For CPL that connected at the common load bus, unidirectional buck converter is utilized. In order to study the performance of the proposed virtual inertia-based controller, a general model of the dc MG with CPLs must be derived.

B. *Small-Signal Model of dc MGs with CPLs*

In order to investigate the effectiveness of the proposed virtual inertia function, a precise and model of the aforementioned dc MG needs to be considered. As mentioned, different types of converters are used in each level. Here, without loss of generality, it is assumed that the source stage fixes its output voltage, and its dynamic is faster than the second stage consist of interfaced buck converter. Thus, dynamic of the first stage is not considered and the simplified dc MG scheme shown in Fig. 2(a) is studied. The detailed analysis of the system model is discussed below. Here, subtitle “1” is used for CPL unidirectional buck converter, and subtitle “2” is used for bidirectional buck converter between source bus and local load bus.

For the point-of-load (POL) converter, a unidirectional buck converter with a resistor as its load is selected as an example to represent the CPL. As suggested in [33], the closed-loop input impedance of the POL converter as follows

$$Z_{IN1}(s) = \left.\frac{\hat{v}_{C2}}{\hat{i}_{o2}}\right|_{\hat{v}_{C1}^{*}(s)=0} = \frac{R_L C_1 L_1 s^3 + L_1 s^2 + R_L\left(1 + V_{C2}k_{p1}\right)s + R_L V_{C2} k_{i1}}{R_L C_1 D_1^2 s^2 + \left(D_1^2 - k_{p1} D_1^2 V_{C2}\right)s - k_{i1} D_1^2 V_{C2}} \tag{7}$$

where C_1, L_1, R_L, V_{C2}, D_1, k_{p1} and k_{i1} are the capacitance, the inductance, the resistance load, the steady-state dc load voltage, the steady-state duty cycle, the proportional and integral terms

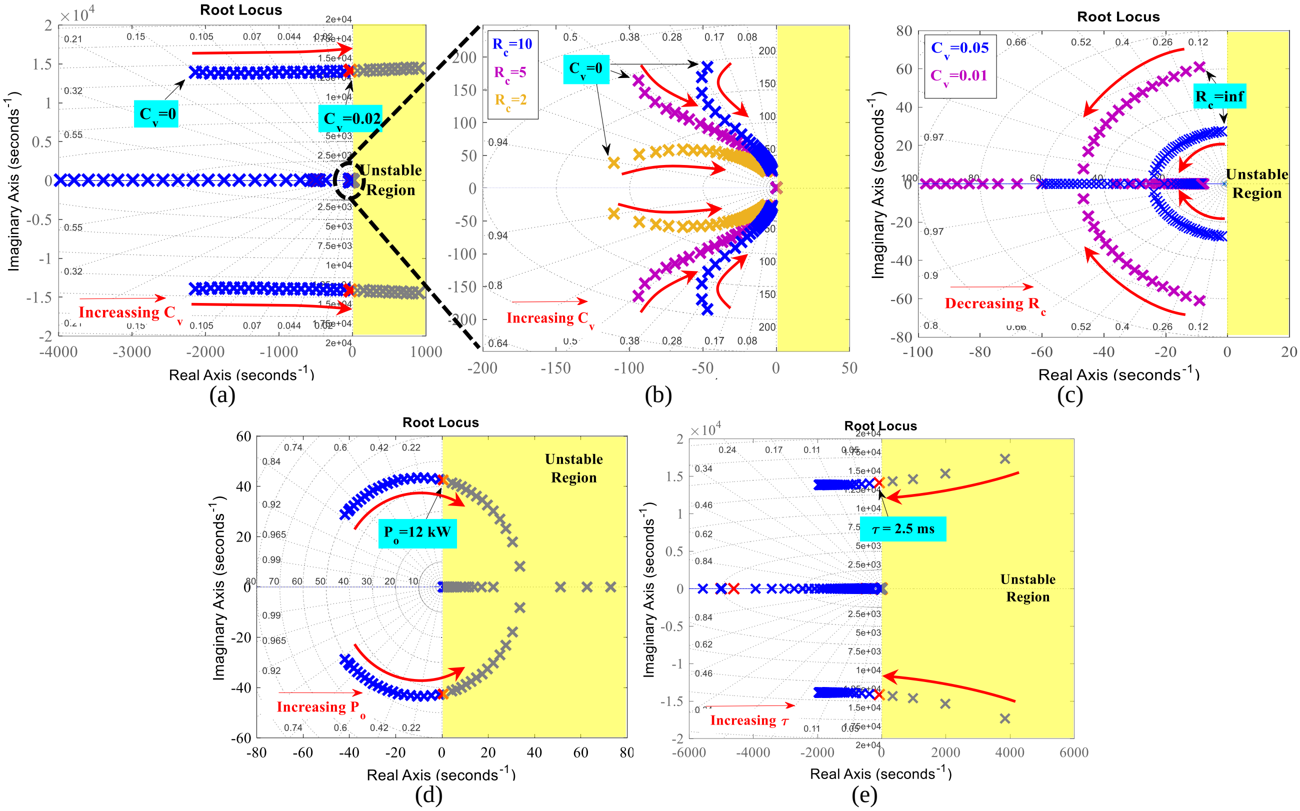

Fig.3. Trajectory of the system eigenvalues for the dc MG test system: (a) varying C_v, R_c and CPL=1kW, (b) a zoomed view of (a) in origin, (c) varying R_c while CPL=1 kW, (d) varying CPL while R_c=1 and C_v =0.01, (e) varying τ while R_c=5 and C_v =0.01 and CPL=1 kW.

of G_{pi1}. Equation (7) indicates a dynamic impedance that is more accurate comparing the pure negative resistance, i.e. $Z_{IN1}(s)= -R_L/D_1^2$.

For the bidirectional buck converters between the dc source (200 V) and dc local bus (100 V) if the switch turns on, it yields [34]

$$\begin{cases} L_2\dfrac{di_{L2}}{dt}=v_{g2}-v_{C2} \\ C_2\dfrac{dv_{C2}}{dt}=i_{L2}-i_{o2} \end{cases} \quad (8)$$

where v_{C2}, i_{L2}, and i_{o2} are the capacitor voltage, the inductor current and the output current, respectively. If the switch turns off, it yields

$$\begin{cases} L_2\dfrac{di_{L2}}{dt}=-v_{C2} \\ C_2\dfrac{dv_{C2}}{dt}=i_{L2}-i_{o2} \end{cases} \quad (9)$$

By applying averaging technique, the state-space equation is obtained as

$$\begin{cases} L_2\dfrac{di_{L2}}{dt}=-v_{C2}+d_2 v_{g2} \\ C_2\dfrac{dv_{C2}}{dt}=i_{L2}-i_{o2} \end{cases} \quad (10)$$

where d_2 is the duty cycle of the switch. From (10) and (7), the small-signal model is obtained as

$$\begin{bmatrix}\dfrac{d\hat{i}_{L2}}{dt}\\[2mm] \dfrac{d\hat{v}_{C2}}{dt}\end{bmatrix}=\begin{bmatrix}0 & -\dfrac{1}{L_2}\\[2mm] \dfrac{1}{C_2} & -\dfrac{1}{Z_{IN1}C_2}\end{bmatrix}\begin{bmatrix}\hat{i}_{L2}\\ \hat{v}_{C2}\end{bmatrix}+\begin{bmatrix}\dfrac{D_2}{L_2}\\ 0\end{bmatrix}\hat{v}_{g2}+\begin{bmatrix}\dfrac{V_{g2}}{L_2}\\ 0\end{bmatrix}\hat{d}_2+\begin{bmatrix}0\\ -\dfrac{1}{C_2}\end{bmatrix}\hat{i}_{o2} \quad (11)$$

where the steady-state values of variables represent with capital letter and the variables with “^” show the small-signal deviation. Let

$$A_2=\begin{bmatrix}0 & -1/L_2\\ 1/C_2 & -1/Z_{IN1}C_2\end{bmatrix}, B_{21}=\begin{bmatrix}D_2/L_2\\ 0\end{bmatrix}$$
$$B_{22}=\begin{bmatrix}V_{g2}/L_2\\ 0\end{bmatrix}, B_{23}=\begin{bmatrix}0\\ -1/C_2\end{bmatrix}, C_{22}=\begin{bmatrix}0 & 1\end{bmatrix}. \quad (12)$$

By taking the Laplace transform of (11) and combining the results, one can write that

$$\begin{aligned}\hat{v}_{C2}(s)&=\left[C_{22}(sI-A_2)^{-1}B_{21}\right]\hat{d}_2(s)\\ &+\left[C_{22}(sI-A_2)^{-1}B_{22}\right]\hat{v}_{g2}(s)\\ &+\left[C_{22}(sI-A_2)^{-1}B_{23}\right]\hat{i}_{o2}(s)\end{aligned} \quad (13)$$

In all dc-dc converters, the output voltage is a function of the control signal *d*, the turbulences caused by the voltage line of v_g and the load current of i_o. Therefore, the output voltage which equals to the capacitor voltage is obtained as a linear combination of these inputs as follows:

$$\hat{v}_{C2}(s)=G_{vd}\hat{d}_2(s)+G_{vg}\hat{v}_{g2}(s)-Z_{o2}\hat{i}_{o2}(s) \tag{14}$$

where

$$\begin{gathered} G_{vd}=\left[C_{22}(sI-A_2)^{-1}B_{21}\right], G_{vg}=\left[C_{22}(sI-A_2)^{-1}B_{22}\right] \\ Z_{o2}=-\left[C_{22}(sI-A_2)^{-1}B_{23}\right]. \end{gathered} \tag{15}$$

By applying the proposed control method in Fig. 2(a), the small-signal model is achieved

$$\begin{aligned} \hat{d}_2(s)=&\hat{v}^*_{C2}G_{pi2}G_{pi3}G_d-\hat{i}_{o2}G_{pi3}G_d\left[G_{pi2}R_d\right]-\hat{i}_{L2}G_{pi3}G_d \\ &-\hat{v}_{C2}G_{pi3}G_d\left[\frac{G_{pi2}R_d}{Z_{IN1}}+G_{pi2}+G_{LPF}C_v s+\frac{1}{R_c}\right] \end{aligned} \tag{16}$$

where, $G_{\mathrm{LPF}} = 1/(\tau s+1)$ and τ is the time constant of the LPF. Also, $G_{\mathrm{d}} = 1/(1.5T_{\mathrm{sPWM}}\, s+1)$ represents the unit pulse width modulation delay and T_{sPWM} is the sampling period. The closed-loop transfer function between the output voltage and the reference voltage is as follows:

$$T_{21}=\frac{\hat{v}_{C2}(s)}{\hat{v}^*_{C2}(s)}=\frac{G_{pi2}G_{pi3}G_{vd}}{1+T(s)} \tag{17}$$

where

$$\begin{aligned} &T(s)= \\ &G_{vd}G_{pi3}G_d\left[Cs+\frac{1}{Z_{IN1}}+G_{LPF}C_v s+\frac{1}{R_c}+G_{pi2}\left(1+\frac{R_d}{Z_{IN1}}\right)\right] \end{aligned} \tag{18}$$

Furthermore, the steady state value of the output voltage is obtained as follows:

$$v_{ss}=\frac{1}{1-R_d D_1^2/R_L}V^*_{C2} \tag{19}$$

The steady state value is only a function of the droop coefficient and load resistance. This value can improve the load division of several DG units into a dc MG by adjusting the steady state output voltage.

Finally, the relation between the output voltage of converter and the load current is obtained as

$$T_{22}=\frac{\hat{v}_{C2}(s)}{\hat{i}_{o2}(s)}=\frac{-Z_{o2}-G_{pi3}G_{vd}G_d\left(1+G_{pi2}R_d\right)}{1+T}. \tag{20}$$

IV. STABILITY ANALYSIS AND PARAMETER SELECTION

According to the precise small-signal model achieved in Section III-B, stability analysis can be studied by analyzing the eigenvalues of the transfer functions (17) and (20). The proposed controller parameters that affect stability are the virtual capacitor C_{v}, virtual resistance R_c and the low-pass filter time constant (τ). In order to obtain the system stable, the dominant poles of the small-signal model in (17) and (20) must be located in the left-half of the s-plane**.** The stability of the proposed controller with CPLs is investigated by varying the value of system parameters, as shown in Fig. 3. The trajectory of dominant poles with changing the virtual capacitance for various value of R_{c} and P_{o}=1kW is shown in Fig. 3(a). It can be seen that two poles move toward the unstable region. By selecting proper virtual capacitance, i.e., $C_{\mathrm{v}} < 0.02$, the system stability is guaranteed. With increasing C_{v}, the dominant poles move toward the imaginary axis and the system behaves like a 2nd order system (see Fig. 3(b)). The trajectory of dominant poles when changing the virtual resistance and P_{o}=1kW is shown in Fig. 3(c). By increasing $1/R_{\mathrm{c}}$ (decreasing R_{c}), the damping ratio of dominant poles increases and the response speed is decreased. Fig. 3(d) shows the unstable system trace when the CPL increases and C_{v}=0.01, R_{c} =1. It can be observed that increasing load power deteriorates the damping and causes instability. Fig. 3(e) shows the dominant poles of the system when the time constant of the LPF increases from 0 to 40 ms. It can be seen that two poles move toward the stable region. By selecting proper time constant, i.e., $\tau > 2.5$ ms, the unstable poles move to the left side s-plane, hence the system stability is guaranteed.

V. SIMULATION RESULTS

In order to validate the performance of the proposed control method, the dc MG test system (Fig. 1) is simulated in MATLAB/Simulink software. The parameters of the system are given in Table I.

A. Case I: Operation of dc MG with PV, Battery and CPL

For testing the proposed control strategy for the injection of virtual inertia, a typical dc MG including PV, battery and CPL is used. In order to track the maximum power from the PV system, a unidirectional boost converter is implemented between PV and dc MG. The bidirectional boost converter for the battery is employed to construct the local source bus with a voltage and current control loops. The source bus voltage is regulated at 200 V. By employing the bidirectional buck converter for interface converter, the load bus of the distributed generation unit is constructed. The load bus is regulated at the rated value of 100 V. The existence of the CPLs in dc MGs is the worst-case scenario from the stability perspective. Therefore, it is assumed that a CPL with power rate of 1kW is connected to the load bus. The PV output power, battery output power and CPL power are shown in Fig. 4, when the PV output power reference changes. In this case unit 1 only feeds the load. PV output power follows its reference value and with battery feed load power. When the output power of PV is more than the load power, the difference in their power is stored in battery (0.5 s < t < 0.6 s). Fig. 5 illustrates the PV output voltage, source bus voltage and load bus voltage when the PV output power reference changes. It can be seen that the load bus voltage is lower than its reference value due to the droop mechanism.

TABLE I
SYSTEM PARAMETERS OF THE DC MG

System	Parameters	Values	Parameters	Values
PV system	L_4	5mH	V_{g4}	55V
	C_4	0.5mF	V_{C4}	200V
Battery system	L_3	4mH	V_{g3}	48V
	C_3	0.8mF	V_{C3}	200V
Interface converter	L_2	1mH	V_{g2}	200V
	C_2	1mF	V_{C2}	100V
Load	L_1	10mH	Load Power	1 kW
	C_1	0.1mF	V_{C1}	50V

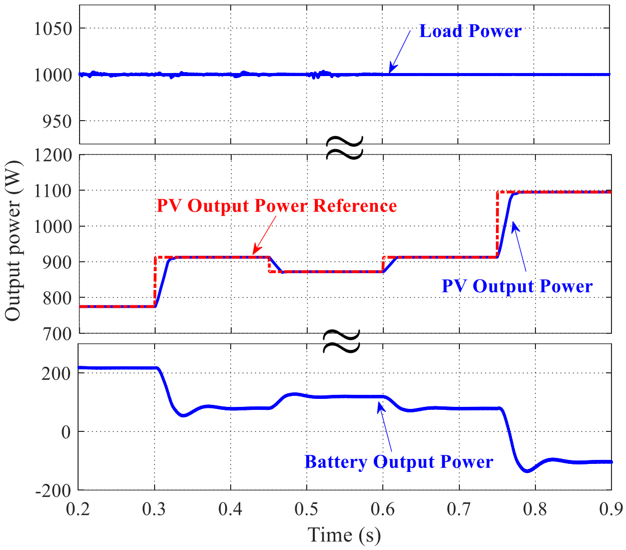

Fig. 4. Output power of different stage unit 1 when the PV output power reference changes.

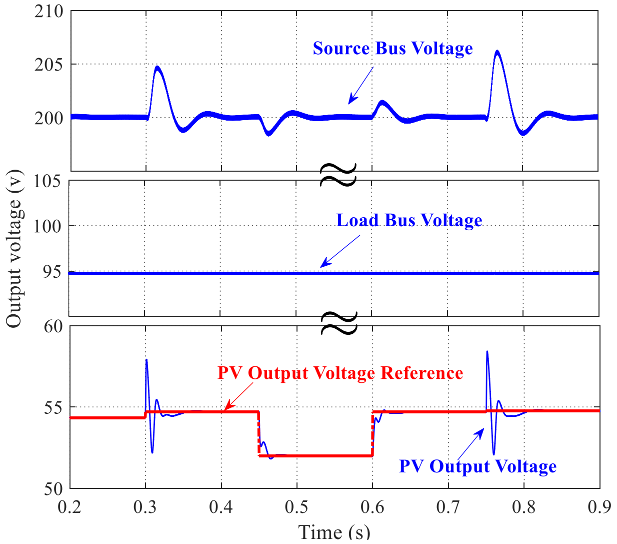

Fig. 5. Output voltage of different stage unit 1 when the PV output power reference changes.

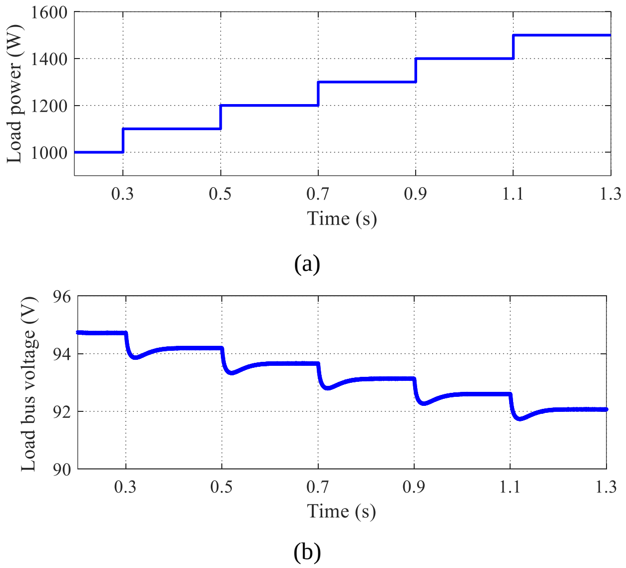

(a)

(b)

Fig. 6. Performance of the proposed VI solution under load power change: (a) load power step-up, (b) load bus voltage.

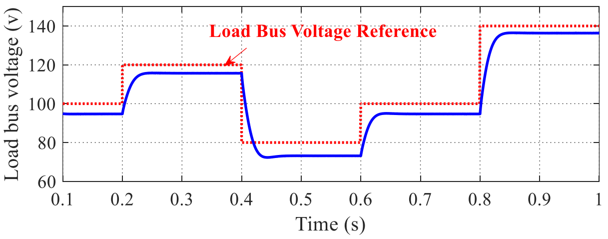

Fig. 7. Load bus voltage (blue solid line) following step changes in the voltage reference (red dashed line).

B. *Case II: Varying of the Reference Voltage and Load Power*

In this scenario, effectiveness of the proposed virtual inertia loop is studied under continuous load step-up change (see Fig. 6). During the test, the CPL varies from 1 to 1.5 kW by 0.1 kW load-step. As can be seen, by using the proposed virtual inertia, virtual damping and droop control, stable operation is guaranteed. In addition, the performance of the proposed controller under continuous voltage reference change is also studied. During the test, the reference voltage varies following the sequence of 100, 120, 80, 100, and 140 V. As it can be seen from Fig. 7, the stable operation is assured with the proposed VI.

C. *Case V: Impact of Virtual Parameters*

Fig. 8 shows the dynamic response of dc load bus voltage for +20% change in voltage reference from V^*_{C2} = 100 V to V^*_{C2} = 120 V at $t=0.4s$. Dc bus voltage for various values of C_v while other system parameters are constant is shown in Fig. 8(a). As the C_v increases, the dc load bus voltage would smoothly change and the RoCoV decreases. This means that

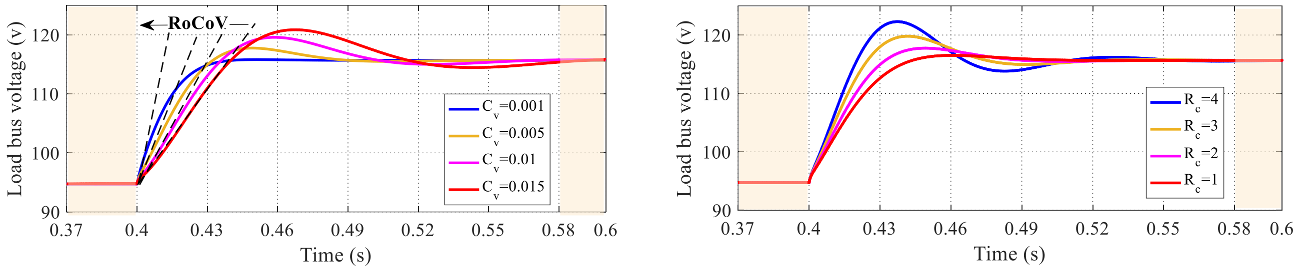

(a) (b)

Fig. 8. Dynamic responses of dc load bus voltage after a step change in voltage reference: (a) varying C_v for R_c=2 and CPL=1kW, (b) varying R_c for C_v =0.005 and CPL=1 kW.

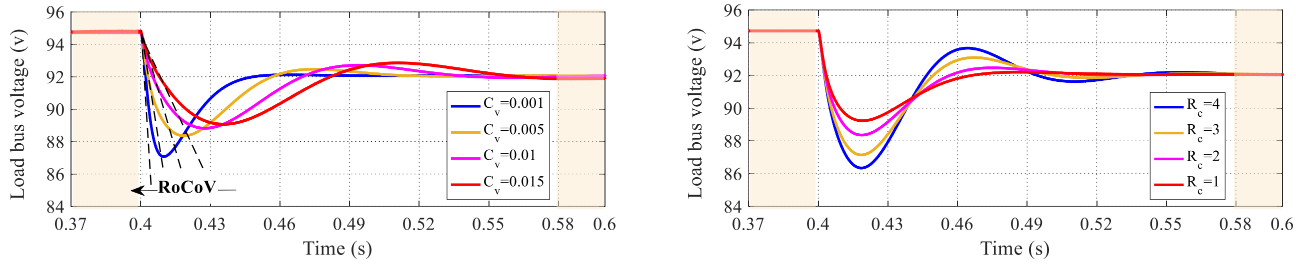

(a) (b)

Fig. 9. Dynamic responses of dc load bus voltage after a step change in load power: (a) varying C_v for R_c=2 and CPL=1kW, (b) varying R_c for C_v =0.005 and CPL=1 kW.

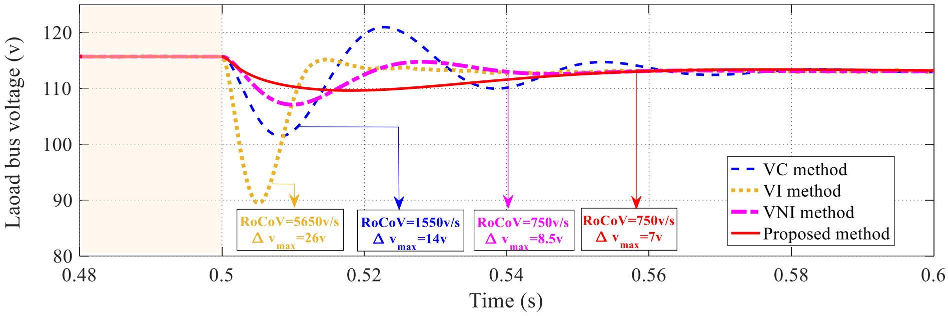

Fig. 10. Behavior of the dc bus voltage during a sudden load increase.

the inertia of the dc MG is increased. Thereby, the value of C_v denotes the synthetic inertia of the dc MG. However, by increasing C_v the system damping decreases and is prone to cause the DC bus voltage oscillation. This issue can be diminished by increasing damping coefficient ($1/R_c$) that effectively eliminates the low-frequency voltage oscillations. Fig. 8(b) shows dc bus voltage for various values of R_c while other system parameters are constant. By decreasing R_c (increasing $1/R_c$), the deviation of dc bus output voltage decreases. One can observe that virtual conductance $1/R_c$ can reduce the deviations of the dc bus output voltage and no influence on the RoCoV when voltage reference changes. Although virtual inertia response is more effective, it increases the settling time of the dc bus voltage. Consequently, a compromization between the settling time and the voltage deviation is needed for selecting the inertia and damping coefficients. The effectiveness of the proposed inertia response is tested under load power variation. Fig. 9 shows the dc load bus voltage for +50% step-change in load power from the initial value of P_o = 1 kW, to the final value of P_o = 1.5 kW at *t=0.4s*. In Fig. 9 (similar to Fig. 8), when C_v and/or $1/R_c$ increase (decrease), the RoCoV and voltage deviation will decrease (increase), respectively. Meanwhile, the parameters of inertia response have no influence on the steady-state performance.

The proposed method can be compared to previous works with implementing virtual parameter. Fig. 10 shows the comparison simulation results between the virtual capacitance (VC) method presented in [16], the virtual impedance (VI) method presented in [33], the virtual negative inductance (VNI) method presented in [32], and the proposed method for the same system parameters, loading conditions, and a 50% step change of load power at $t = 0.5s$. To have a better comparison, the same settling time is considered in the methods. It is shown that the proposed controller provides quite better transient response, smaller RoCoV, smaller undershoot and no overshoot in comparison with other control techniques.

VI. CONCLUSION

This paper presents a control strategy based on virtual inertia to enhance dynamic response and stability of dc MGs interfaced with CPLs. In the proposed method, the derivative feedback coefficient (C_v) mimics the virtual inertia of synchronous machines, while the proportional feedback gains $1/R_c$ and R_d mimics the damping factor of synchronous machines and the conventional droop mechanism, respectively. A multistage dc MG with interface buck converter is considered to verify the effectiveness of the proposed control method. Comprehensive small-signal model of source-side buck converter and load-side buck converter are derived, and parameters selection are discussed based on root-locus analysis. The simulation results indicate that the proportional-derivative control can provide damping and inertia properties. When virtual capacitance and virtual damping coefficient increase (decrease), the RoCoV and the dc voltage deviation are decreased (increased).

REFERENCES

[1] H. Bevrani, B. Francois, T. Ise, *Microgrid Dynamics and Control*, NJ, USA: Wiley, July 2017.

[2] H. Bevrani, M. Watanabe, Y. Mitani, *Power System Monitoring and Control*. Hoboken, NJ, USA: IEEE-Wiley, Jun. 2014.

[3] U. Tamrakar, D. Shrestha, M. Maharjan, B. P. Bhattarai, T. M. Hansen, R. Tonkoski, "Virtual inertia: Current trends and future directions," *Appl. Sci*., vol. 7, no. 7, pp. 654, Jun. 2017.

[4] S. Wei, Y. Zhou, and Y. Huang, "Synchronous Motor-Generator Pair to Enhance Small Signal and Transient Stability of Power System with High Penetration of Renewable Energy," *IEEE Access*, vol. 5, pp. 11505-11512, Jun. 2017.

[5] N. Soni, S. Doolla, M. C. Chandorkar, "Improvement of transient response in microgrids using virtual inertia," *IEEE Trans. Power Del.*, vol. 28, no. 3, pp. 1830-1838 Jul. 2013.

[6] E. Rakhshani, P. Rodriguez, "Inertia emulation in ac/dc interconnected power systems using derivative technique considering frequency measurement effects," *IEEE Trans. Power Syst*., vol. 32, no. 5, pp. 3338–3351, Sep. 2017.

[7] H. Bevrani, T. Ise, Y. Miura, "Virtual synchronous generators: A survey and new perspectives," *Int. J. Elect. Power Energy Syst.*, vol. 54, pp. 244-254, Jan. 2014.

[8] M. Ebrahimi, SA. Khajehoddin, MK. Ghartemani, "An improved damping method for virtual synchronous machines," *IEEE Trans. Sustainable Energy*, vol. 10, no. 3, pp. 1491-1500, Jul. 2019.

[9] A. Karimipouya, S. Karimi, H. Abdi, "Microgrid frequency control using the virtual inertia and ANFIS-based controller," *International Journal of Industrial Electronics, Control and Optimization*, vol. 2, no. 2, pp. 145-154, Apr. 2019.

[10] M. Guan, W. Pan, J. Zhang, Q. Hao, J. Cheng, X. Zheng, "Synchronous generator emulation control strategy for voltage source converter (VSC) stations," *IEEE Trans. Power Syst.*, vol. 30, no. 6, pp. 3093-3101, Nov. 2015.

[11] C. Li, J. Xu, C. Zhao, "A coherency-based equivalence method for MMC inverters using virtual synchronous generator control," *IEEE Trans. Power Del.*, vol. 31, no. 3, pp. 1369-1378, Jun. 2016.

[12] X. Meng, J. Liu, Z. Liu, "A generalized droop control for grid-supporting inverter based on comparison between traditional droop control and virtual synchronous generator control," *IEEE Trans. Power Electron*., pp. 1-1, Sep. 2018.

[13] Y.P. Kumar, R. Bhimasingu, "Fuzzy logic based adaptive virtual inertia in droop control operation of the microgrid for improved transient response," *Asia-Pacific Power and Energy Engineering Conf. (APPEEC)*, 2017, pp. 1-6.

[14] A. Karimi, Y. Jafarian, H. Bevrani, R. Mirzaei, "Frequency response improvement in microgrids: a fuzzy–based virtual synchronous generator approach," *International Journal of Industrial Electronics, Control and Optimization*, vol. 3, no. 2, pp.147-158, Apr. 2020.

[15] A. Fathi, Q. Shafiee, H. Bevrani, "Robust frequency control of microgrids using an extended virtual synchronous generator," *IEEE Trans. Power Syst.*, vol. 33, no. 6, pp. 6289-6297, Nov. 2018.

[16] W. Wu, Y. Chen, A. Luo, L. Zhou, X. Zhou, L. Yang, Y. Dong, J. M. Guerrero, "A virtual inertia control strategy for dc microgrids analogized with virtual synchronous machines," *IEEE Trans. Ind. Electron.*, vol. 64, no. 7, pp. 6005–6016, Jul. 2017.

[17] Z. Yi, X. Zhao, D. Shi, J. Duan, Y. Xiang, Z. Wang, "Accurate power sharing and synthetic inertia control for dc building microgrids with guaranteed performance," *IEEE Access*, vol. 7, no. 7, pp. 63698-708, May. 2019.

[18] W. Im, C. Wang, W. Liu, L. Liu, J. Kim, "Distributed virtual inertia based control of mutiple photovoltaic systems in autonomous microgrid," *IEEE/CAA J.Autom. Sinica*, vol. 4, no. 3, pp. 512-519, Jul. 2017.

[19] J. B. Zhu, C. D. Booth, G. P. Adam, A. J. Roscoe, C. G. Bright, "Inertia emulation control strategy for VSC-HVDC transmission systems," *IEEE Tran. Power Syst.*, vol. 28, no. 2, pp. 1277-1287, May. 2013.

[20] A. Hosseinipour, H. Hojabri, "Virtual inertia control of PV systems for dynamic performance and damping enhancement of dc microgrids with constant power loads," *IET Renew. Power Gener*., vol.12, no.4, pp.430-438, 2017.

[21] S. Samanta, J. P. Mishra, B. K. Roy, "Virtual dc machine: an inertia emulation and control technique for a bidirectional dc–dc converter in a dc microgrid," *IET Electr. Power Appl.*, vol. 12, no. 6, pp. 874-884, Mar. 2018.

[22] L. Herrera, W. Zhang, J. Wang, "Stability analysis and controller design of DC microgrids with constant power loads," *IEEE Trans. Smart Grid*, vol. 8, no. 2, pp. 881-888, Aug. 2015.

[23] M. Su, Z. Liu, Y. Sun, H. Han, X. Hou, "Stability analysis and stabilization methods of DC microgrid with multiple parallel-connected DC–DC converters loaded by CPLs," *IEEE Trans. Smart Grid*, vol. 9, no. 1, pp.132-142, Mar. 2016.

[24] M. Cespedes, X. Lei, S. Jian, "Constant-power load system stabilization by passive damping," *IEEE Trans. Power Electron.*, vol. 26, no. 7, pp. 1832-1836, Jul. 2011.

[25] J. Liu, W. Zhang, G. Rizzoni, "Robust stability analysis of DC microgrids with constant power loads," *IEEE Trans. Power Syst.*, vol. 33, no. 1, pp. 851-860, Apr. 2017.

[26] S. Arora, P. Balsara, D. Bhatia, “Input–Output Linearization of a Boost Converter With Mixed Load (Constant Voltage Load and Constant Power Load),” *IEEE Trans. Power Electron*., vol. 34, no. 1, pp. 815-825, Jan. 2019.

[27] Q. Xu,C. Zhang, C. Wen, P. Wang, “A novel composite nonlinear controller for stabilization of constant power load in DC microgrid,” *IEEE Trans. Smart Grid*, vol. 10, no. 1, pp. 752-761, Sep. 2017.

[28] M. Su, Z. Liu, Y. Sun, H. Han, X. Hou, “Stability analysis and stabilization methods of dc microgrid with multiple parallel-connected dc-dc converters loaded by CPLs,” *IEEE Trans. Smart Grid*, vol.9, no.1, pp.132-142, 2018.

[29] K. A. Potty, E. Bauer, H. Li, J. Wang, “Smart resistor: stabilization of dc microgrids containing constant power loads using high-bandwidth power converters and energy storage,” *IEEE Trans. Power Electron.*, vol. 35, no. 1, pp.957-967, Jan. 2020.

[30] M. Wu, D. D. C. Lu, “a novel stabilization method of LC input filter with constant power loads without load performance compromise in dc microgrids,” *IEEE Trans. Ind. Electron*., vol. 62, no. 7, pp. 4552-4562, July 2015.

[31] M. N. Hussain, R. Mishra, V. Agarwal, “A frequency-dependent virtual impedance for voltage-regulating converters feeding constant power loads in a dc microgrid", *IEEE Trans. Ind. Appl.*, vol. 54, no. 6, pp. 5630-5639, Nov./Dec. 2018.

[32] S. Liu, P. Su, L. Zhang, “A virtual negative inductor stabilizing strategy for dc microgrid with constant power loads,” *IEEE Access*, vol. 6, pp. 59728-59741, 2018.

[33] X. Lu, K. Sun, J.M. Guerrero, J.C. Vasquez, L. Huang, J. Wang, “Stability enhancement based on virtual impedance for dc microgrids with constant power loads,” *IEEE Trans. Smart Grid*, vol. *6*, no. 6, pp. 2770-2783, Jun. 2015.

[34] R. W. Erickson, D. Maksimovic, *Fundamentals of power electronics.* Springer Science & Business Media, 2007.

Mehran Jami was born in Marivan, Iran (1986). He received the B.Sc. degree from University of Tehran, Tehran, Iran, and the M.Sc. degree from Tarbiat Modares University (TMU), Tehran, Iran, both in Electrical Engineering in 2012 and 2014, respectively. He is now working toward the Ph.D. degree in the control of power systems at the University of Kurdistan, Iran. He is currently a member of the Smart/Micro Grids Research Center (SMGRC) at the University of Kurdistan, Sanandaj, Iran. His research interests include modeling, analysis, design, and control of power electronic devices.

Qobad Shafiee (S’13–M’15–SM’17) received PhD degree in electrical engineering from the Department of Energy Technology, Aalborg University (Denmark) in 2014. He is currently an Assistant Professor, Associate Director of International Relations, and the Program Co-Leader of the Smart/Micro Grids Research Center at the University of Kurdistan, Sanandaj, Iran, where he was a lecturer from 2007 to 2011. His current research interests include modeling, energy management, control of power electronics-based systems and microgrids, and model predictive and optimal control of modern power systems.

Hassan Bevrani (S’90 - M’04 - SM’08) received PhD degree in electrical engineering from Osaka University (Japan) in 2004. Currently, he is a full professor and the Program Leader of Smart/Micro Grids Research Center (SMGRC) at the University of Kurdistan (UOK). From 2016 to 2019 he was the UOK vice-chancellor for research and technology. His current research interests include smart grid operation and control, power systems stability and optimization, Microgrid dynamics and control, and Intelligent/robust control applications in power electric industry.

International Journal of Industrial Electronics, Control and Optimization © 2021 IECO
Vol. 4, No. 1, pp. 77-86, Jan (2021)

Design and Analysis of a New Topology of Rotor Magnets in Brushless DC Motors to Reduce Cogging Torque

Seyed Reza Mousavi-Aghdam[1,†], Amin Kholousi[2]

[1,2] Department of Electrical Engineering, University of Mohaghegh Ardabili, Ardabil, Iran

ABSTRACT

This paper presents a novel topology of permanent magnet brushless DC motors. Brushless DC motors usually experience torque ripple mainly caused by cogging torque. In the proposed motor, the whole structure of the rotor's permanent magnets has been changed so that the cogging torque is considerably mitigated. The philosophy behind this modification depends on the way of flux-path production in the rotor structure and it should be similar to the way of motor phases. An initial electromagnetic analysis is, first, carried out using the finite element method. A sensitivity analysis is, next, included to obtain the most important design parameters for the proposed structure. The different performance parameters of the motor are calculated and compared between the proposed structures and the conventional BLDC structures. The results reveal that the proposed motor has a considerably lower torque ripple retaining an average value of the produced torque. The proposed structure is also compared with an asymmetrical V-type structure and the results further show the effectiveness of the proposed structure.

Article Info

Keywords:
BLDC motor, Cogging torque, Finite element analysis, Magnetic topology

Article History:
Received 2020-06-06
Accepted 2020-08-15

I. INTRODUCTION

Nowadays brushless DC (permanent magnet) PM motors have been the main focus of many researchers because of their considerable advantages. In this type of AC motors, some PMs are used instead of field winding in the rotor structure and the phase windings are located on the stator. Generally, PM motor types including brushless DC motors, synchronous motors, and stepper motors are widely used in industrial/home applications and electric vehicles because of their high performance, low maintenance costs, low vibrations and acoustic noises. There are different types of magnet arrangements including inner and outer PMs that are located on the rotor side of the brushless motors. The internal PM rotor types have a proper mechanical structure in which the PMs are fixed in their positions when subjected to a centrifugal force at high speeds. Additionally, these types of brushless DC motors exhibit high torque density and high efficiency [1-3].

Because of the rotor magnetic configuration, brushless DC motors have inherently high cogging torque [4]. The cogging torque is produced by the interaction between the stator teeth and the rotor PM poles. Moreover, the cogging torque is an imposed undesirable torque that is usually called the torque without current and is a function of the rotor position. The periodicity of cogging torque depends on the number of the rotor poles and stator teeth. The main disadvantage of the cogging torque is the ripple exerted on the total torque. This causes not only vibration and noise but it may also influence the drive performance [5-6]. For some applications, the torque should be free of large ripples. These are the reasons why it has been important for the brushless DC motor designers to reduce cogging torque and then electromagnetic torque ripples are also undesired for the motor types that have no cogging torque [7]. Cogging torque may limit the use of different modern control techniques as well. Reference [8] explains a

---

[†] **Corresponding Author**: r.mousaviaghdam@uma.ac.ir
Tel: +98-4531505736, Fax: +98-4533512904, University of mohaghegh ardabili
Faculty of Engineering, University of Mohaghegh Ardabili, Ardabil, Iran

new method to overcome harmonic problems caused by cogging torque when field oriented control is used. However, these techniques can partly eliminate problems since cogging torque is inherently produced in BLDC motors.

There are many different methods in the literature aiming at reducing cogging torque. In some cases, a skewed structure is used in the PM designs [4]-[9], and in some others, an asymmetric PM design is the main contribution to reduce cogging torque [10-11]. Considering different rotor designs, one may conclude that there are two major categories in which the topology has been changed to reduce cogging torque. In the first category, only PM arrangements are changed [12-15] while in the second category, the shape of the PMs is modified [16-19]. The geometric optimization of the PMs is another issue that researchers are focused on. The optimization of the rotor pole width [20-25], and stator pole width [26-27], stator pole arc length [28] as well as the optimization of the rotor pole arc or stator tooth coefficients [29] are the main optimization challenges mitigating cogging torque. Many studies have been carried out on the rotor side, and this exhibits the importance of the rotor design in reducing of the cogging torque. Precise design of pole and tooth ratio [10], asymmetric design of rotor external diameter and the use of the modified pole shoe in the stator [30], reverse lamination [31], the creation of core gaps with different shapes, and an increase in the air gap length are the other recent attempts to reduce the cogging torque. In axial flux BLDC motors, the cogging torque may be differently reduced using some other techniques because different topology of the motor. There may be different layers in axial structure of BLDC motors to improve the cogging torque [32]. However, these techniques increase the 3D complexity of the BLDC motor design. Most of the mentioned methods help reduce peak-cogging torque. However, in most cases, this reduction of the cogging torque may not proportionally result in decreasing electromagnetic torque ripple.

This paper proposes a new rotor topology with a modified PM arrangement to considerably reduce cogging torque. In most cases, the reduction of the cogging torque may inappropriately influence some other characteristics, like average torque. This paper explains how the new design has no undesirable effect on the other motor parameters. The analysis is carried out using a finite element method (FEA) simulation, and the results are compared with that of a conventional brushless DC motor considering similar parameters. The comparison is additionally continued for a new structure like asymmetrical V-type configuration since this structure has already shown low cogging torque. The analysis results show that the proposed topology of brushless DC motors has considerably low cogging torque and, as a result, a low torque ripple while retaining the other main characteristics.

II. COGGING TORQUE IN BRUSHLESS DC MOTORS

The torque produced in the PM motors is the result of the interaction between PM magnetic flux and the flux created by the windings. The total magnetic flux of a motor can be represented by the winding and PM fluxes, i.e. φ_w, φ_{PM}, respectively, as follows [33]:

$$\varphi_t = \varphi_w + \varphi_{PM} = \frac{N_w i_w}{\Re_w + \Re_{ag} + \Re_{PM}} + \frac{\varphi_r \Re_{PM}}{\Re_w + \Re_{ag} + \Re_{PM}}$$

$$= \frac{N_w i_w}{\Re_t} + \frac{\varphi_r \Re_{PM}}{\Re_t} \qquad (1)$$

where N_w and i_w are the winding turn number and current, respectively. $\Re_w$, $\Re_{ag}$, and $\Re_{PM}$ represent the reluctance of the winding core, air gap, and PMs, respectively. Also, φ_r is the internal flux of the permanent magnets linking the winding. It must be mentioned that the Eq. (1) is provided for a specified position and the winding reluctance, for example, is dependent on the position. In other words, Eq. (1) is based on the fluxes summation that dynamically changes. The winding inductance can be written as follows:

$$L_s = \frac{N_w^2}{\Re_w + \Re_{ag} + \Re_{PM}} = \frac{N_w^2}{\Re_t} \qquad (2)$$

Hence, energy can be represented as follows:

$$W(i_w, \theta) = W_L + W_{PM} + W_w$$

$$= \tfrac{1}{2} L_s i_w^2 + \tfrac{1}{2} \Re_t \varphi_{ag}^2 + N_w i_w \varphi_{PM} \qquad (3)$$

where φ_{ag} is the air gap flux. Considering the energy equation, one can represent the produced torque as follows:

$$T = \left.\frac{\partial W_c}{\partial \theta}\right|_{i_w = cons.} = \tfrac{1}{2} i_w^2 \frac{dL_s}{d\theta} - \tfrac{1}{2} \varphi_{ag}^2 \frac{d\Re_t}{d\theta} + N_w i_w \frac{d\varphi_{PM}}{d\theta} \qquad (4)$$

The first and third terms in the torque equation will be zero if no current is considered in motor windings. The cogging torque can, thus, be calculated using the following equation that is the interaction between the PM flux and stator tooth reluctance:

$$T_{cog} = \tfrac{1}{2} \varphi_{ag}^2 \frac{d\Re_t}{d\theta} \qquad (5)$$

The mentioned cogging torque is inherently dictated by the motor geometric topology. The detailed explanations are given in the Sequent III.

III. DESCRIPTION OF THE PROPOSED TOPOLOGY

Fig. 1 shows the proposed structure for brushless DC motors. To get some topological insight into the new design, the conventional structure of a motor is also illustrated. As shown in Fig. 1(a), the proposed topology utilizes an internal PM structure with four magnetic poles. The other pole

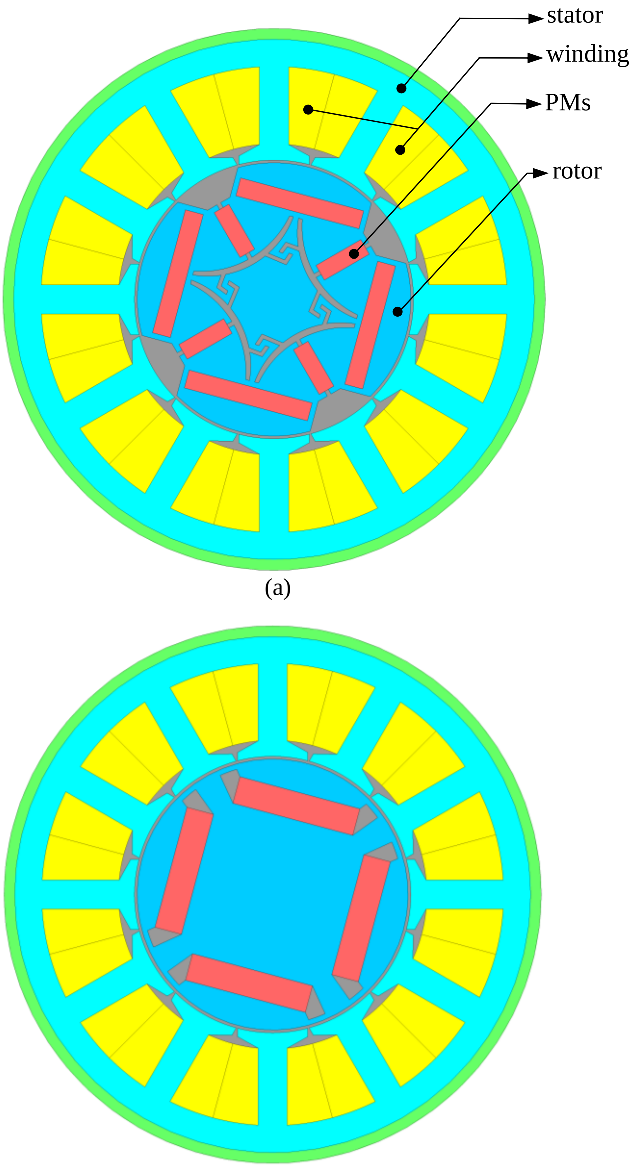

Fig. 1: (a) An illustration of proposed brushless DC motor along with its (b) conventional design.

combinations can, of course, be considered for the proposed topology. In the proposed topology, some different gaps are considered in the rotor core to conduct PM magnetic flux in a specified path. The PM dimension, shape, and orientation are also modified. The total size of the PM is not changed, and it is divided into some smaller PMs. These modifications are made to improve the flux path and maximize the performance of the PMs. To make the comparison more reasonable, it is assumed that the stator dimensions, winding structure, and total PM weight are the same in the proposed and conventional structures. Some other parameters are also assumed the same and summarized in Table I.

The proposed topology has different geometrical design parameters that may affect motor performance. To get an insight into the influences of these geometrical parameters, a sensitivity analysis is included in this section. Fig. 2 illustrates the proposed motor with its main geometric parameters that the topology is based on. Here, ml and mw are the length and width of the large magnets and sl and sw are the length and width of the small magnets, respectively. The point "O'" is the center of the arcs by which the guiding air gaps of the rotor magnetic flux are created. The large magnets have an angle shift of 90° from each other and the small magnets are located between them having an angle shift of 45° from the large magnets. On the internal sides of the rotor guiding air gaps, there are spiral air gaps by which the straight flowing of the magnetic flux is prevented. The final geometric parameter is the iron width, gw, which is considered to support the magnets and also to make the rotor body unified.

In the next step, the mentioned design parameters of the proposed BLDC motor are assessed using the sensitivity analysis. In this analysis, the dimensions of the magnets are modified in ten steps so that their total volume in each step remains constant. The parameter gw is also modified in five steps. The variation details are summarized in Table II.

Table I: Fixed parameters of the brushless DC motor

Parameter	**Value**
Nominal power, Voltage	350W, 80V
Rotor diameter	25.5mm
Stator external diameter	100mm
Stator internal diameter	26mm
Stack length	70mm
Air gap length	1mm
Stator tooth number	12
Pole number	4
Remanence of PMs	1.2T

The results of the sensitivity analysis for small magnet's dimensions of the proposed BLDC motor are illustrated in Fig. 3. As shown in Fig. 3 (a), when the width of the magnets is reduced and the length is, accordingly, increased, the phase produces more torque. However, for an appropriate length of the magnets, the torque change is negligible. The same can be seen for the cogging torque based on Fig. 3-(b). The results exhibit that the cogging torque is slightly low for wide magnets. In the next step, a similar analysis is carried out for the large magnets whose results are depicted in Fig. 4. As shown, the results for the large magnets are completely different in comparison to the small magnets. In this case, when the width of the magnets is reduced, the phase produces less torque. The same can be seen for the cogging torque in which higher values belong to the wider magnet. Comparing two sensitivity analyses, the results exhibit that the large magnet's dimensions have the most important effect on torque production. As a result, for a fixed volume of the large

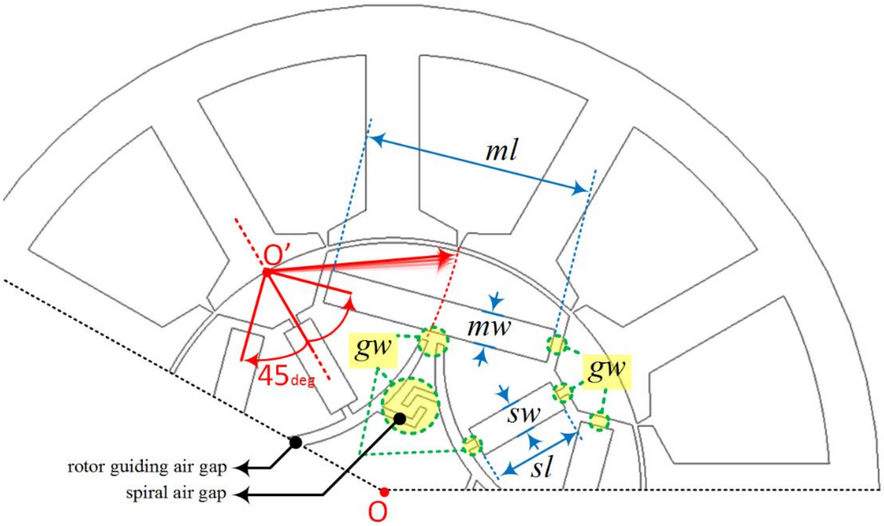

Fig. 2: Geometrical view of the proposed BLDC motor with main design parameters.

Table II: divisions of the main design parameters

Par.*/step	T1	T2	T3	T4	T5	T6	T7	T8	T9	T10	Vol.
sl	9.55	9.5	9.42	9.35	9.28	9.22	9.14	9.07	8.95	8.83	~30.3
sw	3.17	3.19	3.22	3.24	3.26	3.29	3.31	3.34	3.38	3.43	
ml	23.57	23.44	23.22	23.14	22.97	22.84	22.7	22.58	22.45	22.33	~81.7
mw	3.47	3.49	3.52	3.54	3.56	3.58	3.6	3.61	3.63	3.66	
gw	1.02	1.04	1.06	1.08	1.1	-	-	-	-	-	-

*All parameters are presented in mm

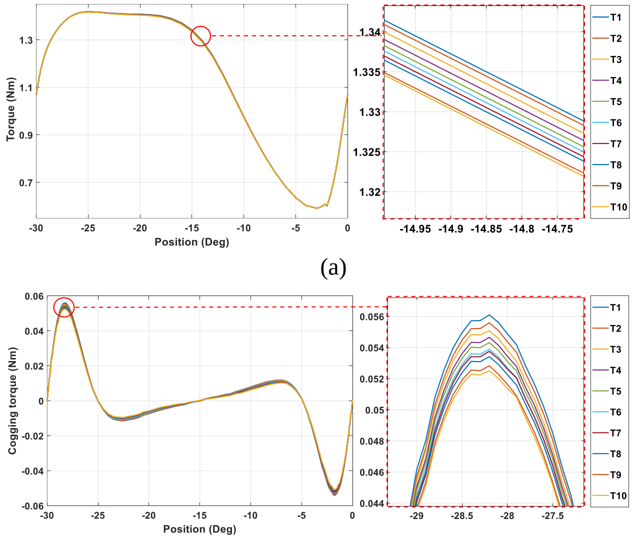

(a)

(b)

Fig. 3: (a) The produced torque and (b) cogging torque in terms of small magnet's dimensions.

magnets, widening of the magnets will lead to high torque. However, this results in high cogging torque as well. The geometric parameter, gw, is also considered in this analysis and the results are illustrated in Fig. 5 accordingly. The results show that widening the mentioned iron path will lead to low torque. On the other hand, there is always an optimum value for which the cogging torque is the lowest. Any increase/decrease from this optimum value will increase the cogging torque. The optimum value for this parameter in the proposed BLDC motor is about 1.05.

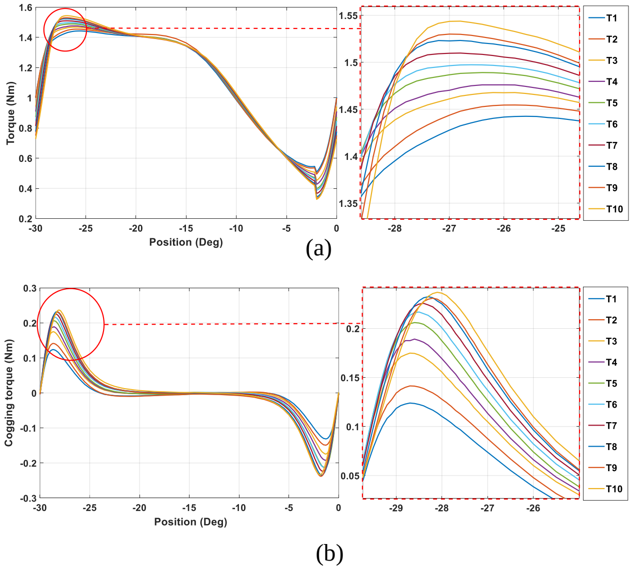

(a)

(b)

Fig. 4: (a) The produced torque and (b) cogging torque in terms of large magnet's dimensions.

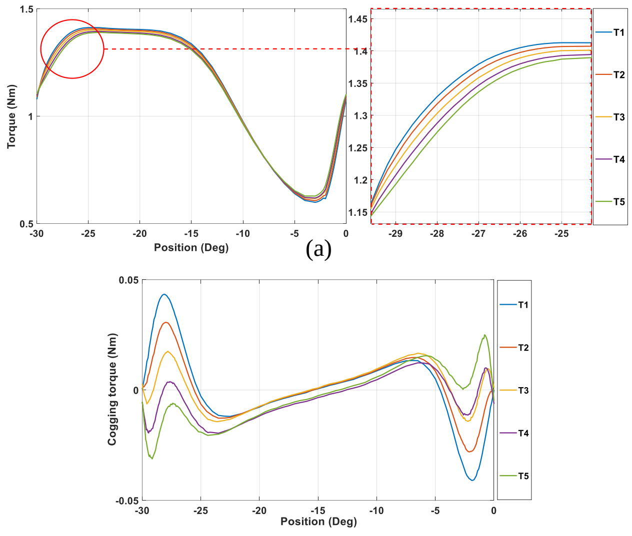

(a)

(b)

Fig. 5: (a) The produced torque and (b) cogging torque in terms of iron width *gw*.

IV. PERFORMANCE ANALYSIS AND COMPARISONS

A. Analysis and Comparison with the Conventional Design

This section provides the results of an analysis of performance parameters for the proposed BLDC design in comparison to the conventional one. Fig. 6 shows the flux lines of the rotor permanent magnets flowing through the rotor and stator. The philosophy behind the proposed magnet topology is so that it produces the magnetic flux as similar as possible to the corresponding phase flux when no magnets are considered in the rotor. Fig. 6 shows the state of the flux path in the proposed structure while comparing it with the conventional flux path.

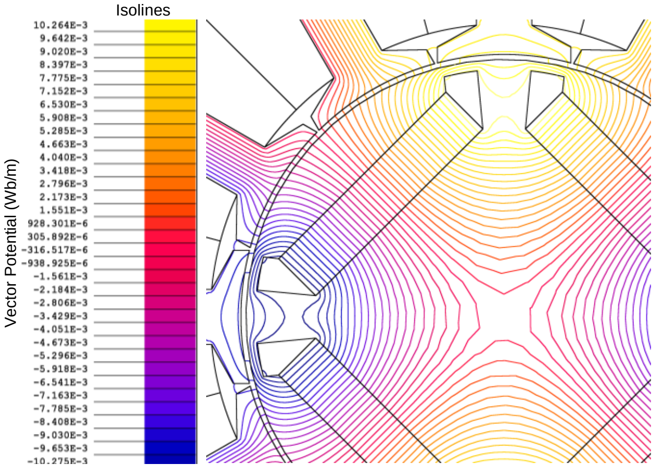

(a)

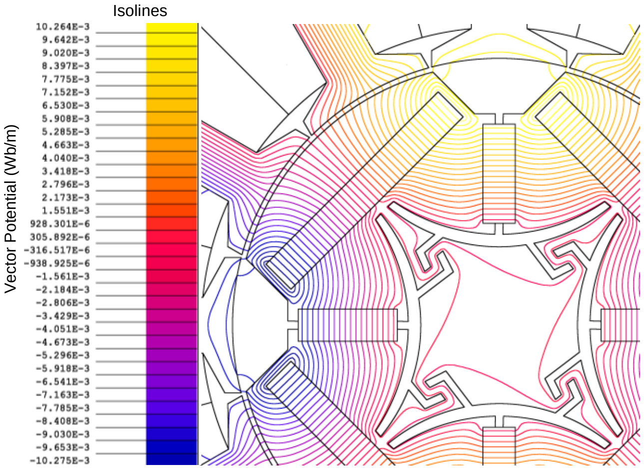

(b)

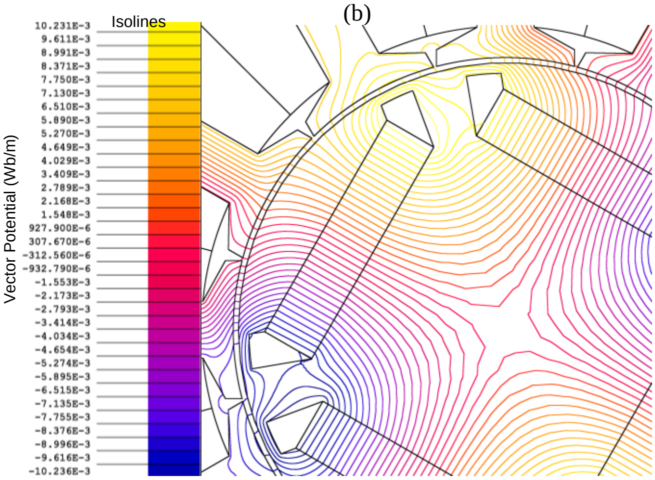

(c)

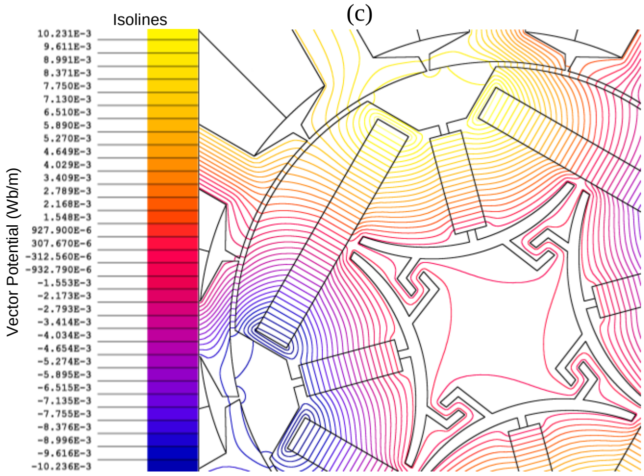

(d)

Fig. 6: The magnetic flux isolines of vector potentials for the proposed and conventional BLDC motors when PMs are aligned with two stator teeth (a), (b), and one stator tooth (c), (d).

Fig. 7 shows the air gap flux density. It is also shown that the maximum air gap flux density remains constant and this possibility may prevent unwanted saturation of the stator teeth. Any changes in the mentioned flux density will affect the motor back-emf. How the flux has been changing determines the back-emf waveform. Fig. 8 shows the produced back-emf for the proposed and initial structure for a typical rotor speed. The back-emf waveform may influence the motor commutation and hence the motor total torque ripple. To precisely understand the difference in torque production capability of the proposed and conventional structure, the cogging and total torque of both motors are analyzed in the subsequent subsection.

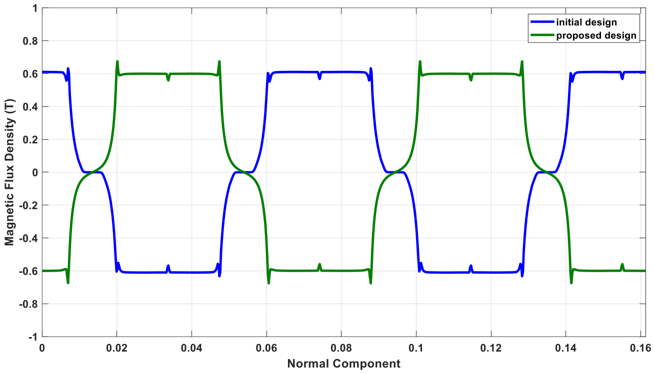

Fig. 7: The distribution of the air gap magnetic flux density in the proposed and conventional BLDC motors.

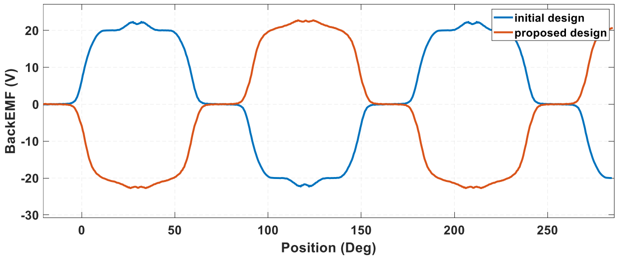

Fig. 8: A comparison of the produced back-emf for the proposed and initial structures.

The main contribution of the proposed BLDC motor is the reduction of cogging torque and hence electromagnetic torque. Fig. 9 compares the produced cogging torques of the proposed and conventional BLDC motors. As can be seen, the cogging torque for the proposed motor is considerably low and it has a small peak-to-peak value of 0.09Nm. This value for the conventional motor is about 0.29Nm and hence there has been a 70% reduction of in the cogging torque for the proposed BLDC motor. In this subsection, to assess the effectiveness of the proposed structure, a Fast Fourier Transform (FFT) analysis is also carried out to extract the cogging torque harmonics in both structures. The harmonic components of the cogging torque are illustrated in Fig. 10. The first to fourth harmonics play an important role in reducing cogging torque. Additionally, the proposed structure produces lower harmonics in comparison to the conventional one that may, in turn, result in a quiet operation and noise reduction in the proposed motor.

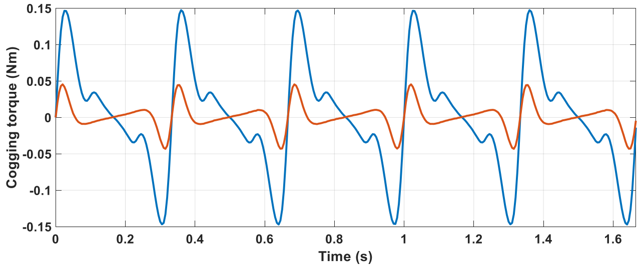

Fig. 9: A comparison of the cogging torque in the proposed and conventional BLDC motors.

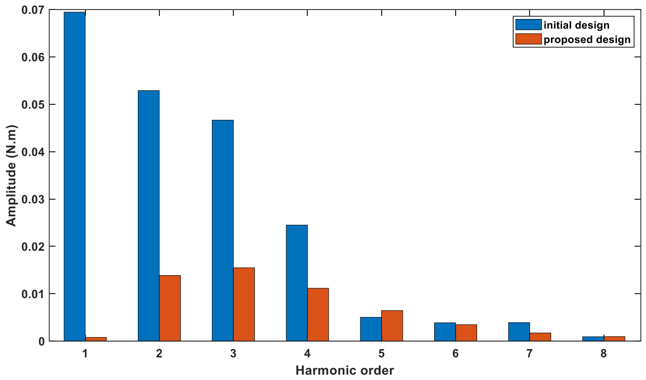

Fig. 10: The harmonic components of the cogging torque in the proposed and conventional motors.

There are different PM topologies that are used for BLDC motors to reduce the cogging torque, but most of them may cause unavoidably a reduction in the motor electromagnetic torque as well. Therefore, in any cogging torque improvement attempts, the electromagnetic torque retention must be considered. In this step, using a three-phase inverter, the proposed and conventional BLDC motors are energized, and the electromagnetic torque is obtained. The results are shown in Fig. 11 for a typical phase current of 4A. The average electromagnetic torque for the proposed and conventional motor is the same and is about 0.88Nm. As can be seen, the torque ripple is comparatively reduced in the proposed motor. The torque ripple for the proposed motor is 10.4% and for the conventional motor is 18%, which exhibits a 42% reduction for the proposed motor. The electromagnetic torque and ripple are verified for some other currents whose results are shown in Fig. 12. For lower values of the current, the average torque for both motors is the same (0.18Nm) but for high values of the current, electromagnetic torque of the proposed motor is slightly high (1.53Nm). Moreover, the torque ripple of the proposed motor for the lower value of the current is 9.1%, which is 60% lower than that of the conventional one. The torque ripple of the proposed motor for the higher values of the current is 13%, which is 27% lower than that of the conventional one. It should be mentioned that in the proposed

BLDC motor, the motor torque ripple is influenced by not only the cogging torque directly but also it is indirectly affected by the way of flux variation and back-emf waveforms. The latter may create torque ripple with the interaction between the back-emf and phase current. It should be mentioned that the iron loss pattern for the efficiency calculations is considered constant for both structures because of no considerable change in the magnetic field and iron volumes of the motors under discussion.

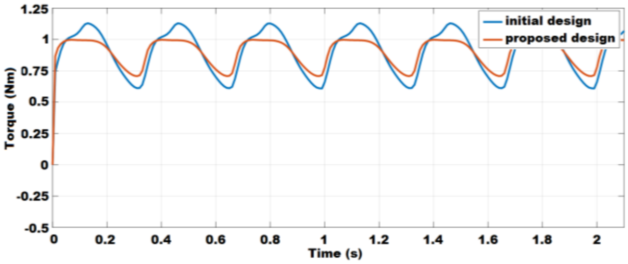

Fig. 11: An electromagnetic torque comparison of the proposed and conventional BLDC motors.

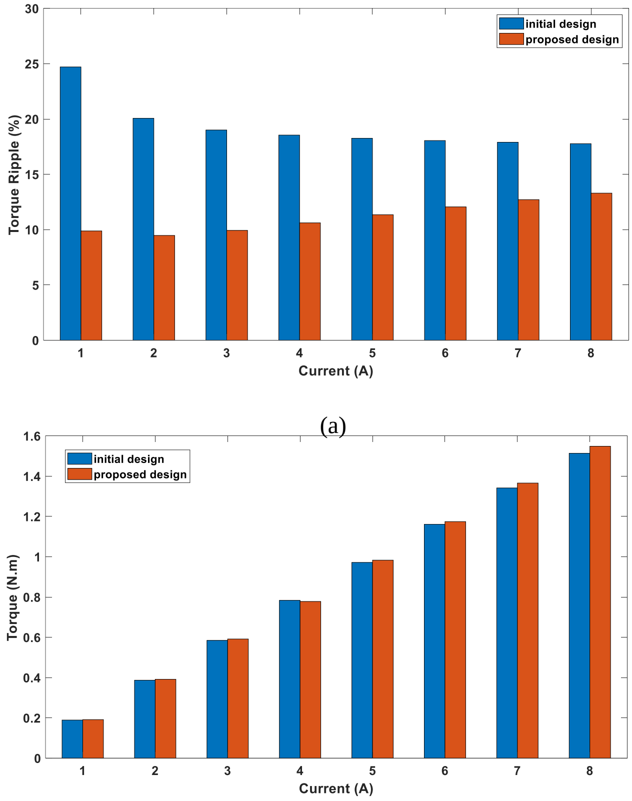

(a)

(b)

Fig. 12: (a) Electromagnetic torque and (b) torque ripple for the proposed and conventional BLDC motors in terms of motor currents.

B. *Comparison with Asymmetrical V-type Design*

In this section, a new comparative analysis is considered to assess the proposed design properly. Among the internal PM BLDC motors, V-type structures have some advantages. In [11], an asymmetrical V-type structure is introduced whose results confirm the reduction of the cogging and total torque in this structure. Therefore, the aforementioned structure is additionally considered in this paper. To make a reasonable comparison, the stator structure is the same as in the proposed motor, and an equal volume of PM is considered for the V-type structure. The value of other parameters in the mentioned structure is selected according to Table I. Fig. 13 shows the asymmetrical V-type design together with its magnetic flux lines.

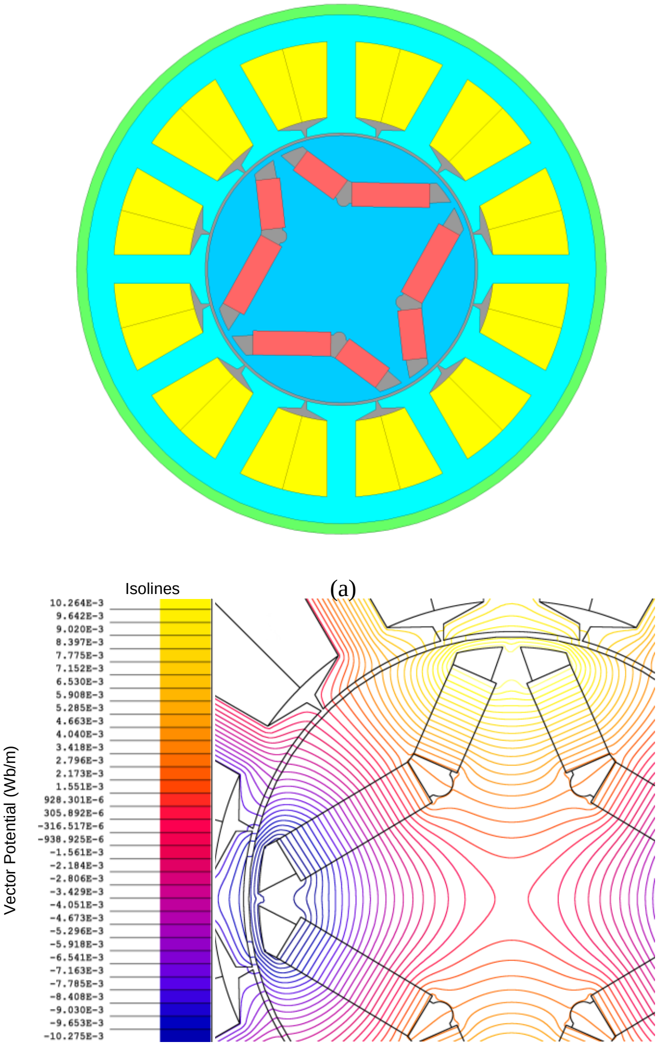

(a)

(b)

Fig. 13: (a) Asymmetrical V-type structure and (b) its magnetic flux lines.

In the next step, the back-emf is calculated for the asymmetrical V-type design and depicted in Fig. 14. In the back-emf flat area, the fluctuations are acceptable. As was already mentioned, torque ripple directly or indirectly depends on the cogging torque and this is comparatively shown in Fig. 15. The cogging torque for the proposed design is considerably low in comparison to the asymmetrical V-type structure.

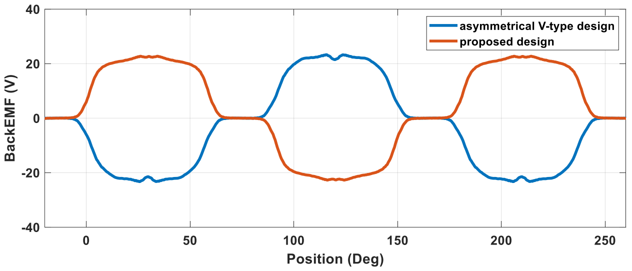

Fig. 14: A comparison of the produced back-emf for the proposed and asymmetrical V-type structures.

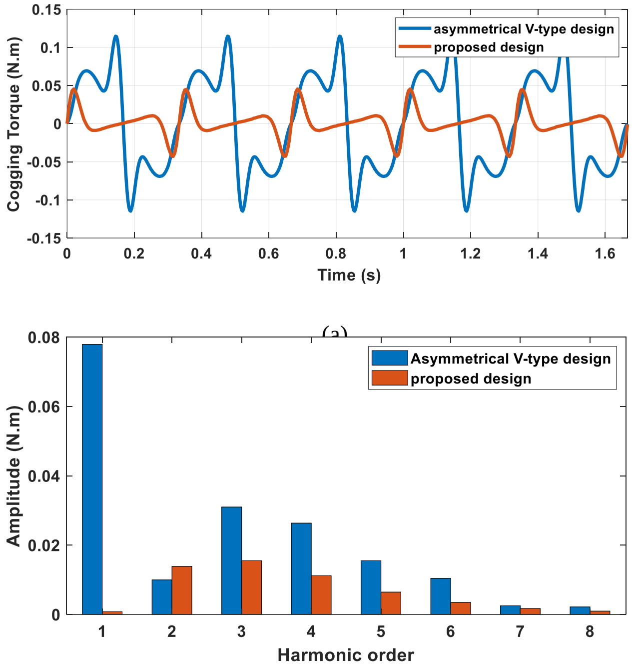

(a)

(b)

Fig. 15: A comparison of (a) the cogging torque and (b) its harmonic components in the proposed and asymmetrical V-type design.

In the next step, the motor torque is calculated for the asymmetrical V-type design and is depicted together with the torque of the proposed motor in Fig. 16. As shown, the proposed motor exhibits low torque ripple. Using different drive techniques, the torque ripple can be further reduced, but this paper focuses on the design of a geometrical topology. Finally, motor performance comparisons are summarized in Table III. The results confirm the effectiveness of the proposed BLDC motor structure. Considering the same configuration for the stator, the manufacturing cost of the proposed motor may be somehow different just because of the rotor structure. On the other hand, it is assumed that an equal volume of the PMs is used in the rotor configuration. Therefore, it seems that the cost difference will depend on the cutting method of the lamination and the number of PM segments as well. However, this difference may be neglected in a large scale production. The motor stack length in the proposed motor, as in internal PM BLDC motors, should be properly designed to ensure the mechanical robustness of the motor.

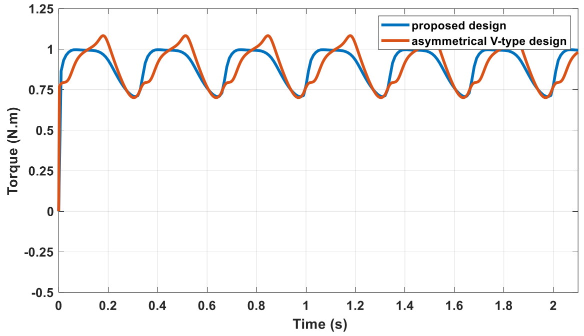

Fig. 16: An Electromagnetic torque comparison of the proposed and asymmetrical V-type designs.

Table III: Comparisons of the motor performance parameters

Parameter	**Conventional BLDCM**	**Asymmetrical V-type BLDCM**	**Proposed BLDCM**
Peak of cogging torque	0.29Nm	0.23Nm	0.09Nm
Average electromagnetic torque	0.882Nm	0.876Nm	0.88N.m
Torque ripple	18%	15%	10.4%
Efficiency	72.3%	74%	73.6%

V. CONCLUSION

This paper introduces a new permanent magnet brushless DC motor. Despite many advantages, torque ripple in BLDC motors is always a big concern for many researchers. The rotor structure together with the permanent magnet arrangement has a great impact on the cogging torque which often affects the torque ripple. This paper proposes and discusses a new BLDC structure in which the rotor is modified and permanent magnets are rearranged based on the magnetic flux path of the stator phases. The proposed structure has different geometric design parameters and in the first step, they are assessed by a sensitivity analysis. The main contribution of the proposed design is the considerable reduction of the torque ripple in comparison to conventional BLDC motors. More importantly, this torque ripple reduction has no undesirable effect on the main characteristics especially the mean torque. Since the proposed design introduces a new rotor PM configuration, it is additionally compared with another recent design of the rotor PM structure, i.e. asymmetrical V-type structure. In any case, the results exhibit low torque ripple for the proposed BLDC motor.

REFERENCES

[1] Y. Chen, X. Zhu, L. Quan, Z. Xiang, Y. Du and X. Bu, “A V-Shaped PM Vernier Motor With Enhanced Flux-Modulated Effect and Low Torque Ripple,” IEEE Trans. Magnetics, vol. 54, no. 11, pp. 1-4, Nov. 2018.

[2] Z. S. Du and T. A. Lipo, "Reducing Torque Ripple Using Axial Pole Shaping in Interior Permanent Magnet Machines," IEEE Trans. Industry Appl., vol. 56, no. 1, pp. 148-157, Jan.-Feb. 2020.

[3] Q. Chen, G. Xu, G. Liu, W. Zhao, L. Liu and Z. Lin, "Torque Ripple Reduction in Five-Phase IPM Motors by Lowering Interactional MMF," IEEE Trans. Ind. Electronics, vol. 65, no. 11, pp. 8520-8531, Nov. 2018.

[4] Bianchini, C., Immovilli, F., Lorenzani, E., Bellini, A., Davoli, M., "Review of design solutions for internal permanent-magnet machines cogging torque reduction," IEEE Trans. Magn., vol. 48, no. 10, pp. 2685 -2693, Oct. 2012.

[5] Hao, L., Lin, M., Xu, D., Li, N., Zhang, W., "Cogging torque reduction of axial-field flux-switching permanent magnet machine by rotor tooth notching," IEEE Trans. Magn., vol. 51, no. 11, pp.1-4, Nov. 2015.

[6] Zhao, W., Lipo, T.A., Kwon, B., "Torque pulsation minimization in spoke-type interior permanent magnet motors with skewing and sinusoidal permanent magnet configurations, IEEE Trans. Magn., vol. 51, no.11, pp.1-4, Nov. 2015.

[7] H. M. Cheshmeh-Beigi, A. Mohamadi, "Torque ripple minimization in SRM based on advanced torque sharing function modified by genetic algorithm combined with fuzzy PSO," International Journal of Industrial Electronics, Control and Optimization (IECO), vol. 1, no. 1, pp. 71-80, 2018.

[8] M. Sumega, P. Rafajdus, M. Stulrajter, "Current harmonics controller for reduction of acoustic noise, vibrations and torque ripple caused by cogging torque in PM motors under FOC operation," Energies, vol. 13, no. 10, pp. 1-23, May 2020.

[9] W. Fei, Z. Q. Zhu, "Comparison of Cogging Torque Reduction in Permanent Magnet Brushless Machines by Conventional and Herringbone Skewing Techniques," IEEE Trans. Energy Convers., vol. 28, no. 3, Sep. 2013.

[10] Gyu-Hong Kang, Young-Dae Son, Gyu-Tak Kim, Jin Hur, "A novel cogging torque reduction method for interior-type permanent-magnet motor," IEEE Trans. Ind. Appl., vol. 45, no. 1, Jan/Feb. 2009.

[11] Wu Ren, Qiang Xu, and Qiong Li, "Reduction of Cogging Torque and Torque Ripple in Interior PM Machines with Asymmetrical V-type Rotor Design," IEEE Trans. Magn., vol. 52, Jul. 2016.

[12] Keun-young Yoon, Byung-il Kwon, "Optimal Design of a New Interior Permanent Magnet Motor Using a Flared-Shape Arrangement of Ferrite Magnets," IEEE Trans. Magn., vol .52, Jul. 2016.

[13] D. Wang, X. Wang, M.-K Kim, and S.-Y. Jung, "Integrated optimization of two design techniques for cogging torque reduction combined with analytical method by a simple gradient descent method," IEEE Trans. Magn., vol. 48, no. 8, pp. 2265–2276, Aug. 2012.

[14] L. Dosiek and P. Pillay, "Cogging torque reduction in permanent-magnet machines," IEEE Trans. Ind. Appl., vol. 43, no. 6, pp. 1565–1571, Nov./Dec. 2007.

[15] T. Tudorache and I. Trifu, "Permanent-magnet synchronous machine cogging torque reduction using a hybrid model," IEEE Trans. Magn., vol. 48, no. 10, pp. 2627–2632, Oct. 2012.

[16] N. Chen, S. L. Ho, and W. N. Fu, "Optimization of permanent magnet surface shapes of electric motors for minimization of cogging torque using FEM," IEEE Trans. Magn., vol. 46, no. 6, pp. 2478–2481, Jun. 2010.

[17] S. M. Hwang, J.-B. Eom, Y.-H. Jung, D.-W. Lee, and B.-S. Kang, "Various design techniques to reduce cogging torque by controlling energy variation in permanent magnet motors," IEEE Trans. Magn., vol. 37, no. 4, pp. 2806–2809, Jul. 2001.

[18] M. R. Dubois, H. Polinder, and J. A. Ferreira, "Magnet shaping for minimal magnet volume in machines," IEEE Trans. Magn., vol. 38, no. 5, pp. 2985–2987, Sep. 2002.

[19] Hsing-Cheng Yu, Bo-Syun Yu, Jen-te Yu, and Cheng-Kai Lin, "A Dual Notched Design of Radial-Flux Permanent Magnet Motors with Low Cogging Torque and Rare Earth Material," IEEE Trans. Magn., vol. 50, no. 11, Nov. 2014.

[20] W. Fei, P. C. K. Luk, J. X. Shen, B. Xia, and Y.Wang, "Permanent-magnet flux-switching integrated starter generator with different rotor configurations for cogging torque and torque ripple mitigations," IEEE Trans. Ind. Appl., vol. 47, no. 3, pp. 1247–1256, May/Jun. 2011.

[21] Z. Q. Zhu and D. Howe, "Influence of design parameters on cogging torque in permanent magnet machines," IEEE Trans. Energy Convers., vol. 15, no. 4, pp. 407–412, Dec. 2000.

[22] W. Fei and P. C. K. Luk, "A new technique of cogging torque suppression in direct-drive permanent-magnet brushless machines," IEEE Trans. Ind. Appl., vol. 46, no. 4, pp. 1332–1340, Jul./Aug. 2009.

[23] N. Bianchi and S. Bolognani, "Design techniques for reducing the cogging torque in surface-mounted PM motors," IEEE Trans. Ind. Appl., vol. 38, no. 5, pp. 1259–1265, Sep./Oct. 2002.

[24] T. Li and G. Slemon, "Reduction of cogging torque in permanent magnet motors," IEEE Trans. Magn., vol. 24, no. 6, pp. 2901–2903, Nov. 1988.

[25] Y. Yang, X. Wang, R. Zhang, T. Ding, and R. Tang, "The optimization of pole-arc coefficient to reduce cogging torque in surface-mounted permanent magnet motors," IEEE Trans. Magn., vol. 42, no. 4, pp. 1135–1138, Apr. 2006.

[26] B. Ackermann, J. H. H. Janssen, R. Sotteck, and R. I. van Steen, "New technique for reducing cogging torque in a class of brushless DC motors," Proc. IEE—Electr. Power Appl., vol. 139, no. 4, pp. 315–320, Jul. 1992.

[27] X. Jiang, J. Xing, Y. Li, and Y. Lu, "Theoretical and simulation analysis of influences of stator tooth width on cogging torque of BLDC motors," IEEE Trans. Magn., vol. 45, no. 10, pp. 4601–4604, Oct. 2009.

[28] L. Petkovska, P. Lefley, G. V. Cvetkovski, "Design techniques for cogging torque reduction in a fractional-slot PMBLDC motor," COMPEL-The international journal for computation and mathematics in electrical and electronic engineering, vol. 39, no. 3, May 2020.

[29] Zhu,Z.Q., Ruangsinchaiwanich, S., Schofield, N., Howe, D., "Reduction of cogging torque in interior-magnet brushless machines," IEEE Trans. Magn., vol. 39, no. 5, pp. 3238-3240, Sept. 2003.

[30] Sun-Kwon Lee, Gyu-Hong Kang, Jin Hur, Byoung-Woo Kim, "Stator and rotor shape designs of interior permanent magnet type brushless DC motor for reducing torque fluctuation," IEEE Trans. Magn., vol.48, no.11, pp.4662,4665, Nov. 2012.

[31] Ki-Chan Kim, "A novel method for minimization of cogging torque and torque ripple for interior permanent magnet synchronous motor," IEEE Trans. Magn., vol. 50, no. 2, pp. 793-796, Feb. 2014.

[32] A. N. Patel, B. N. Suthar, "Double layer magnet design technique for cogging torque reduction of dual rotor single stator axial flux brushless DC motor," Iranian Journal of Electrical and Electronic Engineering (IJEEE), vol. 16, no. 1, pp. 58-65, Mar. 2020.

[33] D. C. Hanselman, Brushless Permanent Magnet Motor Design, 2nd ed. Cranston, RI, USA: The Writers' Collective, 2003.

Seyed Reza Mousavi-Aghdam received his B.Sc. degree with first-class honor from the Azarbaijan University of Shahid Madani in 2009, Tabriz, Iran, and M.Sc. and Ph.D. Degrees from the University of Tabriz, Iran, in 2011 and 2015 respectively all in Electrical Engineering. From September 2014 to March 2015, he has been a visiting research scholar at the Department of Industrial Engineering, University of Padova, Italy. Since 2016, he has joined the Department of Electrical Engineering, University of Mohaghegh Ardabili, Ardabil, Iran, as an assistant professor. His current research interests include design of electrical machines, electric drives, and analysis of special electrical machines.

Amin Kholousi was born in Ardabil, Iran. He received his B.Sc. degree in Electrical Engineering from the University of Mohaghegh Ardabili, Ardabil, Iran, in 2020. His current research interests include electric machines, modeling, and design of permanent-magnet machines.

International Journal of Industrial Electronics, Control and Optimization © 2021 IECO
Vol. 4, No. 1, pp. 87-98, Jan (2021)

Cooperative Distributed Constrained Model Predictive Control for Uncertain Nonlinear Large-Scale Systems

Ahmad Mirzaei[1], and Amin Ramezani[2,†]

[1,2] Center of Advanced Control Systems, School of Electrical and Computer Engineering, Tarbiat Modares University, Tehran, Iran

ABSTRACT

In this paper, two linear constrained cooperative distributed extended dynamic matrix control (CDEDMC) and adaptive generalized predictive control (CDGPC) are proposed to control the uncertain nonlinear large-scale systems. In these approaches, a proposed cooperative optimization is employed which improves the global cost function. The cost values and convergence time are reduced using the proposed cooperative optimization strategy. The proposed approaches are designed based on the compensation of the mismatch between linearized and nominal nonlinear models. In CDEDMC the mismatch is considered as a disturbance and compensated; Also in CDGPC, it is compensated using online identification of the linearized model. The typical distributed linear algorithms like DMC leads to an unstable response if the reference trajectory is a little far from the equilibrium point. This problem will be partially solved using the CDEDMC and will be completely solved using the CDGPC even if the reference trajectory is too far from the equilibrium point. The performance and effectiveness of proposed approaches are demonstrated through simulation of a typical uncertain nonlinear large-scale system.

Article Info

Keywords:
Cooperative distributed extended dynamic matrix control, Cooperative distributed adaptive generalized predictive control, Cooperative optimization approach.

Article History:
Received 2020-04-25
Accepted 2020-10-02

I. INTRODUCTION

Distributed model predictive control (DMPC) is one of the most appropriate and practical approaches for dealing with uncertain nonlinear large-scale systems, which are a major part of industrial systems. Linear DMPC approaches are divided into two categories in terms of how the subsystems interconnect with each other in the optimization process; cooperative and non-cooperative, both of which could be implemented in nonlinear large-scale systems [1]. In dual-mode DMPC methods, based on the displacement of the states from the origin, the DMPC algorithm changes from the linear algorithm to a nonlinear one or vice versa. When the states are in the neighborhood of the origin, the linear DMPC algorithm is applied and vice versa, when they are far from the origin, the nonlinear algorithm is applied. The main advantage of dual-mode methods is that the complexity is reduced in comparison with fully nonlinear algorithms. However, the main disadvantage of these methods is that the convergence time and the probability of errors in the optimization process are increased compared to fully linear or nonlinear methods [2]. Some large-scale systems require the coordination layer in their optimization process, depending on their control objectives and the interaction between their local controllers [3, 4, and 5]. The advantage of coordination based methods is that they allow full interconnection between subsystems. However, the disadvantages of these methods are that they add a layer to the design and increase the likelihood of optimization errors and also increase the complexity of the design. On the other hand, in some other large-scale systems, the mentioned goals are provided by alternative methods like the Gradient Projection method, without the need for a coordinator layer [6, 7]. The interconnections between local controllers could be considered as constraints in their

---

[†] **Corresponding Author**: ramezani@modares.ac.ir
Tel: +982182883592, Fax: +982182884325, Tarbiat Modares University. Center of advanced Control systems, School of Electrical and Computer Engineering, Tarbiat Modares University, Tehran, Iran.

optimization process instead of applying the coordination layer. The advantage of this approach is that it is proper and applicable for weakly coupled large-scale systems [8, 9]. The most important concern in methods that use the coordination layer in the optimization process or methods that each subsystem computes its own optimal control separately and then dispatches to its neighboring subsystems is communication delay. Most of these methods take this communication delay as a constraint [10]. Robust DMPC approaches are useful for constrained large-scale systems. One of these robust approaches is designed based on the two-layer robust method. In this method, each local controller receives control information of its neighboring subsystems and calculates its own optimal control. In the first layer, the recursive feasibility of convergence of whole system states is presented. A robust DMPC algorithm is applied in the second layer [11, 12]. The main advantage of robust approaches is that the inherent constraints of the system can be considered and taken into account in the optimization process. However, the main disadvantages of these approaches are their high cost and long convergence time. The Sequential DMPC approach is another useful strategy for constrained nonlinear large-scale systems. In this strategy, each local controller computes its own optimal control and dispatches to its neighbors via the communication channel to obtain the global optimality [13, 14]. The coupling between subsystems can be invigorated and also sampling intervals can be larger via applying contraction theory in DMPC approaches [15, 16]. The main disadvantage of sequential approaches is that they increase the convergence time.

DMPC approaches based on hierarchical strategy are practical methods for uncertain large-scale systems. These methods consider the inaccurate information of the actuators of the large-scale system and are designed at two levels. The faults of actuators are retrieved to retain the design specifications of all subsystems at the first level. The retrieval process is applied by enhancing the performance of the system at the second level. The developed hierarchical DMPC satisfies the retrieval design specifications by lower fault compensation. Thus, the cost is reduced in comparison with centralized and decentralized strategies [17, 18].

The linear and nonlinear constrained DMPC approaches could be applied to uncertain nonlinear large-scale systems. If a nonlinear large-scale system can be controlled using a linear distributed controller, it is rational to use linear methods because of their less complexity. The design complexity and cost in the linear DMPC approaches are less than nonlinear approaches [19, 20]. If the nonlinear large-scale system has a high degree of nonlinearity, then there may be limitations for applying the linear algorithms.

The contribution of this paper is that a novel CDMPC algorithm is proposed which decreases the complexity of optimization, cost values, and convergence time. Moreover, two reconstructed linear algorithms are proposed based on Dynamic Matrix Control (DMC) and Generalized Predictive Control (GPC) methods to profit from the advantages of linear DMPC approaches to control the uncertain nonlinear large-scale systems. If the reference trajectory deviates too close to the equilibrium point then the nonlinear system could be controlled by linear algorithms. However, there are many nonlinear industrial plants with a high degree of nonlinearity which could not be controlled using linear algorithms like DMC. Moreover, if the reference trajectory deviates farther away from the equilibrium point, these plants may be unstable. These problems will be solved using the proposed cooperative distributed linear algorithms in this paper; Cooperative Distributed Extended Dynamic Matrix Control (CDEDMC) and Cooperative Distributed Adaptive Generalized Predictive Control (CDGPC).

The remainder of the paper is organized as follows. In section 2, the problem statement for nonlinear interconnected large-scale systems is given. In section 3, the new cooperative optimization approach is proposed. The reconstructed distributed model predictive controllers are proposed in section 4. Section 5, presents the simulation results for a typical nonlinear large-scale system. Finally, concluding remarks are expressed in section 6.

II. MATHEMATICAL MODEL OF NONLINEAR LARGE-SCALE SYSTEMS

A typical nonlinear large-scale system is considered which consists of M interconnected subsystems. The nonlinear dynamic of subsystem i is described by the following input-output implementation:

$$\dot{y}_i(t) = f_i\left(y_i, u_i, u_j\right), \qquad i = 1,2,\dots,M \tag{1}$$

where $y_i \in R^{n_{y_i}}$ and $u_i \in R^{n_{u_i}}$ present the vectors of outputs and inputs of subsystem i respectively and $u_j(t)$ $(j = 1,2,\dots,M, j \neq i)$ is the vector of inputs of the subsystem j which is the neighboring subsystem of subsystem i. f_i is a nonlinear Lipschitz function. The M sets of control inputs are constrained to be in M convex sets, $U_i \subset R^{M_{u_i}}, i = 1,\dots,M$ which are expressed as:

$$U_i = \{u_i \in R^{n_{u_i}} : |u_i| \leq u_i^{Max}\} \tag{2}$$

where $u_i^{Max}, i = 1,\dots,M$ are the magnitudes of constraints of the inputs.

The continuous-time nonlinear model of subsystem i in (1) is discretized by applying Euler derivative approximation with sampling time T_s:

$$y_i(k+1) = g_i\left(y_i(k), u_i(k), u_j(k)\right), i = 1,2,\dots,M \tag{3}$$

where, g_i is also a nonlinear function. In the present paper, a new cooperative optimization approach is proposed. Moreover, two reconstructed distributed linear constrained algorithms; CDEDMC and CDGPC, are proposed to employ the proposed cooperative optimization approach and control the nominal uncertain nonlinear large-scale system in (1).

III. PROPOSED COOPERATIVE OPTIMIZATION APPROACH

According to the interconnection protocol of local controllers in large-scale systems, DMPC approaches are classified into two main categories, cooperative and non-cooperative. In cooperative methods unlike the non-cooperative ones, and in each local controller the global cost function, which is a combination of cost functions of all subsystems, is optimized to investigate the effect of each optimal control input on the whole system. In this approach, each control input is optimized in the corresponding local controller via optimizing the global cost function assuming that the control inputs of other subsystems are fixed to their optimal values of the previous iteration [1, 21]. The aforementioned global cost function is modified in the proposed CDMPC which is redefined as a convex combination of its own and its neighboring subsystems' cost functions instead of all other subsystems' cost functions. Therefore, the proposed CDMPC approach in this manuscript supposes that, if according to Equ. 1, two nominal subsystems are not neighbors to each other, then their local cost functions are not included in each other's global cost functions. The complexity and computational burden of optimization are reduced using the proposed approach. The proposed CDMPC approach applies the following cooperative strategy:

1. At time k, all local controllers receive the information of the whole large-scale system in (3).
2. At iteration c:

2.1. Each subsystem i computes its own future input vector U_{+_i} along the assigned control horizon based on the input vectors of its neighboring subsystems which are fixed to their optimal vectors of previous iteration $c-1$.

2.2. All neighboring subsystems dispatch their input vectors to each other and each local controller i computes the current iteration optimal vector $U_i^{Opt^c}$.

2.3. Based on receding horizon criteria, the current iteration optimal control $u_i^{Opt^c}$, is the first component of the current iteration optimal vector $U_i^{Opt^c}$.

3. If the termination error condition which is taken into account in the global cost function is satisfied, each subsystem i exchanges its optimal control $u_i^{Opt^c}$ to its actuators; if not satisfied, go back to step 2 and let $c+1 \rightarrow c$.
4. The models of subsystems are updated using achieved corresponding optimal controls.
5. Whenever the control inputs of all local controllers are obtained, go back to the first step and let $k+1 \rightarrow k$.

The local controller i solves the following proposed optimization problem at each iteration c:

$$\min_{\Delta u_i(k),\dots,\Delta u_i(k+m-1)} J(k) \\ U_i = [\Delta u_i(k) \dots \Delta u_i(k+m-1)]^T \tag{4}$$

Subject to Equ. 3.

$$u_i(k+j) \in U_i, j = 0, \dots, m-1 \tag{5}$$

$$U_l^c = U_l^{c-1}, \forall l \in L \; and \; l \neq i \tag{6}$$

$$\|\hat{y}_i(\tau) - W(\tau)\|^2_{Q_i} \in \frac{p}{\tau-(k-1)} y_t, \tau \in [k, k+p] \tag{7}$$

with:

$$J(k) = \alpha_i J_i + \sum_l \alpha_l J_l \tag{8}$$

$$\alpha_i, \alpha_l > 0, \alpha_i + \sum_l \alpha_l = 1 \tag{9}$$

and:

$$J_i(k) = \sum_{j=1}^{p} \left[\|\hat{y}_i(k+j) - W(k+j)\|^2_{Q_i}\right] \\ + \sum_{j=1}^{m} \|\Delta u_i(k+j-1)\|^2_{R_i} \tag{10}$$

where m and p are control and prediction horizons respectively, $L \subset M$ is the set of neighbors of subsystem i. Equ. 7, denotes the termination error condition in which y_t is the symmetric closed set in the neighborhood of origin. The termination error condition expresses that if the system is closed-loop stable, then the prediction error goes to zero. $\hat{y}_i(k+j), j = 1, \dots p$ is the subsystem's i predicted output that in each linear MPC algorithm is computed via a special method. W denotes the reference trajectory. Q_i and R_i are positive definite diagonal weighting matrices of prediction errors and control inputs respectively. $J(k)$ is presented as a convex combination of cost functions subsystem i and its neighbors with convenient α_i and α_l coefficients to obtain global optimality.

IV. PROPOSED CONSTRAINED CDMPC APPROACHES

The application of linear algorithms to control nonlinear systems has been proposed in many methods for two main reasons. First, according to experimental data, a linear system is much easier identified than a nonlinear system. Second, most practical nonlinear systems like liquid level control, pressure control, and temperature control of a furnace just have one equilibrium point, so they can be identified by an accurate linear first-order model, and then linear DMPCs can be employed to control the linearized system and determine the optimal controls of subsystems.

In this manuscript, two reconstructed constrained cooperative distributed linear algorithms; CDEDMC and CDGPC are proposed to control the nonlinear uncertain large-scale systems. These algorithms are distinguished via how the nonlinear model is applied in the optimization process. In CDEDMC the linearized version of the nominal nonlinear model is applied and the mismatch between linearized and nonlinear models is considered as a constraint and will be compensated. So the predicted outputs calculated via both models are similar to each other. The CDGPC algorithm identifies the numerator and denominator polynomials of the transfer function of the linearized model which indeed provides the nonlinear dynamics of the system.

A. Proposed Constrained CDEDMC Approach

In fact, EDMC is the extended version of the DMC algorithm that takes the nonlinear model into account, so this algorithm also uses the system’s step response to determine the predicted outputs similar to DMC [22].

The predicted output of the subsystem i in distributed DMC algorithm is represented as follows:

$$\begin{aligned}\hat{y}_i(k+j) &= \sum_{q=1}^{N} g_{iq}\Delta u_i(k+j-q)\\ &\quad + \sum_{l}\sum_{q=1}^{N} g_{ilq}\Delta u_l(k+j-q)\\ &\quad + \hat{n}_i(k+j), i=1,\dots,M, l\in L, l\neq i\end{aligned} \tag{11}$$

where g_{iq} and g_{ilq} are the step responses coefficients of subsystem i and its interconnected neighboring subsystem l, N is the model horizon, and Δu_i and Δu_l are the increment control inputs of subsystems i and l respectively. An integrator should be added to remove the steady-state error so increment of control inputs are used instead of control input in DMC and so in EDMC methods. $\hat{n}_i(k+j)$ is the estimation of the future time disturbances assuming that disturbance and other signals of plant, until time j, are presented. In distributed DMC, $\hat{n}_i(k+j)$ is considered as external disturbances applied to the system. Moreover, it is assumed that the future disturbance is constant along the prediction horizon and equal to the current disturbance $\hat{n}_i(k)$. The disturbance is defined as the difference between measured and predicted outputs:

$$\begin{aligned}\hat{n}_i(k+j) = \hat{n}_i(k) &= y_{m_i}(k) - \sum_{q=1}^{N} g_{iq}\Delta u_i(k-q)\\ &\quad - \sum_{l}\sum_{q=1}^{N} g_{ilq}\Delta u_l(k-q)\end{aligned} \tag{12}$$

where the $y_{m_i}(k)$ is the measured output. The cost function of subsystem i in distributed DMC is:

$$\begin{aligned}J_i(k) &= \sum_{j=1}^{p}\|\hat{y}_i(k+j) - W(k+j)\|_{Q_i}^2\\ &\quad + \sum_{j=1}^{m}\|\Delta u_i(k+j-1)\|_{R_i}^2\end{aligned} \tag{13}$$

and also the cost function is represented as the matrix form of:

$$J_i = (Y_i - W)^T Q_i (Y_i - W) + {U_i}^T R_i U_i \tag{14}$$

in which elements of the Y_i are obtained using Equs. 11-12 and series characteristics:

$$Y_i = G_i U_i + \sum_{l\neq i} G_{il} U_l + Free\ Response_i \tag{15}$$

$$Free\ Response_i = H_i U_{-_i} + \sum_{l\neq i} H_{il} U_{-_l} + y_{m_i} I_{p\times 1} \tag{16}$$

where Y_i is the predicted outputs vector, U_{+_i} and U_{+_l} are the future control input vectors, and U_{-_i} and U_{-_l} are the determined past control input vectors of subsystems i and l respectively. According to the cooperative optimization approach proposed in section 3 the future control inputs vector of neighboring subsystem l in iteration c is constant and equal to its latest optimal value. G_i,G_{il},H_i, and H_{il} are MPC matrices with appropriate dimensions:

$$Y_i = \begin{bmatrix}\hat{y}_i(k+1)\\ \vdots\\ \hat{y}_i(k+p)\end{bmatrix}, U_i = \begin{bmatrix}\Delta u_i(k)\\ \vdots\\ \Delta u_i(k+m-1)\end{bmatrix}, U_l = U_l^{c-1}$$

$$U_{-_i} = \begin{bmatrix}\Delta u_i(k-1)\\ \vdots\\ \Delta u_i(k-N)\end{bmatrix}, U_{-_l} = \begin{bmatrix}\Delta u_l(k-1)\\ \vdots\\ \Delta u_l(k-N)\end{bmatrix}$$

$$G_i = \begin{bmatrix} g_{i1} & 0 & & \dots & 0\\ g_{i2} & g_{i1} & & \dots & 0\\ \vdots & \vdots & \ddots & & \vdots\\ g_{ip} & g_{i(p-1)} & \dots & & g_{i(p-m+1)}\end{bmatrix}_{p*m}$$

$$G_{il} = \begin{bmatrix} g_{il1} & 0 & & \dots & 0\\ g_{il2} & g_{il1} & & \dots & 0\\ \vdots & \vdots & \ddots & & \vdots\\ g_{ilp} & g_{il(p-1)} & \dots & & g_{il(p-m+1)}\end{bmatrix}_{p*m}$$

$$H_i = \begin{bmatrix} g_{i2} - g_{i1} & \dots & g_{i(N+1)} - g_{iN}\\ \vdots & \ddots & \vdots\\ g_{i(p+1)} - g_{i1} & \dots & g_{i(N+p)} - g_{iN}\end{bmatrix}_{p*N}$$

$$H_{il} = \begin{bmatrix} g_{il2} - g_{il1} & \dots & g_{il(N+1)} - g_{ilN}\\ \vdots & \ddots & \vdots\\ g_{il(p+1)} - g_{il1} & \dots & g_{il(N+p)} - g_{ilN}\end{bmatrix}_{p*N}$$

The closed-form solution of optimal future control inputs vector of subsystem i could be analytically calculated by computing the following derivative equation:

$$\begin{aligned}\frac{\partial J_i}{U_i} = 0 \rightarrow {U_i}^{Opt} &= \left({G_i}^T Q_i G_i + R_i\right)^{-1} {G_i}^T Q_i \Bigg(W\\ &\quad - \sum_{l\neq i} G_{il} U_l - Free\ Response_i \Bigg)\end{aligned} \tag{17}$$

It should be noted that the linear DMPC algorithms could have any limitations, for example in a distributed DMC algorithm, it must be considered that the nominal nonlinear system should not be unstable [22].

In the EDMC algorithm the $\hat{n}_i(k+j)$ consists of two parts, one part is measurable or unmeasurable external disturbances similar to DMC, and the other part is the disturbances due to the mismatch (uncertainty) between the linearized and nonlinear models which will be presented by mismatch disturbance matrix D_{nl_i}. The objective of the proposed CDEDMC algorithm is to compensate for this mismatch.

In the proposed CDEDMC algorithm the disturbance matrix is added to the free response to compensate for the mismatch between linearized and nonlinear models. So the prediction vector of subsystem i is reconstructed as:

$$Y_i = G_i U_i + \sum_{l \neq i} G_{il} U_l + Free\ Response_i + D_{nl_i} \tag{18}$$

where $Free\ Response_i$ is presented in Equ. 16 and:

$$D_{nl_i} = [d_{nl_i}(k+1) \quad d_{nl_i}(k+2) \quad \cdots \quad d_{nl_i}(k+p)]^T$$

where $d_{nl_i} \in R^{n_{d_{nl_i}}}$. The mismatch between linearized and nonlinear models of all subsystems should be compensated. Thus, the following equation should be solved in which the predicted outputs of the linearized and nonlinear models must be equal to each other:

$$Y_i^{linearized\ predictor} = Y_i^{nonlinear\ predictor} \tag{19}$$

The elements of D_{nl_i} will be calculated via solving the Equ. 19, and so the mismatch will be compensated. The proposed CDEDMC algorithm solves the following optimization problem for subsystem i at each iteration which has been established based on the novel cooperative optimization approach proposed in section 3. At the first step, the vector of future control inputs which was calculated using distributed DMC algorithm (Equ. 17) is defined as a function of mismatch disturbance matrix D_{nl_i}:

$$U_i(D_{nl_i}) = \left(G_i{}^T Q_i G_i + R_i\right)^{-1} G_i{}^T Q_i \left(W - \sum_{l \neq i} G_{il} \mathrm{U}_l - Free\ Response_i - D_{nl_i}\right) \tag{20}$$

$$\min_{D_{nl_i}} J(k)\,, \qquad i = 1,2,\dots,M \tag{21}$$

Subject to Equ. 3, and Equ. 19.

$$u_i(k+j) \in U_i, j = 0,\dots,m-1 \tag{22}$$

$$U_l^c(D_{nl_i}) = U_{\mathrm{l}}^{c-1}(D_{nl_i}), \forall l \in L \ and\ l \neq i \tag{23}$$

$$\left\|\hat{y}_i(k+p) - \hat{y}_{NL_i}(k+p)\right\|_{Q_i}^2 \in \frac{p}{k} y_t \tag{24}$$

with:

$$J(k) = \alpha_i J_i + \sum_l \alpha_l J_l \tag{25}$$

$$\alpha_i, \alpha_l > 0, \alpha_i + \sum_l \alpha_l = 1 \tag{26}$$

and:

$$J_i(k) = \sum_{j=1}^{p} \left[\left\|\hat{y}_i(k+j) - \hat{y}_{NL_i}(k+j)\right\|_{Q_i}^2 + \left\|d_{nl_i}(k+j)\right\|_{R_i}^2\right] \tag{27}$$

the cost function is represented as the matrix form of:

$$J_i = \left(Y_i - Y_{NL_i}\right)^T Q_i \left(Y_i - Y_{NL_i}\right) + D_{nl_i}{}^T R_i D_{nl_i} \tag{28}$$

where Y_i is defined in Equ. 18 and Y_{NL_i} is the nonlinear prediction vector:

$$Y_{NL_i} = [\hat{y}_{NL_i}(k+1) \quad \hat{y}_{NL_i}(k+2) \quad \cdots \quad \hat{y}_{NL_i}(k+p)]^T$$

By solving the optimization problem in Equs. 20-27, the mismatch between linearized and nonlinear models is compensated and the optimal control input trajectory $U_i^{Opt}(D_{nl_i})$ is obtained. The optimal control input is then calculated as:

$$u_i{}^{Opt}(k) = \Delta u_i{}^{Opt}(k) + u_i{}^{Opt}(k-1) \tag{29}$$

where according to receding horizon criteria the optimal increment control input $\Delta u_i{}^{Opt}(k)$ is the first element of $U_i^{Opt}(D_{nl_i})$. The order of $U_i^{Opt}(D_{nl_i})$ is $m \times 1$ and the order of nonlinear prediction vector Y_{NL_i} is $p \times 1$ so to calculate the $u_i{}^{Opt}$ in the nonlinear prediction process in MATLAB, the control signal vector $U_{+_i}(D_{nl_i})$ is considered as follows:

$$U_i\left(D_{nl_i}\right) = [U_i(D_{nl_i}) \quad 0_{(p-m)\times 1}]^T$$

where the $0_{(p-m)\times 1}$ is the zero-column matrix.

In the proposed constrained CDEDMC algorithm, the mismatch between linearized and nonlinear models is compensated so if the reference trajectory moves farther away from the equilibrium point, the simulation results illustrate the desirable effect of this algorithm, while the system may be unstable using the distributed DMC algorithm. However, if the reference trajectory is farther away from the equilibrium point too much or the nonlinearity of the system is high, then the proposed CDEDMC algorithm will also lead to an unstable response. This problem will be completely solved by the following proposed constrained CDGPC method.

B. Proposed Constrained CDGPC Approach

The concept of the GPC algorithm is established based on the transfer function of the system [22]. The distinctive feature of this method is that it can be used in the non-minimum phase and unstable systems. The mismatch between linearized and nonlinear models is compensated via the online identification procedure in the proposed CDGPC approach. The denominator and numerator polynomials of the linearized model are identified using input and output information of the nonlinear large-scale system and an online RLS algorithm. The linearized model of each nonlinear subsystem is obtained using online identification in each time step and then by means of the identified numerator and denominator polynomials, free responses of nominal nonlinear subsystems, and GPC algorithm, the vector of optimal control inputs will be calculated using the proposed cooperative optimization approach in section 3. The obtained optimal control inputs are applied to the nonlinear system and this procedure iterates in the next iteration. The free responses of nonlinear subsystems are yielded from their corresponding past information.

Suppose that the linearized version of the nonlinear model of subsystem i is identified as the following transfer function:

$$y_i(k) = \frac{B_{ii}^I(z^{-1})}{A_{ii}^I(z^{-1})} u_i(k) + \sum_{l \neq i} \frac{B_{il}^I(z^{-1})}{A_{ii}^I(z^{-1})} u_l(k) \tag{30}$$

The CDGPC matrices will be calculated using the newly identified polynomials of the linearized model and finally, the optimal control input will be obtained using these new CDGPC matrices. The optimal controls will be achieved using the new CDGPC matrices which are obtained using the identified polynomials. The proposed CDGPC approach solves the following optimization problem at each iteration for subsystem i, which is established based on the proposed cooperative optimization approach in section 3:

$$\min_{\Delta u_i(k),\ldots,\Delta u_i(k+m-1)} J(k) \\ U_i = [\Delta u_i(k), \ldots, \Delta u_i(k+m-1)]^T \tag{31}$$

Subject to Equ. 30 $\forall i = 1, \ldots, M$ and $l \subset L, l \neq i$.

$$u_i(k+j) \in U_i, j = 0, \ldots, m-1 \tag{32}$$

$$U_l^c = U_l^{c-1}, \forall l \in L \; and \; l \neq i \tag{33}$$

$$\|\hat{y}_i(k+p) - W(k+p)\|_{Q_i}^2 \in \frac{p}{k} y_t \tag{34}$$

with:

$$J(k) = \alpha_i J_i + \sum_l \alpha_l J_l \tag{35}$$

$$\alpha_i, \alpha_l > 0, \alpha_i + \sum_l \alpha_l = 1 \tag{36}$$

and:

$$J_i(k) = \sum_{j=1}^{p} \|\hat{y}_i(k+j) - W(k+j)\|_{Q_i}^2 + \sum_{j=1}^{m} \|\Delta u_i(k+j-1)\|_{R_i}^2 \tag{37}$$

the cost function is represented as the following matrix form:

$$J_i = (Y_i - W)^T Q_i (Y_i - W) + U_i{}^T R_i U_i \tag{38}$$

where the predicted output matrix is as follows:

$$Y_i = \emptyset_i^I Y_{-_i} + \pi_i^I U_{-_i} + \sum_{l \neq i} \pi_{il}^I U_{-_l} + \Omega_i^I U_i + \sum_{l \neq i} \Omega_{il}^I U_l \tag{39}$$

The closed-form solution of the vector of optimal future control of subsystem i could be analytically calculated by solving the following equation:

$$\frac{\partial J_i}{U_i} = 0 \rightarrow U_i{}^{Opt} = \left(\Omega_i^{I^T} Q_i \Omega_i^I + R_i\right)^{-1} G_i{}^T Q_i \left(W - \emptyset_i^I Y_{-_i} - \pi_i^I U_{-_i} - \sum_{l \neq i} \pi_{il}^I U_{-_l} - \sum_{l \neq i} \Omega_{il}^I U_l\right) \tag{40}$$

where:

$$Y_i = \begin{bmatrix} \hat{y}_i(k+1) \\ \vdots \\ \hat{y}_i(k+p) \end{bmatrix}_{p \times 1}, Y_{-_i} = \begin{bmatrix} y_i(k) \\ \vdots \\ y_i(k - n_{a_i}^I) \end{bmatrix}_{(n_{a_i}^I + 1) \times 1}$$

$$U_i = \begin{bmatrix} \Delta u_i(k) \\ \vdots \\ \Delta u_i(k+m-1) \end{bmatrix}_{m \times 1}, \qquad U_l = U_l^{c-1}$$

$$U_{-_i} = \begin{bmatrix} \Delta u_i(k-1) \\ \vdots \\ \Delta u_i(k - n_{b_i}^I) \end{bmatrix}_{n_b^I \times 1}, U_{-_l} = \begin{bmatrix} \Delta u_l(k-1) \\ \vdots \\ \Delta u_l\left(k - n_{b_{il}}^I\right) \end{bmatrix}$$

in which $n_{a_i}^I$, $n_{b_i}^I$ and $n_{b_{il}}^I$ are the orders of the A_{ii}^I, B_{ii}^I and B_{il}^I identified polynomials respectively.

The $\hat{y}_i(k+j), (j = 1,2, \ldots p)$, is calculated using extended CARIMA and Diophantine equations via the following process and supposing that the time delay is zero:

$$\Delta A_{ii}^I(z^{-1}) y_i(k) = \left[B_{ii}^I(z^{-1}) \Delta u_i(k-1) + \sum_{l \neq i} B_{il}^I(z^{-1}) \Delta u_l(k-1)\right] + C_i^I(z^{-1}) e_i(k) \tag{41}$$

$$1 = E_{i\ j}^I(z^{-1}) \Delta A_{ii}^I(z^{-1}) + z^{-j} F_{i\ j}^I(z^{-1}) \tag{42}$$

where:

$$F_{i\ j}^I(z^{-1}) = f_{i_{(j,0)}} + f_{i_{(j,1)}} z^{-1} + \cdots + f_{i_{(j,n_{a_i}^I)}} z^{-n_{a_i}^I} \tag{43}$$

$$E_{i\ j}^I(z^{-1}) = e_{i_{(j,0)}} + e_{i_{(j,1)}} z^{-1} + \cdots + e_{i_{(j,j-1)}} z^{-(j-1)} \tag{44}$$

in which the coefficients of $F_{i\ j}^I(z^{-1})$ and $E_{i\ j}^I(z^{-1})$ are computed using the recursive procedure as follows:

$$F_{i\ 1}^I = z(1 - \Delta A_{ii}^I(z^{-1})) \tag{45}$$

$$E_{i\ 1}^I = 1 \tag{46}$$

$$E_{i\ j+1}^I(z^{-1}) = E_{i\ j}^I(z^{-1}) + f_{i_{(j,0)}} z^{-j} \tag{47}$$

$$f_{i_{(j+1,q)}} = f_{i_{(j,q+1)}} - f_{i_{(j,0)}} - f_{j,0} \tilde{a}_{i_{(q+1)}} \tag{48}$$

where $\tilde{a}_{i_{(q+1)}}$ $(q = 0, 1, \ldots, n_{a_i}^I)$ are the coefficients of the $\Delta A_{ii}^I(z^{-1})$ polynomial. The future outputs are achieved using Equs. 41-42:

$$y_i(k+j) = F^I_{i\,j}(z^{-1})y_i(k) + E^I_{i\,j}(z^{-1})\left[B^I_{ii}(z^{-1})\Delta u_i(k+j-1) + \sum_{l\neq i} B^I_{il}(z^{-1})\Delta u_l(k+j-1)\right] + E^I_{i\,j}(z^{-1})e_i(k+j) \tag{49}$$

The appropriate estimation of prediction of $y_i(k+j)$ is its average so we have:

$$\hat{y}_i(k+j) = G^I_{i\,j}(z^{-1})\Delta u_i(k+j-1) + \sum_{l\neq i} G^I_{il\,j}(z^{-1})\Delta u_l(k+j-1) + F^I_{i\,j}(z^{-1})y_i(k), \qquad j = 1,\dots,p \tag{50}$$

$$G^I_{i\,j}(z^{-1}) = B^I_{ii}(z^{-1})E^I_{i\,j}(z^{-1}) \tag{51}$$

$$G^I_{il\,j}(z^{-1}) = B^I_{il}(z^{-1})E^I_{i\,j}(z^{-1}) \tag{52}$$

Since the $e_i(k+j)$ is the white Gaussian noise thus, its average is zero. The new CDGPC matrices in Equ. 39 are expressed as:

$$\emptyset^I_i = \begin{bmatrix} f_{i(1,0)} & \cdots & f_{i(1,n^I_{a_i})} \\ \vdots & \ddots & \vdots \\ f_{i(p,0)} & \cdots & f_{i(p,n^I_{a_i})} \end{bmatrix}$$

$$\pi^I_i = \begin{bmatrix} g_{i(1,1)} & g_{i(1,2)} & \cdots & g_{i\left(1,n^I_{b_i}\right)} \\ \vdots & \vdots & \ddots & \vdots \\ g_{i(p,p)} & g_{i(p,p+1)} & \cdots & g_{i\left(p,n^I_{b_i}\right)} \end{bmatrix}$$

$$\pi^I_{il} = \begin{bmatrix} g_{il(1,1)} & g_{il(1,2)} & \cdots & g_{il(1,n^I_{b_{il}})} \\ \vdots & \vdots & \ddots & \vdots \\ g_{il(p,p)} & g_{il(p,p+1)} & \cdots & g_{il(p,n^I_{b_{il}})} \end{bmatrix}$$

$$\Omega^I_i = \begin{bmatrix} g_{i(1,0)} & 0 & 0 & \cdots & 0 \\ g_{i(2,1)} & g_{i(2,0)} & 0 & & 0 \\ & \vdots & & \ddots & \vdots \\ g_{i(p,p-1)} & g_{i(p,p-2)} & \cdots & \cdots & g_{i(p,0)} \end{bmatrix}$$

$$\Omega^I_{il} = \begin{bmatrix} g_{il(1,0)} & 0 & 0 & \cdots & 0 \\ g_{il(2,1)} & g_{il(2,0)} & 0 & & 0 \\ & \vdots & & \ddots & \vdots \\ g_{il(p,p-1)} & g_{il(p,p-2)} & \cdots & \cdots & g_{il(p,0)} \end{bmatrix}$$

where $g_{i(j,q)}$ and $g_{il(j,q)}$ $(j = 1,2,\dots,p, q = 1,2,\dots)$ are the corresponding coefficients of the $G^I_{i\,j}(z^{-1})$ and $G^I_{i\,j}(z^{-1})$ polynomials respectively.

V. SIMULATION RESULTS

A typical nonlinear large-scale system consisting of three coupled subsystems is employed as following input-output models to investigate the proposed approaches:

$$\begin{cases} \dot{y}_1(t) = -y_1(t) + y_1(t)^2 + 7u_1(t) + 4u_2(t) \\ \dot{y}_2(t) = -3y_2(t) + 2y_2(t)^2 + 10u_2(t) + u_3(t)^2 \\ \dot{y}_3(t) = -2y_3(t) + y_3(t)^2 + 2u_3(t) + u_2(t) \end{cases}$$

The subsystems are coupled through inputs. The discrete-time system could be obtained using the following Euler derivative approximation:

$$\dot{y}_i(t) = \big(y_i(k+1) - y_i(k)\big)/T_s$$

so the discrete-time system is concluded as:

$$\begin{cases} y_1(k+1) = a_1y_1(k) + 0.1y_1(k)^2 + 0.7u_1(k) + 0.4u_2(k) \\ y_2(k+1) = a_2y_2(k) + 0.2y_2(k)^2 + u_2(k) + 0.1u_3(k)^2 \\ y_3(k+1) = a_3y_3(k) + 0.1y_3(k)^2 + 0.2u_3(k) + 0.1u_2(k) \end{cases}$$

where the sampling time is $T_s = 0.1$ and:

$a_1 = 0.9, a_2 = 0.7, a_3 = 0.8$

The step responses of subsystems are drawn in Fig. 1. According to the step responses the subsystems' settling times are approximately 6, 2, and 3 respectively. So the subsystems' optimal model horizons are:

$N = (Settling\ Time)/T_s \rightarrow N_1 = 60, N_2 = 20, N_3 = 30$

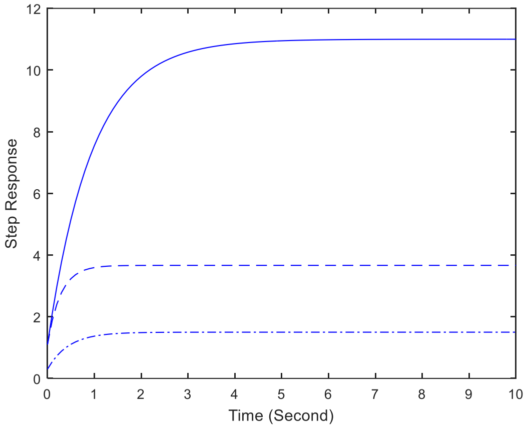

Fig. 1. Step responses, subsystem 1 (solid line), subsystem 2 (dash line), subsystem 3 (dash dot line).

Note that in all simulations the subsystems' model horizons are considered $N_1 = 60, N_2 = 20$ and $N_3 = 30$ respectively and also the subsystems' prediction and control horizons are considered 5 and 4 respectively.

The following constraint is imposed to control inputs:

$-4 \leq u_i \leq 4, i = 1,2,3$

The reference trajectory is considered as the following equation:

$$W(t) = g_W * \begin{cases} 0.01 & 0 \leq t < 2.5 \\ 0.02 & 2.5 \leq t < 5 \\ -0.01 & 5 \leq t < 7.5 \\ 0 & 7.5 \leq t < 10 \end{cases}$$

where the g_W is the amplitude's coefficient of the reference trajectory. In the first step of the simulation, we set the amplitude's coefficient as $g_W = 10$ to consider the reference trajectory a little farther away from the origin (equilibrium point). Therefore, the subsystems' predicted outputs are illustrated in Figs. 2-4 using distributed DMC and proposed constrained CDEDMC and CDGPC algorithms respectively.

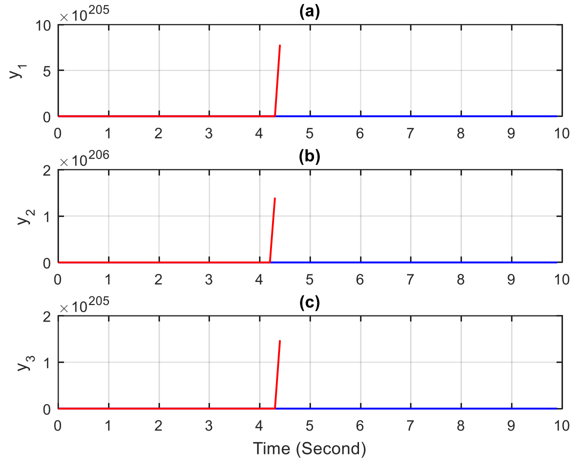

Fig. 2. The predicted outputs of the nonlinear large-scale system with $g_W = 10$ and using cooperative distributed DMC algorithm. (a) Subsystem 1; (b) subsystem 2; (c) subsystem 3.

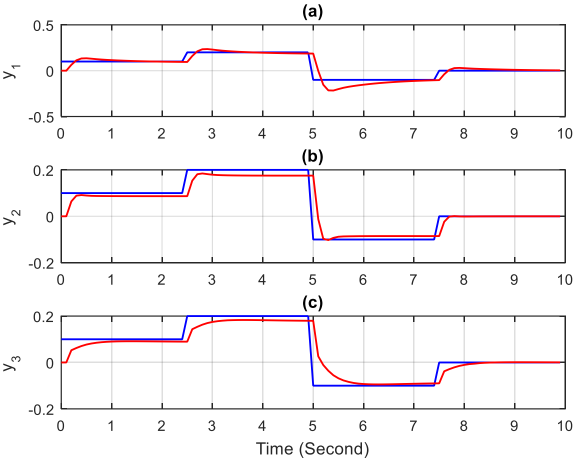

Fig. 3. The predicted outputs of the nonlinear large-scale system with $g_W = 10$ and using proposed constrained CDEDMC algorithm. (a) Subsystem 1; (b) subsystem 2; (c) subsystem 3.

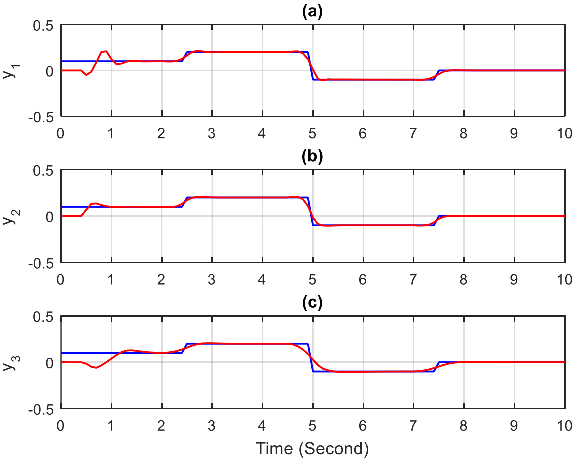

Fig. 4. The predicted outputs of the nonlinear large-scale system with $g_W = 10$ and using proposed constrained CDGPC algorithm. (a) Subsystem 1; (b) subsystem 2; (c) subsystem 3.

Since in both CDEDMC and CDGPC algorithms the mismatch between linearized and nonlinear models is compensated, it is expected to obtain appropriate responses. The illustrated predicted output curves in Figs. 3-4 confirm this from design criteria points of view such as convergence, reference trajectory's tracking and stability. However, even though the reference trajectory is not too far from the origin, according to Fig. 2, the system has become unstable using the distributed DMC algorithm.

To further emphasize the effectiveness of proposed constrained CDEDMC and CDGPC algorithms and compare them to each other, the reference trajectory's amplitude is gradually increased; $g_W = 50, 80, 110$, and simulation results are shown in Figs. 5-10.

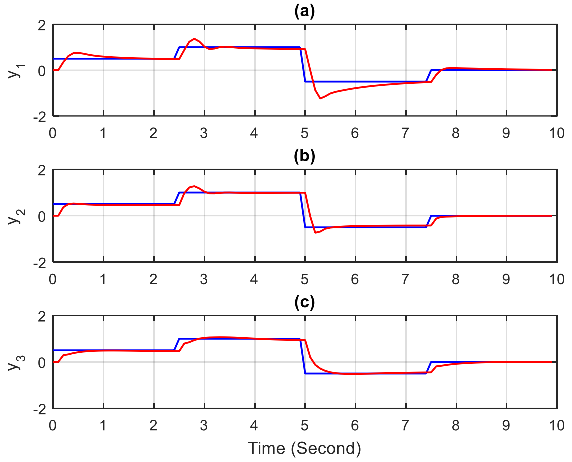

Fig. 5. The predicted outputs of the nonlinear large-scale system with $g_W = 50$ and using proposed constrained CDEDMC algorithm. (a) Subsystem 1; (b) subsystem 2; (c) subsystem 3.

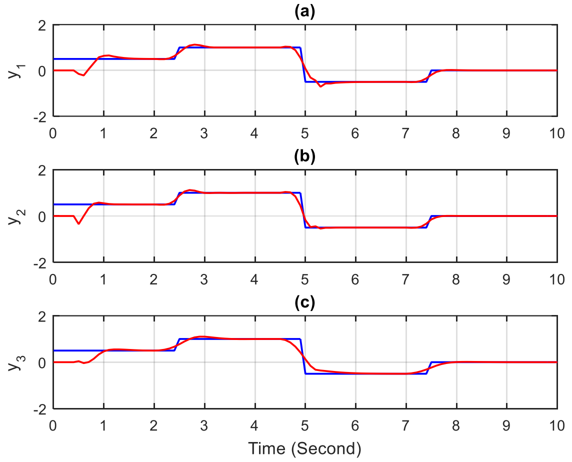

Fig. 6. The predicted outputs of the nonlinear large-scale system with $g_W = 50$ and using proposed constrained CDGPC algorithm. (a) Subsystem 1; (b) subsystem 2; (c) subsystem 3.

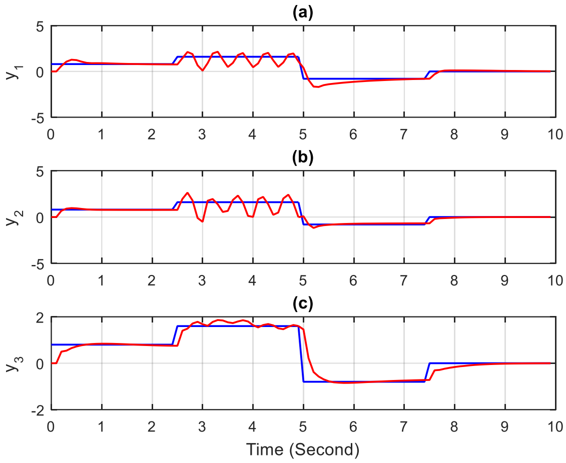

Fig. 7. The predicted outputs of the nonlinear large-scale system with $g_W = 80$ and using proposed constrained CDEDMC algorithm. (a) Subsystem 1; (b) subsystem 2; (c) subsystem 3.

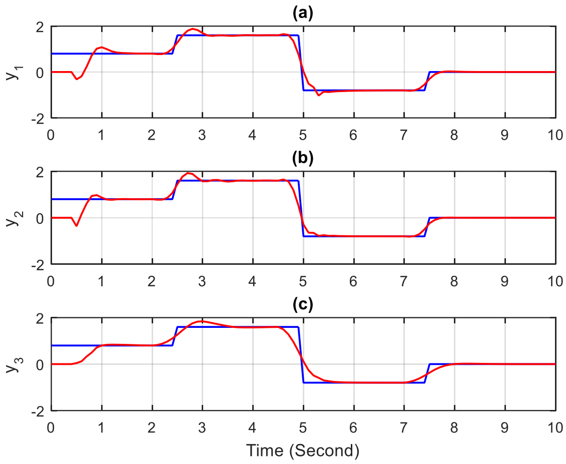

Fig. 8. The predicted outputs of the nonlinear large-scale system with $g_W = 80$ and using proposed constrained CDGPC algorithm. (a) Subsystem 1; (b) subsystem 2; (c) subsystem 3.

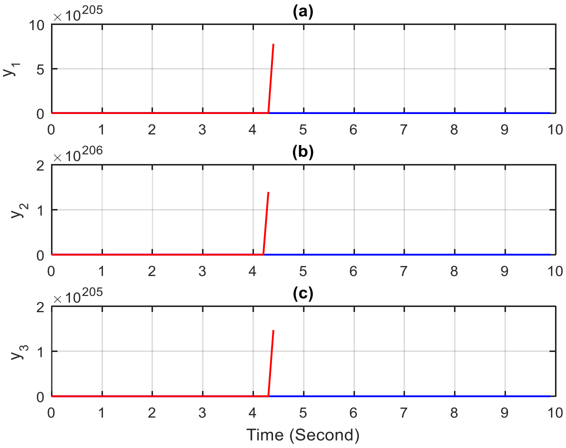

Fig. 9. The predicted outputs of the nonlinear large-scale system with $g_W = 110$ and using proposed constrained CDEDMC algorithm. (a) Subsystem 1; (b) subsystem 2; (c) subsystem 3.

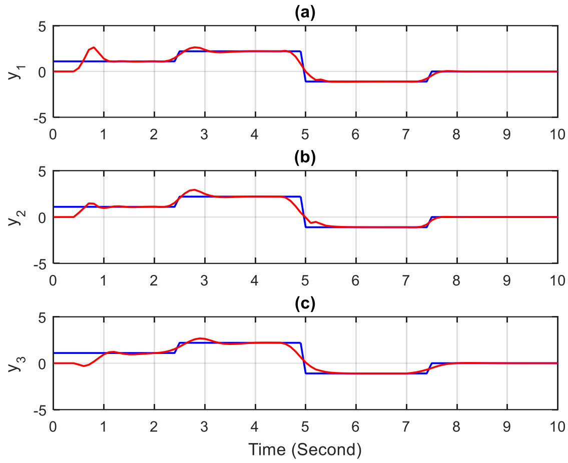

Fig. 10. The predicted outputs of the nonlinear large-scale system with $g_W = 110$ and using proposed constrained CDGPC algorithm. (a) Subsystem 1; (b) subsystem 2; (c) subsystem 3.

when the amplitude's coefficient is $g_W = 50$, both methods have proper responses according to results in Figs. 5-6, however, according to Fig. 7 by increasing the g_W to 80 some fluctuations appear when the CDEDMC is applied, while based on illustrated results in Fig. 8, the CDGPC shows appropriate predictions. The initial overshoots or undershoots in CDGPC's results are due to its online identification of the mismatch between linearized and nominal nonlinear models, and after a short time that the identification of the linearized system's numerator and denominator polynomials is done, the response becomes convergent. The usefulness of the proposed constrained CDGPC algorithm is more demonstrated when the reference trajectory is too farther away from the origin, hence to investigate this issue the amplitude's coefficient of the reference is increased to $g_W = 110$ and the simulation results are drawn in Figs. 9-10 using proposed constrained CDEDMC and CDGPC algorithms respectively. According to Fig. 9, the system has become unstable using the DEDMC algorithm, while based on illustrated results in Fig. 10, the CDGPC shows appropriate predictions and the closed-loop system is stable.

Now the proposed approaches are examined when uncertainty is applied. Assuming that in the fourth second of simulation, a_1, a_2 and a_3 change as:

$$a_1^{new} = a_2^{new} = a_1^{new} = 0.4$$

The simulation results are depicted in Figs. 11-12 with $g_W = 50$. The results emphasize the effectiveness of proposed algorithms in dealing with uncertainty. Although the responses fluctuate when the uncertainties are imposed, they quickly converge.

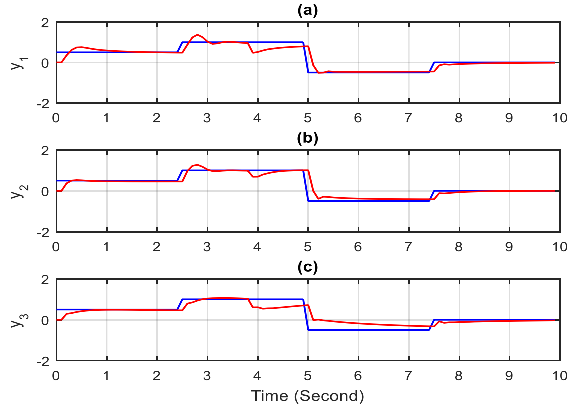

Fig. 11. The predicted outputs of the nonlinear large-scale system with imposed uncertainties and $g_W = 50$ and using proposed constrained CDEDMC algorithm. (a) Subsystem 1; (b) subsystem 2; (c) subsystem 3.

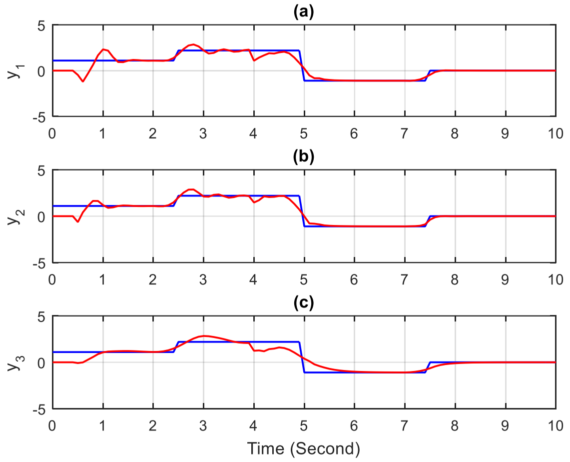

Fig. 12. The predicted outputs of the nonlinear large-scale system with imposed uncertainties and $g_W = 50$ and using proposed constrained CDGPC algorithm. (a) Subsystem 1; (b) subsystem 2; (c) subsystem 3.

All the above-mentioned results are yielded using the novel cooperative optimization approach proposed in section 3 where each subsystem optimizes a corresponding global cost function which is a convex combination of its cost function and cost functions of its neighbors. For example in the large-scale system which is analyzed in this section, subsystem 1 is neighbor to subsystem 2, but not to subsystem 3. Therefore, according to the proposed optimization approach, the global cost function, which is optimized in the local controller of subsystem 1 is represented as follows:

$$J = \alpha_1 J_1 + \alpha_2 J_2, \qquad \alpha_1 + \alpha_2 = 1$$

while according to typical cooperative DMPC methods, the global cost function is defined based on all three subsystems [1, 21]:

$$J = J_1 + J_2 + J_3$$

So the control efforts, cost function values, and convergence time are reduced using the proposed cooperative optimization approach. These criteria are examined by means of the following simulation results in which the proposed optimization approach and the DGPC algorithm are used. The cost function values of the local controllers of the nonlinear large-scale system with the mentioned imposed uncertainties are illustrated in Figs. 13-15 respectively with $g_W = 50$ and applying typical [1, 21] and proposed cooperative optimization strategies. It is cleared that the cost function values have decreased in the proposed cooperative optimization approach compared to the typical one.

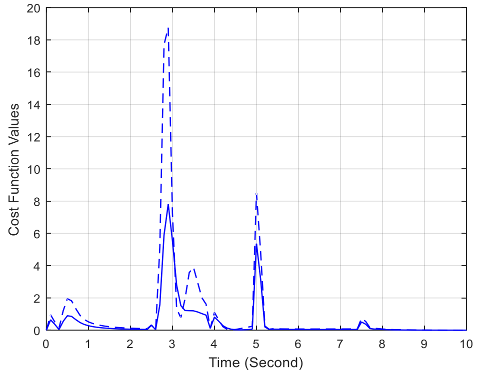

Fig. 13. The cost function values of the local controller of the uncertain subsystem 1 with $g_W = 50$ and using typical (dash line) and proposed (solid line) cooperative optimization strategies.

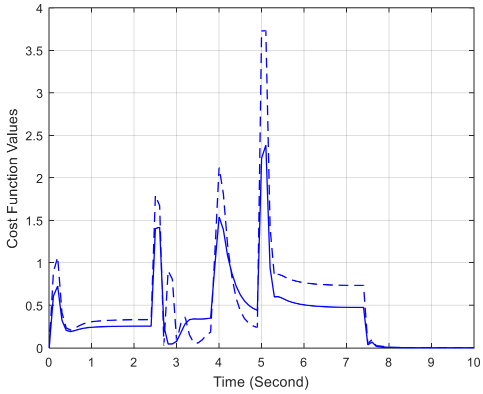

Fig. 14. The cost function values of the local controller of the uncertain subsystem 2 with $g_W = 50$ and using typical (dash line) and proposed (solid line) cooperative optimization strategies.

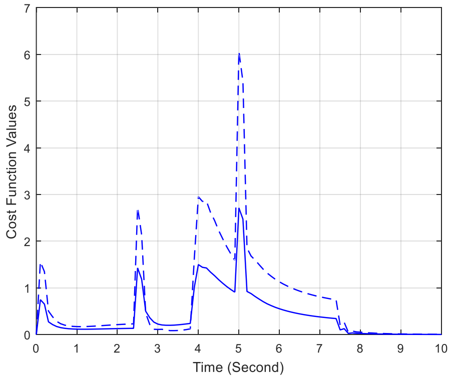

Fig. 15. The cost function values of the local controller of the uncertain subsystem 3 with $g_W = 50$ and using typical (dash line) and proposed (solid line) cooperative optimization strategies.

To further investigate and clarify the performance and effectiveness of the proposed cooperative optimization approach, besides the comparison of the cost function values in Figs. 13-15, additional indicators including maximum, average, and standard deviation of cost function values are also calculated and collected in the following tables [23, 24].

TABLE I

Maximum, Average And Standard Deviation Indicators Of Cost Function Values Of Subsystem 1

Subsystem 1	Max	Avg	Std
Proposed cooperative optimization strategy	12.3619	0.8072	2.0687
Typical cooperative optimization strategy	18.7688	0.9912	2.8268

TABLE II

Maximum, Average And Standard Deviation Indicators Of Cost Function Values Of Subsystem 2

Subsystem 2	Max	Avg	Std
Proposed cooperative optimization strategy	2.4535	0.3947	0.45
Typical cooperative optimization strategy	3.7308	0.5011	0.64

TABLE III

Maximum, Average And Standard Deviation Indicators Of Cost Function Values Of Subsystem 3

Subsystem 3	Max	Avg	Std
Proposed cooperative optimization strategy	2.6338	0.3152	0.4367
Typical cooperative optimization strategy	6.0683	0.7612	1.0638

According to the values of indicators in Table 1-3, it is clear that all three maximum, average, and standard deviation of cost function values are decreased in the proposed cooperative optimization approach compared to the typical one.

Fig. 16, illustrates the predicted outputs of the nonlinear large-scale system without uncertainty, which are obtained using a typical cooperative optimization approach in [1, 21] and DGPC algorithm with $g_W = 50$, and also Fig. 6, illustrates the predicted outputs of the nonlinear large-scale system without uncertainty using the proposed cooperative optimization approach in this paper and DGPC algorithm with $g_W = 50$. By comparing the results in Fig. 6 and Fig. 16, it is concluded that the time and quality of convergence have improved in the proposed constrained CDGPC (Fig. 6) compared to the typical one in [1, 21] (Fig. 16).

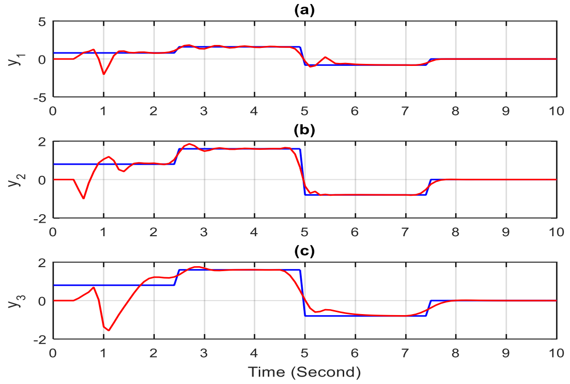

Fig. 16. The predicted outputs of the nonlinear large-scale system with $g_W = 50$ and using typical CDGPC algorithm. (a) Subsystem 1; (b) subsystem 2; (c) subsystem 3.

VI. CONCLUSION

In this manuscript, a novel cooperative DMPC approach is proposed which improves the global cost function. Each local controller optimizes the global cost function which is a convex combination of its own and its neighbors' cost functions instead of the combination of its own and all other subsystems' cost functions. So the computational burden of optimization, cost values, and convergence time are reduced compared to typical cooperative DMPC methods. Two linear cooperative constrained distributed model predictive controllers; CDEDMC and CDGPC are proposed which employ the proposed cooperative optimization approach to control the uncertain nonlinear large-scale systems. The simulation results of an uncertain nonlinear large-scale system consisting of three interconnected subsystems demonstrate the effectiveness of the proposed approaches. According to simulation results, typical distributed linear algorithms like DMC lead to an unstable closed-loop response if the reference trajectory is far from the equilibrium point, while this problem is solved using proposed CDEDMC and CDGPC algorithms even if the reference trajectory is too far from the equilibrium point.

REFERENCES

[1] P. D. Christofides, R. Scattolini, D. M. De la Pena, and J. Liu, "Distributed model predictive control: A tutorial review and future research directions" *Journal of Computers and Chemical Engineering*, Vol. 51, pp. 21-41, Apr. 2013.

[2] A. Grancharova, T. A. Johansen, and S. Olaru, "Dual-Mode distributed model predictive control of a quadruple-tank system" *Journal of Chemical Technology and Metallurgy*, Vol. 53, No. 4, pp. 674-682, May. 2018.

[3] N. Sadati, M. Rahmani, and M. Saif, "Two-Level Robust Optimal Control of Large-Scale Nonlinear Systems" *IEEE Systems Journal*, Vol. 9, No. 1, pp. 242-251, Mar. 2015.

[4] I. Stoyanova, E. Gumrukcu, G. Aragon, D. I.

Hidalgo-Rodriguez, A. Monti, and J. Myrzik, "Distributed model predictive control strategies for coordination of electro-thermal devices in a cooperative energy management concept" *Optimal Control Applications and Methods*, Vol. 41, pp. 170–189, Aug. 2019.

[5] Y. Zou, X. Su, S. Li, Y. Niu, and D. Li, "Event-triggered distributed predictive control for asynchronous coordination of multi-agent systems" *Automatica*, Vol. 99, pp. 92–98, Jan. 2019.

[6] W. Jiao, Q. Wu, S. Huang, and J. Chen, "Decentralized voltage control of wind farm based on gradient projection method" *International Journal of Electrical Power & Energy Systems*, Vol. 123, pp. 1-8, Dec. 2020.

[7] Y. Gao, L. Dai, Y. Xia, and Y. Liu, "Distributed model predictive control for consensus of nonlinear second-order multi-agent systems" *International Journal of Robust and Nonlinear Control*, Vol. 27, pp. 830-842, Jul. 2016.

[8] X. Liu, Y. Shi, and D. Constantinescu, "Distributed model predictive control of constrained weakly coupled nonlinear systems" *Systems & Control Letters*, Vol. 74, pp. 41-49, Dec. 2014.

[9] S. Rahmati, and H. Eliasi, "Robust Decentralized Model Predictive Control for a Class of Interconnected systems" *International Journal of Industrial Electronics, Control and Optimization*, Vol. 3, No. 3, pp. 327-336, Jul. 2020.

[10] M. H. Yamchi, and R. M. Esfanjani, "Distributed predictive formation control of networked mobile robots subject to communication delay" *Robotics and Autonomous Systems*, Vol. 91, pp. 194-207, May. 2017.

[11] X. Liu, Y. Shi, and D. Constantinescu, "Robust Distributed Model Predictive Control of Constrained Continuous-Time Nonlinear Systems Using Two-Layer Invariant Sets" *Journal of Dynamic Systems, Measurement, and Control*, Vol. 138, pp.1-7, Jun. 2016.

[12] Y. Zheng, S. Eben Li, K. Li, F. Borrelli, and J. Karl Hedrick, "Distributed Model Predictive Control for Heterogeneous Vehicle Platoons under Unidirectional Topologies" *IEEE Transactions on Control Systems Technology*, Vol. 25, No. 3, pp. 899-910, May. 2017.

[13] X. Yang, L. Zhang, W. Xie, and J. Zhang, "Sequential and Iterative Distributed Model Predictive Control of Multi-Motor Driving Cutterhead System for TBM" *IEEE Access*, Vol. 7, pp. 46977-46989, Apr. 2019.

[14] S. Iles, J. Matusko, and F. Kolonic, "Sequential distributed predictive control of a 3D tower crane" *Control Engineering Practice*, Vol. 79, pp. 22-35, Oct. 2018.

[15] Y. Long, S. Liu, L. Xie, and K. H. Johansson, "Distributed nonlinear model predictive control based on contraction theory" *International Journal of Robust and Nonlinear Control*, Vol. 28, pp. 1–12, Jul. 2017.

[16] X. Liu, Y. Shi, and D. Constantinescu, "Robust distributed model predictive control of constrained dynamically decoupled nonlinear systems: A contraction theory perspective" *Systems & Control Letters*, Vol. 105, pp. 84-91, Jul. 2017.

[17] N. R. Esfahani and K. Khorasani, "A Distributed Model Predictive Control (MPC) Fault Reconfiguration Strategy for Formation Flying Satellites" *International Journal of Control*, Vol. 89, No. 5, pp. 960-983, Nov. 2015.

[18] X. Kong, X. Liu, L. Ma, and K. Y. Lee, "Hierarchical Distributed Model Predictive Control of Standalone Wind/Solar/Battery Power System" *IEEE Transactions on Systems, Man, and Cybernetics: Systems*, Vol. 49, No. 8, pp. 1570-1581, Aug. 2019.

[19] A. Mirzaei, and A. Ramezani, "Cooperative Distributed Constrained Adaptive Generalized Predictive Control for Uncertain Nonlinear Large-Scale Systems: Application to Quadruple-Tank System" *Journal of Electrical and Computer Engineering Innovations*, Vol. 7, No. 2, pp. 183-194, Jul. 2020.

[20] M. Ehsani, M. Saeidi, H. Radmanesh, and A. Abrishamifar, "Comparisons between Generalized Predictive Control and Linear Controllers in Multi-Input DC-DC Boost Converter" *International Journal of Industrial Electronics, Control and Optimization*, Vol. 1, No. 3, pp. 27-34, Jan. 2020.

[21] X. Xing, L. Xie, and H. Meng, "Cooperative energy management optimization based on distributed MPC in grid-connected microgrids community" *Electrical Power and Energy Systems*, Vol. 107, pp. 186–199, May. 2019.

[22] E. F. Camacho, and C. Bordons, "Model Predictive Control", Springer, Second Edition, Jul. 2007.

[23] E. Zakeri, S. A. Moezi, and M. Eghtesad, "Optimal interval type-2 fuzzy fractional order super twisting algorithm: A second order sliding mode controller for fully-actuated and under-actuated nonlinear systems" *ISA Transactions*, Vol. 85, pp. 13-32, Feb. 2019.

[24] E. Zakeri, and H. Moeinkhah, "Digital control design for an IPMC actuator using adaptive optimal proportional integral plus method: Simulation and experimental study" *Sensors and Actuators A: Physical*, Vol. 298, pp. 1-14, Oct. 2019.

Ahmad Mirzaei was born in Tehran, Iran, in 1983. He received the B.E. degree in Electronics Engineering majoring in Control from University of Tabriz, Tabriz, Iran, in 2007, and his M.S. in Control Engineering from Tarbiat Modares University, Tehran, Iran, in 2013. Currently he is a Ph.D. candidate in Tarbiat Modares University, Tehran, Iran. He is also a research assistant at Advanced Control Systems Laboratory in Tarbiat Modares University. His research interests include Distributed Model Predictive Control, Large-Scale Systems, Cooperative Optimization, and Robust Control.

Amin Ramezani was born in Khuzestan, Iran, in 1979. He received his B.E. degree in Electronics Engineering from Shahid Beheshti University of Tehran, Tehran, Iran, in 2001, and his M.S. degree in Control systems from Sharif University of Technology, Tehran, Iran, in 2004. He received his Ph.D. degree in Electronics Engineering from the University of Tehran, Tehran, Iran, in 2011. In 2012, he joined the Department of Electrical Engineering, Tarbiat Modares University, Tehran, Iran, as a Lecturer. He is the chair of Advanced Control Laboratory and cooperates as the PC members of some conferences and special editor and reviewer of international journals in the field of control systems. His current research interests include Fault Tolerant Control Systems, Model-Based Predictive Control Systems, Stochastic Control Systems, and Hybrid Systems. He is a member of IEEE since 2005 and a member of Iranian Community Instrument and Control Engineers since 2012.

International Journal of Industrial Electronics, Control and Optimization © 2021 IECO
Vol. 4, No. 1, pp. 99-113 , Jan (2021)

A Controllable Bidirectional Rectifier for EV Home Charging Station with G2H/G2VH/V2H/V2G Functions

Homayon Soltani Gohari [1,†], Karim Abbaszadeh [2], and Jafar Gholami Gorji [3]

[1,2,3] Department of Electrical Engineering, K.N.Toosi University of Technology, Tehran, Iran.

ABSTRACT

Finding effective solutions to enhance the process of electric vehicle charging has been the main subject of numerous studies. This paper presents a novel bidirectional multiport rectifier that can be used as a wall-box converter that is installed in the parking lot of smart buildings and is capable of providing DC-link for local DC loads, such as DC home appliances and charge connected EV, simultaneously. The proposed converter is capable of working in G2H/G2VH/V2H/V2G modes, enabling the utility grid and costumers to use the EV as a mobile power source and reactive power compensator. A control method is also presented that enables the converter to control active and reactive power according to the smart grid or customer processed commands. To validate the features of the proposed converter, it is simulated in MATLAB/SIMULINK and the results are analyzed. A reduced-scale experimental setup of the proposed converter is built and tested, and the experimental results confirm the simulation ones.

Article Info

Keywords:
Active and Reactive Power Control, Bidirectional Rectifier, EV Charge Station, Vehicle to Grid, Vehicle to Home,

Article History:
Received 2020-06-12
Accepted 2020-09-04

I. INTRODUCTION

The use of different types of electric vehicles (EVs) is an effective solution for increasing environmental problems, such as greenhouse emissions, because of its enormous impact on the reduction of massive oil consumption in the transportation sector [1-3]. This has caused a significant rise in EVs usage. The pervasiveness of EVs and their charging needs have caused extensive concerns about their probable effects on the grid [4]. These concerns have led designers and researchers to consider controllable chargers (in terms of power factor (PF)) with low total harmonic distortion (THD) to confirm international standards [5].

Besides all the aforementioned adverse effects of the EVs, the increasing deployment of these cars have opened up several opportunities for users and smart grids [6-8]. The batteries of EVs have enabled them to work as mobile power sources that can retune their extra stored energy to the grid or suitable load [9-11]. Using appropriate topologies for EV chargers enables them to work in Vehicle-to-Grid (V2G) mode in which active power flows from EV to the grid, in addition to the traditional Grid-to-Vehicle (G2V) mode. A massive number of parked EVs with surplus stored energy provides an opportunity for smart grids to use them for peak shaving purposes. Additionally, EVs can be used as auxiliary power sources to handle AC and DC home appliances to reduce grid energy consumption, or as a backup generator during power outages [12, 13]. EVs can also be used as reactive power compensators that are located near loads and inject reactive power to the power grid [14, 15]. An appropriate topology is, however, required for chargers to allow grasping all these opportunities.

On the other hand, several benefits of a DC power distribution system (DC PDS), such as the absence of reactive

---

[†] **Corresponding Author**: Hsoltani@email.kntu.ac.ir
Tel: +98-9162490139
Faculty of Electrical Engineering, K.N.Toosi University of technology, Tehran, Iran

power and skin effect, which cause a rise in system efficiency and the reduction of the number of AC-DC converters, make that as a predictable future of PDS. Additionally, the flexibility and high efficiency provided by recent advances in power electronics and control methods have made it possible to integrate and merge different DC renewable energy sources efficiently in DC PDSs, primarily residential DC PDSs with undeniable increasing DC load demand due to DC home appliances [16-19]. The operation of EVs' chargers in different modes and applying their capabilities, such as operating as a mobile power source, is more efficient and more accessible in DC PDSs. In these systems, using renewable energies to charge EVs, handling DC home appliances, or returning the battery stored energy to the home or grid can be done quickly and efficiently. A very effective solution for increasing the entire system efficiency is to merge various power converters. AC-DC converters utilized for feeding home DC-Bus and chargers used for EVs are two types of conventional power converters that can be merged.

Although several converters in charging and rectification applications have already been introduced in previous studies, few works have focused on designing an appropriate topology for a converter capable of charging EVs' battery and providing a home DC-Bus simultaneously. The isolated bidirectional AC-DC converter introduced in [19] can be used only as a rectifier to feed the home DC-bus and charging the battery is not considered for that. The bidirectional chargers proposed in [20-22] can charge EV battery and return battery energy to the grid and household loads. Though they have several advantages because of their topologies, they cannot provide any DC-bus, so handling DC loads in V2H mode requires another AC-DC converter which may decrease system efficiency. The multiport converter proposed in [23] is suitable for integrating EVs in smart parking lots, but they can work only as a DC-DC converter and cannot rectify AC grid voltage. All high-performance converters introduced in [5, 24-27] can only charge the connected battery and cannot provide DC-bus for home applications simultaneously. The buck-boost rectifier presented in [28] can provide residential DC-link and cannot charge any EV simultaneously. In [29], a bidirectional rectifier is proposed that can provide two or more outputs. Although it can charge the battery and provide DC-bus simultaneously, the proposed converter cannot work in the V2H mode.

This paper presents a novel bidirectional multiport rectifier that can be installed in the parking lot of smart buildings and is capable of providing DC-bus for DC loads such as lighting systems, air conditioning systems, and charging connected EV batteries simultaneously. As illustrated in Fig. 1(a), the proposed converter can work in four operating modes according to the customer requirements and utility grid conditions. Working as a rectifier to feed DC-bus (G2H; Mode 1), feeding home DC loads and charging connected EV simultaneously (G2VH; Mode 2), handling DC loads during power outages by the stored energy of battery (V2H; Mode 3), and returning stored energy of batteries to the grid for peak shaving during peak hours (V2G; Mode 4) are the operating modes of the proposed converter. By adopting the control method introduced in this paper, the exchanged active and reactive power between the grid and the converter can be controlled according to the smart grid processed commands or costumer requirements, which enables it to be controlled during peak hours and operate as a reactive power compensator that is located very close to the loads. This ability not only causes a reduction in installation and maintenance costs of different reactive power compensators, such as capacitor banks or static synchronous compensators, but it also has no effect on battery performance.

II. ANALYSIS OF THE PROPOSED CONVERTER

A. *Configuration*

The structure of the presented converter is depicted in Fig.1(b). This two-stage converter consists of an AC-DC stage, as the primary stage, and a DC-DC stage, as the secondary stage. The primary stage includes an AC-DC H-bridge and a DC-link capacitor. Due to the introduced switching pattern, the switches of the left leg (S_{P1} and S_{P2}) have a high-frequency operation and switches of the right leg (S_{P3} and S_{P4}) are OFF or operate with grid frequency depending on the selected operating mode. The secondary stage is a three-port DC-DC converter that has the capability of working in different operating modes according to the status of the relays.

B. *Operation Principle and Steady-State Analysis*

The operation of each stage of the proposed converter depends upon the converter's operating mode that can be selected by the customer. The primary stage has the same operation in the two first modes (G2H and G2VH). In these modes, the primary stage rectifies the grid voltage with a changeable power factor, thanks to the control strategy introduced in section IV. In the third mode (V2H), the primary stage does not have any function and in the fourth mode (V2G), it works as a single-phase full-bridge inverter and delivers the stored energy of PEV's battery to the grid. The analysis of the converter is presented below in detail.

1- Mode1 (G2H)

- Primary Stage

As already mentioned, rectifying and boosting the grid voltage and controlling active and reactive power depending on the smart grid's commands or the customer's requirements are the tasks of the primary stage during this mode. As shown in Fig. 2, due to the selected high-efficiency switching method [30], in each half cycle of the grid voltage, the switching cycle is divided into two states. It is worth mentioning that only S_{P1} and S_{P2} have a high-frequency operation and S_{P3} and S_{P4} are OFF.

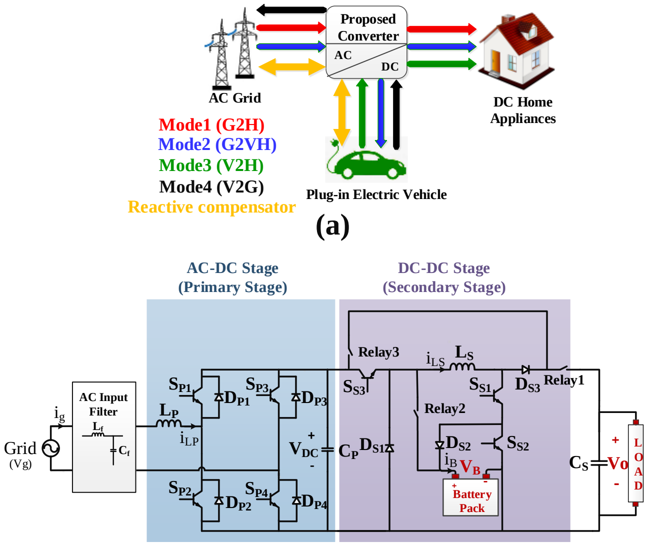

(a)

(b)

Fig.1. (a) The operating modes and (b) topology of the proposed converter

Vg>0: In the first state (0<t<DTs), the L_P is magnetized by (V_g) via the path provided by S_{P2} and D_{P4} [Fig. 2(a)]. In the next state (DTs<t<Ts), S_{P2} is turned OFF, so C_P is charged by the energy of L_P and the grid [Fig. 2(b)].

Vg<0: In this condition, as shown in Fig. 2(c)-(d), S_{P1} has a high-frequency operation. First, S_{P1} is ON, so L_P is magnetized by ($-V_g$) via D_{P3} and S_{P1} path [Fig. 2(c)]. Then, S_{P1} is turned OFF, so C_P is charged and L_P is demagnetized [Fig. 2(d)].

The voltage of L_P is obtained in the positive cycle of grid voltage by Eq. (1):

$$\begin{cases} V_{Lp} = V_g & 0<t<DT_s \\ V_{Lp} = V_g - V_{DC} & DT_s<t<T_s \end{cases} \qquad (1)$$

By applying the volt-sec balance law, the voltage gain of the boost rectifier can be achieved by Eq. (2):

$$\frac{V_{DC}}{V_g} = \frac{1}{1-D} \qquad (2)$$

- Secondary Stage

In this mode, the DC-DC stage can work as a buck and boost converter and control the V_o voltage according to V_o reference. When the converter is operated in this mode, relay1 is turned ON and relays 2 and 3 are turned OFF.

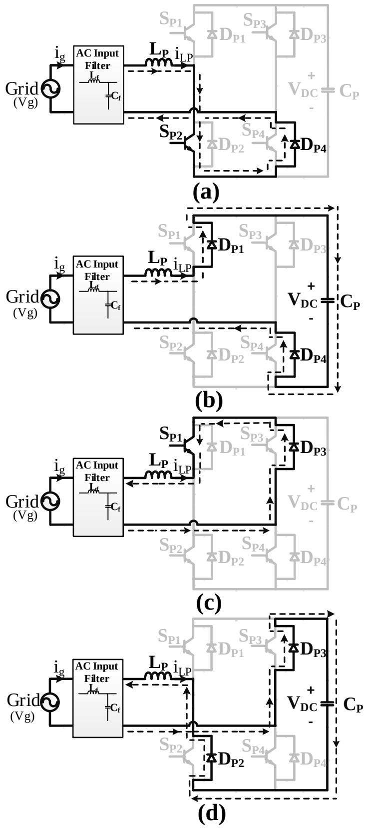

(a)

(b)

(c)

(d)

Fig.2. The operation states of the primary stage during mode 1 and mode 2 (a)-(b) Vg>0 (c)-(d) Vg<0

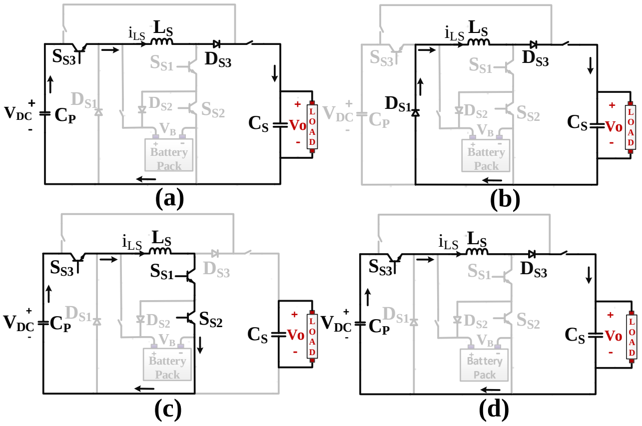

(a)

(b)

(c)

(d)

Fig.3. The operation states of the secondary stage during mode 1 (a)-(b) Buck (c)-(d) Boost

A- Buck

S_{S3}, L_s, and D_{S1} are the main components of the secondary stage in the buck condition. The switches S_{S1} and S_{S2} are OFF in this condition.

State 1 (0<t<DTs): In this state, S_{S3} is ON, so D_{S1} is reversely biased and L_s is magnetized with (V_{DC}-V_o) [Fig.3(a)].

State 2 (DTs<t<Ts): at t=DTs the S_{S3} is turned OFF, so D_{S1} is directly biased. L_s is demagnetized with ($-V_o$) and C_s is

charged [Fig. 3(b)].

As depicted in Fig. 3(a)-(b), the voltage and current of L_s and C_s are obtained as follows:

$$\begin{cases} V_{Ls} = V_{DC} - V_O & 0 < t < DT_s \\ V_{Ls} = -V_O & DT_s < t < T_s \end{cases} \tag{3}$$

$$\begin{cases} i_{CS} = i_{Ls} - \dfrac{P_o}{V_o} & 0 < t < DT_s \\ i_{CS} = i_{Ls} - \dfrac{P_o}{V_o} & DT_s < t < T_s \end{cases} \tag{4}$$

The volt-sec principle can be written as:

$$\frac{1}{T_s}\left[\int_0^{DTs}(V_{DC} - V_o)dt + \int_{DTs}^{Ts}(-V_o)\,dt\right] = 0 \tag{5}$$

So, the voltage gain is obtained by:

$$\frac{V_O}{V_{DC}} = D \tag{6}$$

And the average of L_s current is calculated by:

$$\langle i_{Ls}\rangle = \frac{Po}{Vo} \tag{7}$$

B- Boost

In the boost condition, S_{S2} and S_{S3} are ON and S_{S1} has a high-frequency operation. As depicted in Fig. 3(c)-(d), the operation of this stage is divided into two states in this mode.

State 1 (0<t<DTs): In this state, S_{S1} is ON, so D_{S3} is reversely biased and L_s is magnetized with (V_{DC}) [Fig. 3(c)]. Since S_{S2} is ON, the D_{S2} is reversely biased.

State 2 (DTs<t<Ts): at t=DTs, the S_{S1} is turned OFF, so D_{S3} is directly biased. L_s is demagnetized with (V_{DC} – V_{out}) and C_s is charged [Fig. 3(d)].

The voltage and current of L_s and C_s are obtained as follows:

$$\begin{cases} V_{Ls} = V_{DC} & 0 < t < DT_s \\ V_{Ls} = V_{DC} - V_O & DT_s < t < T_s \end{cases} \tag{8}$$

$$\begin{cases} i_{CS} = -\dfrac{P_o}{V_o} & 0 < t < DT_s \\ i_{CS} = i_{Ls} - \dfrac{P_o}{V_o} & DT_s < t < T_s \end{cases} \tag{9}$$

The volt-sec balance can be written as:

$$\frac{1}{T_s}\left[\int_0^{DTs}(V_{DC})dt + \int_{DTs}^{Ts}(V_{DC} - V_o)\,dt\right] = 0 \tag{10}$$

So, voltage gain can be obtained from:

$$\frac{V_O}{V_{DC}} = \frac{1}{1-D} \tag{11}$$

And the average of Ls current is calculated as:

$$\langle i_{Ls}\rangle = \frac{1}{1-D}\frac{Po}{Vo} \tag{12}$$

2- Mode 2 (G2VH)

- Primary Stage

The operation of this stage in the second mode is exactly similar to the first mode and rectifies grid voltage [Fig. 2].

- Secondary Stage

In the G2VH mode, the switches of the secondary stage are controlled so as to feed the DC load and charge the connected battery simultaneously. Like the G2H mode, when the converter is operated in the G2VH mode, S_{S3} and relay 1 are turned ON, and relays 2 and 3 are turned OFF. The switching cycle is divided into three states:

State1 (0<t<D_1Ts): In this time interval, both S_{S1} and S_{S2} are ON, so D_{S2} and D_{S3} are reversely biased. L_S is magnetized with V_{DC} [Fig. 4(a)].

State 2 (D_1Ts<t<D_2Ts): at t=D_1Ts, S_{S2} is turned OFF and D_{S2} is directly biased and the battery is consequently charged. L_S keeps charging with (V_{DC}-V_B). Until t=D_2Ts, the C_S handles the DC load [Fig. 4(b)].

State 3 (D_2Ts<t<Ts): at the beginning of this time interval, S_{S1} is turned OFF, so D_{S3} is directly biased, and L_S is demagnetized via D_{S3} and C_S path [Fig. 4(c)].

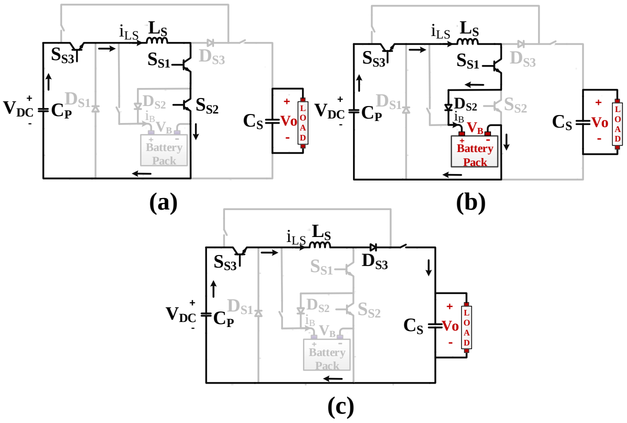

Fig.4. the operation states of the secondary stage during mode2

The voltage and current of L_S and C_S are obtained as follows:

$$\begin{cases} V_{Ls} = V_{DC} & 0 < t < D_1T_s \\ V_{Ls} = V_{DC} - V_B & D_1T_s < t < D_2T_s \\ V_{Ls} = V_{DC} - V_o & D_2T_s < t < Ts \end{cases} \tag{13}$$

$$\begin{cases} i_{CS} = -\dfrac{P_o}{V_o} & 0 < t < D_1T_s \\ i_{CS} = -\dfrac{P_o}{V_o} & D_1T_s < t < D_2T_s \\ i_{CS} = i_{Ls} - \dfrac{P_o}{V_o} & D_2T_s < t < T_s \end{cases} \tag{14}$$

The pertinent equation for the volt-sec balance can be written as follows:

$$\frac{1}{T_s}\left[\int_0^{D1Ts}(V_{DC})dt + \int_{D1Ts}^{D2Ts}(V_{DC}-V_B)\,dt + \int_{D2Ts}^{Ts}(V_{DC}-V_o)\,dt\right] = 0 \tag{15}$$

The output voltage (V$_O$) of mode 2 can be calculated using Eq. (16):

$$V_o = \frac{1}{1-D_2}V_{DC} - \frac{D_2-D_1}{1-D_2}V_B \tag{16}$$

By applying the current-sec principle on C$_S$, the average current of L$_S$ is obtained as:

$$\langle i_{Ls} \rangle = \frac{1}{1-D_2}\frac{Po}{Vo} \tag{17}$$

3- Mode 3 (V2H)

Transferring the battery's stored energy to DC load is the task of the proposed converter in this mode. By turning OFF the S$_{S3}$ and relay 3 and also turning ON the relays 1 and 2, the converter receives the power from the battery and is disconnected from the primary stage. So, the primary stage does not have any task in this mode.

- Secondary Stage

In this mode, S$_{S2}$ is ON and only S$_{S1}$ has a high-frequency operation.

State 1 (0<t<DTs): in this time interval, S$_{S1}$ is ON, so L$_S$ is magnetized with (V$_B$) [Fig. 5(a)].

State 2 (DTs<t<Ts): at the beginning of this time interval, S$_{S1}$ is turned OFF, so D$_{S3}$ is directly biased, and L$_S$ is demagnetized by (V$_B$ - V$_O$) [Fig. 5(b)].

The voltage across L$_S$ in mode 3 is determined by the following equations:

$$\begin{cases} V_{Ls} = V_B & 0 < t < DT_s \\ V_{Ls} = V_B - V_O & DT_s < t < T_s \end{cases} \tag{18}$$

The L$_S$ volt-sec principle can be written as:

$$\frac{1}{T_s}\left[\int_0^{DTs}(V_B)dt + \int_{DTs}^{Ts}(V_B - V_o)\,dt\right] = 0 \tag{19}$$

So, the voltage gain is be obtained by:

$$\frac{V_O}{V_B} = \frac{1}{1-D} \tag{20}$$

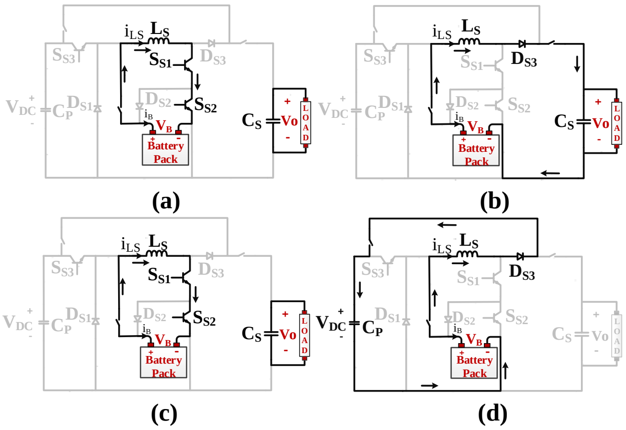

Fig. 5. The operation states of the secondary stage during (a)-(b) mode 3 (c)-(d) mode 4

4- Mode 4 (V2G):

In this mode, the converter delivers the battery's stored energy to the grid with controllable active and reactive power. First, the DC-DC stage regulates the battery voltage according to V$_{DC,ref}$. Then, the AC-DC stage works as a single-phase full-bridge inverter and inverts the DC voltage of DC-link to AC. So, in this part, the DC-DC stage is analyzed before the AC-DC stage.

- Secondary Stage

The operation of the DC-DC stage in this stage is similar to mode 3 with a minor difference. In this mode, relays 2 and 3 are turned ON, and relay 1 is turned OFF, so the secondary stage charges C$_P$ instead of C$_S$.

State 1 (0<t<DTs): in this time interval, S$_{S1}$ is ON, so L$_S$ is magnetized by (V$_B$) [Fig. 5(c)].

State 2 (DTs<t<Ts): at t=DTs, the S$_{S1}$ is turned OFF, so D$_{S3}$ is directly biased, and since R1 is ON, LS is demagnetized by (V$_B$ - V$_{DC}$) [Fig. 5(d)].

The Ls volt-sec balance law can be written as:

$$\frac{1}{T_s}\left[\int_0^{DTs}(V_B)dt + \int_{DTs}^{Ts}(V_B - V_{DC})\,dt\right] = 0 \tag{21}$$

And voltage gain is obtained by:

$$\frac{V_{DC}}{V_B} = \frac{1}{1-D} \tag{22}$$

- Primary Stage

In this mode, the primary stage works as a single-phase full-bridge inverter that inverts the DC voltage of the DC-link to AC with controllable active and reactive power according to the smart grid commands or customer. Similar to the G2H and G2VH modes, the switching pattern of this stage depends on the grid voltage sign. The switching states and current paths are shown in Fig. 6.

The voltage of LP is obtained by Eq. (23):

$$\begin{cases} V_{Lp} = V_{DC} - V_g & 0 < t < DT_s \\ V_{Lp} = -V_g & DT_s < t < T_s \end{cases} \tag{23}$$

By applying the volt-sec balance law, the voltage gain of the buck inverter can be estimated by Eq. (24):

$$\frac{V_g}{V_{DC}} = D \tag{24}$$

C. Design Considerations

- **L_P**

The analysis of the L_P's current ripple during inductor magnetizing time (kTs < t < D(k+1)Ts) is the key to calculating the required inductor value. The L_P's current ripple can be written as Eq. (25):

$$\Delta i_g = \frac{V_{LP} \times D \times T_s}{L_P} \tag{25}$$

By using KVL during inductor magnetizing time, the inductor voltage is achieved as:

$$V_{LP} = V_g \tag{26}$$

By substituting the voltage gain of boost rectifier (27) into (26), the L_P's current ripple is obtained as Eq. (28):

$$V_g = (1-D) \times V_{DC} \tag{27}$$

$$\Delta i_g = \frac{V_{DC} \times D \times (1-D)}{L_P \times f_s} \tag{28}$$

The worst case in calculating L_P is related to the maximum value of (D(1-D)), which is 0.25, so the L_P's value can be obtained by using Eq. (30):

$$Max(D(1-D)) = 0.25 \tag{29}$$

$$L_P = \frac{V_{DC}}{4 \times \Delta i_g \times f_s} \tag{30}$$

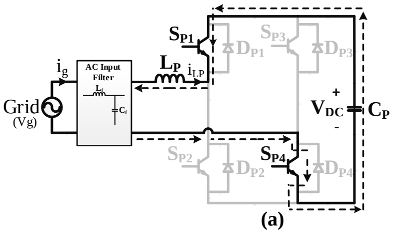

Fig. 6(a)

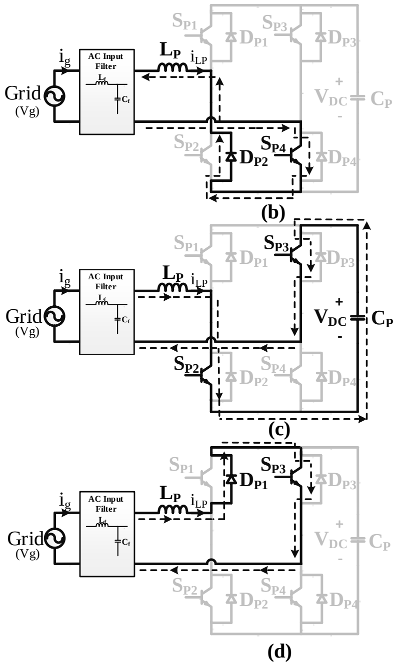

Fig. 6. The operation states of the primary stage during mode4 (a)-(b) Vg>0 (c)-(d) Vg<0

- **C_{DC}**

Handling constant-power loads from a single-phase power grid needs an intermediary device, which is named C_P in this converter. Having appropriate voltage and current in each output ports in terms of ripple depends on the suitable DC-link capacitor (C_P). The DC-link voltage has two terms:

$$v_{DC} = V_{DC} + \Delta v_{DC} \tag{31}$$

where V_{DC} and Δv_{DC} are the average value and oscillating amplitude of DC-link voltage, respectively. The energy of C_P can be calculated as follows:

$$\frac{1}{2} \cdot C_P \cdot v_{DC}{}^2 = \int \tilde{p} dt \tag{32}$$

where $\tilde{p}$ is the oscillating value of the instantaneous power:

$$\tilde{p} = 2VI\cos(2\omega t + \varphi) \tag{33}$$

By substituting Eq. (33) into Eq. (32), the required value of C_P is obtained as:

$$C_P = \frac{2V_g I_g}{\omega \Delta v_{DC} V_{DC}} \tag{34}$$

- **L_S**

The DC-DC stage operation in the CCM condition depends on the L_S value, which can be calculated as follows:

$$L_{S\,\min} = \frac{D_3{}^2 (V_{DC} - V_o) V_o}{P_{out} f_S} \tag{35}$$

- **C_f and L_f**

To design an effective input filter, the maximum value of the capacitor of the filter can be obtained as:

$$C_{f\,\max} = \frac{I_m}{\omega V_m}\tan(\theta) = \frac{\sqrt{2}P_{\max}}{\omega_L V_m V_g}\tan(\theta) \tag{36}$$

where V_m and I_m are the peak values of the grid voltage and input current, respectively. θ is the displacement angle between the grid voltage and input current, respectively [31]. The required inductive component (L_{req}) can be calculated by using Eq. (37):

$$L_f = L_{req} + L_g \rightarrow L_{req} = \frac{1}{4\pi^2 f_c^2 C_f} - 4\times10^{-2}\times\left[\frac{1}{\omega_L}\right]\times\left[\frac{V_g^2}{P_{out}}\right] \tag{37}$$

where f_c is the cut-off frequency and L_g is the grid impedance, which is considered 4-5% of the base impedance [32].

D. Efficiency Analysis

To analyze the efficiency of the proposed converter, the parasitic resistance of different components should be considered in addition to the threshold voltage of diodes. R_{Lp} and R_{Ls} are the equivalent series resistance (ESR) of the primary and secondary inductors, respectively. The primary and secondary stage diodes forward resistance are R_{FDpi} and R_{FDsi}, respectively, with V_{FDpi} and V_{FDsi} threshold voltages. Similarly, r_{DSpi} and r_{DSsi} are the primary and secondary switches ON-state resistance. ESR of the capacitors is assumed to be r_{cp} and r_{cs}. It is worth mentioning that the efficiency analysis is done in mode 2, which contains the most parasitic resistance counts.

The conduction losses of inductors can be calculated by using the RMS currents of inductors and their ESR as follows:

$$P_{R_{Ls}} = R_{Ls} I^2_{rms,Ls} = R_{Ls}\left(\frac{I_o}{1-D_2}\right)^2 \tag{38}$$

$$P_{R_{Lp}} = R_{Lp} I^2_{rms,Lp} = R_{Lp}\left(\frac{I_{rms,Lp}}{1-D_p}\right)^2 = R_{Lp}\left(\frac{I_o}{(1-D_p)(1-D_2)}\right)^2 \tag{39}$$

where D_P is the duty cycle of the primary stage.

To calculate the conduction losses of the power switches, RMS values switches currents are needed, which can be calculated as:

$$I_{rms,SP2} = \sqrt{\frac{1}{Ts}\int_0^{D_pTs} i_{SP2}^2 dt} = \sqrt{\frac{1}{Ts}\int_0^{D_pTs} i_{L_p}^2 dt} = \sqrt{D_p}\, i_{L_p} = \frac{\sqrt{D_p}}{(1-D_p)(1-D_2)} I_o \tag{40}$$

$$I_{rms,S1} = \sqrt{\frac{1}{Ts}\int_0^{D_2Ts} i_{Ls}^2 dt} = \sqrt{D_2}\, i_{Ls} = \frac{\sqrt{D_2}}{(1-D_2)} I_o \tag{41}$$

$$I_{rms,S2} = \sqrt{\frac{1}{Ts}\int_0^{D_1Ts} i_{Ls}^2 dt} = \frac{\sqrt{D_1}}{(1-D_2)} I_o \tag{42}$$

$$I_{rms,S3} = \frac{1}{(1-D_2)} I_o \tag{43}$$

So, the conduction losses are calculated as:

$$\mathrm{P}_{r\,DSP2} = r_{DSP2} I^2_{rms,SP2} = r_{DSP2}\left(\frac{\sqrt{D_p}}{(1-D_p)(1-D_2)} Io\right)^2 \tag{44}$$

$$\mathrm{P}_{r\,DSS1} = r_{DSS1} I^2_{rms,S1} = r_{DSS1}\left(\frac{\sqrt{D_2}}{1-D_2} I_o\right)^2 \tag{45}$$

$$\mathrm{P}_{r\,DSS2} = r_{DSS2} I^2_{rms,S2} = r_{DSS2}\left(\frac{\sqrt{D_1}}{1-D_2} I_o\right)^2 \tag{46}$$

$$\mathrm{P}_{r\,DSS3} = r_{DSS3} I^2_{rms,S3} = r_{DSS3}\left(\frac{1}{1-D_2} I_o\right)^2 \tag{47}$$

The switching losses should also be considered that can be calculated by the following equations:

$$P_{SWP2} = f_s C_s V_{P2}^2 = f_s C_s \left(\frac{V_g}{1-D_p}\right)^2 \tag{48}$$

$$P_{SWS1} = f_s C_s V_{S1}^2 = f_s C_s \left(\frac{V_o}{2}\right)^2 \tag{49}$$

$$P_{SWS2} = f_s C_s V_{S2}^2 = f_s C_s \left(\frac{V_o}{2}\right)^2 \tag{50}$$

RMS values of the diodes' currents can be calculated as:

$$I_{rms,DP1} = \sqrt{\frac{1}{Ts}\int_0^{Ts} i_{DP1}^2 dt} = \sqrt{\frac{1}{Ts}\int_{D_pTs}^{Ts} i_{L_p}^2 dt} = \sqrt{1-D_p}\, i_{L_p} = \frac{\sqrt{1-D_p}}{(1-D_p)(1-D_2)} I_o \tag{51}$$

$$I_{rms,DP4} = \sqrt{\frac{1}{Ts}\int_0^{Ts} i_{DP4}^2 dt} = \sqrt{\frac{1}{Ts}\int_0^{Ts} i_{L_p}^2 dt} = i_{L_p} = \frac{1}{(1-D_p)(1-D_2)} I_o \tag{52}$$

$$I_{rms,DS2} = \sqrt{\frac{1}{Ts}\int_{D_1Ts}^{D_2Ts} i_{Ls}^2 dt} = \frac{\sqrt{D_2-D_1}}{1-D_2} I_o \tag{53}$$

$$I_{rms,DS3} = \sqrt{\frac{1}{Ts}\int_{D_2Ts}^{Ts} i_{Ls}^2 dt} = \frac{1}{\sqrt{1-D_2}} I_o \tag{54}$$

So, the diodes' forward resistance losses can be calculated as:

$$\mathrm{P}_{R_{FDP1}} = R_{FDP1} I^2_{rms,DP1} = R_{FDP1}\left(\frac{\sqrt{1-D_p}}{(1-D_p)(1-D_2)} I_o\right)^2 \tag{55}$$

$$\mathrm{P}_{RFDP4} = R_{FDP4} I^{2}_{rms,DP4} = R_{FDP4}\left(\frac{1}{(1-D_p)(1-D_2)} I_o\right)^2 \tag{56}$$

$$\mathrm{P}_{RFDS2} = R_{FDS2} I^{2}_{rms,DS2} = R_{FDS2}\left(\frac{\sqrt{D_2-D_1}}{1-D_2} I_o\right)^2 \tag{57}$$

$$\mathrm{P}_{RFDS3} = R_{FDS3} I^{2}_{rms,DS3} = R_{FDS3}\left(\frac{1}{\sqrt{1-D_2}} I_o\right)^2 \tag{58}$$

And their forward voltage losses are calculated by Eq. (59)-(62).

$$P_{VF,DP1} = V_{FDP1} I_{DP1} = (V_{FDP1})\left(\frac{1}{1-D_2} I_o\right) \tag{59}$$

$$P_{VF,DP4} = V_{FDP4} I_{DP4} = (V_{FDP4})\left(\frac{1}{(1-D_p)(1-D_2)} I_o\right) \tag{60}$$

$$P_{VF,DS2} = V_{FDS2} I_{DS2} = (V_{FDS2})\left(\frac{D_2-D_1}{1-D_2} I_o\right) \tag{61}$$

$$P_{VF,DS3} = V_{FDS3} I_{DS3} = (V_{FDS3})(I_o) \tag{62}$$

To calculate the capacitors' power losses, their RMS currents are needed, so:

$$I_{rms,CS} = \sqrt{\frac{1}{Ts}\left[\int_0^{D_2Ts} (-I_o)^2 dt + \int_{D_2Ts}^{Ts} (i_{Ls}-I_o)^2 dt\right]} = \sqrt{(D_2 I_o^{\,2}) + (1-D_2)(i_{Ls}-I_o)^2} = \sqrt{\frac{D_2}{1-D_2}} I_o \tag{63}$$

$$I_{rms,Cp} = \sqrt{\frac{1}{Ts}\left[\int_0^{D_pTs} (iLs)^2 dt + \int_{D_pTs}^{Ts} (i_{Lp})^2 dt\right]} = \sqrt{\left(\frac{D_p}{(1-D_2)^2}\right) I_o^{\,2} + \left(\frac{D_p^{\,2}}{(1-D_p)(1-D_2)}\right) I_o^{\,2}} = \sqrt{\frac{D_p}{(1-D_p)(1-D_2)^2}} I_o \tag{64}$$

So, the capacitors' power losses are obtained as follows:

$$\mathrm{P}_{\mathrm{r}\,CS} = r_{CS} I^{2}_{rms,CS} = r_{CS}\left(\sqrt{\frac{D_2}{1-D_2}} I_o\right)^2 \tag{65}$$

$$\mathrm{P}_{\mathrm{r}\,Cp} = r_{Cp} I^{2}_{rms,Cp} = r_{Cp}\left(\sqrt{\frac{D_p}{(1-D_p)(1-D_2)^2}} I_o\right)^2 \tag{66}$$

The total power loss is the sum of the calculated losses, which is obtained by:

$$P_{Loss} = \sum P_{RL} + \sum \mathrm{Pr}_{DS} + \sum P_{SW} + \sum P_{RFD} + \sum P_{VFD} + \sum \mathrm{P}_{\mathrm{r}\,C} \tag{67}$$

And finally, the efficiency of the proposed converter in mode2 is calculated by Eq. (68):

$$\eta = \frac{1}{1+\frac{P_{LOSS}}{P_o}} \frac{1}{1+\frac{A}{R_o(1-D_2)^2} + \frac{B}{R_o(1-D_p)^2(1-D_2)^2} + \frac{C}{P_o(1-D_p)^2} + \frac{D}{2P_o}} \cdots$$
$$\cdots \frac{1}{+\frac{E}{R_o(1-D_2)} + \frac{F}{1-D_2} + \frac{G}{R_o(1-D_p)(1-D_2)^2} + \frac{H}{(1-D_p)(1-D_2)}} \tag{68}$$

where

$$\begin{aligned}
A &= R_{Ls} + r_{DSS1} D_2 + r_{DSS2} D_1 + r_{DSS3} + R_{FDS2}(D_2 - D_1)\\
B &= R_{Lp} + r_{DSP2} D_p + R_{FDP1}(1-D_p) + R_{FDP4}\\
C &= f_s C_s V_g^{\,2}\\
D &= f_s C_s V_o^{\,2} + 2V_{FDS3} I_o\\
E &= R_{FDS3} + r_{CS} D2\\
F &= V_{FDP1} + V_{FDS2}(D_2 - D_1)\\
G &= r_{Cp} D_p\\
H &= V_{FDP4} I_o
\end{aligned} \tag{69}$$

III. COMPARISON STUDY

The presented converter is compared with similar converters introduced in recent years in terms of operating modes that they can work in and the number of high-frequency switches. The results are provided in Table 1.

TABLE I. THE COMPARISON OF THE PROPOSED CONVERTER WITH CONVENTIONAL CONVERTERS

Reference	Operating modes					Number of high-freque-ncy switches
	G2H	**G2VH**	**V2H**	**V2G**	**G2V**	
[5]	×	×	×	×	✓	1
[19]	✓	×	×	✓	×	12
[20]	×	×	×	✓	✓	6
[21]	×	×	×	✓	✓	6
[22]	×	×	×	✓	✓	8
[23]	×	×	×	✓	✓	3
[24]	×	×	×	×	✓	2
[25]	×	×	×	×	✓	8
[26]	×	×	×	×	✓	3
[27]	×	×	×	×	✓	2
[28]	✓	×	×	×	×	1
[29]	✓	✓	×	✓	✓	6
The proposed converter	✓	✓	✓	✓	✓	7

IV. CONTROL METHOD

Designing an appropriate controller is necessary to control the input current waveform and also active and reactive power flowing between the grid and the proposed converter. Similar to other two-stage converters, the proposed converter needs two interrelated controllers. They can work dependently or independently with one another depending on the system operation. The system condition simulated and implemented in the experimental setup in this paper needs independent controller subsections, so only the primary stage controller is analyzed and the secondary stage operates open loop.

In this paper, a dual-loop Proportional-Integral (PI) controller is considered for the AC-DC stage. Using a dual-loop PI controller improves the converter performance and also input current and output voltage in terms of THD and ripple, respectively. The first loop controls the active and reactive power according to the utility grid commands or customer requirements by calculating input current reference. It is possible to control the DC-link voltage directly by setting $V_{DC,ref}$ manually. In this case, the controller is allowed to control only reactive power. The second loop generates gate pulses by calculating the difference between reference and measured input current.

As illustrated in Fig. 7, the quadrature signals of grid voltage and input current are first driven by using delay blocks. Then, the single-phase active and reactive power is computed by using the instantaneous pq theory introduced in [33]. After that, there are P-loop and Q-loop controllers. In the P-loop, a PI controller is first used to modify $V_{DC,ref}$ in order to track active power command (P_C). Afterward, another PI controller is used to track the calculated $V_{DC,ref}$. Similarly, in the Q-loop, a PI controller is used to track reactive power command (Q_C). In this step, there are two options: (1) controlling the DC-link voltage directly by setting $V_{DC,ref}$ and controlling reactive power; and (2) controlling active and reactive power simultaneously according to the processed commands from the utility grid or customer. In the first case (the method simulated and tested in this paper), the two stages' controllers can work independently, but in the second case, they have to work dependently. The computed active and reactive power is used to calculate input current reference via Eq. (70)-(72):

$$\theta = \tan^{-1}\left(\frac{Q_{ref}}{P_{ref}}\right) \tag{70}$$

$$I_{ref} = \frac{P_{ref}}{V_g \operatorname{Cos}(\theta)} \tag{71}$$

$$i_{ref}^{\ *} = \sqrt{2} I_{ref} \operatorname{Sin}(\omega t - \theta) \tag{72}$$

In the second loop, the calculated reference and measured currents are used to obtain the error signal that is fed to the PI controller. The output of the PI controller is compared with a 30kHz triangle waveform and finally, the gate pulses are generated using logic blocks as shown in Fig. 7.

The dynamic of this converter is nonlinear. If the dynamic of the system is linearized, a linear controller can be used. With attention to the system dynamic, it can be linearized around its set point, and then a linear cascade controller via the bode diagram technique in frequency space can be designed. Fig. 8 shows the bode plot of the DC-link voltage in open loop, open loop via a controller, and closed-loop via controller conditions with properties provided in Table 2. As shown in Fig. 8, the AC-DC stage can be controlled by using a properly designed PI controller with PI parameters calculated according to Fig. 8 and Table.2.

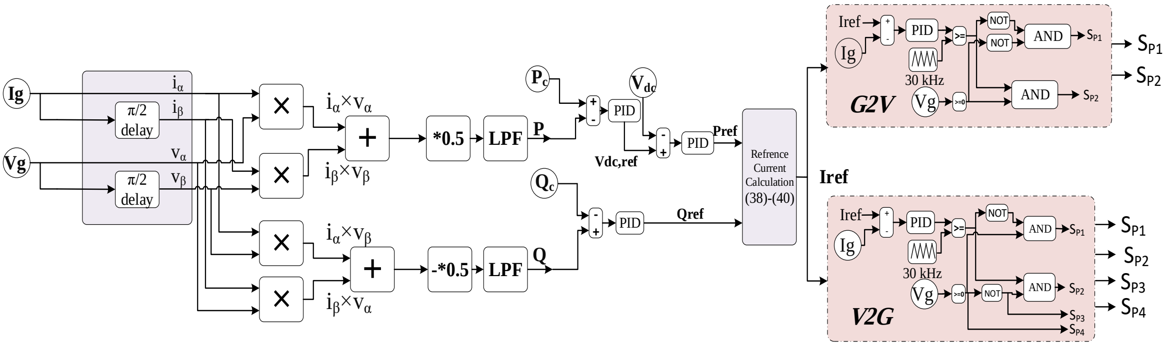

Fig. 7. The proposed control method

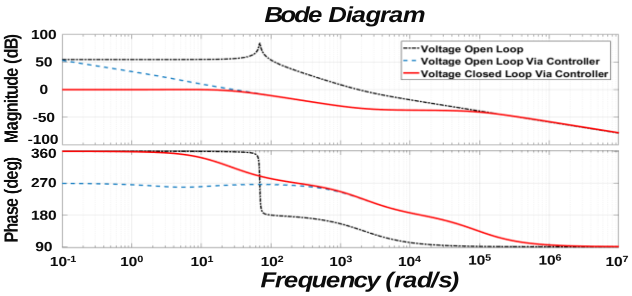

Fig. 8. The bode plot of the DC-link voltage

TABLE II. THE BODE PLOT PROPERTIES

Closed-loop via controller Bandwidth	31.9 rad/S
Open-loop	
Gain Margin	-54.5 dB
Phase Margin	-40.1 deg
Open-loop via Controller	
Gain Margin	37.3 dB
Phase Margin	85.1 deg
Closed-loop	
Gain Margin	37.2 dB
Phase Margin	161 deg

V. SIMULATION RESULTS

The presented converter has been simulated in different modes in the MATLAB/SIMULINK software to validate system analysis. The converter specifications are tabulated in Table 3. It is assumed that the converter is connected to the grid (220 V_{rms}), and the battery pack voltage is considered 320V. The home DC link is 400V with a 5kW DC load.

The proposed converter is simulated in unity power condition in mode 1 and results are presented in Fig. 9 through Fig. 15. Fig. 9 shows the grid voltage (V_g) and input current (I_g) in the UPF condition. The FFT analysis in three cycles of the input current is shown in Fig. 10, which illustrates the THD value as 3.47% with acceptable harmonic orders. Figs. 11 and 12 are related to the control unit operation in either mode1 or mode 2. Fig. 11 shows the current loop PID output which is compared with a 30 kHz triangular wave. The S_{P1} and S_{P2} gate pulses are depicted in Fig. 12. As already mentioned, S_{P1} and S_{P2} have a high-frequency operation in the negative and positive half cycle of the grid voltage, respectively.

TABLE III. THE PROPOSED CONVERTER'S SPECIFICATIONS

	Simulation	*Experimental*
Input voltage (Vg)	220 V(RMS)	30 V(RMS)
Output voltage (Vo)	400 V	160 V
DC-link voltage (V_{DC})	340 V	110 V
Output Power	5 kW	200 W
Battery Voltage	320 V	70 V
L_P	4.4 mH	4 mH
Ls	1.5 mH	1.5 mH
C_P	9 mF	6 mF
Cs	680 uF	470 uF
Maximum input current THD	4.24%	-
AC Input Frequency	50 Hz	50 Hz
Switching Frequency	30kHz	30 kHz
Maximum Output Voltage Ripple	2%	-
Power Factor	0.99	0.99
Controller	-	ARMSTM32F103RET
Mosfet	-	KF13N60
Current Sensor	-	ACS712

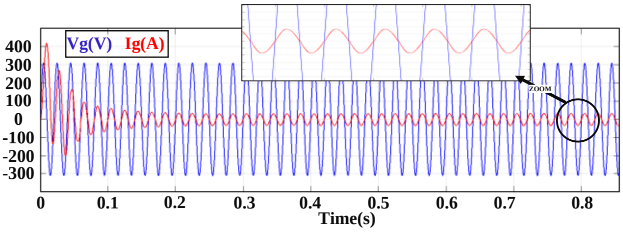

Fig. 9. The grid voltage and input current in mode 1

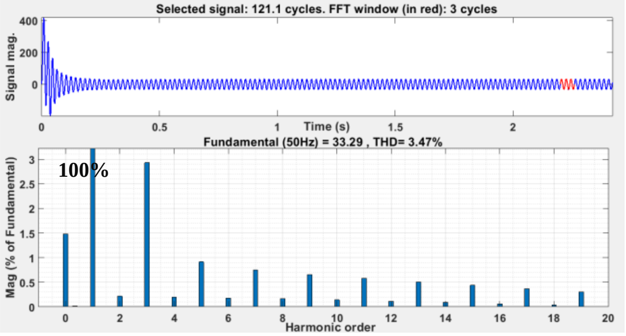

Fig. 10. The FFT analysis of input current in mode 1

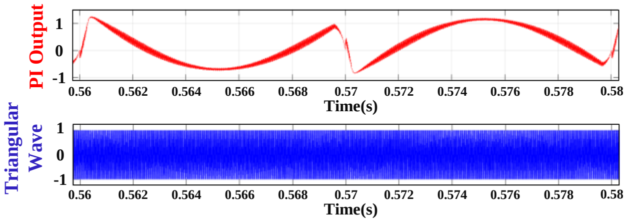

Fig. 11. The current loop PID output and triangular wave

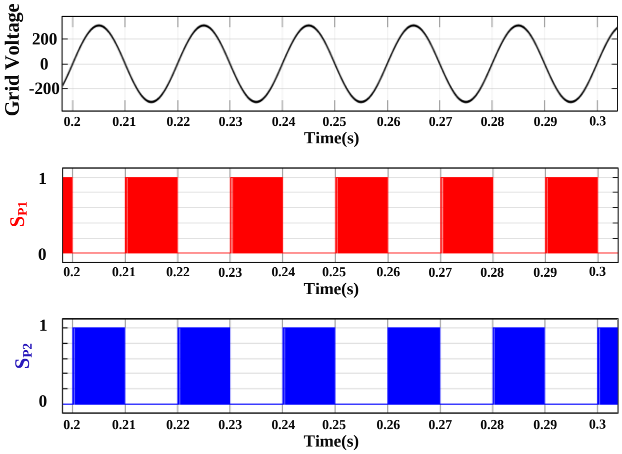

Fig. 12. The gate pulses of S_{P1} and S_{P2} in mode 1

Fig.13 illustrates the reference and measured input current, which shows the perfect capability of the converter to track the current reference generated by the controller. The desired DC-link and output voltages are tracked with a good transient, as shown in Fig. 14. Fig. 15 displays the voltage and current of L_S in mode 1.

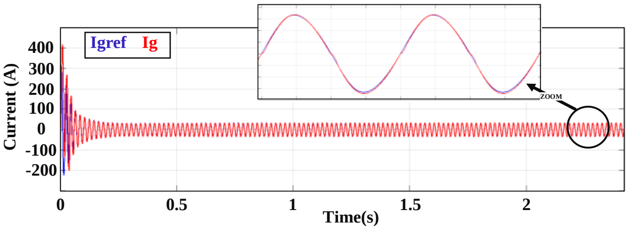

Fig. 13. The measured and reference input current in mode 1

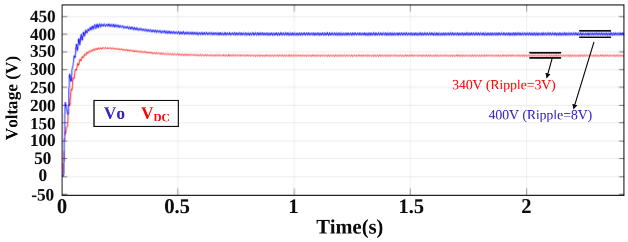

Fig. 14. The DC-link voltage and output voltage in mode 1

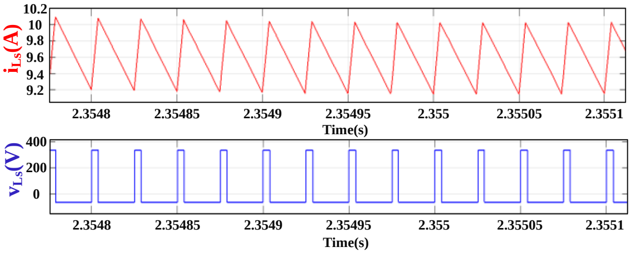

Fig. 15. The voltage and current of L_S in mode 1

The converter's behavior during load changing in mode 1 is illustrated in Figs. 16 and 17. The output power is increased in three steps (1kW, 2kW, and 5kW) at t=1 and 2s. The current rise due to load increase is shown in Fig. 16(a). As shown in Fig. 16(b), at all loads, the PF is more than 0.99 with the sinusoidal input current.

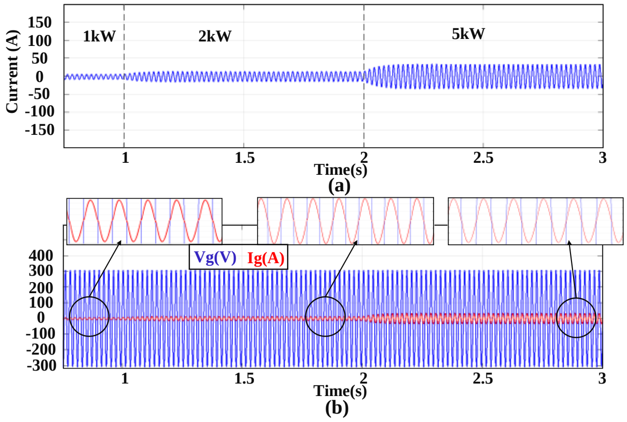

Fig. 16. (a) The input current and (b) grid voltage and input current during load changing in mode1

Transient and steady-state of DC-link voltage and output voltage are shown in Fig. 17. The steady-state of DC-link and output voltages are fixed on their set point (340V and 400V, respectively), which shows the robustness of the adopted control method.

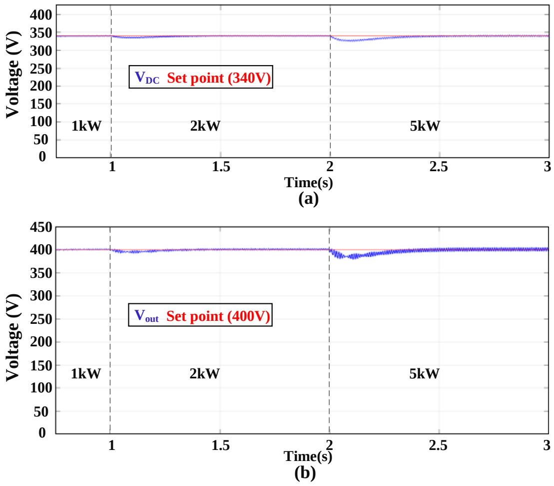

Fig. 17. (a) DC-link and (b) output voltages during load changing in mode1

The second operating mode (G2VH) is also simulated, and the results are provided. Fig. 18 displays the grid voltage and input current of the converter in mode 2 and also the converter's capability of correcting the power factor. As illustrated in Fig. 19, the THD of the input current is 4.09%. The operation of the converter in this mode is divided into three states. The voltage and current of L_S in different states are shown in Fig. 20. The transient and steady-state of V_{DC} and V_O are depicted in Fig. 21. The output voltage ripple is less than 1.5%.

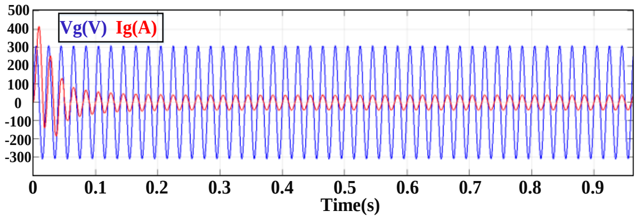

Fig. 18. The grid voltage and input current in mode 2

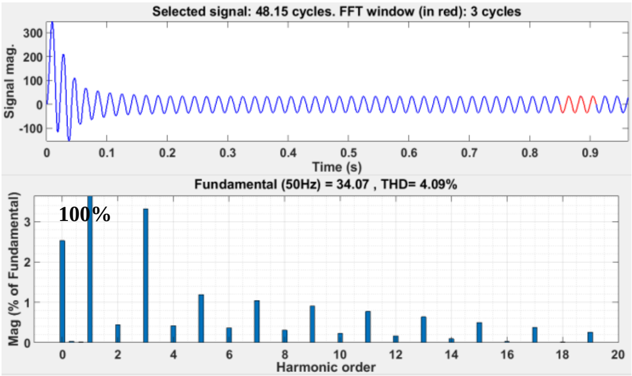

Fig. 19. The FFT analysis of the input current in mode 2

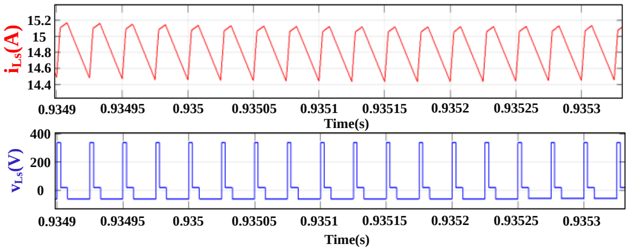

Fig. 20. The voltage and current of L_S in mode 2

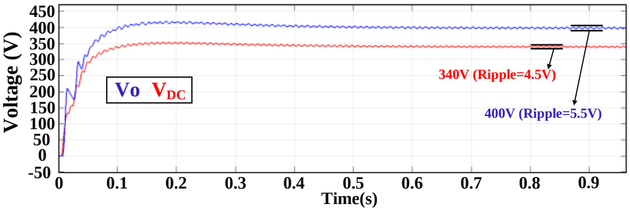

Fig. 21. The DC-link voltage and output voltage in mode 2

The behavior of the converter during load changing in mode2 is also analyzed and results are shown in Fig. 22.

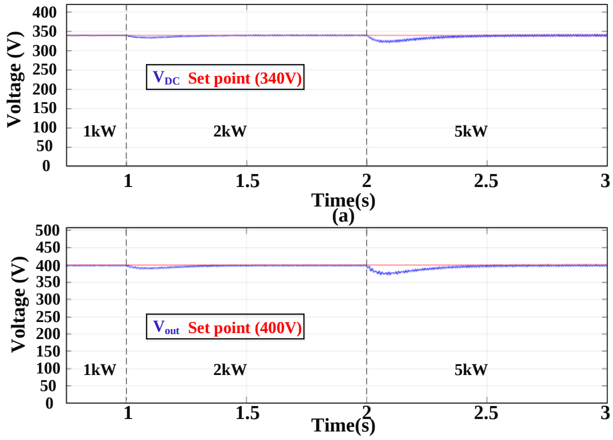

(b)

Fig. 22. The DC-link and output voltages during load changing in mode 2

The proposed converter is simulated with real components (considering ON-state resistance and forward voltages for diodes and switches and resistance for inductor) during mode2 and its efficiency is measured as illustrated in Fig. 23.

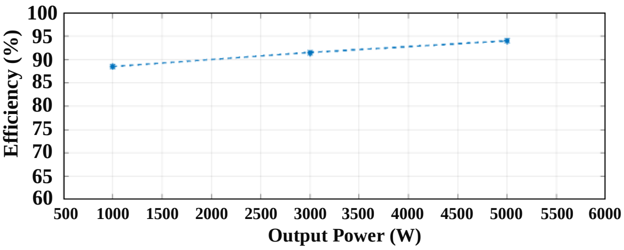

Fig. 23. The converter efficiency in mode 2

The primary stage does not have any task in mode 3. In this mode, the battery provides the energy needed by the DC load. Fig. 24 shows the output voltage in mode 3. As can be seen, the output voltage has an acceptable ripple.

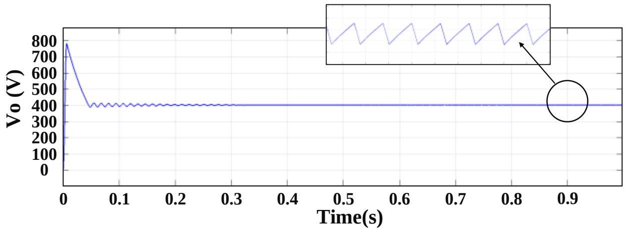

Fig. 24. The output voltage in mode 3

The results of the mode 4 simulation are provided in Figs. 25-27. Fig. 25 shows the switching pattern of S_{P1}~S_{P4}. S_{P1} and S_{P2} have a high-frequency operation, and S_{P3} and S_{P4} operate with grid frequency. Figs. 26 and 27 illustrate the input current waveform and its FFT analysis, respectively.

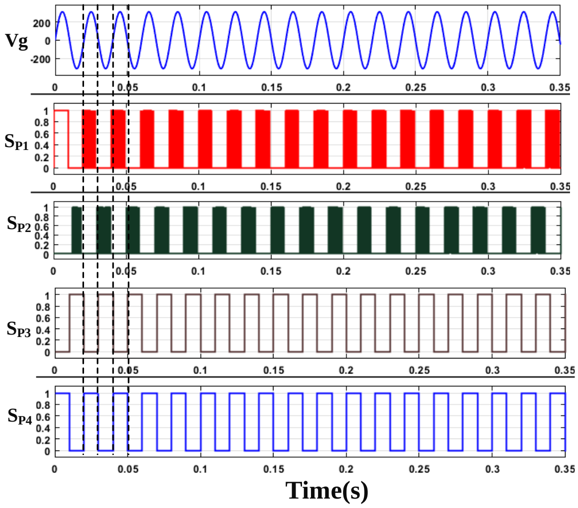

Fig. 25. The gate pulses of S_{P1} ~ S_{P4} in mode 4

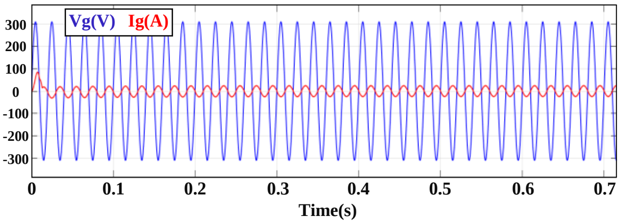

Fig. 26. The grid voltage and input current in mode 4

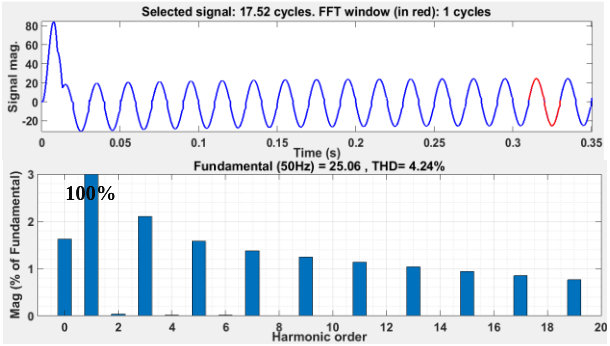

Fig. 27. The FFT analysis of input current in mode 4

VI. EXPERIMENTAL VERIFICATION

To confirm the simulation results, an experimental prototype has been built and tested. The reduced-scale experimental setup is shown in Fig. 28 and its specifications are tabulated in Table 3.

The grid voltage and input current are shown in Fig. 29(a) in the unity PF condition. The gate pulses of the primary stage switches (S_{P1} and S_{P2}) generated with the controller (STM32F103RET) are depicted in Fig. 29(b)-(c). The converter is tested in mode 1 under buck and boost conditions and the DC-link and output voltages are shown in Figs. 29(d) and 29(e), respectively. Fig. 29(f) shows the voltage across L_S in mode 1 boost condition.

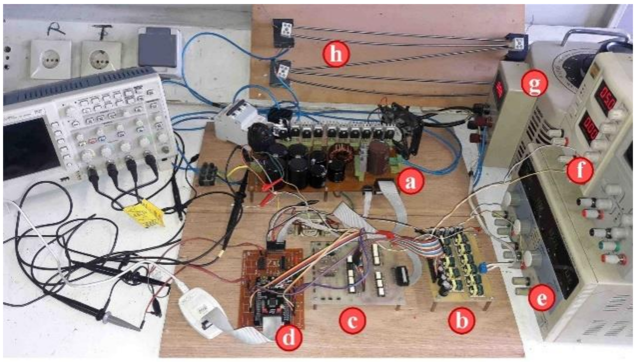

Fig. 28. The implemented overall system composed of (a) power circuit, (b) isolated gate drive supply, (c) gate drive board, (d) controller board, (e) supply of op-amps, (f) supply of ACS712, (g) autotransformer, and (h) load

The proposed converter is simulated in the unity power condition in mode 1. The results are presented in Figs. 9-15. Fig. 9 shows the grid voltage (V_g) and input current (I_g) in the UPF condition. The FFT analysis in three cycles of the input current is shown in Fig. 10, which illustrates the THD value as 3.47% with acceptable harmonic orders. Figs. 11 and 12 are related to the control unit operation in either mode 1 or mode 2. Fig. 11 shows the current loop PID output compared with a 30 kHz triangular wave. The S_{P1} and S_{P2} gate pulses are depicted in Fig. 12. As aforementioned, S_{P1} and S_{P2} have a high-frequency operation in a negative and positive half cycle of the grid voltage, respectively.

The converter is tested in mode 2 and the DC-link, battery port, and output voltages are depicted in Fig. 30(a). Fig. 30(b) shows the voltage of L_S in this mode.

Fig. 31(a) shows the battery port and output voltages in mode3. The converter is also tested in mode 4, and the grid voltage and input current of the converter are shown in Fig.31(b).

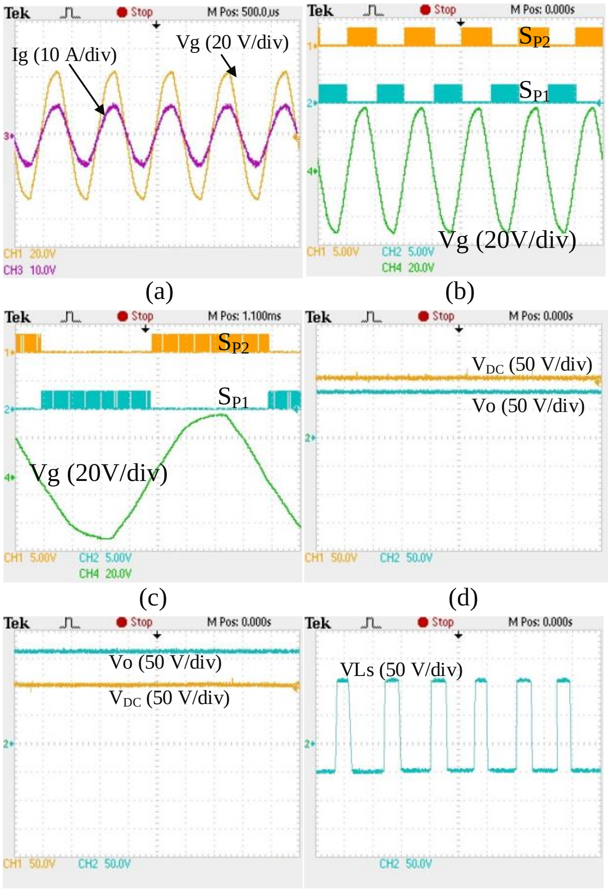

(a) (b)

(c) (d)

(e) (f)

Fig.29. Experimental results of mode1

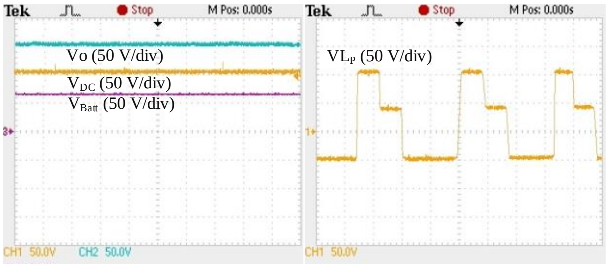

(a) (b)

Fig. 30. The experimental results for mode 2

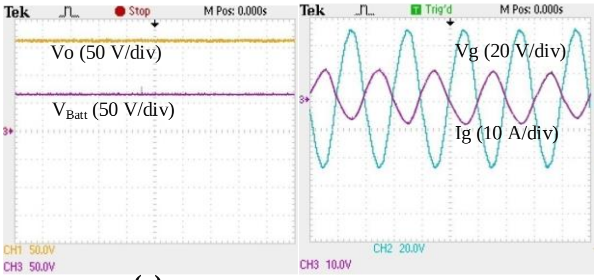

(a) **(b)**

Fig. 31. (a) Battery voltage and output voltage in mode 3, and (b) grid voltage and input current in mode4

VII. CONCLUSION

A novel bidirectional multiport rectifier has been presented in this paper. The proposed converter can be used as a wall-box converter that can be installed in the parking lot of smart buildings and can provide DC-link for local DC loads, such as DC home appliances and charge the connected EV, simultaneously. The ability to work in four operating modes (G2H, G2VH, V2H, and V2G) is the main feature of this converter. A control method is also explained that enables the proposed converter to control active and reactive power according to the processed smart grid or customer commands. The operation of the presented converter is explained and analyzed during all operating modes, and simulation is done to validate system analysis. A reduced-scale experimental setup has been built, and the performance of this converter has been assessed through an experimental test. The results confirm the simulation ones.

REFERENCES

[1] U. R. Prasanna, A. K. Singh, and K. Rajashekara, "Novel bidirectional single-phase single-stage isolated AC–DC converter with PFC for charging of electric vehicles," *IEEE Transactions on Transportation Electrification,* vol. 3, no. 3, pp. 536-544, 2017.

[2] A. K. Seth and M. Singh, "Resonant controller of single-stage off-board EV charger in G2V and V2G modes," *IET Power Electronics,* vol. 13, no. 5, pp. 1086-1092, 2020.

[3] M. Ramzanzadeh, M. Jafari Nokandi, T. Barforoushi, and J. Saebi, "Security-Constrained Unit Commitment in the Presence of Demand Response Programs and Electric Vehicles," *International Journal of Industrial Electronics, Control and Optimization,* 2020.

[4] M. Lillebo, S. Zaferanlouei, A. Zecchino, and H. Farahmand, "Impact of large-scale EV integration and fast chargers in a Norwegian LV grid," *The Journal of Engineering,* vol. 2019, no. 18, pp. 5104-5108, 2019.

[5] R. Kushwaha and B. Singh, "UPF-isolated zeta converter-based battery charger for electric vehicle," *IET Electrical Systems in Transportation,* vol. 9, no. 3, pp. 103-112, 2019.

[6] A. G. Boulanger, A. C. Chu, S. Maxx, and D. L. Waltz, "Vehicle electrification: Status and issues," *Proceedings of the IEEE,* vol. 99, no. 6, pp. 1116-1138, 2011.

[7] T. Morgan, "Smart grids and electric vehicles: Made for each other?," 2012: International Transport Forum Discussion Paper.

[8] F. Kennel, D. Görges, and S. Liu, "Energy management for smart grids with electric vehicles based on hierarchical MPC," *IEEE Transactions on industrial informatics,* vol. 9, no. 3, pp. 1528-1537, 2012.

[9] C. Pang, P. Dutta, and M. Kezunovic, "BEVs/PHEVs as dispersed energy storage for V2B uses in the smart grid," *IEEE Transactions on Smart Grid,* vol. 3, no. 1, pp. 473-482, 2011.

[10] R. C. Green II, L. Wang, and M. Alam, "The impact of plug-in hybrid electric vehicles on distribution networks: A review and outlook," *Renewable and sustainable energy reviews,* vol. 15, no. 1, pp. 544-553, 2011.

[11] S. Rezaee, E. Farjah, and B. Khorramdel, "Probabilistic analysis of plug-in electric vehicles impact on electrical grid through homes and parking lots," *IEEE Transactions on Sustainable Energy,* vol. 4, no. 4, pp. 1024-1033, 2013.

[12] J. Pinto *et al.*, "Bidirectional battery charger with grid-to-vehicle, vehicle-to-grid and vehicle-to-home technologies," in *IECON 2013-39th Annual Conference of the IEEE Industrial Electronics Society,* 2013, pp. 5934-5939: IEEE.

[13] D. P. Tuttle, R. L. Fares, R. Baldick, and M. E. Webber, "Plug-in vehicle to home (V2H) duration and power output capability," in *2013 IEEE Transportation Electrification Conference and Expo (ITEC)*, 2013, pp. 1-7: IEEE.

[14] V. Monteiro *et al.*, "Assessment of a battery charger for electric vehicles with reactive power control," in *IECON 2012-38th Annual Conference on IEEE Industrial Electronics Society*, 2012, pp. 5142-5147: IEEE.

[15] M. C. Kisacikoglu, B. Ozpineci, L. M. Tolbert, and F. Wang, "Single-phase inverter design for V2G reactive power compensation," in *2011 Twenty-Sixth Annual IEEE Applied Power Electronics Conference and Exposition (APEC)*, 2011, pp. 808-814: IEEE.

[16] A. M. Mohamad and Y. A.-R. I. Mohamed, "Investigation and Enhancement of Stability in Grid-Connected Active DC Distribution Systems With High Penetration Level of Dynamic Loads," *IEEE Transactions on Power Electronics,* vol. 34, no. 9, pp. 9170-9190, 2018.

[17] H. Abdollahi, S. Arrua, T. Roinila, and E. Santi, "A novel dc power distribution system stabilization method based on adaptive resonance-enhanced voltage controller," *IEEE Transactions on Industrial Electronics,* vol. 66, no. 7, pp. 5653-5662, 2018.

[18] Y. Yu, D. Jiang, Y. Liang, and J. Chen, "Research on the transformerless connection mode for DC power distribution system," *The Journal of Engineering,* vol. 2019, no. 16, pp. 3378-3382, 2019.

[19] H.-S. Kim, M.-H. Ryu, J.-W. Baek, and J.-H. Jung, "High-efficiency isolated bidirectional AC–DC converter for a DC distribution system," *IEEE transactions on Power Electronics,* vol. 28, no. 4, pp. 1642-1654, 2012.

[20] N. Tashakor, E. Farjah, and T. Ghanbari, "A bidirectional battery charger with modular integrated charge equalization circuit," *IEEE Transactions on Power Electronics,* vol. 32, no. 3, pp. 2133-2145, 2016.

[21] M. C. Kisacikoglu, M. Kesler, and L. M. Tolbert, "Single-phase on-board bidirectional PEV charger for V2G reactive power operation," *IEEE Transactions on Smart Grid,* vol. 6, no. 2, pp. 767-775, 2014.

[22] M. Kwon and S. Choi, "An electrolytic capacitorless bidirectional EV charger for V2G and V2H applications," *IEEE Transactions on Power Electronics,* vol. 32, no. 9, pp. 6792-6799, 2016.

[23] S. Rezaee and E. Farjah, "A DC–DC multiport module for integrating plug-in electric vehicles in a parking lot: Topology and operation," *IEEE Transactions on Power Electronics,* vol. 29, no. 11, pp. 5688-5695, 2014.

[24] S.-G. Jeong, J.-M. Kwon, and B.-H. Kwon, "High-efficiency bridgeless single-power-conversion battery charger for light electric vehicles," *IEEE Transactions on Industrial Electronics,* vol. 66, no. 1, pp. 215-222, 2019.

[25] A. Tausif, H. Jung, and S. Choi, "Single-stage isolated electrolytic capacitor-less ev onboard charger with power decoupling," *CPSS Transactions on Power Electronics and Applications,* vol. 4, no. 1, pp. 30-39, 2019.

[26] R. Kushwaha and B. Singh, "A Power Quality Improved EV

Charger With Bridgeless Cuk Converter," *IEEE Transactions on Industry Applications*, vol. 55, no. 5, pp. 5190-5203, 2019.

[27] B. Singh and R. Kushwaha, "A PFC Based EV Battery Charger Using a Bridgeless Isolated SEPIC Converter," *IEEE Transactions on Industry Applications*, vol. 56, no. 1, pp. 477-487, 2019.

[28] M. Monfard, M. Babaei, and S. Sharifi, "A Z-Source Network Integrated Buck-Boost PFC Rectifier," *International Journal of Industrial Electronics, Control and Optimization*, vol. 2, no. 4, pp. 289-296, 2019.

[29] H. Vahedi and K. Al-Haddad, "A novel multilevel multioutput bidirectional active buck PFC rectifier," *IEEE Transactions on Industrial Electronics*, vol. 63, no. 9, pp. 5442-5450, 2016.

[30] H. S. Gohari and K. Abbaszadeh, "A Novel Controllable Bidirectional switching-capacitor based Buck-Boost Charger for EVs," in *2020 11th Power Electronics, Drive Systems, and Technologies Conference (PEDSTC)*, 2020, pp. 1-6: IEEE.

[31] V. Vlatkovic, D. Borojevic, and F. C. Lee, "Input filter design for power factor correction circuits," *IEEE Transactions on Power Electronics*, vol. 11, no. 1, pp. 199-205, 1996.

[32] V. Bist and B. Singh, "PFC Cuk converter-fed BLDC motor drive," *IEEE Transactions on Power Electronics*, vol. 30, no. 2, pp. 871-887, 2014.

[33] H. Akagi, Y. Kanazawa, and A. Nabae, "Instantaneous reactive power compensators comprising switching devices without energy storage components," *IEEE Transactions on industry applications*, no. 3, pp. 625-630, 1984.

Homayon Soltani Gohari received his B.Sc. degree in electrical power engineering from Shahid Bahonar University of Kerman, Kerman, Iran in 2017, and his M.Sc. degree in electrical power engineering, power electronics, from the K.N. Toosi University of Technology, Tehran, Iran in 2020. His research field includes power electronics, EVs power converter, energy management, and different power converters, especially rectifiers with PFC.

Karim Abbaszadeh received his B.S. degree in communication engineering from the K.N.Toosi University of Technology, Tehran, Iran in 1991, and his M.Sc. and Ph.D. degrees in electrical engineering from the Amir Kabir University of Technology, Tehran, Iran in 1997 and 2000, respectively. From 2001 to 2003, he has been a research assistant at the Department of Electrical Engineering, Texas A&M University, College Station, TX, USA. He is currently a professor at the Department of Electrical Engineering, the K.N.Toosi University of Technology. His research interests include power electronic and dc–dc and dc–ac converters, electric machinery, variable-speed drives, and propulsion applications. He is the author of more than 50 published journal papers. He is actively involved in presenting short courses and consulting in his area of expertise to various industries.

Jafar Gholamei Gorji was born in Behshahr, Mazandaran, Iran in 1994. He received his B.S. degree (first-class Hons.) in electronic engineering from the Quchan University of Technology, Khorasan Razavi, Iran in 2016 and his M.Sc. degree in electrical power engineering from the K.N. Toosi University of Technology, Tehran, Iran in 2019. His research interests include power electronic converters, renewable energy systems, and power quality and management. He currently focuses on the multi-input and high gain converters.

IECO

This page intentionally left blank.

International Journal of Industrial Electronics, Control and Optimization © 2021 IECO
Vol. 4, No. 1, pp. 117-128, Jan (2021)

An Investigation of a New Method to Detect Loss of Excitation of Synchronous Generators

Reza Fathi Shoob [1], Milad Niaz Azari [2,†]

[1] Department of Electrical Engineering, Sari branch, Islamic Azad University, Sari, Iran
[2] Department of Electrical Engineering, University of Science and Technology of Mazandaran, Behshahr, Iran

ABSTRACT

Synchronous generators are one of the most important components of power systems. Problems a generator may face are internal faults, system disturbances, or operational hazards. The operation of a generator may easily be affected by faults within the machine itself as opposed to external disturbances occurring on the network to which it is connected. Generator protection must therefore be designed to react efficiently in both conditions. Loss of excitation (LOE) is a common fault in synchronous generators. The most common causes of LOE include the loss of field to the main exciter, accidental tripping of the field breaker, short circuits in the field circuit, and poor brush contact in the exciter. The most widely applied method to detect a generator loss of field condition on major generators is the use of distance relays to sense the variations of impedance as viewed from the generator terminals. This approach may not be able to distinguish between LOE and stable power swing (SPS). This paper further explores a new method proposed for LOE detection and corrects its shortcomings. It also presents a new approach for LOE detection that exploits a combined scheme based on the derivative of the terminal voltage and the derivative power angle of the generator. Comprehensive simulation studies are conducted on various generator conditions and system disturbances to determine the relay setting and to evaluate its performance. These studies demonstrate that the proposed strategy enhances the security and operation time of the LOE relay compared with some existing methods.

Article Info

Keywords:
Detection, LOE relay Loss-of-excitation (LOE) fault, Stable Power Swing (SPS), Synchronous generator.

Article History:
Received 2020-05-23
Accepted 2020-10*-18

I. INTRODUCTION

A. An Introduction to Power Systems

Secure and fast protection of a power system's components should be ensured to isolate the faulted area, minimize its effects on the nearby areas, and maintain system stability. The problem of the stability of a power system has been considered by electrical engineers in recent years. Increasing loads and deregulating a power system make the power system more complex than ever. Major blackouts due to power instability indicate the importance of this issue [1]. Due to the continuing growth of power systems such as in interconnections, use of new controls and technologies, and so on, different forms of system stability have emerged. Voltage stability and transient stability have become more problematic than in the past [1]. To prevent major blackouts such as August 2003's blackout in the northeast of the United States and August 1996's blackout from a western connection in North America that cost billions of dollars [2]-[5], real-time monitoring tools require the operator to take prompt action to correct problems.

B. Motivation and Problem Description

The loss-of-excitation (LOE) condition of a generator in a power system may be caused by faults or unexpected problems in the automatic field voltage control in synchronous generators. A generator may completely or partially lose its excitation due to casual field breaker tripping, field open circuit, short circuits in the field winding, poor brush contact in the exciter, field circuit breaker latch failure, voltage regulator failure, or loss-of-excitation system ac-supply [3]. The LOE fault is mostly minor, but in very rare cases, a stimulus may be completely eliminated in a synchronous generator. LOE causes the generator to absorb a large amount

---

[†] **Corresponding author**: miladniazazari@mazust.ac.ir
Department of Electrical Engineering, University of Science and Technology of Mazandaran, Behshahr, Iran.

of reactive power from the power grid. Also, it causes the machine speed to go above the synchronous speed in which case the machine will start to operate like an induction generator, [6]-[14]. Due to LOE, the generator will start to consume reactive power in a very large amount from the power system, and this will result in a voltage drop.

This means an increasing reactive power demand on the neighboring system near the LOE generator. It also reduces the terminal voltage of the generator. LOE condition at a large generator, e.g. major fossil plants, can drag down nearby voltage of the system very fast and jeopardize the voltage stability of the rest of the power system. This can have a very serious impact on the power system if the system is not stable enough. A large increase in reactive power causes an increase in the stator currents, resulting in an overheating rotor, thermal heating in the rotor windings, loss of magnetic coupling between the rotor and the stator, and large voltage drop in the transmission system [5]-[14]. Therefore, it is necessary to identify the LOE fault on the synchronous generator in a power system as soon as possible. Furthermore, the effect of LOE on the stability of the power system and voltage stability must be determined in order to avoid voltage collapse.

Also, the loss of excitation causes the stator to overload and the rotor to overheat. The worst-case scenario for generator excitation is when the generator has a heavy load in which case there will be a higher probability of synchronization disappearing because the system impedance will be lower despite the high load and the final slip frequency of the system will be reduced [15]. During light loads, the generator may not lose synchronism and will operate as a synchronous generator depending on the principle of reluctance [16]. There is no determined time length the generator can operate without excitation [15], but to avoid possible voltage collapse resulting from reactive power demand and machine damage, secure fast and dependable LOE detection methods are required [17].

C. Literature Review

The conventional detection method, which is based on impedance measurement to detect LOE, is the most popular technique for LOE detection. The impedance scheme is the most utilized scheme for LOE detection. During an LOE event, Zones 1 and 2 are for detecting LOE with a full load and a light load, respectively. In other words, during heavy loads, the impedance trajectory enters the operating area faster than light loads. Also, Zone 2 is considered to be the backup of Zone 1, and during power swings, there is a high probability for the entrance of the impedance trajectory into Zone 2. When the measured impedance falls into the operating region, the relay function is picked up and, after a certain time delay to enhance the security of the power swing, a trip signal is sent to the generator's main breaker. The offset of the protection zones from the principle of the impedance plane is half of the transient reactance ($X'_d/2$). Two methods of LOE detection are presented in the SEL-300G relay manual [18]. These two cases are shown in Fig. 1.

X_d ≡ Generator direct-axis reactance

X_s ≡ The sum of the step-up transformer reactance and system reactance

X' ≡ Generator transient reactance

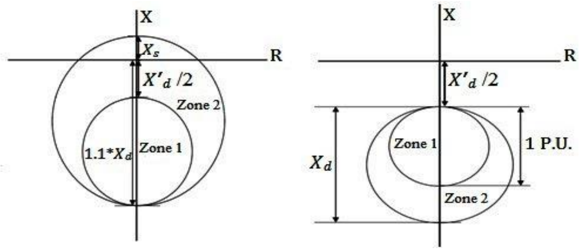

(a) (b)

Fig.1. Loss-of- excitation protection: (a) positive-offset mho element and (b) negative-offset mho element

The conventional method shows mal-operation during severe stable power swing (SPS) conditions; for instance, a severe fault near the generator [15]. It was reported in a NERC technical reference document that 13 out of 290 generator tripping resulted from LOE mal-operation during such disturbances [17]. Besides, the additional elements can be introduced to implement the protection function, such as directional element, under-voltage element, over-current element, minimum excitation limit, steady-state stability limit, etc.

What is certain is that conventional methods are unable to detect SPS. Therefore, methods should be created that do not have the problems of impedance methods. The techniques used to detect LOE are described in Section 2.

II. LOSS OF EXCITATION FAULT

A .Techniques Proposed

As discussed in Section 1, the conventional method is not reliable during SPS conditions. In addition, it requires a time delay that results in more stress in the generator and the network. Therefore, other techniques have been proposed to eliminate these pitfalls. In [15], a new method of LOE detection is introduced based on the fuzzy set theory. It depends on the concept of the conventional LOE detection method, which relies on the variations in the terminal voltage and apparent impedance. This method works when the voltage range is between 0.5 and 0.8 p.u, so if the system is strong, it will not work. Its performance depends on the strength of the system and a lot of data is required.

A setting-free approach to detecting LOE of a synchronous generator is presented in [18]. This approach does not need threshold settings, so it does not depend on system parameters. This approach relies on the resistance variations because it has a fixed polarity during LOE (it remains negative). This method discriminates between LOE and a disturbance by setting a time delay before tripping. The performance of the method is evaluated during peak hours, off-peak hours, and disturbances for a 2-bus system. The results show that it is faster than the conventional method. In [19], a new strategy is presented to detect a synchronous generator's LOE. This method depends on the value and duration of voltage and reactive power amount.

Its performance has been compared with the conventional method and the proposed method in [15] for different loading conditions, generator ratings, and system configurations. The index presented in [19] has difficulty discriminating between SPS and LOE. Also, a solution is presented in [20]. The discrimination between SPS and LOE is based on the variations in the fast Fourier transform coefficient of the three-phase active power at the relay location. Therefore, the delay associated with the other methods is avoided through an additional threshold value. The second threshold is the active power based on the FFT coefficient. When the indicators are calculated and they exceed two threshold values, the LOE fault is detected; otherwise, it shows an SPS condition on the grid. There are several techniques based on magnetic flux variations in the air gap ([21], [22]), but these techniques have been criticized because, to measure the machine flux, the search sensors coil should be utilized but there is, naturally, no desire to install it due to the damage to the generator [20]. A new method based on PMU measurement in the presence of flexible alternating current transmission systems (FACTS) is presented in [23], but this method needs measurement synchronization and lots of information. The algorithms presented in [18] and [20] start their calculations with the initial condition that the terminal voltage of the machine is less than 0.95 p.u. When the system is strong or there are several generators on the same bus, the generator's terminal voltage does not reach 0.95 or less. This indicates that the calculations are not started by the algorithm and LOE will not be recognized. Also, these methods have not been studied in a larger system.

B. Contribution

This paper presents an event to find LOE occurrence and distinguish it from SPS. The proposed approach detects the LOE event using the rate of variations in the generator's terminal voltage and output angle power. The proposed method is investigated for different conditions and parameters. It is examined by considering various parameters of the generator, system disturbances, and the structure of the system under the existing conditions. Also, according to the studies, a comparison is made to identify two SPS and LOE approaches. In the second part, the strategy of the proposed method for LOE detection is discussed. Also, the concept of strategy and its algorithm are explained in this section. In Section 3, the studied system and its components include different parts of the generator and loads based on the proposed strategy. The proposed index identifies faults based on the relevant algorithm and according to the simulation. Section 4 addresses the concluding points of the proposed method.

C. Synchronous Generator Modeling for LOE Transient Analysis

Synchronous generators supply almost all the electric power we consume today. The rotor of a synchronous generator needs to be driven by a source of mechanical power or a prime mover and the field winding needs to be fed by a source of DC power to provide active and reactive power to the power system. These exclusive combinations of electrical and mechanical equipment need to be protected against different kinds of faults. Generator faults are always considered to be serious since they can cause severe and costly damage to insulation, windings, core, shafts, and couplings [1]. Generally, there are two types of excitation systems – rotating and static. Rotating systems use a dc or an ac generator as the source, but static systems apply rectifiers as sources that are directly fed from the generator terminals via a step-down transformer. Today, most excitation systems are ac or static types because of their fast response capability. When a generator loses its excitation, the rotor current gradually decreases and the field voltage decays by the field time constant as well. As mentioned in the previous section, in this case, the generator operates as an induction generator and draws reactive power from the power system instead of generating reactive power.

Considering the generator active power output equation:

$$Pe = \frac{Eq.Us}{Xd+Xs}\sin\delta \tag{1}$$

where P_e is the active power output to the system, E_q is the generator internal voltage behind the d-axis synchronous reactance, Us is the equivalent system voltage, X_d is the d-axis synchronous reactance, X_d is the system impedance, and δ is the angle between E_q and U.

The active power output is proportional to the system voltage, the generator internal voltage, and its sine. As the generator internal voltage E_q is a function of field voltage, the generator active power output is a function of field voltage as well.

In the steady-state, the operation point is the point where the mechanical power input equals the electrical power output. When the mechanical power increases, the load angle δ increases. The maximum mechanical power can increase until the load angle reaches $\delta = 90^\circ$, after which the mechanical power will be greater than the electrical power and the generator will lose synchronism as there is no equilibrium point between mechanical power input and electrical power output. For the same reason, when the mechanical power input is fixed and the maximum electrical power output decreases due to the field voltage reduction, the load angle δ increases as the intersection of mechanical power and electrical power moves up to the peak. The generator electric power output versus the load angle is shown in Fig. 2.

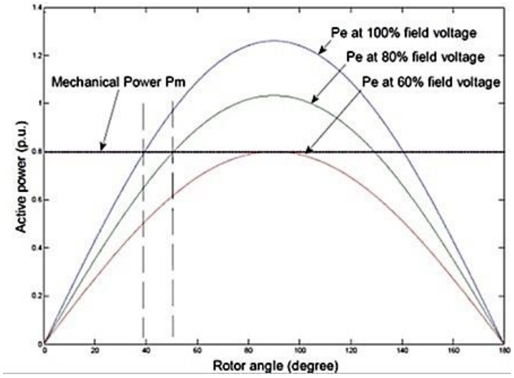

Fig. 2. Generator active power – angle diagram

When a generator operates at δ =90°, any increase in mechanical power or decrease in electrical power will lead to the generator's loss of synchronism. As a result, the generator will operate asynchronously as an induction machine, typically with a 2% to 5% slip, and will draw the reactive power from the system for the excitation instead of generating reactive power to the system [24]. Normally, a generator's field voltage cannot be measured directly, so to detect the LOE, the protection scheme applies the generator's terminal voltage, current, power angle, active power, or reactive power output as the input value and calculates the generator characteristic values to determine the LOE fault.

III. GENERATOR CAPABILITY LIMITATION

A. Generator Capability Curve

First of all, the generator capability is limited by the rated MVA, which represents the generator maximum continuous output in the steady-state without overheating. However, concerning the voltage stability and long-term stability, it is essential to consider the reactive power capability which is limited by field current limit, armature current limit, and stator end region heating limit [25]. The generator thermal limits are shown in Fig. 3.

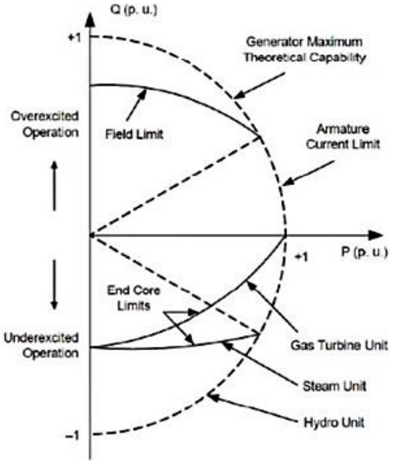

Fig.3. Generator operation thermal limits [26]

B. Dynamic Performance of a Synchronous Generator during LOE

The field circuit of a synchronous generator needs to be excited by a direct current supply in order to keep the generator in synchronism with the power grid and to keep the voltage constant. Basically, synchronism between the power system and the generator is maintained due to the interaction of fluxes produced by the stator and rotor windings [27]. Excitation can be provided in many ways including rotating dc exciters with commutators, rotating alternator rectifiers, or static supplies. Power and torque pulsation due to the LOE conditions will be more severe in a generator with a rectifier bridge supply than in a generator supplied by a dc exciter [28]. After LOE occurs, a decrease in the field current will reduce the electromagnetic torque, while the mechanical torque from the prime-mover cannot change immediately, thus the rotor will accelerate. Under such a condition, the generator speed will be above the synchronous speed and the synchronous generator will operate as an induction generator. Due to the slip between the rotating magnetic fields of the stator and the rotor, ac currents are induced in the field winding body and damper windings [27]. Because of the reactive power drawn by the LOE generator, the system voltage is immediately reduced while the armature current of the generator is increased [29]. Under such circumstances, disturbance in the power system would take place.

Since the rotor of large turbo-generators is not laminated, instead of being machined from a steel alloy forging, under an LOE condition, substantial heat will be generated by eddy currents [27]. Excess rotor heat is likely to affect the integrity of the field windings, insulation, wedges, or retaining rings [28]. Damage to the generator may occur in a timescale of between 10 seconds and several minutes.

A generator converts mechanical energy into electrical energy, so the input power is the mechanical prime mover, e.g. diesel engine, steam turbine, water turbine, and so on. Regardless of the prime mover type, the rotor velocity must remain constant to maintain a stable system frequency. The transient analysis of a synchronous machine is thus concerned with determining transient fluxes and currents and their influence on the electrical and electromechanical behavior of the machine.

The electromechanical equation for a synchronous generator follows directly from equating the inertia torque (equal to the moment of inertia j times the angular acceleration) to the net mechanical and electric torque acting on the rotor. Thus, we have

$$\mathrm{j}\frac{\mathrm{d}^2\theta}{\mathrm{d}^2\mathrm{t}} = \mathrm{T_{mech}} - \mathrm{T_{elec}} \tag{2}$$

where

θ= the angular position of the rotor

$\mathrm{T_{mech}}$ = the mechanical accelerating shaft torque applied to the rotor

T_{elec} = the electromagnetic torque acting to decelerate the rotor

The equation, like those that follow, is written with a certain generator in mind.

It is often convenient to express the rotor angular position ***δ*** in terms of a synchronous rotating reference frame as

$$\theta = \frac{2}{\text{poles}}(\omega t + \delta) \tag{3}$$

where ω is the synchronous electric frequency and δ is the electrical angle between a point on the rotor and the synchronous reference frame. δ is often taken equal to the synchronous-machine power angle, so, Eq. (4) becomes as follows for a generator with two poles:

$$j\frac{d^2\delta}{d^2t} = T_{mech} - T_{elec} \tag{4}$$

Known as the swing equation, it can be solved for the electromechanical dynamics of the synchronous machine. The key to its use is the accurate representation of the torques acting on the rotor. The mechanical shaft torques must be determined from a representation of the dynamics of the prime mover (or load in the case of a motor).

Since this model results in an expression for electric power output (4) as a function of the rotor angle, it is convenient to rewrite Eq. (5) in terms of power. This can be done by multiplying by the rotor mechanical velocity ω_m.

Since for most situations of practical interest, deviations of ω_m from synchronous speed are very small, ω_m can be replaced by the synchronous rotor velocity $\omega_s = (2/poles)\omega$, giving

$$j\omega_s\frac{d^2\delta}{d^2t} = P_{mech} - P_{elec} \tag{5}$$

In the LOE condition, the load angle (i.e δ) fluctuates and reaches the maximum and then decreases. It, then, shows that the power system is stable. At that moment, due to the inherent permanence of the power system, the derivative of the load angle (dδ/dt) is zero. As a result, the fluctuations will be smaller and smaller. It should be noted that while the load angle is different, if the derivative of the load angle (dδ/dt) is zero at a certain moment, stability will be guaranteed. If the load angle increases indefinitely, it will imply that the power system is unstable. To find the derivative of the load angle (dδ/dt), both sides of (6) with dδ/dt are multiplied as follows:

$$j\omega_s\left(\frac{d^2\delta}{d^2t}\right)\frac{d\delta}{dt} = (P_{mech} - P_{elec})\frac{d\delta}{dt} \tag{6}$$

or

$$\frac{1}{2}j\omega_s\frac{d}{dt}\left(\frac{d\delta}{dt}\right)^2 = (P_{mech} - P_{elec})\frac{d\delta}{dt} \tag{7}$$

Using Eq. (7) and performing some trigonometric derivatives and integrating, the derivative of the load angle can, finally, be found as follows:

$$\frac{d\delta}{dt} = \sqrt{\int_{\delta_0}^{\delta}\left(\frac{2}{j\omega_s}\right)(P_{mech} - P_{elec})d\delta} \tag{8}$$

Before LOE occurs, δ_0 is the load angle and at this time dδ/dt=0. As soon as LOE happens, dδ/dt is no longer zero, and the load angle changes. When dδ/dt=0, i.e., the load angle stops and the generator operates in a new stable condition with motor performance.

$$\frac{d\delta}{dt} = \int_{\delta_0}^{\delta}\left(\frac{2}{j\omega_s}\right)(P_{mech} - P_{elec})d\delta = 0 \tag{9}$$

It should be noted when dδ/dt = 0, the synchronous generator will not stay at rest with a connection to the power system at the first time. However, according to balancing available in the power system, the maximum load angle is reduced during the subsequent fluctuations. That is, the power system is stable and the generator will achieve a new operating point with the motoring function often known as the swing equation, it can be used to solve for the electromechanical dynamics of the synchronous-machine. The key to its use is the accurate representation of the torques acting on the rotor. The mechanical shaft torques should be determined from the presentation of the dynamics of the prime mover (or the load in the case of a motor).The basic electromechanical equation, the so-called swing equation, states that the product of a rotor moment of inertia times its angular acceleration is equal to the net torque applied to the rotor (mechanical shaft torque and electromagnetic torque). Under steady-state conditions, the net torque is zero and the rotor remains at constant (synchronous) speed. Transient analysis is performed to investigate the nature of the transients resulting from a disturbance and whether or not the stable steady-state operation will be reestablished.

C. The Proposed Strategy Concept

When LOE occurs, due to the mechanical inertia, the mechanical input and load angle keeps constant temporarily. The reactive power output decreases to zero quickly and the generator starts to import the reactive power from the system. The generator’s internal voltage decays because of the field voltage reduction, and the phase current goes up due to a large amount of reactive power imported. As already mentioned under LOE conditions, a synchronous generator will continue providing pulsing active power and draw a large amount of reactive power from the grid, which can jeopardize the system’s voltage stability [30].

After a short-circuit fault on the generator's excitation winding terminal, which leads to LOE, the dc current flowing through the excitation winding disappears. Therefore, the output voltage of the generator slowly decreases, as shown in Fig. 4(a), and LOE occurs in 15 s. In such a situation, the generator starts to absorb reactive power from the grid, and the reactive power of the generator begins to decrease. Consequently, the signals derived from the terminal voltage and reactive power are the same (Fig. 4(b)). In addition, the speed of the generator is increased and this will increase the power angle (δ). The load angle variations and speed are depicted in Figs. 5(a) and (b) after LOE occurs.

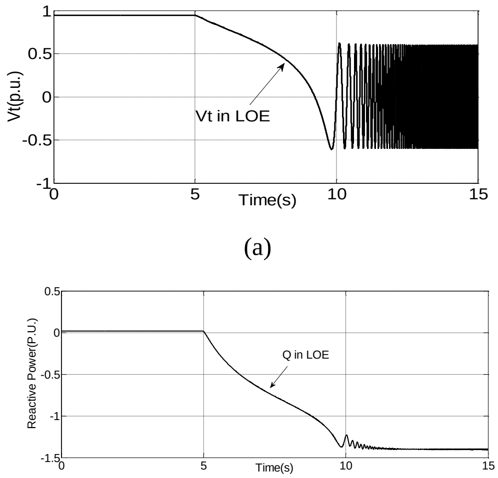

(a)

(b)

Fig.4. The generator's terminal voltage and Q after LOE

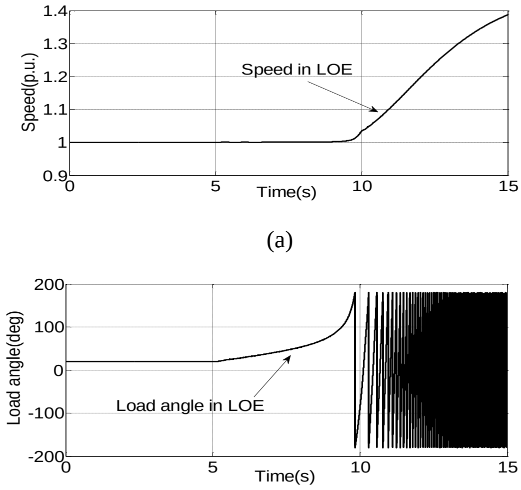

(a)

(b)

Fig.5.The generator's speed and load angle after LOE

If the voltage changes in two consecutive, samples of this quantity will be equal to:

$$\Delta V = V_k - V_{k-1} \qquad (10)$$

In addition, the value of dv/dt is significant, even for a relatively long time after the LOE event.

In this case, after the LOE event, the output voltage of the generator gradually decreases, and ΔV becomes negative. Also, we will have for δ after the LOE event:

$$\Delta\delta = \delta_k - \delta_{k-1} \qquad (11)$$

According to Figure 4(a), it can be said that after the LOE event, the value of Δδ is positive and it will increase. Also, dδ/dt is positive.

With the multiplication of derivatives of the two sides (1) and (2), we will have:

$$\Delta V * \Delta\delta = (V_k - V_{k-1}) * (\delta_k - \delta_{k-1}) \text{ and:}$$

$$(dV/dt) * (\,d\delta/dt) = (d(V_k - V_{k-1})/\mathrm{dt}) * (\frac{d(\delta_k - \delta_{k-1})}{\mathrm{dt}}) \qquad (12)$$

It should be noted that the terms $(V_k - V_{k-1})$ and $(\delta_k - \delta_{k-1})$, respectively, represent the derivatives of the terminal voltage and the rotor angle, respectively. Regarding the voltage and load angle variations, in the LOE event, Eq. (12) indicates an index in that the direction is negative and its value is increasing. By applying the changes in Eq. (12), which is considered as Loss of Excitation Detection Index (LOEDI), is obtained as below.

$$\mathrm{LOEDI} = K_G * ((dV/dt) * (\,d\delta/dt)) \qquad (13)$$

Various permutations of the electrical quantities are multiplied to one another for better detectors as expressed in Eq. (3). K_G is an amplified quantity to increase the detection index value and it depends on the index parameters and $k_G = 10^5$. If the calculated index is larger than the specified threshold *Th* for five samples, the LOE event will be detected. The LOE relay function depends on the *Th* settings. The function of this logic is that after starting the algorithm if the value of the LOEDI increases from *Th*, one unit is added to the Loss Of Excitation Detection Counter (LOEDC); otherwise, it will be reduced by a unit. If the LOEDI value reaches the final value (N), LOE occurs and the relay trip signal is issued. The parameter *N* represents the maximum value of the LOEDI to ensure the occurrence of LOE.

C. Strategy Algorithm

Fig. 6 shows the flowchart of LOE detection to calculate the initial values where terminal voltage, apparent power, and power factor are given as inputs. Then, the load angle (δ) of the machine can be calculated. Generator terminal voltage decreases after LOE due to the short circuit or open circuit in the excitation winding. Therefore, the voltage of 0.95 per-unit is considered a fault. After the fault detection operation, the terminal voltage of the generator is first determined. Subsequently, the generator power angle changes are specified. Given that this algorithm uses the derivative of sample signals from the voltage and rotor angles, we use a low-pass filter to eliminate negative fluctuations to obtain the indicated signals. Using this method, it accurately distinguishes LOE and Sustainable Power Swing (SPS). To calculate *Th*, the following should be considered. Due to the fact that the rotor voltage and power angles are almost constant and do not change under normal generator conditions, the LOEDI changes are negligible.

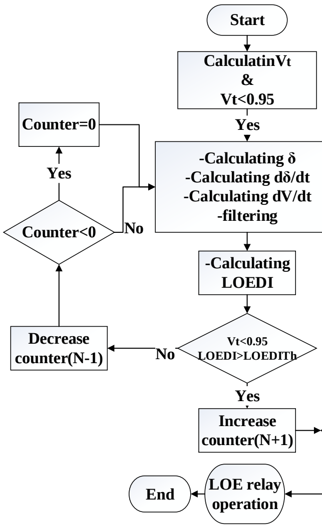

Fig.6.The flowchart of the proposed LOE relay

In addition, the simplified trip logic diagram on the LOEDI index is shown in Fig. 7.

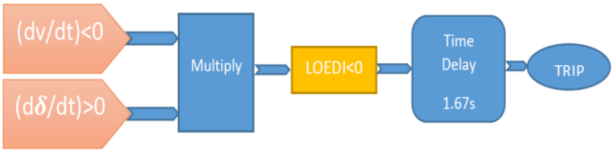

Fig.7.The Trip logic for LOEDI

Eventually, the phase angle of the generator's internal voltage remains positive in half of the period depicted. According to [31]-[37], the power system swing frequency range is 0.3-7 Hz. In this paper, the minimum value (0.3 Hz) will be considered as the network swing frequency. The longest time period for the expected angle oscillation is then 1/0.3 s or 3.33 second as shown in Fig. 8. The delta variation will change its polarity after half a cycle or 1.67s.

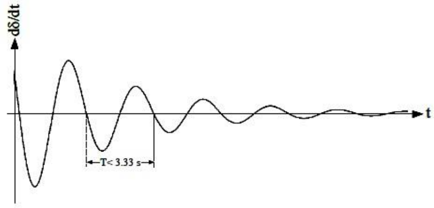

Fig.8. The $d\delta/dt$ oscillations during the slowest power swing [31]-[36]

IV. EVALUATION OF THE PROPOSED STRATEGY

Given that the amount of LOEDI may depend on the configuration of the generator's power system and output power, different items will be studied in the following sections. Table 1 presents the different loadings of the generator for simulation conditions. Simulation with different loads and under the conditions of complete interruption of LOE excitation and reduction of PLOE excitation in MATLAB/SIMULINK software has been done completely.

TABLE I

The Loadings of the Generator

Loading (p.u.)							
S=P+JQ P.U.							
L1	0.1+j0.2	L5	0.5+j0.4	L9	0.9-j0.2	L13	0.5-j0.6
L2	0.1+j0.3	L6	0.7+j0.2	L10	0.7-j0.5	L14	0.3-j0.6
L3	0.3+j0.4	L7	0.8+j0.4	L11	0.6-j0.4	L15	0.3-j0.4
L4	0.3+j0.5	L8	0.9+j0.3	L12	0.5-j0.2	L16	0.1-j0.2

A.Case Study

The studied network is a single machine infinite bus (SMIB) shown in Fig. 9. The full power network data is presented in [23]. The simulation model includes a salient-pole generator 250 MVA connected to a common bus via connection step-up transformer. The common bus connects to the infinite bus via a 100-km transmission line. The transformer's primary side voltage is 20 kV and its secondary side voltage is 230 kV. The generator model comprises a synchronous generator, a hydro turbine with a governor, an automatic voltage regulator (AVR), and a power system stabilizer (PSS). The exciter used in the model is a static exciter that is a standard IEEE type ST1A. The power supply for the exciter is obtained from the generator terminal voltage via a step-down transformer and controlled rectifier. In this type of exciter, the inherent time constant is very small and it can operate without a stabilizer [32]. But in this model, PSS is implemented to accelerate the stabilization.

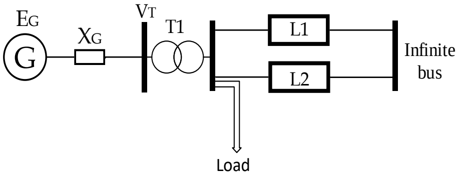

Fig.9. The simulated system to investigate the performance of the LOE detection methods

The generator data and control system data are listed in Appendix A. In this case, based on the mentioned model, the simulation was performed according to the system specifications. After the LOE event, the signal generated by the voltage and the power angle derivative are shown in Fig. 10(a) and (b). This figure shows that after the LOE occurs, the output voltage decreases, and the power angle output increases. The signal generated by the voltage is negative while the power angle signal is positive. The main idea is to use the index mark to detect the error after simulating the analysis based on the positive or negative signals after the LOE occurs. The simulation is performed in 15 seconds and after 5 seconds of the threshold.

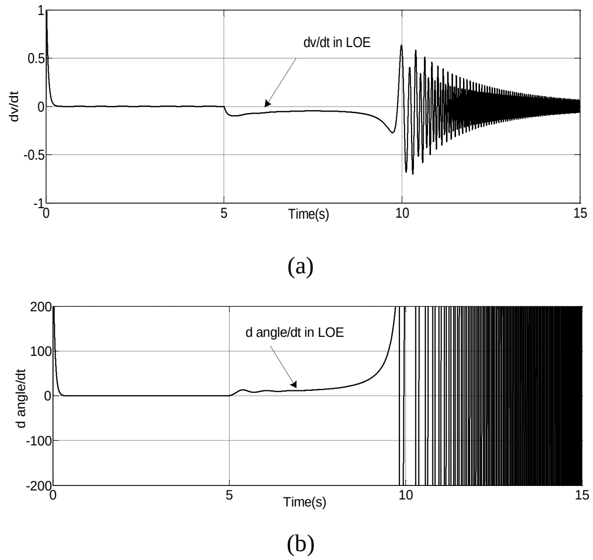

(a)

(b)

Fig.10. The generator’s derivative terminal voltage and derivative angle power after LOE

One of the main outputs of the simulation is the LOEDI index. Fig. 11 shows the LOEDI after the LOE occurs. The positivity or negativity of the index is considered a very important parameter. The LOEDI value is, initially, zero before the LOE occurs and its value is negative after the LOE occurs. As a result, if the index is negative, an LOE has occurred. The LOE relay must operate and issue a stop command.

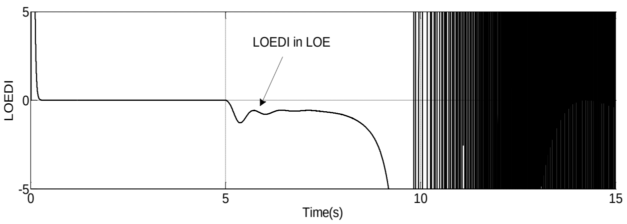

Fig.11. LOEDI after LOE

Next, the algorithm performance is tested under swing conditions since this is the main reason behind conventional relay mal-operation. A stable power swing is defined as an oscillatory disturbance that is controlled by the power system. After the disturbance is removed, the system will remain stable. For example, a fault on any line within the system that is cleared after a designated time will potentially give rise to an SPS.

For security evaluation of the proposed index, non-loss of field disturbances was applied to the simulated system. There were no trip commands generated, so the index can be considered a secure index. The proposed algorithm can correctly identify the LOE event. Since the LOEDI index depends on power system parameters, such as generator power, output power, and power system, if a short-circuit fault occurs and a stable power swing (SPS) is generated, the simulation results show that in the event of SPS, the LOEDI will be swinging.

In this case, if the generator is fully excited, a three-phase short circuit to the ground fault will occur within 2 seconds (in 7 s to 9 s). The simulation was performed for 15 seconds with a 5-s threshold. After a 1.67-s delay (10.67 s), the derivative of the voltage will be negative and fluctuate, and the power angle derivative will have low-amplitude oscillations; consequently, the magnitude of their increment, which is the LODEI index, will also be positive. A stable power swing is defined as an oscillatory disturbance that is controlled by the power system. After the disturbance is removed, the system will remain stable. For example, a fault on any line within the system that is cleared after a designated time will potentially give rise to an SPS.

In Fig. 12(a)-(c), the derivative of the voltage, the derivative of the power angle, and the LOEDI index are shown when the SPS occurs. The value of the LOEDI index is zero before the fault. Therefore, the index after oscillation will occur after 1.67 seconds (in 10.67 s). By changing the sign from positive to negative in a half-cycle, we realize that no LOE has occurred. Therefore, if this indicator is not negative, an SPS has occurred and the LOE relay will not give a trip. This will be a way to distinguish between the two errors (LOE and SPS).

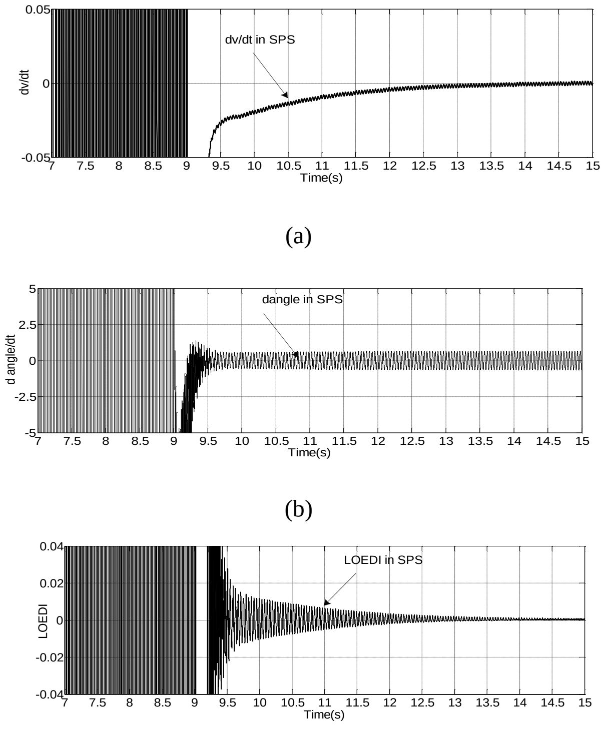

(a)

(b)

(c)

Fig.12. The generator’s derivative terminal voltage, derivative angle power, and LOEDI after SPS

By reducing the generator excitation, we repeat the simulation and check the output of the output signals. For example, suppose that the generator excitation is reduced to

0.4 p.u. (PLOE). According to the simulation outputs, we conclude that the voltage derivative in this case is negative and the power angle is positive. The corresponding index will also be negative. This result is similar to when the generator has full excitation. It detects and operates the error rate after 1.67 seconds. Figs. 13(a),(b),(c) present the simulation results. The behavior of the generator shows that the index detects the LOE error and cuts off the command relay correctly and in the shortest time in PLOE mode. The simulation is performed in 20 seconds and after 5 seconds of the threshold.

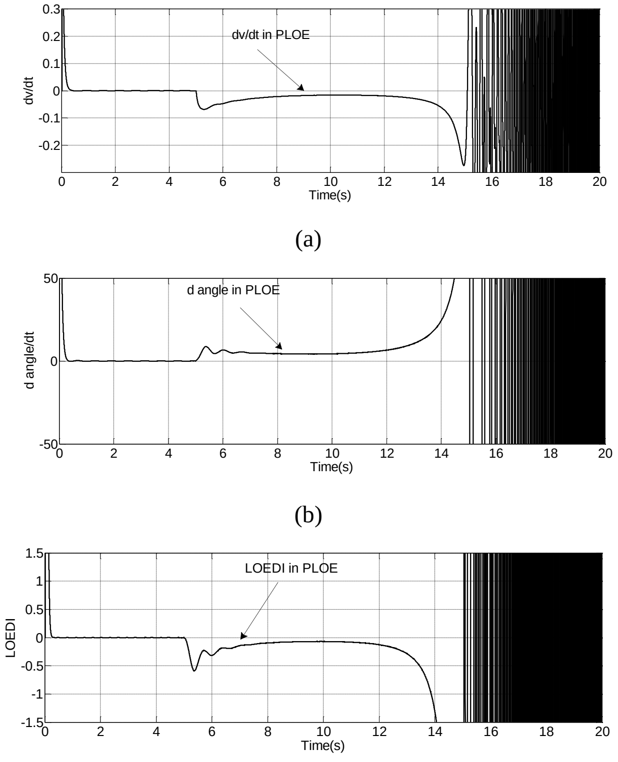

(a)

(b)

(c)

Fig.13. The generator's derivative terminal voltage, derivative angle power, and LOEDI after PLOE

Whether the index is positive or negative is considered a very important parameter in determining the LOE. Initially, the value of the LOEDI indicator is zero before the PLOE occurs, and the LOEDI value is negative after the PLOE occurs. Therefore, the index is similar to the time when the LOE occurs in the previous section. As a result, if the index is negative, an LOE has occurred. In this case, the LOE relay must act and issue a stop command. Therefore, in the PLOE mode, the LOEDI indicator correctly detects the LOE event and commands the LOE relay to prevent damage to the generator. Similar to this case, with a reduction in excitation to 0.4 p.u. (PLOE), the road performance will be the same as the previous part of LOE.

In the next case, we examine the behavior of the generator under heavy load conditions. Given that the generator is under a lot of stress in these conditions, it is crucial to detect the fault in the shortest possible time. The simulation is done with the previous specifications. According to Table II, different simulated loads and the LOEDI index signal were investigated in two modes (LOE and PLOE). The results are shown in Fig. 14.

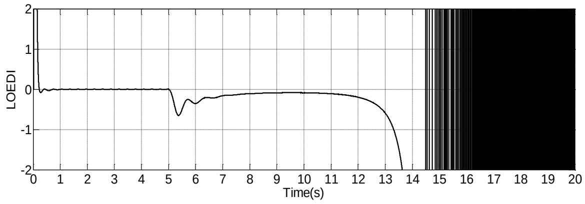

Fig.14. LOEDI after LOE and PLOE in the heavy load case

Fig. 14 shows that the system will oscillate in 9.6 seconds in the LOE mode, as well as in PLOE mode after 13.6 seconds. Simulation with different loads indicates that the proposed algorithm will operate without error affecting the behavior of different loads in LOE detection and will operate after 1.67 seconds if the index is negative.

Examining different modes under heavy and light load conditions in both LOE and PLOE conditions (0.2,0.4) are presented in Table 4. The simulation results indicate that the type of load in the fault detection is not affected by the LOEDI index and the index is independent of the load. It also detects LOE by reducing the excitation by 20% and 40% with different loads of the proposed algorithm. One of the important features of the index is the detection of partial reduction of excitation.

TABLE II

Supplementary Data of the Simulated Generator

Type of Loading (P.u.)		P.F	Mode of LOE
Heavy loading	L8=0.9+j0.3	Laging	LOE,EF=0
			PLOE,EF=0.2
			PLOE,EF=0.4
Heavy loading	L10=0.7-j0.5	Leading	LOE,EF=0
			PLOE,EF=0.2
			PLOE,EF=0.4
Light loading	L2=0.1+j0.3	Laging	LOE,EF=0
			PLOE,EF=0.2
			PLOE,EF=0.4
Light loading	L16=0.1-j0.2	Leading	LOE,EF=0
			PLOE,EF=0.2
			PLOE,EF=0.4

V. COMPARISON OF THE PROPOSED METHOD WITH OTHER LOE DETECTION METHODS

The performance of the LOE-DVA method for the case study synchronous generator, loading at S= 0.5-j0.4 p.u [33], was evaluated and compared with the following methods.

- Positive offset
- Berdy
- LOE protection based on fuzzy inference mechanism (LOE-FIM)
- LOE protection based on flux method (LOE-FBM)
- LOE protection based on flux method combined with negative sequence current (LOE-FVNSC)
- LOE-TDFM

The results are presented in Table III.

TABLE III

The Comparison of Different LOE Detction Methods

Relay type	Trip Time(s)
Positive Offset	11.2s
Berdy	10.4s
LOE-FIM	9.1s
LOE-FBM	3.1s
LOE-FVNSC	3.1s
LOE-TDFM	1.7s
LOE-DVAM	1.67s

According to the methods in Table III, Fig. 15 depicts the faster performance of the LOE-DVAM relay.

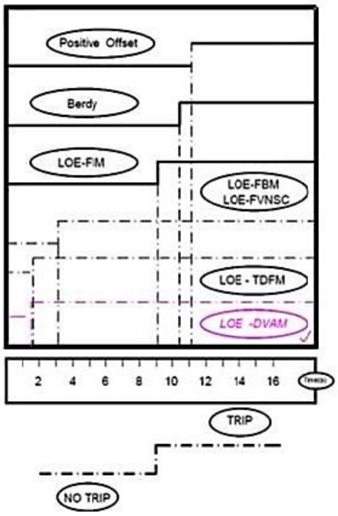

Fig.15. Various relay performance comparison

VI.CONCLUTION

In a synchronous generator, fault detection is one of the most important parameters to prevent serious damage to the generator. This paper introduced a new method for LOE and SPS detection. This method quickly detects faults, distinguishes between different faults (LOE, SPS), and prevents malfunction of the fault detection relay. The method is based on the generator's output signals, which use the terminal voltage derivative and the generator's power angle derivative. Using simulation in the MATLAB software, the behavior of the signals before and after the occurrence of the LOE error was investigated. The simulation output shows various behaviors caused by changes in the system, such as reduced generator excitation, short-circuit fault, and network load changes. Thus, according to this theory, an index is defined as LOEDI, which recognizes the LOE fault based on the calculation of the output voltage derivative signals. The LOEDI index detects the LOE fault within 1.67 seconds and reports the LOE detection relay. Table III shows that our proposed method outperforms all other methods. In the LOE fault detection method, comprehensive simulation studies for different system conditions and generators were examined by designing and simulating the synchronous generator simulation circuit. The results of these studies have shown that the proposed strategy is faster and more accurate. The algorithm distinguishes the LOE fault from the stable power swing (SPS) and prevents the relay from malfunctioning. It also prevents damage to the generator if the LOE occurs with the correct operation. With the proposed method, the protection and security of the synchronous generator as the most important device of power grids increases, and the LOE detection time is reduced.

APPENDIX

System data

Positive sequence equivalent impedance 0.0068+j0.096 p.u. (230kV, 200 MVA)

System voltage 230 kV, L-L, RMS

System frequency 60 Hz

Generator data	Transformer data	Transmission lines
S=200MVA, f=60 HZ H=3.2 s, V=13.8 KV Xd= 1.305pu, Xq=1.274 pu X'd= 0.3 pu, X'q= 0.243pu X"d= 0.23 puX"q= 0.24 pu T'do=5 s, T'qo=1.01 s T d=, T q= 0.09s Rated power factor 0.9 lagging	Rated MVA 210 MVA Rated voltage 13.8/230 kV Uk=12.5 % Connection mode DY11	L_1=L_2=100 km V=230 KV Z- = Z+ =0.042+0.139 Ohm/Km Z0 =0.159+0.736Ohm/Km

REFERENCES

[1] P. Kundur, A. Bose et al., “Definition and Classification of Power System Stability”,IEEE Trans. On PS, Vol. 19, No. 2, pp. 1387-1401, May, 2004.

[2] “Blackout of 2003: Description and Responses”, Dennis Ray PSERC, Nov. 5th 2003.

[3] “Final Report on the August 14th Blackout in the United States and Canada,” U.S.-Canada Power System Outage Task Force.

[4] V. Venkatasubramanian, Y. Li, “Analysis of 1996 Western American Electric Blackouts”, Bulk Power System Dynamics and Control-VI, August 24-27, 2004,Italy.

[5] O. Usta, M.H. Musa, M. Bayrak, M.A. Redfern, “A New Relaying Algorithm to Detect Loss of Excitation of Synchronous Generators”, Turk J Elec. Engin. Vol. 15,No. 3, pp. 339-349, 2007.

[6] R. Sandoval, A. Guzman, H.J. Altuve, “Dynamic Simulations Help Improve Generator Protection”, SEL 2006.

[7] IEEE Committee Report, “IEEE Guide for AC Generator Protection”, Trans. on PWRD, Vol. 4, No. 2, pp.957-964, 1989.

[8] C.R.ST. Pierre, “Loss-of-Excitation Protection for Synchronous Generators on Isolated Systems”, IEEE Trans on IA, Vol. IA-21, NO.1, 1985.

[9] J. Berdy, “Loss of excitation protection for modern synchronous generators”, IEEE Trans. on PAS, Vol. 94, No.5, pp.1457-1463, 1975.

[10] W.F. Mackenzie, J.A. Imhof, C. Dewey, E.J. Emmerling, F.H. Freer, S.H. Horowitz ,C.L. Wagner, “Loss-of-field Relay Operation During System Disturbances Working Group Report”, IEEE on PAS, Vol. 94, No. 5, pp.1464-74, 1971.

[11] D.C. Lee, P. Kundur, R.D. Brown, “A high speed discriminating generator loss of excitation protection”, IEEE Trans. on PAS, Vol. 94, pp. 1865-1899, 1979.

[12] A.R. Charles, M. Rogers, “A study of loss of excitation relaying and stability of a 595 MVA generator on the Detroit Edison System”, IEEE Trans. on PAS, Vol. 94, No. 5,pp. 1449-1456, 1975.

[13] H.G. Darron, J.L. Koepfinger, J.R. Mather, P.A. Rusch, “The influence of generator loss of excitation on bulk power system stability”, IEEE Trans. on PAS, Vol. 96, No.5, pp. 1473-1483, 1975.

[14] P. Kundur, Power System Stability and Control, Vol. I, New York, McGraw-Hill Inc., 1993.

[15] A. P. d. Morais, G. Cardoso, and L. Mariotto, "An Innovative Loss-of-Excitation Protection Based on the Fuzzy Inference Mechanism," IEEE Transactions on Power Delivery, vol. 25, no. 4, pp. 2197-2204, 2010.

[16] N. P. C. W. Series, P. Tatro, and J. Gardell, "Power Plant and Transmission System Protection Coordination Phase Distance (21) and Voltage-Controlled or Voltage-Restrained Overcurrent Protection (51V)," 2010.

[17] R. Sandoval, A. Guzman, and H. J. Altuve, "Dynamic simulations help improve generator protection," in 2007 Power Systems Conference: Advanced Metering,Protection, Control, Communication, and Distributed Resources, 2007, pp. 16-38.

[18] "SEL-300G Multifunction Generator Relay Instruction Manual," ed. Pullman WA:Schweitzer Engineering Laboratories, March 1998.

[19] B. Mahamedi, J. G. Zhu, and S. M. Hashemi, "A Setting-Free Approach to Detecting Loss of Excitation in Synchronous Generators," *IEEE Transactions on Power Delivery*,vol. 31, no. 5, pp. 2270-2278, 2016.

[20] H. Yaghobi, "Fast discrimination of stable power swing with synchronous generator loss of excitation," *IET Generation, Transmission & Distribution*, vol. 10, no. 7, pp. 1682-1690, 2016.

[21] H. Yaghobi, "Impact of static synchronous compensator on flux-based synchronous generator loss of excitation protection," *IET Generation, Transmission & Distribution* ,vol. 9, no. 9, pp. 874-883, 2015.

[22] H. Yaghobi and H. Mortazavi, "A novel method to prevent incorrect operation of synchronous generator loss of excitation relay during and after different external faults, "*International Transactions on Electrical Energy Systems*, vol. 25, no. 9, pp. 1717-1735,2015.

[23] A. Ghorbani, S. Soleymani, and B. Mozafari, "A PMU-Based LOE Protection of Synchronous Generator in the Presence of GIPFC," *IEEE Transactions on Power Delivery*, vol. 31, no. 2, pp. 551-558, 2016.

[24] Donalt. Reiment; Protective Relaying for Power Generation Syatems; Boca Raton: CRC Press, 2006.

[25] Ramón Sandoval, Comisión Federal de Electricidad; Dynamic Simulation Help Improve Generator Protection; Armando Guzmán and Héctor J. Altuve, Schweitzer Engineering Laboratories, Inc; 2006.

[26] Gabriel Benmouyal, The Impact of Synchronous Generators Excitation Supply on Protection and Relays, Scheweitzer Engineering Laboratories, Inc.

[27] P.J. Moore, A. Stangenberg , “An investigation into the impedance characteristics o f a synchronous generator under loss of excitation condition ”,*International Conference on Energy Management and Power Delivery* Vo. 2, 3-5 March 1998 pp.619 - 624.

[28] R.D. Rana, R.P. Schulz, M j. Heyeck, and T.R. Jr Boyer, “Generator loss of field study for AEP's Rockport plant” IEEE on Computer Applications in Power, Vol. 3, Issue 2, April 1990 pp.44 - 49.

[29] K.Z. Guo , W.D. Zhu, F.W.Tan , R.L. Jih , and G.Wang , “Analysis of large turbogenerator's asynchronous operation during loss of field”, *IEEE International*

Conference on Power System Technology, Vol. 2, 18-21 Aug.1998, p p .9 3 5 – 940.

[30] S. R. Tambay and Y. G. Paithankar, “A new adaptive loss of excitation relay augmented by the rate of change of reactance," in Proc. IEEE Power Eng. Soc. Gen. Meeting, Jun. 2005, vol. 2, pp. 1831–1835.

[31] Behnam Mahamedi, Jian Guo Zhu, and Sayyed Mohammad Hashemi, “A setting-free approach to detecting loss of excitation in synchronous generators,” IEEE Transactions on Power Delivery, vol. 31, no. 5, pp. 2270-2278, 2016.

[32] IEEE RECOMMENDED PRACTICE FOR EXCITATION SYSTEM; IEEE Std 421.5_1992.

[33] Hamid Yaghobi, and Hashem Mortazavi, “A novel method to prevent incorrect operation of synchronous generator loss of excitation relay during and after different external faults,” European Transactions on Electrical Power, Vol. 25, No. 9, pp. 1717-1735, 2014.

[34] Milad NiazAzari, "A setting-free flux-based synchronous generator loss of excitation protection." Electrical Engineering 100.4 (2018): 2329-2339.

[35] T. Amraee, “Loss-of-field detection in synchronous generators using decision tree technique,” IET Gener. Transm. Distrib., vol. 7, no. 9, pp. 943–954, 2013.

[36] M. Amini, M. Davarpanah, and M. Sanaye-Pasand, “A novel approach to detect the synchronous generator loss of excitation,” IEEE Trans. Power Del., vol. 30, no. 3, pp. 1429–1438, Jun. 2015.

[37] Sirus Salehimehr; Behrooz Taheri; Seyed Amir Hosseini; Hossein Askarian Abyaneh; Farzad Razavi. "A New Power Swing Detection Method Based on Hilbert Transform",International Journal of Industrial Elecronics, Control and Optimization, 3, 2, 2020, pp.103-114.

Reza Fathi Shoob was born in Babol, Iran,. He received his B.S degree in electrical engineering from Power and Water University of Technology (PWUT), Tehran, Iran in 2003, and his M.S degree in Electrical Engineering the Noshirvani University of Technology, Babol, Iran in 2005.He is currently a Ph.D. candidate in electrical engineering at Sari branch, Azad University, Sari, Iran.

Milad Niaz Azari was born in Babol, Iran. He received his B.S degree in electrical engineering from Noshirvani University of Technology, Babol, Iran in 2007. and his M.S. and Ph.D. degrees in Electrical Engineering from the, Amir Kabir University of Technology, Tehran, Iran in 2009 and 2013 respectively. Since 2014, he has been at University of Science and Technology of Mazandaran, Behshahr, Iran, as an assistant Professor in the department of Electrical Engineering. His current research interests include electrical machines design and power electronics.

International Journal of Industrial Electronics, Control and Optimization © 2021 IECO
Vol. 4, No. 1, pp. 127-139, Jan (2021)

Coordinated Operation of Wind Farms, Cascaded Hydro, Photo-voltaic, and Pump-storage Considering WT-ANN-ICA Hybrid Prediction Method

Ehsan Jafari †

1, † Department of Electrical Engineering, Lenjan Branch, Islamic Azad University, Isfahan, Iran

ABSTRACT

In this paper, a new algorithm is presented to reduce the uncertainty effects of wind farms power generation (WFPG) and photo-voltaic generation (PVG) in both day-ahead energy and ancillary services markets. Firstly, this research tries to predict the uncertainty of short-term WFPG with acceptable accuracy. Indeed, it uses the hybrid method of wavelet transform (WT) in order to reduce the fluctuations in the input historical data along with the improved artificial neural network (ANN) based on the nonlinear structure for better training and learning. Furthermore, the imperialist competitive algorithm (ICA) is adopted to find the best weights and biases for minimizing the mean square error of predictions.

In addition, regarding the high-level penetration of wind farms (WFs) on the power system, cascaded hydro units (CHUs) and pump-storage units (PSUs) are taken for the first time as supplementary units. Therefore, they are coordinated with WFs and photo-voltaic (PV) operations. Considering uncertainties of energy price, spinning and non-spinning reserves in the electricity market, WFPG, PVG and the availability of WFs, PV, CHUs and PSUs along with their effects on energy supply reliability lead to a scenario-based stochastic optimization problem. The aim of this problem is to increase the profit and decrease the financial risk (FR) of all of the units. The proposed method is implemented on WFs, PV, CHUs and PSUs of IEEE 118-bus standard system. Studying the results of profit and FR in the coordinated operation (CO) and the independent operation (IO) confirms that the profit is increased and the FR is reduced in the CO. Hence, the ability and merit of hybrid method of WT-ANN-ICA is verified.

Article Info

Keywords:
Availability, Cascaded hydro units, Photo-voltaic, Pump-storage units, and Wind farms.

Article History:
Received 2019-07-30
Accepted 2020-04-26

NOMENCLATURE

i	Index of each energy resources,	T/t	Total number / index of time intervals
$M(i,t)$	Commitment state of i-th generation unit	α/β	Surplus/Deficit charge
$N(i,t)$/ $N'(i,t)$	Status/Shutdown operation state	η	Coefficient of imbalance cost

---

[†] **Corresponding Author**: jafari@iauln.ac.ir Tel: +98-3152437001 Fax: +98-3152432211, Faculty of Department of Electrical Engineering, Lenjan Branch, Islamic Azad University, Isfahan, Iran.

$Z_{CH}(pv,t)/Z_{DCH}(pv,t)$	Charge/discharge state of energy saving battery	W_N, PV_N, PS_N, H_N	Number of units
$U_{COST}(i,t)/\ D_{COST}(i,t)$	Startup/shutdown cost of $i-th$ generation unit	$P_{WN}(W)$	Rated power of W-th wind farm
$\rho(s_w, s_P, s_{pv}, s_{ps}, s_h)$	Probability of each scenarios	δ	Efficiency factor
$S_{NP}, S_{NW}, S_{Npv}, S_{Nps}, S_{Nh}$	Total number of scenarios	$P_{BATT}^{DCH}(K,t)\ P_{BATT}^{\max DCH}(K)$	Power delivered
$s_p, s_w, s_{pv}, s_h, s_{ps}$	Index of scenarios	$R_T(i,t), R_S(i,t), C_T(i,t)$, $C_{imb}(i,t)$	Values of total profit, revenue from selling, total generation cost and imbalanced revenue/cost
$E_P(s_p,t)$ $E_{SR}(s_p,t)$, $E_{NSR}(s_p,t)$	Price of the market for energy, spinning and non-spinning reserve for s_p-th scenario of price($/MW)	$v(ps,end)/v(ps,ini), v(ps,t)$:	Terminal/Initial reservoir water volume, reservoir water volume of $ps-th$ pump-storage unit
$pr_{\max}(ps)/\ pr_{\min}(ps)$	Max/Min of water charge rate in $ps-th$ pump-storage unit	$v_{\min}(ps)/v_{\max}(ps)$	Min/Max reservoir water volume limit
$gr_{\max}(ps), gr_{\min}(ps)$	Max/Min of water discharge rate	$I^p(ps,t)/I^g(ps,t)$	Commitment condition of generating/pumping
$gr_{(s_w,s_p,s_{pv},s_{ps},s_h,ps,t)}$ $/\ pr_{(s_w,s_p,s_{pv},s_{ps},s_h,ps,t)}$	Generation-discharge/pumping-charge water	$\mathrm{p}_{\min}^{\mathrm{g}}(ps)/\ \mathrm{p}_{\max}^{\mathrm{g}}(ps)$	Min / Max power generation
$\mathrm{p}_{\max}^{\mathrm{p}}(ps)$	Maximum purchased power of pumping operation	$\mathrm{N.SR.on}_{(s_w,s_p,s_{pv},s_{ps},s_h,ps,t)}$ $\mathrm{N.SR.down}_{(s_w,s_p,s_{pv},s_{ps},s_h,ps,t)}$	non spinning reserve of up/down condition
A_w, A_{ps}, A_h, B_h	Cost coefficients	$\hat{y}_{in}\ /\ y_{in}$	Predicted/ Real value for in-th input
$SR^g_{(s_w,s_p,s_{pv},s_{ps},s_h,ps,t)}$ / $SR^p_{(s_w,s_p,s_{pv},s_{ps},s_h,ps,t)}$	spinning reserve of generation / pumping operation	$QSC(ps)$	Generation capacity in the rapid startup
$\mathrm{SR}(ps,t)$, $\mathrm{R}_{\mathrm{C,PS}}(ps,t)$ / $\mathrm{N}_{\mathrm{C,PS}}(ps,t)$	Total spinning reserve, spinning/non spinning reserve bids	$P_{BATT}^{CH}(k,t)$, $P_{BATT}^{\max CH}(k)$	Charging power of $k-th$ battery at hour t and its maximum limit
$BATT_{COST}$	The cost of buying energy for battery charging	$\mathrm{ENR}(k,t)$	The amount of saved energy in $k-th$ battery
$P_{BATT}^{DCH}(k,t)$, $P_{BATT}^{\max DCH}(k)$	Power delivered while discharging $k-th$ battery and its maximum limit	$QT_h(\hat{h}, t-\tau_{h,\hat{h}})$:	Discharge to $\hat{h}-th$ unit from turbine path of upstream $h-th$ unit
$R_{\hat{h},h}$	The vector of reservoir connection, if $h-th$ hydro unit is directly upstream of the $\hat{h}-th$	$q(s_w, s_p, s_{pv}, s_{ps}, s_h, h, t)$ $/\ S(s_w, s_p, s_{pv}, s_{ps}, s_h, h, t)$	discharge/spillage water volume from $h-th$ hydro unit
$u(h,t)$	Natural inflow of $h-th$ hydro unit in Hm^3/h	k_{1h}, k_{2h}, k_{3h}	Water to power conversion coefficients

I. INTRODUCTION

One of the main goals in countries with restructured electricity market where governmental support and subsidies are omitted is to establish a complete competition in the market. Additionally, lack of financial support from renewable resources like wind and photo-voltaic resources in one hand, and compulsory expansion of them due to environmental reasons in the other hand along with the uprising cost of fossil fuels could make this market unlikely prolific for the investors and producers. Therefore, optimal planning is of particular importance [1-3]. In [1], A chance-constrained model is developed to handle optimal operation and emergency conditions of Microgrid including renewable resources outage and unwanted islanding. An optimization method to optimize the parameters of the Microgrid controller in islanding mode. The controller optimal parameters have been obtained by using the particle swarm optimization (PSO) [2]. In [3], a method has been proposed that can be used to determine the location, power, and capacity of the energy storage systems with consideration of the technical and economic aspects, simultaneously.

Owners of renewable resources need to predict the uncertainties for optimal planning such as WF power generation/wind speed [2-9], market price, and load forecasting. In [4] Autoregressive Moving Average (ARMA) was used to predict WFPG. In addition, [5] used adaptive neuro-fuzzy inference system (ANFIS) and [6] hired ANFIS and PSO together for prediction of WFPG. In [7], firstly, historical data of WF is decomposed using WT; then, WFPG is predicted by ANN. This method is tested in two regions of china. Afterwards, comparing WT-ANN, ANN, and ARMA methods reveal that WT-ANN can significantly reduce the error in spite of ANN and ARMA methods. In [8], the optimal weights and biases of ANN are determined by genetic algorithm (GA), ICA, and ICA-GA methods; then tested on six specified data-bases. In the end, the obtained results confirmed that ICA has higher capabilities. Similarly, ANN is employed to predict WFPG and ICA, GA and PSO are chosen to determine the optimal weights and biases [9]. The prediction results were more satisfactory when ICA algorithm was utilized.

The second solution for uncertainty reduction in renewable units including WF is to coordinate other energy resources which are quite expensive, but available and more reliable, such as PSU, CHU, gas turbines, combine cycle power plants and energy storage batteries. However, the share of these energy sources should diminish for many reasons [10]. In [11] the coordinated planning of WF, PSU, and thermal units is presented by the multi-stage stochastic planning and solved by scenario decreasing algorithm of PSO. In [12], the required reserve level is estimated in presence of high-level WF penetration. In [13], the optimal strategy of WF is determined in the real-time market. The wind speed and market price are predicted by ARMA. Also the expected profit is limited by FR and the required reserve is determined because of error prediction in WFPG. In [14], the coordinated planning problem of WF and thermal power plants is solved by artificial immune optimization method. This optimization method is implemented on a system including ten thermal power plants and two WFs. A mixed integer programing algorithm is adopted for period planning of operation status/shutdown and generating/pumping mode of PSU to maximize the profit in CO of WF and PSU [15]. A scenario-based and chance constrained optimization method is hired to consider the WFPG prediction error. The optimal coordinated strategy in stochastic planning for WF and CHUs is discussed in [16]. This stochastic planning is based on PBUC, and includes the imbalance cost in WF. A chance-based method is chosen to solve the optimization problem, and the results were compared with Monte Carlo method. Studying the risk and the limitation of FR in GENCOs is discussed in [17]. A rolling optimization method for WF coordination with the energy-storage systems in the day-ahead market is presented to increase the profit of these power plants. The CO and IO of a system including a WF, PSUs, and photovoltaic resources are compared in [18]. Predicting WFPG is carried out through ARMA method. The results show growth in profit and decline in FR of CO. The optimal cascaded hydro unit scheduling and biding strategies considering price uncertainty and risk management is analyzed in [19]. The optimal scenario-based operation management of Micro-Grid including WF, Photovoltaic, Micro-Turbine/Fuel Cell, and Energy Storage devices were studied in [20]. In this paper, the considered uncertainties are load, WFPG, Photovoltaic power generation, and market price. Optimal biding strategy model in an electricity distributed company in order to make maximum profit in a day-ahead market is considered in [21]. In [22], the reliability of WF in coordination with PSU in power system is estimated. This research uses a Monte Carlo simulation method to establish coordination between WF and PSU with an objective function to compute the adequacy indexes for one-year period.

The presented issue, in this paper, can be shortly explained as follows:

1-Prediction of WFPG via hybrid method (HM) of WT-ANN-ICA. According to the studies in [7-9], prediction of WFPG using the proposed method can lessen errors of prediction in comparison to ARMA, ANN, WT-ANN, WT-ANN-PSO, and WT-ANN-GA methods. Therefore, this approach may generate scenarios closer to reality and lead to the optimal programming.

2-Generating the scenarios of WFPG, PVG, market price (energy, spinning reserve and non-spinning reserve) and decreasing the scenarios with the Scenario-reduction backward method, availability of WFs, PV, CHUs and PSUs, and modeling them by scenario tree method.

3-The coordination programming of WFs, PV, CHUs and PSUs, by considering constraints of these units and the uncertainties of WFPG, PVG, market price and availability of WFs, PV, CHUs and PSUs.

4-Studying the expected profit and FR in the CO and IO of all four unit types with and without considering the availability.

II. THE PROPOSED METHOD

The proposed algorithm for programming of generation and unit commitment of WFs, PV, CHUs and PSUs including two WFs, one PV, three CHUs and three PSUs in both CO and IO states in both day-ahead energy and ancillary services markets is shown in Fig. (1).

A. Publication Prediction and scenario generation

a) WFPG prediction using HM of WT-ANN-ICA: The proposed method for prediction of WFPG is depicted in Fig. (1). First, it is assumed that the prediction for d-th day can be done and historical data is available for every hour of 24 hours since 100 days ago.

Stage 1: data homogenization: the historical data is recalled and normalized to improve data homogenization through MinMax normalization method.

Stage 2: Data Processing Using Wavelet Theory: the components and features of data can be extracted via mathematical equations. More specifically, the components and features of time and frequency domain of data signal can be extracted using wavelet technique. The basic equations of WT are as Eq. (1), (2).

$$WT(a,b) = \frac{1}{\sqrt{a}} \int_{-\infty}^{+\infty} f(t)\psi(\frac{t-b}{a})dt \quad (1)$$

$$a = 2^{-j}, b = k2^{-j} \in R, a \neq 0$$
$$f(t) = \frac{1}{C_{\Psi}^{2}} \iint_{a,b} \Psi_{\psi} \frac{1}{a^{2}} \psi(\frac{t-b}{a})dadb \quad (2)$$

Where, ψ (a,b) is wavelet function and f(t) is input signal on which wavelet function is done until resulting the WT (a,b) signal. Also a and b are the parameters related to the WT which depend on the kind of wavelet function. The approximated values are again decomposed after some iterations; therefore, the signal is decomposed into smaller parts [7, 23]. In Fig. (2, a) the output power of wind farm 1(WF1) is shown along with its WT signal for every hour of the past year. WT is useful here to suppress the disturbances in historical data and to alleviate the fluctuation of input data. A fast technique to execute WT has been used, which contains two stages: decomposition and reconstruction. At first, the original wind data series is decomposed into one approximation series and some detail series. Next, detail and approximation series are assembled back into the original series. More mathematical details of the technique can be found in [20]. Fig. (3) depicts the corresponding wavelet decomposition. The input data is decomposed into three approximated components (Dh1, Dh2, Dh3) with lower accuracy along with a more precise component (Ah) which plays the most important role in the prediction process.

Stage 3: Artificial Neural Network (ANN): McCulloch and Pitts tried to simulate the ANN by a logical model for the first time but today it is widely used in many fields. The chosen ANN here in this paper comprises three perception layers (multi-level perceptron method); the output layer with one neuron, the input layer with five neurons, and the hidden layer with three neurons. This ANN can predict the information of hours d(t+1,……t+24) for the output signals of WT as the initial data.

Stage 4: Imperialist Competitive Algorithm (ICA): ICA is a new optimization strategy based on political and social evolution of human. More precisely, this algorithm is the mathematical model of social-political process of imperialists. Basically, GA and PSO are inspired of biological evolutions, chromosomes and particles, to determine the best solution. However, the source of inspiration in ICA is the social-political evolution, and it uses colonies (countries) as the variable for finding the optimal solution [8, 9]. The steps of ICA can be summarized as follow:

- Creating the initial colonies: according to the neural network input signals (Ah,Dh1,Dh2,Dh3), and the five neurons in the input layer (IL), three neurons in hidden layer (HL), and one neuron in output layer(OL), the matrixes of weights (W) and biases (B) are respectively.
- Hence, each colony constitutes 47 variables. Initial colonies are selected randomly through specific range based on initial training of ANN. Then, regarding the cost function based on decreasing the prediction error, the optimization of weights and biases are performed within the neural network for better training. A multi-layer feed forward neural network is considered to predict the wind power. Since the input data and target data of the system are normalized between -1 and 1, Tan-Sigmoid transfer function is used in the neurons of hidden layers. The linear transfer function is also used in the neurons of output layer. The proposed neural network is feed forward with one hidden layers trained by ICA. Table 1 represents Layer's transfer functions of neural network layers and number of layer's neurons. Table 2 represents the characteristic of neural network. The cost function here is mean square error (MSE) which is implied as Eq. (3).

$$\min FunctionCost \qquad MSE = \frac{1}{IN} \sum_{in=1}^{IN} \left| \hat{y}_{in} - y_{in} \right|^{2} \quad (3)$$

TABLE I

Number of Layer's Neurons and Layer's Transfer Function of Neural Network

Number of Layers	Number of Neurons	Transfer Function
1	5	Tan-Sigmoid
2	3	Tan-Sigmoid
3	1	Liner

TABLE II

Characteristic of Neural Network.

Network Type	Feed Forward
Training Function	Gradient Descent Momentum and an Adaptive Learning Rate
Adaption Learning Function	Gradient Descent Weight and Bias
Performance Function	Mean of Squared Errors

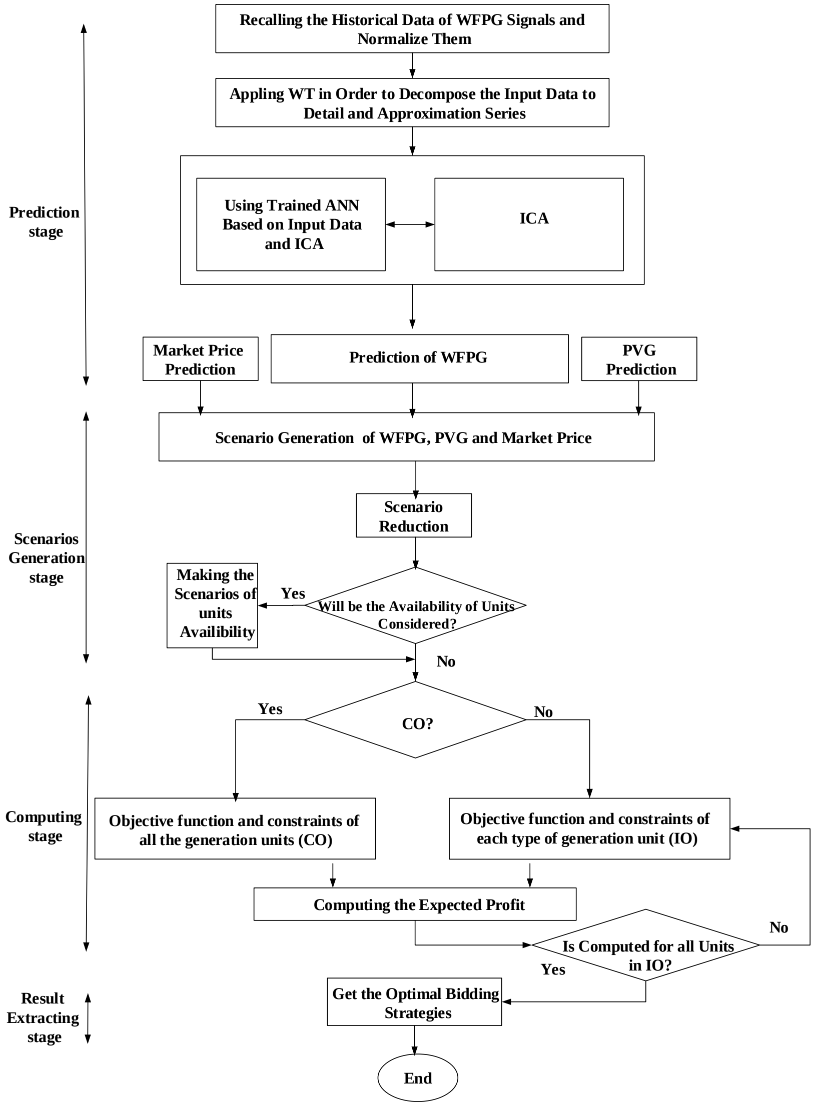

Fig. 1: The flowchart of the proposed method

- Selecting the imperialist: in this stage the colonies which have minimum cost are selected as the imperialists.
- Allocating the other countries as the colony to the imperialists: in this step, some colonies are allocated to each of imperialists and empires. This allocation is done according to imperialists fitness (fewer cost) by stochastic universal sampling method. The stages of 1-3 are the initialization stages of ICA.
- Performing the act of assimilation or absorption policy: in this stage, each of the colonies is moved towards the imperialist in each empire. This stage proceeds to improve the exploitation of algorithm.
- Performing the act of revolution: In this stage, the random changes are applied on each of the colonies. This action can improve the exploration of algorithm, and prevent from involving the optimization in the local optimal points.
- Computing the cost of colonies and imperialists
- Comparing the cost of colonies with imperialist in each empire: if a colony has a lower cost than the imperialist, it will take its place.
- Evaluating the empires: the cost for each empire is computed according to Eq. (4).

$$Cost_{empire} = Cost_{imperialist} + \frac{0.1}{N_{COL}} \sum_{n=1}^{N_{COL}} (Cost_n) \qquad (4)$$

where: N_{CLO} is the number of colonies.

- Decreasing the colonies: in this stage, a colony is omitted from the weakest empire and transmitted to another empire by roulette wheel method. According this method, the empire with the lower cost has more chance to seize the colony.

-Omitting the empire: if the weakest empire has no colony, the related imperialist will be transmitted to another empire as a colony.

Stage 5: Studying the termination condition: the stop condition is set based on the number of iterations obtained by trial and error method. If the stop condition of program is satisfied, the results move to the scenario generation stage; otherwise, the algorithm returns to (4) to generate new colonies. ICA flowchart is illustrated in Fig. (4). WFPG prediction curves are shown in Fig. (2, b-c).

b) Generating scenarios for WFPG, PVG and market price: After predicting the uncertainty variables, the predicted error of each one is considered with a known probability distribution function. This distribution function is discretized to N parts with the mean of zero from the center with the width of α. It is allocated to the occurrence probability and specific error percentage for each level as shown in Fig. (5). The probability of each occurrence is normalized so that their accumulated distribution function is equal to 1. Then a number is randomly selected for each uncertainty variable and each time interval by roulette wheel method; hence, an intended scenario is generated.

The rate of each scenario is obtained by the sum of the error and the predicted amount of variable [20]. Eq. (5) shows the amount of scenario for the WFPG. Consequently, 500 scenarios are generated for each WFPG, PVG, and market price.

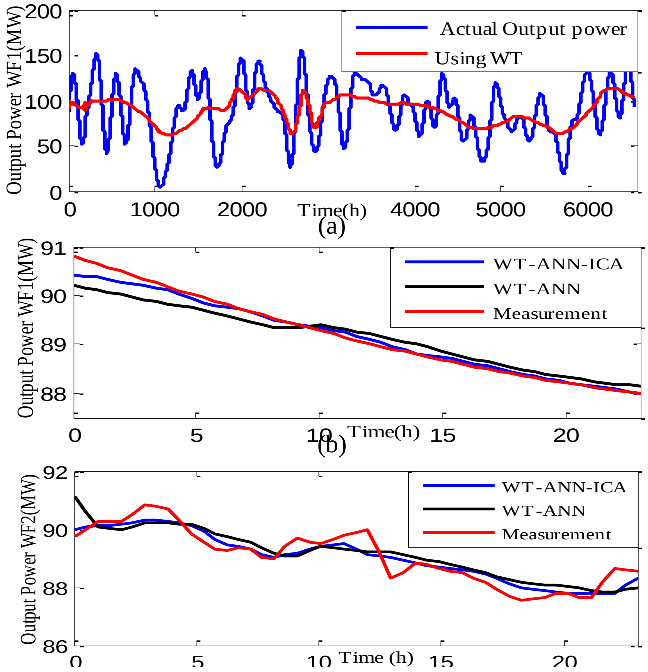

(c)

Fig. 2: (a): The real output power after noise removal by WT in a period of one year of WF1. The output power measured and predicted by methods of WT-ANN and WT-ANN-ICA related to (b):WF1 (c):WF2 in d=101.

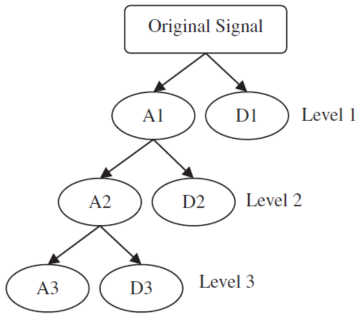

Fig. 3: Wavelet decomposition

$$P_G^W(w,s,t) = P_{Gforcasted}^W + \Delta P_G^W(w,s,t) \qquad (5)$$

$$t = 1,....,24, \qquad s = 1,......, s_w, \qquad w = 1,......, W_N$$

c) Backward method scenarios reduction: For modelling all three uncertainty parameters including WFPG, PVG and market price many scenarios are generated. However, the huge number of scenarios makes it burdensome to solve the stochastic problem. In order to solve this problem, the number of scenarios should decline by the backward method. The basis of this method is to merge the scenarios with close probability into one. This process could continue until reaching the favorable numbers [18, 20]. In this research, the number of scenarios abates down to 10 for each state. WFPG scenarios are shown in Fig. (6).

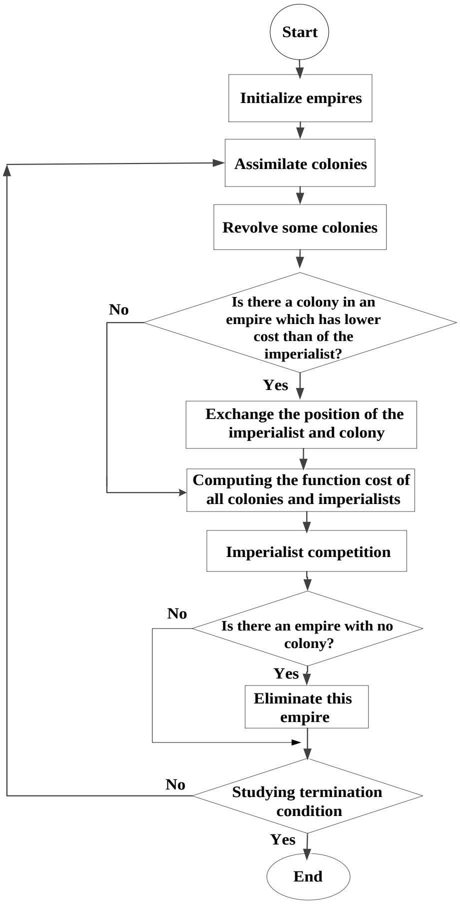

Fig. 4: Flowchart of ICA

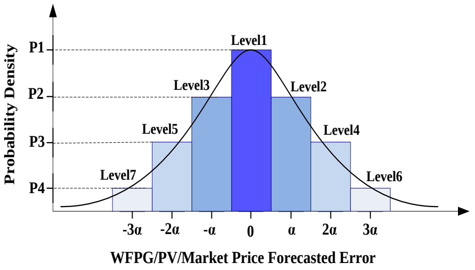

Fig. 5: The probability density of function of the WFPG, PVG and market price.

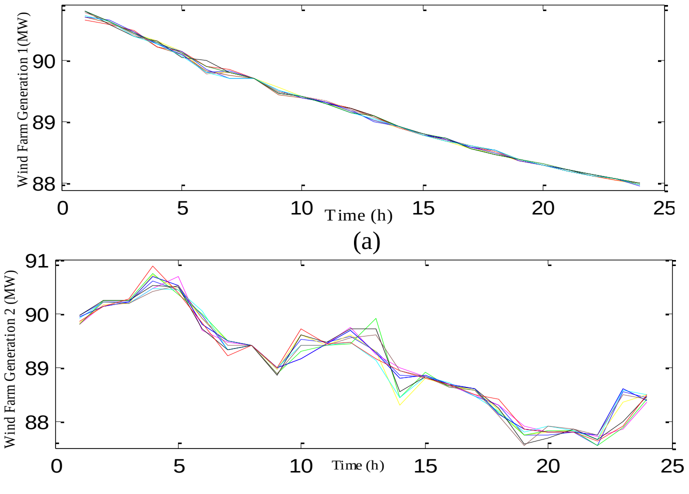

(a)

(b)

Fig. 6: WFPG scenarios (a):WF1 (b):WF2.

d) Modelling of the units availability uncertainty: An important issue in a restructured market is the reliability and availability effects on the behavior of generation unit owners. In fact, the reliability of the overall system may not be of concern; however, the main objective of these owners is to maximize their own profit. Hence, the owners need to pay extra attention to availability and reliability of their proposed generation values. A scenario-based method is proposed to generate the units' availability scenarios. In this paper, the two-stage Markov model is selected. Since the operation of each WFs, PV, CHUs and PSUs in each hour is dependent to the system operation at the previous hour, Monte-Carlo simulation method is employed for generating the availability scenarios of WFs, PV, CHUs and PSUs. Therefore, availability scenarios of each unit in each hour (5 scenarios for each unit) are achieved based on random numbers between 0 and 1 with normal distribution.

Then, each of these random numbers is compared with the force outage rate (FOR) of the intended unit. If the intended random number is greater than FOR, the unit is available in that scenario and hour. Otherwise, the unit is not available by the number of hours of mean time to repair (MTTR) in that scenario. Practically, if a unit is switched off because of the failure, it will not be available until the complete repair [22].

After determining the availability/unavailability of each unit in each scenario and hour, the capacity of generation units is achieved from aggregating of available capacity in each unit.

B.Coordinated operation (CO) of WFs, PV, CHUs and PSUs

In the day-ahead market, GENCOs and consumers submit their bids to ISO according to the predicted market price and demand. In this condition, the profit of generation units is determined with regard to the market clearing price, operation cost, imbalance revenue/cost, proposed energy, and delivered energy as Eq. (6). These parameters are computed in Eq. (7)-Eq. (9) [13, 15]. Where Eq. (7), shows the revenue earned from the sold energy equal to $P_S(i,t)$ with price $E_P(t)$. Eq. (8) also shows the operation cost as a function of unit generation power $P_G(i,t)$. Eq. (9) shows the imbalance revenue/cost of unit as a function of difference between proposed and generation (delivered) energy $(P_S(i,t)-P_G(i,t))$. Eq. (10) indicates imbalance revenue/cost function. Where $\alpha(t)$ and $\beta(t)$ are variously defined in different markets. In this paper, the relation between imbalance penalty factor and generation power is illustrated as Eq. (11). In Eq. (11) η is a number between zero and one, also three variables $P_G(t)$‘ $\tilde{C}_{imb}(t)$, and $E_P(t)$ are unknown before the energy delivery time. These three variables cause uncertainties and risks in programming.

$$R_T(i,t)=R_S(i,t)-C_T(i,t)-C_{imb}(i,t) \tag{6}$$

$$R_S(i,t)=P_S(i,t).E_P(t)+P_{SR}(i,t).E_{SR}(t)+P_{NSR}(i,t).E_{NSR}(t) \tag{7}$$

$$\begin{aligned}C_T(i,t)&=(a_i+b_i.P_G(i,t)+c_i.P_G^2(i,t)).M(i,t).AV(s,i,t)\\&+(U_{COST}(i,t)+D_{COST}(i,t)).AV(s,i,t)\end{aligned} \tag{8}$$

$$C_{imb}(i,t)=\tilde{C}_{imb}(i,t).f(P_S(i,t)-P_G(i,t)) \tag{9}$$

$$C_{imb}(i,t)=\left(\alpha(t)+\beta(t).(\frac{P_S(t)}{P_G(t)})^2\right).(P_S(t)-P_G(t)) \tag{10}$$

$$\begin{cases}\beta(t)=(1+\eta).E_P(t),\alpha(t)=0 & P_S\rangle P_G\\ \alpha(t)=(1-\eta)E_P(t),\beta(t)=0 & P_S\langle P_G\end{cases} \tag{11}$$

a) Problem modeling of unit coordination programming:

In this section, an optimal bidding strategy is modeled and analyzed. The objective function of this optimization problem utilized for the first time is as Eq. (12). The aim is to maximize the expected profit (difference between incomes and costs (Eq. (13)) of units considering constraints related to unit usages. The revenues are earned from selling energy and reserve delivered to the market. In fact, the revenue from generation is more than the proposed amounts to the market (positive imbalance revenue) by all of the units (Eq. (14). Also the costs include the expenditure of operation, startup and shutdown, purchased power of PSUs in the state of pumping operation, the cost of battery of PV resources and also imbalance cost as

Eq. (15), Eq. (16).

$$\max \quad ER_T=\sum_{t=1}^{T}\ \sum_{s_p=1}^{S_{NP}}\sum_{s_w=1}^{S_{NW}}\sum_{s_h=1}^{S_{NH}}\sum_{s_{ps}=1}^{S_{NPS}}\sum_{s_{pv}=1}^{S_{NPV}} \rho(s_w,s_p,s_{pv},s_{ps},s_h).\left(\sum_{w=1}^{W_N}\ \sum_{ps=1}^{PS_N}\sum_{h=1}^{H_N}\sum_{pv=1}^{PV_N} R_T(s_w,s_p,s_{pv},s_{ps},s_h,w,pv,ps,h,t)\right) \tag{12}$$

$$R_T(s_w,s_p,s_{pv},s_{ps},s_h,w,pv,ps,h,t)=\begin{pmatrix} R_S(s_p,t)-C_T(s_w,s_p,s_{pv},s_{ps},s_h,w,pv,ps,h,t)- \\ C_{imb}(s_w,s_p,s_{pv},s_{ps},s_h,w,pv,ps,h,t)\end{pmatrix} \tag{13}$$

$$R_S(s_p,t)=\left(E_P(s_p,t).P_S(t)+E_{SR}(s_p,t).P_{SR}(t)+E_{NSR}(s_p,t).P_{NSR}(t)\right) \tag{14}$$

$$C_{imb}(s_w,s_p,s_{pv},s_{ps},s_h,w,pv,ps,h,t)=\tilde{C}_{imb}(s,t).f\left(P_S(t)-P_G(s_w,s_p,s_{pv},s_{ps},s_h,w,pv,ps,h,t)\right) \tag{15}$$

$$C_T(s_w,s_p,s_{pv},s_{ps},s_h,w,pv,ps,h,t)= \tag{16}$$

$$\begin{pmatrix} \left(\sum_{w=1}^{W_N} A_w.AV(s_w,w,t)\right)+\left(\sum_{ps=1}^{PS_N}(A_{ps}+U_{COST}(ps,t)).AV(s_{ps},ps,t)\right) \\ +\left(\sum_{h=1}^{H_N}(A_h+B_h.P_G^H(s_w,s_p,s_{pv},s_{ps},s_h,w,pv,ps,h,t)+U_{COST}(h,t).N(h,t)+D_{COST}(h,t).N'(h,t)).AV(s_h,h,t)\right) \\ +\left(\sum_{pv=1}^{PV_N}(BATT_{COST}(k=pv,t)).AV(s_{pv},pv,t)\right)\end{pmatrix}$$

Where: $BATT_{COST}(k,t)=[a^{CH}(k)Z_{BATT}^{CH}(k,t)+b^{CH}(k)P_{BATT}^{CH}(k,t)]+[a^{DCH}(k)Z_{BATT}^{DCH}+b^{DCH}P_{BATT}^{DCH}(k,t)]+CC(k)$

a) Constraints of the proposed optimization problem:

1. General constraints:

- Maximum energy propose limit (Eq. (A.1)).
- Available output generation power of the CO (Eq. (A.2)).

2. Constraints of PSUs:

-Produced/consumed power of PSU in Generation/pumping operation: (Eq. (A.3).

- Balance of water constraints: (Eq. (A.4), Eq. (A.5)).
- Upper/lower water reservoir volume limits: (Eq. (A.6), Eq. (A.7)).

-Initial /terminal water reservoir volume: (Eq. (A.8)-Eq. (A.9)).

- Charge/discharge of water limits: (Eq. (A.10), Eq. (A.11)).
- Proposed power to the energy and ancillary services markets limits: (Eq. (A.12), Eq. (A.13)).

Non-spinning reserve limit in down state: (Eq. (A.14)).

Operation in pumping /generating mode: (Eq. (A.15)).

-Reserve power supply generated in pumping mode: (Eq. (A.16)).

- Proposed spinning/non-spinning reserve limits: (Eq. (A.17), Eq. (A.18)).

3. WFs constraint:

- Wind power generation limit: (Eq. (A.19)).

4. CHUs Constraints: In this section, the programming constraints used in this paper are presented. These constraints consist of both electrical and hydro operation parts. Because of the complicated nature of stream on a reservoir, a matrix model is assumed [26]. In this matrix model indicates each variable of charge and discharge water from the dam, turbine, and units. Subsequently, two main variables in the matrix modeling constraints of hydro system are taken as Eq. (A.20).

It should be mentioned that unit is directly upstream of unit (Eq. (A.21)).

- The balance constraint of water for CHUs: According to this constraint, the volume of water stored in hydro unit at hour is obtained based on the reservoir water volume at hour, the reservoir natural inflow at hour, the reservoir discharge, and the reservoir spillage at hour (t-1), as Eq. (A.22):
- Water discharge rate limit: (Eq. (A.23)).
- Reservoir water volume limit: (Eq. (A.24)).
- Initial /terminal reservoir water volume: (Eq. (A.25)).
- The generation power of CHU: (Eq. (A.26)).
- Ramping up/down limits: (Eq. (A.27), Eq. (A.28)).
- Water spillage limit: (Eq. (A.29)).
- Operation status/shutdown state: (Eq. (A.30), Eq. (A.31)).

5. PV Constraints:

- Limits on the battery of the photo-voltaic unit while getting charged and discharged: (Eq. (A.32), Eq. (A.33)).
- Charge/discharge switching constraint: (Eq. (A.34)).
- Initial / terminal energy of the PV: (Eq. (A.35)).
- Amount of saved energy in the battery: (Eq. (A.36)).
- The power generation of the photo-voltaic unit and battery: (Eq. (A.37)).

C. Coordinated operation (CO) and independent operation (IO) without considering availability

In order to consider an independent or coordinated planning of units without reliability, uncertainty parameters are WFPG, PVG and market price (s_w, s_p, s_{pv}) and the availability of the units are taken constantly equal to 1 ($AV(s,i,t)=1$). First, the objective function of each type of unit and related constraints are optimized separately. Then, the generation bids and in turn the expected profit and FR are calculated.

This process is repeated for CO, so that the objective function of WFs, PV, CHUs and PSUs units (Eq. (12)) is optimized considering constraints of all four unit types in parallel with other constraints forced by CO. Afterwards, a generation bid is offered to ISO, and WFs, CHUs and PSUs will participate in a day-ahead energy and ancillary services markets considering maximum generation power of each unit. In this case, the expected profit and FR are calculated and compared. This optimization problem is solved using GAMS / CPLEX software.

D. Coordinated operation (CO) and independent operation (IO) considering availability

Due to the increasing number of units and generation volume, reliability and availability of each unit may have a great effect on determine the biding strategy of WFs, CHUs and PSUs in CO and IO.

In this case, uncertainty parameters are WFPG, PVG, market price and availability of WFs, PV, CHUs and PSUs ($s_w, s_p, s_{pv}, s_{ps}, s_h$).

III. NUMERICAL EXAMPLE

The improved IEEE 118-bus standard system contains two WFs, one PV, three CHUs and three PSUs. The WFs nominal power rates are $P_{\max}^{MW} = 300$ and $P_{\min}^{MW} = 10$. IEEE standard values are assumed for the historical data of WFPG. The PV nominal generation power is $P_{\max}^{MW} = 4.68, P_{\min}^{MW} = 0$ and $\delta = 0.75$. The CHUs nominal power limits are $H_1 : P_{\max}^{MW} = 70, P_{\min}^{MW} = 9$, $H_2 : P_{\max}^{MW} = 70, P_{\min}^{MW} = 4$ and $H_3 : P_{\max}^{MW} = 115, P_{\min}^{MW} = 17$, where, H_1 and H_2 are upstream units of H_3 as shown in Fig. (7). Besides, their additional information is listed in [16]. The information related to PSUs is presented in [25]. In this paper, η is equal to 0.9. Finally, the market price data are available in Fig. (8).

a. Without considering availability: The generation bids of CO and IO of units and the expected profit of CO and IO of units are shown in table (3) and table (4) respectively. Without considering reliability through WT-ANN-ICA method, the expected profit in CO (WFs, PV, CHUs and PSUs coordinated) is $198318.3, which is increased by $15764.84 in comparison with sum of expected profit in IO. Using WT-ANN-ICA method is more accurate comparing with WT-ANN method in which the mathematical expected profit is respectively increased to 7034.47 and $4292.8 for IO and CO.

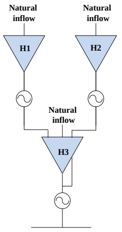

Fig. 7: Hydro system configuration used in this study

b. With considering availability: The energy generation bids, when availability is taken into account in some hours, are less than its amounts without considering availability as listed in table (3); indeed, they may downsize the expected profit. These are the same expected results because if availability is considered the less number of units are available in some hours. Since FOR of WFs are quite low, in most hours, WFs bids are the same in two states.

Considering reliability and using WT-ANN-ICA method, the expected profit can increase to the rate of $13474.32 in CO (WFs, PV, CHUs and PSUs coordinated) than IO as displayed in table (4). It is observed that the expected profit when availability is ignored is more than the state where availability is taken into account.

The sum of expected profits gained by CO of three types of generation units and the other type of unit, are also given in table (2). The obtained results confirm the growth of profit in CO of four unit types.

c. Financial risk (FR)

Because risk assessment is one of the important quantities in environments involving uncertainties [26], In order to study the imbalance revenue/cost, which is one of the main factors of FR in the proposed model, imbalance revenue is provided in a table (5). Vividly, its value is elevated in CO comparing with IO. Using WT-ANN-ICA method, imbalance revenue decreases in both CO and IO. Obviously, when the generation units fail in delivering scheduled power, they will get penalties; on the other hand, if they generate more than enough, they will get paid in lower prices.

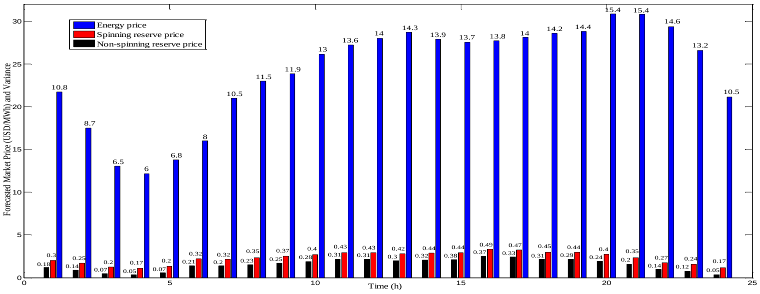

Fig. 8: The forecasted market price (energy price, spinning reserve and non-spinning reserve) and their variance.

TABLE III

Power generation bids (MW) of WFs, PV, CHUs and PSUs in CO and IO with and without availability using WT-ANN-ICA method

Reliability		Without Availability					With availability				
State operation		IO				CO	IO				CO
Load	Time	WFs	PV	CHUs	PSUs		WFs	PV	CHUs	PSUs	
250	t1	171	0	93	-36	240.5	171	0	93	-26	248
180	t2	171.5	0	57.6	-98	129.1	۸۴	0	57.6	-98	46.5
185	t3	171	0	26	-98	85	۸۴	0	26	-98	22
190	t4	170	0	27.3	-98	110.7	83.5	0	27.3	-98	24.5
195	t5	168.5	0	30.3	-98	115.6	168.5	0	30.3	-68	125.5
200	t6	168.5	1.008	40	-98	125	168.5	1.008	40	-98	125
260	t7	167.3	1.548	57.7	12	259.5	167.3	1.548	57.7	2	239.7
250	t8	168	1.95	80.1	-89	178	168	1.95	80.1	-89	178
310.5	t9	166.5	2.002	101.5	44	310.5	166.5	0	101.5	-16	256.1
355	t10	165.5	2.56	111.2	58	349	165.5	0	111.2	68	355
355.5	t11	165	3.2	118.9	58	355.5	165	3.2	118.9	58	355.5
361	t12	165	4.12	121.5	58	361	165	4.12	121.5	58	361
350	t13	164.5	4.68	124	58	349.5	164.5	4.68	63.5	58	295
365	t14	165.7	4.61	126.2	58	365	165.7	4.61	65.7	58	300.5
375.5	t15	163	4.2	130.7	58	371.4	163	4.2	130.7	62	375.2
381	t16	163.6	3.31	145.87	58	380.6	163.6	3.31	109.4	58	329
378	t17	164	3	147.3	58	378	164	3	110.5	58	341
394	t18	163	2.145	148.9	58	382.3	163	2.145	148.9	68	393.1
390	t19	159.5	1.45	152.6	-36	281	159.5	1.45	152.6	-16	298
395	t20	161.5	0	162.5	98	431.5	161.5	0	162.5	98	431.5
390	t21	161	0	162.8	58	386.8	161	0	162.8	58	386.8
395	t22	159	0	162.8	68	395	159	0	162.8	68	395
380	t23	158.6	0	140.1	-4	308.8	158.6	0	140.1	-4	308.8
360	t24	158.5	0	120.5	58	349	158.5	0	120.5	68	358

TABLE IV

Expected profit in CO and IO with and without availability using WT-ANN-ICA and WT-ANN methods

		Expected Profit (USD)			
		Without Reliability		With Reliability	
		WT+ANN	WT+ANN+ICA	WT+ANN	WT+ANN+ICA
IO	WFs	89915.82	94208.77	86175.65	90389.54
	PV	1068.28	1068.28	955.7	955.7
	CHUs	74525.01	74525.01	62671.24	62671.24
	PSUs	12751.42	12751.4	12307.9	12307.9
	Total	178260.57	182553.46	162110.49	166324.38
CO	(WFs+PV+CHUs)&PSUs	182378.65	188355.37	166523.1	171265.45
	(WFs + PSUs+PV)&CHUs	186856.3	192123.42	170272.6	175434.6
	WFs+PV+CHUs+PSUs	191283.83	198318.3	174183	179798.7

TABLE V

Imbalance revenue ($) in CO (WFs+PV+CHUs+PSUs) and IO using WT-ANN-ICA and WT-ANN methods

	Without Reliability				With Reliability			
	WT-ANN		WT-ANN-ICA		WT-ANN		WT-ANN-ICA	
State Operation	IO	CO	IO	CO	IO	CO	IO	CO
Imbalance revenue	24946.63	28904.77	21162.3	25863.65	22008.45	25018.52	28721.33	22417.84
[16]	24396.54	28585.21	20771	24639.9	Not studied			
[18]	24435.76	25311.74	21082	25761.2				

IV. CONCLUSIONS

In this paper, two methods were proposed for decreasing WFPG and PVG uncertainty as a main factor of decreasing profit and increasing FR.

The first method, HM of WT-ANN-ICA, tries to predict more accurately and improve short-term errors of WFPG. Proposed method results in less error prediction than previous studies. Therefore, more real scenarios might be generated with a greater probability and WFs optimal programming is done more accurately. As a result, the expected profit may enhance.

In the second method, for the first time, establishing a unit commitment policy among WFs, PV, CHUs and PSUs, the uncertainty and FR of WFs can diminish using two pumping and generating PSUs and CHUs. Indeed, CHUs utilization occurs when PSUs generation mode does not have enough capacity while WFPG and PVG drops severely. In addition, considering shift capabilities of WFPG and PVG based on PSUs and CHUs capabilities during peak time, the profit of these units might accrue in comparison with IO.

In the end, probabilistic programming model of WFs, PV, CHUs and PSUs with consideration of reliability is presented. Since the generation bids are based on this model, it is possible to achieve them in real time generation with acceptable reliability.

APPENDIX

$$P_S(t) \le \begin{pmatrix} \sum_{w=1}^{W_N} P^{W}_{G\max}(w).AV(s_w,w,t) + \sum_{ps=1}^{PS_N} P^{PS}_{G\max}(ps).AV(s_{ps},ps,t) + \sum_{h=1}^{H_N} P^{H}_{G\max}(h).AV(s_h,h,t) \\ + \sum_{pv=1}^{PV_N} (P^{PV}_{G\max}(pv) + \delta P^{\max DCH}_{BATT}(k=pv)).AV(s_{pv},pv,t) \end{pmatrix} \tag{A.1}$$

$$P_G(s_w,s_p,s_{pv},s_{ps},s_h,t) = \begin{pmatrix} \sum_{ps=1}^{PS_N} P^{PS}_{G}(s_w,s_p,s_{pv},s_{ps},s_h,ps,t) + \sum_{w=1}^{W_N} P^{W}_{G}(s_w,w,t) + \\ \sum_{h=1}^{H_N} P^{H}_{G}(s_w,s_p,s_{pv},s_{ps},s_h,h,t) + \sum_{pv=1}^{PV_N} P^{PV}_{G}(s_{pv},pv,t) \end{pmatrix} \tag{A.2}$$

$$P^{PS}_G = \tag{A.3}$$
$$\begin{Bmatrix} P^{PS}_g(s_w,s_p,s_{pv},s_{ps},s_h,ps,t) = (a_{ps}(qr(s_w,s_p,s_{pv},s_{ps},s_h,ps,t))^2 + b_{ps}qr(s_w,s_p,s_{pv},s_{ps},s_h,ps,t) + c_{ps})generationMOD \\ -P^{PS}_P(s_w,s_p,s_{pv},s_{ps},s_h,ps,t) = -(a_{ps}(pr(s_w,s_p,s_{pv},s_{ps},s_h,ps,t))^2 + b_{ps}pr(s_w,s_p,s_{pv},s_{ps},s_h,ps,t) + c_{ps})pumpingMOD \end{Bmatrix}$$

$$v^u(ps,t) = v^u(ps,t-1) - gr(s_w,s_p,s_{pv},s_{ps},s_h,ps,t-1) + pr(s_w,s_p,s_{pv},s_{ps},s_h,ps,t-1) \tag{A.4}$$

$$v^L(ps,t) = v^L(ps,t-1) + gr(s_w,s_p,s_{pv},s_{ps},s_h,ps,t-1) - pr(s_w,s_p,s_{pv},s_{ps},s_h,ps,t-1) \tag{A.5}$$

$$v^u_{\min}(ps) \le v(s_w,s_p,s_{pv},s_{ps},s_h,ps,t) \le v^u_{\max}(ps) \tag{A.6}$$

$$v^L_{\min}(ps) \le v(s_w,s_p,s_{pv},s_{ps},s_h,ps,t) \le v^L_{\max}(ps) \tag{A.7}$$

$$v^u(ps,t=T) > v^u(ps,end) \;\; v^u(ps,t=1) = v^u(ps,ini), \tag{A.8}$$

$$v^l(ps,t=T) = v^l(ps,end) \;\; v^l(ps,t=1) = v^l(ps,ini), \tag{A.9}$$

$$gr_{\min}(ps).I^g(ps,t).AV(s_{ps},ps,t) \le gr(s_w,s_p,s_{pv},s_{ps},s_h,ps,t) \le gr_{\max}(ps).I^g(ps,t).AV(s_{ps},ps,t) \tag{A.10}$$

$$pr_{\min}(ps).I^p(ps,t).AV(s_{ps},ps,t) \le pr(s_w,s_p,s_{pv},s_{ps},s_h,ps,t) \le pr_{\max}(ps).I^p(ps,t).AV(s_{ps},ps,t) \tag{A.11}$$

$$\begin{pmatrix} P^{PS}_G(s_w,s_p,s_{pv},s_{ps},s_h,ps,t).I^g(ps,t) \\ + SR^g(s_w,s_p,s_{pv},s_{ps},s_h,ps,t) + N.SR.on(s_w,s_p,s_{pv},s_{ps},s_h,ps,t) \end{pmatrix} \le p^{PS}_{G\max}(ps).I^g(ps,t).AV(s_{ps},ps,t) \tag{A.12}$$

$$\begin{pmatrix} P^{PS}_P(s_w,s_p,s_{pv},s_{ps},s_h,ps,t).I^p(ps,t) \\ + SR^p(s_w,s_p,s_{pv},s_{ps},s_h,ps,t) + \mathrm{N.SR.down}\,(s_w,s_p,s_{pv},s_{ps},s_h,ps,t) \end{pmatrix} \ge -\mathrm{p}^{\mathrm{p}}_{\max}(ps).I^p(ps,t).AV(s_{ps},ps,t) \tag{A.13}$$

$$\mathrm{N.SR.down}\,(s_w,s_p,s_{pv},s_{ps},s_h,ps,t) \le \left(QSC(ps).(1 - I^g(ps,t) - I^p(ps,t))\right).AV(s_{ps},ps,t) \tag{A.14}$$

$$I^g(ps,t) + I^p(ps,t) \le 1 \tag{A.15}$$

$$\begin{pmatrix} SR^p(s_w,s_p,s_{pv},ps,t).I^p(ps,t) \\ + \mathrm{N.SR.down}\,(ps,t).I^p(s_w,s_p,s_{pv},ps,t) \end{pmatrix} \le P^{PS}_p(s_w,s_p,s_{pv},ps,t).I^p(ps,t) \tag{A.16}$$

$$R_{C,PS}(ps,t) \le (SR^p(s_w,s_p,s_{pv},s_{ps},s_h,ps,t) + SR^g(s_w,s_p,s_{pv},s_{ps},s_h,ps,t)) \tag{A.17}$$

$$N_{C,PS}(ps,t) \le (N.SR.on(s_w,s_p,s_{pv},s_{ps},s_h,ps,t) + N.SR.down(s_w,s_p,s_{pv},s_{ps},s_h,ps,t)) \tag{A.18}$$

$$P^W_G(w,t) \le P^W_{G\max}(w).AV(s_w,w,t) \tag{A.19}$$

$$Q_h(\hat{h},t) = QS_h(\hat{h},t-\tau_{h,\hat{h}}) + QT_h(\hat{h},t-\tau_{h,\hat{h}}) \tag{A.20}$$

$$Q_h(\hat{h},t+\tau_{h,\hat{h}}) = q(h,t) + S(h,t) = QS_h(\hat{h},t) + QT_h(\hat{h},t) \tag{A.21}$$

$$v(h,t) = v(h,t-1) + \left(\sum_{\hat{h}=1}^{H_N} (R_{\hat{h},h}.Q_{\hat{h}}(s_w,s_p,s_{pv},s_{ps},s_h,h,t-1)) - q(s_w,s_p,s_{ps},s_{pv},s_{ps},s_h,h,t-1) + u(h,t-1) - S(s_w,s_p,s_{pv},s_{ps},s_h,h,t-1) \right) \tag{A.22}$$

$$q_{\min}(h).M(h,t).AV(s_h h,t) \le q(s_w,s_p,s_{pv},s_{ps},s_h,h,t) \le q_{\max}(h).M(h,t).AV(s_h,h,t) \qquad t \in \{1,\dots.T\} \tag{A.23}$$

$$v_{\min}(h) \le v(h,t) \le v_{\max}(h) \qquad t \in \{1,....T\} \tag{A.24}$$

$$v(h,0) = v(h,ini), v(h,T) = v(h,end), \qquad t \in \{1,.....T\} \tag{A.25}$$

$$P_G^H(s_w, s_p, s_{pv}, s_{ps}, s_h, w, ps, h, t) = \tag{A.26}$$

$$(k_{1h} \times q^2(s_w, s_p, s_{pv}, s_{ps}, s_h, w, ps, h, t) + k_{2h} \times q(s_w, s_p, s_{pv}, s_{ps}, s_h, w, ps, h, t) + k_{3h}) \qquad t \in \{1,....T\}$$

$$P_G^H(s_w, s_p, s_{pv}, s_{ps}, s_h, w, ps, h, t+1) - P_G^H(s_w, s_p, s_{pv}, s_{ps}, s_h, w, ps, h, t) \le 60.RU_h.AV(s_h, h, t) \tag{A.27}$$

$$P_G^H(s_w, s_p, s_{pv}, s_{ps}, s_h, w, ps, h, t) - P_G^H(s_w, s_p, s_{pv}, s_{ps}, s_h, w, ps, h, t+1) \le 60.RD_h.AV(s_h, h, t) \tag{A.28}$$

$$S_h^{\min}.AV(s_h, h, t) \le S_h(s_w, s_p, s_{pv}, s_{ps}, s_h, w, ps, h, t) \le S_h^{\max}.AV(s_h, h, t) \tag{A.29}$$

$$M(h,t) - M(h,t-1) = N'(h,t) - N(h,t) \tag{A.30}$$

$$N'(h,t) - N(h,t) \le 1 \tag{A.31}$$

$$0 \le P_{BATT}^{CH}(pv, s_{pv}, t) \le P_{BATT}^{\max CH}(pv) Z_{CH}(pv, s_{pv}, t) \tag{A.32}$$

$$0 \le P_{BATT}^{DCH}(pv, s_{pv}, t) \le P_{BATT}^{\max DCH}(pv) Z_{DCH}(pv, s_{pv}, t) \tag{A.33}$$

$$Z_{CH}(pv,t) + Z_{DCH}(pv,t) \le 1 \tag{A.34}$$

$$ENR(k, t=1) = ENR_{ini}(k), ENR(k, s_{pv}, t=24) \ge ENR_{end} \tag{A.35}$$

$$ENR(k, s_{pv}, t) = ENR(k, s_{pv}, t-1) + P_{BATT}^{CH}(k, s_{pv}, t-1) - P_{BATT}^{DCH}(k, s_{pv}, t-1) \tag{A.36}$$

$$P_S^{pv}(pv, s_{pv}, t) = P_G^{pv}(pv, s_{pv}, t) - P_{BATT}^{CH}(pv, s_{pv}, t) + \delta P_{BATT}^{DCH}(pv, s_{pv}, t) \tag{A.37}$$

REFERENCES

[1] Ali Sefidgar-dezfouli Mahmood Joorabian Elaheh Mashhour, “Microgrid optimal scheduling considering normal and emergency operation,” 10.22111/IECO.2019.27484.1100.

[2] Mehrdad Ahmadi Kamarposhti, “Optimal Control of Islanded Micro grid Using Particle Swarm Optimization Algorithm,” 10.22111/IECO.2018.24354.1022.

[3] Reza Safipour 1 Mahmoud Oukati Sadegh, “Optimal Planning of Energy Storage Systems using Symbiotic Organisms Search Algorithm,” 10.22111/IECO.2018.23950.1004.

[4] Pousinho. H.M.I., Mendes. V.M.F., Catalão.J.P.S, “A hybrid PSO–ANFIS approach for short-term wind power prediction in Portugal,” Energy Conversion and Management, 52:397e402, 2011.

[5] Mohandes. M., Rehman. S., Rahman. S.M., “Estimation of wind speed profile using adaptive Neuro-Fuzzy inference system (ANFIS),” Applied Energy, vol. 88, Issue 11, pp.4024-4032, 2011.

[6] Lijie Wang, Lei Dong, Ying Hao, Xiaozhong Liao, “Wind Power Prediction Using Wavelet Transform and Chaotic Characteristics,” IEEE Conf, 2009.

[7] Vahid Khorani, Nafiseh Forouzideh, Ali Motie Nasrabadi, “Artificial Neural Network Weights Optimization Using ICA, GA, ICA-GA and R-ICA-GA: Comparing Performances,” IEEE Conf, 2011.

[8] Amin Shokri Gazafroudi, Nooshin Bigdeli, Mostafa Yousefi Ramandi, Arim Afshar, “A hybrid model for wind power prediction composed of ANN and imperialist competitive algorithm (ICA),” The 22nd Iranian Conference on Electrical Engineering (ICEE 2014), May 20-22, 2014.

[9] Juan M. Morales, Antonio J. Conejo, Juan Perez-Ruiz, “short term trading for a wind power producer,” IEEE Trans. Power Syst., vol. 25, no. 1, Feb 2010.

[10] L. Bayón, J.M. Grau, M.M. Ruiz, P.M. Suárez, A comparative economic study of two configurations of hydro-wind power plants, Energy, 112: 8e16, 2016.

[11] A. Tiohy, P. Meibom, E. Denny, and M. O’Malley, “Unit Commitment for Systems with Significant Wind Penetration,” IEEE Trans. on Power Syst, vol. 24, no. 2, pp. 592–601, May 2009.

[12] J. M. Morales, A. J. Conejo, and J. Pérez-Ruiz, “Economic Valuation of Reserves in Power Systems with High Penetration of Wind Power,” IEEE Trans. on Power Syst, vol. 24, no. 2, pp. 900–910, May 2009.

[13] Mansour Hosseini-Firouz, “Optimal offering strategy considering the risk management for wind power producers in electricity market,” Int J Electr Power Energy Syst 49-359-368, 2013.

[14] K. Lakshmi, S. Vasantharathna, “Gencos wind–thermal scheduling problem using Artificial Immune System algorithm,” Int J Electr Power Energy Syst 54:112-122, 2014.

[15] Huajie Ding, Zechun Hu, Yonghua Song, “Stochastic optimization of the daily operation of wind farm and pumped-hydro-storage plant,” Renewable Energy 48-571e578, 2012.

[16] Lisias V. L. Abreu, Mohammad E. Khodayar, Mohammad Shahidehpour and Lei Wu, “Risk-Constrained Coordination of Cascaded Hydro Units with Variable Wind Power Generation,” IEEE Trans. on Sustainable Energy, vol. 3, no. 3, July 2012.

[17] Huajie Ding, Zechun Hu, Yonghua Song, “Rolling Optimization of Wind Farm and Energy Storage System in Electricity Markets,” IEEE Trans. on Power Syst, vol. 30, no. 5, September 2015.

[18] Moein Parastegari, Rahmat-Allah Hooshmand, Amin Khodabakhshian, Amir-Hossein Zare, “Joint operation of wind farm, photovoltaic, pump-storage and energy storage devices in energy and reserve markets,” Int J Electr Power Energy Syst 64-275-284, 2015.

[19] J.P.S. Catalão, H.M.I. Pousinho, J. Contreras, “Optimal hydro scheduling and offering strategies considering price uncertainty and risk management,” Energy, 37: 237e244, 2012.

[20] E. Jafari, S. Soleymani, B. Mozafari, T. Amraee, “Optimal operation of a micro-grid containing energy resources and demand response program” Int. J. Environ. Sci. Techno, DOI 10.1007/s13762-017-1525-6, 2018.

[21] E. Jafari. "Determining Optimal Strategy of a Micro-Grid through Hybrid Method of Nash Equilibrium –Genetic Algorithm", International J. Emerging Electric Power Systems, DOI: 10.1515/ijeeps-2017-0148, 2019.

[22] Karki R, Hu P, Billinton R, “Reliability Evaluation Considering Wind and Hydro Power Coordination,” IEEE Trans. on Power Syst, vol. 25, pp. 685-693, 2010.

[23] Mosayeb Afshari Igder, Taher Niknam, Mohammad-Hassan Khooban, “Bidding strategies of the joint wind, hydro, and pumped-storage in generation company using novel improved clonal selection optimization algorithm,” 10.1049/IET-SMT.2017.0014.

[24] Amjady N. and Vahidinasab V, “Security-constrained self-scheduling of generation companies in day-ahead electricity markets considering financial risk,” Energy Conversion and Management, vol. 65, pp. 164-172, 2013.

[25] Parastegari M, Hooshmand R-A, Khodabakhshian A, Forghani Z. “Joint operation of wind farms and pump-storage units in the electricity markets: modeling, simulation and evaluation,” Simulat Modell Pract Theory, 37(11):56–69, 2013.

[26] Hooman Khaloie Amir Abdollahi, “Risk-Averse Pre-Extreme Weather Events Self-Scheduling of a Wind Power Plant: A Hybrid Possibilistic-Scenario Model,” 10.22111/IECO.2018.24149.1010.

Ehsan Jafari was born in Shahrekord, Iran, in 1986. He received Ph.D. degree in Department of Electrical Engineering, Science and Research Branch, Islamic Azad University, Tehran, Iran in 2017. He is now a Assistant Professor in Department of Electrical Engineering, Lenjan Branch, Islamic Azad University, Isfahan, Iran. His research interests are operation and planning of deregulated power system, load and energy management, renewable energy and smart grids.

IECO

This page intentionally left blank.